A Quantum Mechanical Study of the Phase Stability and Phase Transition Mechanisms in $CaCO_3$ at Finite Temperature and Pressure

David Carrasco de Busturia

Department of Chemistry

Imperial College London

A thesis submitted for the degree of

Doctor of Philosophy

November 2018

Declaration of Originality

I hereby declare that the research presented in this thesis is my own. It has not been submitted in any form for another degree or academic qualification at any university or institution of higher education. Information derived from any Internet sources, books, and published or unpublished work of others has been acknowledged in the text and a list of references is given in the bibliography. Any additional sources of information have been appropriately referenced.

The research presented in this thesis was conducted under the supervision and guidance of Professor Nicholas M. Harrison at Imperial College London in South Kensington.

David Carrasco de Busturia

November 2018

Declaration of Copyright

Abstract

First-principles calculations have been performed to explore the temperature-pressure phase diagram of calcium carbonate ($CaCO_3$) in a range of temperatures and pressures up to 1000 K and 10 GPa respectively. The calcite I - calcite II and calcite I - aragonite phase boundaries have been obtained. Imaginary phonon modes in the aragonite phase suggest pathways to three distinct alternative phases that involve symmetry breaking and distortion of the unit cell. The variation of the Gibbs free energy with pressure and temperature has been computed in the quasi-harmonic approximation. Several approaches have been discussed in this thesis for the most accurate determination of the temperature - pressure phase boundary. A method for determining the calcite I - calcite II second order phase boundary has been described in this work. Hybrid exchange and GGA density functional theory in the all-electron linear combination of atomic orbitals approximation have been exploited, as well as the effect of the inclusion of van der Waals dispersion corrections. The resultant theoretical phase diagram is compared to the available measurements.

The detailed theoretical understanding of the phase transitions mechanisms developed in this thesis sets the basis for a future exploration of the thermodynamic stability phase of $CaCO_3$. In this respect, the methodology described in this work could be used to predict the temperature - pressure phase boundaries of the rest of the polymorphs of this complex system, e.g. phase transitions occurring in calcite III, IIIb, IV, V and VI.

Acknowledgements

I would like to thank my supervisor Prof. Nicholas Harrison for sharing his enormous scientific knowledge and wisdom, and for giving me the opportunity to pursue a PhD at Imperial College as a Marie Skłodowska-Curie Fellow, in the Innovative Training Network NanoHeal, a project funded by the European Union's Horizon 2020 research and innovation programme. This Network and the conferences held for the project have served as an excellent opportunity for exchanging results, ideas and knowledge, among scientists from completely different expertises. This has allowed me to acquire invaluable transferable, communication and networking skills, as well as contributing enormously to my professional development. I am incredibly grateful for having had the chance to share knowledge and ideas with the Early Stage Researchers and Professors from this Network. Specially, I would heartily like to thank Juan, Gøran, Gaute, Giu, Thomas and Alessandro for all their help. Finally, I would like to thank my family for their love and support since the beginning; for that I am forever grateful. I dedicate this work to them.

Publications

Publications based on this work:

Carrasco-Busturia, D. and Harrison, N. M. “The computed temperature-pressure phase diagram of the calcite I - calcite II phase transition“. *In preparation.*

Carrasco-Busturia, D. and Harrison, N. M. “Computed phase transition mechanisms in the thermodynamic stability field of aragonite”. *In preparation.*

Presentations

Selection of the presentations based on this work:

TALKS

Postgraduate Symposium, Imperial College London, 4 July 2018.

6th NanoHeal Meeting, 23-28 April 2018, Tromsø/Loen/Kalvåg, Norway.

4th NanoHeal Meeting and 5th NanoHeal School, 2-5 May 2017, Nurnberg, Germany

3rd NanoHeal Meeting and 4th NanoHeal School, 20-25 November 2017, Ein Bokek, Dead Sea, Israel

UK's High Performance Computing Materials Chemistry Consortium, University College London, 21 December 2016.

2nd NanoHeal Meeting and 3rd NanoHeal school, 12-17 June 2016, Magleås, Denmark

2nd NanoHeal School, 15-19 February 2016, Gran Canaria, Spain

1st NanoHeal Network Meeting and 1st NanoHeal School, 19-23 October 2015, Lyon, France

POSTERS

Computed Phase Stability and Phase Transition Mechanisms in $CaCO_3$ *at Finite Temperature and Pressure* , Goldschmidt Conference, Paris, 13-18 August 2017

Postgraduate Symposium, Imperial College London, 5 July 2017.

MSSC2018: Ab initio Modelling in Solid State Chemistry, Imperial College London, 17-21 September 2018.

MSSC2017: Ab initio Modelling in Solid State Chemistry, Imperial College London, 18-22 September 2017.

MSSC2016: Ab initio Modelling in Solid State Chemistry, Imperial College London, 19-23 September 2016.

MSSC2015: Ab initio Modelling in Solid State Chemistry, Imperial College London, 14-18 September 2015.

Contents

1 Introduction **35**

1.1 The Temperature-Pressure phase diagram of $CaCO_3$ 37

1.2 Core motivation, research question and thesis outline 38

2 Background Theory **40**

2.1 Elements of Crystallography 40

2.1.1 Bravais Lattices 40

2.1.2 The Unit cell 42

2.1.3 Fractional coordinates 43

2.1.4 The crystal structure 44

2.1.5 The reciprocal lattice 46

2.2 Elements of Quantum Mechanics 48

2.2.1 The Electronic Problem 48

2.2.2 The Born-Oppenheimer Approximation 51

2.2.3 The Variational Principle 54

2.2.4 Spin Orbitals and Slater determinant 55

2.2.5 Hartree-Fock Approximation 56

2.2.6 Density Functional Theory 59

2.2.6.1 The First Hohenberg-Kohn Theorem 60

2.2.6.2 The Second Hohenberg-Kohn Theorem 62

2.2.6.3 The Kohn-Sham Approach 63

2.2.6.4 Approximate Exchange-Correlation Functionals 68

2.2.6.5 Dispersion correction 70

2.2.7 From Atomic Orbitals to Bloch Functions 71

2.2.7.1 One-dimensional chain of atoms 71

2.2.7.2 Two-dimensional crystal 80

2.2.7.3 Three-dimensional crystal 83

2.2.8 From Molecular Orbitals to Crystalline Orbitals 87

2.2.9 Building the matrices 88

2.2.10 The Self Consistent Field 90

2.3 Elements of Thermodynamics 91

2.3.1 Work, Heat and the First Law of Thermodynamics 91

2.3.2 Second Law of Thermodynamics 93

2.3.3 Third Law of Thermodynamics 93

2.4 Elements of Statistical Mechanics 94

2.4.1 The Partition Function 94

2.4.2 The definition of Entropy 101

2.4.3 The definition of Energy 107

2.4.4 The definition of Pressure 108

2.4.5 Decomposition of the total partition function 110

2.5 Partition Function in a periodic system 112

2.5.1 The Vibrational Partition Function 112

2.5.2 The Helmholtz Free energy 116

2.5.3 The Vibrational Entropy 117

2.5.4 The Energy at finite temperature 119

2.5.5 The Heat Capacity 120

2.5.6 The Gibbs Free energy 123

2.6 Classification of phase transitions 123

3 Methodology 126

3.1 Harmonic and quasi-harmonic approximations 126

3.1.1 Elements of Harmonic Lattice Dyanmics 126

3.1.1.1 Dimer in one dimension 126

3.1.1.2 Vibrations for a collection of atoms 133

3.1.1.3 Periodic system 137

3.1.1.4 Deficencies of the Harmonic approximation 141

3.1.2 Framework of the Quasi-Harmonic Approximation 141

3.1.3 Deficiencies of the quasi-harmonic approximation 145

3.2 Distortion of the geometry along a soft phonon mode 145

4 The polymorphism of the calcite system 149

4.1 Calcite I 153

4.1.1 The direct lattice 153

4.1.2 The reciprocal lattice 157

4.1.3 Crystal structure 158

4.2 Aragonite 160

4.3 Vaterite 161

4.4 High-pressure polymorphs 165

4.4.1 Calcite II 165

4.4.2 Calcite III and IIIb 168

4.4.3 Calcite VI 169

4.5 High temperature polymorphs 170

4.5.1 Calcite IV and V 170

5 Benchmarking accurate thresholds and description of higher symmetry structures found 173

6 Electronic structure of Calcite I 180

6.1 Electronic and charge distribution 180

6.2 Electronic band structure and density of states 181

7 Calcite I - calcite II phase transition 186

7.1 Literature review on the CI-CII phase transition 186

7.2 The theoretical approach 188

7.3 Mechanism of the phase transition in the athermal limit 189

7.4 Automation of the process 198

7.5 Influence of finite temperature 199

7.6 Determination of the phase boundary 206

7.6.1 Intersection between Gibbs free energy surfaces, $G(P, T)$ 206

7.6.1.1 First approach: calculation of $P(V, T)$ by summing directly over frequencies 208

7.6.1.2 Second approach: calculation of $P(V, T)$ as the derivative of $F(V, T)$ 210

7.6.1.3 Discussion of first and second approaches 210

7.6.2 Intersection between Gibbs free energy curves, $G(P)$, at a fixed temperature 210

7.7 Justification of the theoretical results based on the Clapeyron equation 217

7.8 Phase transition on expanded supercells 218

7.9 Convergence study on calcite I 220

7.10 Convergence study on calcite II 222

7.11 Stability of calcite II in expanded supercells 223

7.12 A possible explanation for imaginary frequencies found at expanded supercells . 233

7.13 Linear fit and other approaches for modeling $G(P)$ 233

7.13.1 Second order phase transition at higher temperatures 237

7.14 Common tangent approach 243

7.15 Comparison between the common tangent approach and the cubic fit approach . 246

7.16 Determination of the TP phase boundary above the critical temperature 246

8 Phase transitions in the thermodynamic stability field of Aragonite 252

9 Conclusions 261

10 Appendix **265**

10.1 Codes generated for this thesis 265

10.2 Bulk Modulus 266

Bibliography **267**

List of Tables

5.1 A difference in energy of 0.036 Ha/F.U. or 95.29 KJ/mol is observed for calcite I between two different basis sets: BSA (triple-zeta valence with polarization quality for the calcium and oxygen atoms and double-zeta valence with polarization for the carbon atom) and pob-TVPZ (triple zeta in all three atoms of calcium, carbon and oxygen). All computational thresholds are maintained constant for this comparison. 178

5.2 Calcite I numerically integrated density (in units of the charge of one electron). There are 100 electrons in the unit cell of calcite I, thus the exact value is $100|e|$. Using a finer grid (`XXLGRID`), the difference in the integrated density with respect to the exact value is $1.42 \cdot 10^{-4}|e|$. 179

6.1 The result of the Mulliken Analysis of Calcite I shows that the calcium ion in the solid is charged positively with 1.78 times the charge of the electron and the carbonate group is charged negatively with 1.78 times the charge of the electron. 181

6.2 Number of electrons per atom and total number of electrons in the primitive cell. There is a total of 100 electrons for calcite I. 182

6.3 Band gaps obtained for calcite I, for PBE and B3LYP (with and without dispersion) and LDA levels of theory, well as the experimental value. 183

7.1 Summary of the imaginary frequencies found in all the explored constrained volumes of calcite I for the PBE-D3 level of theory. The space group found is a result of a symmetry search (imposing a low tolerance) over the broken symmetry structure found as a consequence of the distortion of the atomic positions along the phonon eigenvector. Space groups 14 and 161 have no imaginary frequencies at the $\mathbf{\Gamma}$ point. 190

7.2 Different space groups obtained when analyzing the symmetry of the structure at the bottom of the curve (Fig. 7.3b) of the most compressed calcite I volume ($54.7 \mathring{A}^3$). The column "Tolerance" refers to a FINDSYM threshold in $\mathring{A}$ on the lattice parameters and atomic coordinates. Both the symbol and the space group number corresponding to that symbol in parentheses are shown on the second column. 192

7.3 Imaginary frequencies found in all the explored constrained volumes of calcite I for the PBE level of theory 197

7.4 Imaginary frequencies found in all the explored constrained volumes of calcite I for the B3LYP level of theory 197

7.5 Imaginary frequencies found in all the explored constrained volumes of calcite I for the B3LYP-D3 level of theory 197

7.6 List of the eight first frequencies at the Γ point for calcite I at two of the stable volumes considered in Fig. 7.3a,b. These frequencies are shown in ascending order, so that the i label only accounts for the position of the sorted list of frequencies. It may occur that the frequency labelled as $i = 3$ on both volumes does not correspond to the same eigenvector and thus the same vibration. . . . 208

7.7 Lattice parameters for the calcite I (CI) and calcite II (CII) structures, both volume-constrained at the same volume, 56.9 $\mathring{A}^3$/formula unit. The Landau supercell (sc) is the supercell expansion matrix (Eq. 7.5) studied for calcite I. Regarding calcite II, the primitive cell and an integer multiple of the diagonal supercell expansion matrix (Eq 7.6) have been studied. The number of dispersion k-points for the phonon calculation, the number of atomic orbitals (A.O.), number of atoms and the number of k-points in the Irreducible part of the Brillouin Zone (IBZ) according to the Monkhorst-Pack scheme are also reported. 219

7.8 Entropy and entropy difference between the Landau supercells studied for the equilibrium volume of calcite I 221

7.9 Entropy and entropy difference between the diagonal supercells studied for the calcite II at the constrained volume of 56.948 $\mathring{A}^3$/F.U. 223

7.10 Imaginary frequencies found in all the explored constrained volumes of the expanded supercells of calcite I for the PBE-D3 level of theory. 224

7.11 Imaginary frequencies found in all the explored constrained volumes of the expanded supercells of calcite I for the PBE level of theory. 224

7.12 Imaginary frequencies found in all the explored constrained volumes of the expanded supercells of calcite I for the B3LYP-D3 level of theory. 225

7.13 Imaginary frequencies found in all the explored constrained volumes of the expanded supercells of calcite I for the B3LYP level of theory. 225

7.14 Critical temperature T_c found for PBE-D3, PBE, B3LYP-D3 and B3LYP levels of theory 248

8.1 Experimentally, calcite I is found to be more stable than aragonite at 1 atm and 298K. This result is in agreement with PBE and B3LYP levels of theory. B3LYP-D3 stabilizes aragonite only by -0.094 KJ/mol, as opposed to PBE-D3 (-2.102 KJ/mol). ΔG has been calculated at 298 K and 1 atm, considering the transformation Calcite I $\rightarrow$ Aragonite, i.e. $\Delta G = G_{\mathrm{Arag}} - G_{\mathrm{CI}}$. ΔE has been calculated at 0 K and zero pressure. 253

8.2 Imaginary phonon modes observed at Γ on the expanded volumes of aragonite. Once the broken symmetry structure has been isolated, a frequency calculation at Γ is conducted. There are some cases where an imaginary frequency is observed as well over this broken symmetry structure. All PBE level of theory. Note a: the constant volume optimization of this structure is a long process that requires more than 100 steps. 255

9.1 Summary of the Gibbs free energy thermodynamic stability of calcite I, II and aragonite. 264

10.1 Experimental and calculated bulk modulus for calcite I in the athermal limit (including zero point motion effects), and at 291.41 K with PBE-D3 level of theory and using molecular dynamics. 267

List of Figures

1.1 (1.1a) and (1.1b) show, respectively, the profile of temperature and pressure versus the distance from the surface of the earth. Figure adapted from Refs. [23]. 36

1.2 Experimental phase diagram of $CaCO_3$ gathering all the available information so far for this material. 38

2.1 Three types of Bravais lattices with the most symmetric disposition of the three lattice vectors in each case: simple cubic (sc), body-centered cubic (bbc) and face-centered cubic (fcc) with coordination numbers of 6, 8 and 12 respectively. Figure adapted from Ref. [36] 41

2.2 Primitive (grey) and conventional (white) unit cells for the bcc (2.2a) and fcc (2.2b) Bravais lattices. The primitive cell for the bcc has half the volume of the conventional cubic cell. The primitive cell for the fcc has one quarter the volume of the conventional cubic cell. Figure reproduced from Ref. [36]. 42

2.3 Wigner-Seitz primitive cell for a two dimensional lattice. 43

2.4 Any atomic position in space is given by $\mathbf{R} + \mathbf{r}$. This situation is applicable in 3D. 43

2.5 A basis and a lattice gives the crystal structure. Figure reproduced from Ref. [37]. 44

2.6 The seven crystal systems and 14 Bravais lattices. The lattice points (black and gray points) do not represent atoms. They represent places in space that are indistinguishable from each other. Symbols P, C, I, F and R refer to different lattice types: P = primitive; C = centered in the faces perpendicular to the c axis; I = centered in the body of the cell; F = centered in all faces of the cell; R = primitive, identical cell axes and cell angles. Figure reproduced from Ref. [38]. 45

2.7 First Brillouin zone for an oblique lattice in two dimensions. From O we draw a set of vectors to the nearby points in the reciprocal lattice. Then we construct lines perpendicular to these vectors at their midpoints. The first Brillouin zone is the smallest enclosed area. 47

2.8 Summary of the DFT formulation 67

2.9 Direct (upper panel) and reciprocal (lower panel) lattices for a one-dimensional chain of atoms. 72

2.10 One-dimensonal chain of atoms described by an orbital φ_μ centered on each atom. The position of each atom inside each nth cell is described by the vector $\mathbf{A}_\mu$. 73

2.11 One-dimensonal chain of atoms described by an orbital φ_μ centered on each atom. $\mathbf{r}$ is the position of an electron in orbital φ_μ. The position of each atom inside each nth cell is described by the vector $\mathbf{A}_\mu$, so that $\mathbf{r} = \mathbf{A}_\mu + \mathbf{m}$. 74

2.12 Four unit cells of length a, each of them containing one atom represented by a black dot. $\varphi_\mu(\mathbf{r})$ is some arbitrary orbital located on some atom in the chain; $\varphi_\mu(\mathbf{r} - \mathbf{A}_\mu - \mathbf{a})$ lies at a distance $\mathbf{a}$ along the chain, $\varphi_\mu(\mathbf{r} - \mathbf{A}_\mu - 2\mathbf{a})$ at a distance $2\mathbf{a}$, and so on, from $\varphi_\mu(\mathbf{r} - \mathbf{A}_\mu)$. For simplicity, the shape of the orbitals is omitted, but is to be considered as an arbitrary orbital. 75

2.13 Dispersion $E(\mathbf{k})$ versus $\mathbf{k}$ band for a situation described in Figure (2.12), where there is only one atom per unit cell, described by an orbital $\mathbf{A}_\mu$. For simplicity, this orbital is described in this figure as a spheric s type orbital. 76

2.14 Four unit cells of length a, each of them containing two atoms. The labels represent the same as in 2.12, where $\mathbf{a}' = 2\mathbf{a}$. 76

2.15 Wavefunctions for the one-dimensional lattice (Equations (2.115) to (2.121b)). . 78

2.16 Dispersion $E(\mathbf{k})$ versus $\mathbf{k}$ band for a situation described in Figure (2.14), where there are two atoms per unit cell, each of them described by an orbital $\mathbf{A}_\mu$. For simplicity, this orbital is described in this figure as a spheric s type orbital. . . . 79

2.17 Process by which the “folding back” of the dispersion curve for the one orbital cell results in the dispersion curve for the two orbital cell. Image obtained from Ref. [64]. 79

2.18 Dispersion curve for the three (a) and four (b) orbital cell. Image obtained from Ref. [64]. 80

2.19 Square 2D lattice described by the translation vectors $\mathbf{a}_1$ and $\mathbf{a}_2$. 80

2.20 First Brillouin zone of a 2D square lattice. The points X, M and Γ are points in reciprocal space. 81

2.21 Wavefunctions for the two-dimensional lattice 82

2.22 Band structure for a square lattice of H atoms. Γ, X and M points correspond to the wavefunctions shown in Fig. 2.21. Image reproduced from Ref. [64]. . . . 83

2.23 First Brillouin zone for a simple cubic lattice. The points R, X, M and Γ are indicated, as explained in the text. Figure obtained from Ref. [65]. 84

2.24 First Brillouin zone for a body centered cubic lattice. The points N, is indicated, as explained in the text. Figure reproduced from Ref. [65]. 86

2.25 First Brillouin zone for a face centered cubic lattice. The points L is indicated, as explained in the text. Figure reproduced from Ref. [65]. 87

2.26 The infinite hamiltonian matrix of AOs (left) is transformed to a infinite block-diagonal matrix. Once we set a finite number of **k** points, the matrix becomes finite. 88

2.27 Sign convention for work and heat in thermodynamics 92

2.28 An ensemble of $\mathcal{A}$ macroscopic systems in thermal equilibrium provided by a heat bath. a_j is the number of systems in the state j with energy $E_j\,(N, V)$. Since an ensemble is a conceptual idea, we shall consider $\mathcal{A}$ to be as large as we want. 95

2.29 Representation of each of the possibilities reported in Eq. 2.189. 100

2.30 This is an ensemble consisted of $\mathcal{A} = 8$ systems. In each system there are 4 states. There are 3 systems in the first state, 2 systems in the second state, 2 systems in the third state and 1 system in the fourth state. Thus, $a_1 = 3, a_2 = a_3 = 2$ and $a_4 = 1$. Note that $\sum_j a_j = 8 = \mathcal{A}$. 101

2.31 This is an ensemble consisted of $\mathcal{A} = 8$ systems. All the systems are in state 1, therefore $W = 1$ (Eq. 2.192), which is the minimum value that W can adopt, and corresponds to a situation of maximum order. 102

2.32 This is an ensemble consisted of $\mathcal{A} = 6$ systems. There are only $j = 2$ possible states in each system. In a situation of maximum disorder, $a_1 = a_2 = ... = a_j$, and since $\sum_j a_j = \mathcal{A}$, then $a_j = \frac{\mathcal{A}}{j}$. Thus, $a_1 = a_2 = 6/2 = 3$, which is what is shown in the figure. 102

2.33 First three energy levels for a quantum harmonic oscillator. 113

2.34 Representation of the function $y = |\exp\,(-x)|$. 114

2.35 Summary with the shape of the main thermodynamic functions for a first order and second order phase transition. 124

3.1 Two masses m_1 and m_2 connected by a spring separated by a distance x_{eq}. . . . 127

3.2 For the HCl molecule, the harmonic potential (Eq. 3.10) is shown in black and the experimental intermolecular potential is shown in red. Figure adapted from Ref. [74]. 129

3.3 Brown circles: energy scan along the soft phonon mode of frequency -87.6 cm^{-1} observed in the calcite I structure for a percentage of compression corresponding to 15% using the PBE-D3 level of theory. A symmetric double well potential is observed (for more details refer to text). 146

4.1 Experimental phase diagram of $CaCO_3$ gathering all the available information so far for this material. 150

4.2 (4.2a) Hexagonal cell. (4.2b) rhombohedral cell 153

4.3 (a): The basis of the rhombohedral cell is labelled as $\mathbf{a_R}$, $\mathbf{b_R}$ and $\mathbf{c_R}$. (b): Projection along $\mathbf{c_H}$. The basis of the hexagonal centered cell is labelled as $\mathbf{a_H}$, $\mathbf{b_H}$ and $\mathbf{c_H}$. 154

4.4 Different projections of an hexagonal Bravais Lattice: 4.6a: three-dimensional projection, where the vectors $\mathbf{a}_1$, $\mathbf{a}_2$, $\mathbf{a}_3$ are shown, as well as the unitary vectors $\hat{x}, \hat{y}$ and $\hat{z}$. 6.4e and 4.4c: two-dimensional representation. The unitary vector $\hat{y}$ and $\hat{z}$ coincide with the $\mathbf{a}_2$ and $\mathbf{a}_3$ vectors respectively. The $\mathbf{a}_1$ vector is at an angle of α with respect to $\hat{x}$, and at an angle of β with respect to $-\hat{y}$ 154

4.5 First Brillouin Zone of the trigonal crystal of calcite I. On green, a path along several reciprocal lattice points is shown: $\mathbf{L} = [1/2, 0, 0]$, $\mathbf{F} = [1/2, 1/2, 0]$, $\mathbf{\Gamma} = [0, 0, 0]$, $\mathbf{T} = [1/2, 1/2, 1/2]$. The k-point **T** can also be labeled as **Z**. Some of these reciprocal lattice points will be crucial for understanding phase transitions in this material. 158

4.6 View of the crystallographic (4.6a) and primitive (6.4e) cells of Calcite I. Fig. 4.6b: all carbonate groups are located at planes parallel to (001), pointing to opposite directions, as shown with two different colors: blue and purple. 159

4.7 Two types of angles are described in the octahedral environment of a calcium ion: 87.425° and 92.575°. 159

4.8 Structure of Aragonite: 4 formula units in the unit cell, where the carbonate planes are one on top of the other in different planes, oriented in opposite directions. Fig. (4.8a) is a projection on the *ab* plane, showing the ninefold coordination of calcium ion. Fig. (4.8b) highlights a single calcium atom and the 6 types of bonds (bonds to 2 Oxygen atoms in each of 3 carbonate groups) and the 3 types of bonds (bonds to 1 Oxygen atom in 3 other carbonate groups). For more details, refer to text. 161

4.9 Structures of vaterite proposed so far. Models are based on hexagonal, monoclinic, or orthorhombic lattices. Figure updated and inspired from Burgess *et al.* [111]. Rectangles filled in blue and yellow indicate theoretical and experimental studies respectively. For more details refer to text. 162

4.10 Wang's proposed structure for Vaterite, with two types of Ca sites: octahedras **1**(Ca−O distances of about 2.350−2.440 Å) and octahedras **2** (Ca−O distances of about 2.313−2.460 Å). 164

4.11 Structure of calcite II: (4.11a) shows the octahedral coordination of the four calcium ions per formula unit, and the carbonate groups pointing alternately in two different directions. (4.11b) shows the polyhedron and again the alternate orientation of the carbonate groups. Unlike in Aragonite, each calcium atom is coordinated to only one oxygen atom of a carbonate group. (4.11c) is a similar projection as (4.11a) but shows only the Ca−O distances in each octahedron. From this figure we can define 4 types of octahedrons: $\mathrm{Oh}_1 - \mathrm{Oh}_4$, not oriented in the same way. An inversion symmetry operation relates Oh_1 and Oh_3, and similarly between Oh_2 and Oh_4, as is shown in (4.11d). 166

4.12 Structure of calcite III: (4.12a) and (4.12b) show a projection on the *ab* and *ac* plane respectively. (4.12c) shows the unit cell of Calcite III, with 10 formula units. (4.12d) shows the three different sites of the calcium atoms with coordination numbers of 7, 8 and 9. 167

4.13 Structure of Calcite IIIb: (4.13b) and (4.13b) show the projection on the planes *ab* and *ac* respectively (the same planes from which Calcite III was visualized in Figures (4.12a) and (4.12b). (4.13c) shows the unit cell of Calcite IIIb, with 4 formula units. (4.13d) shows the the calcium atoms with coordination numbers of 8. 169

4.14 Structure of Calcite VI: (4.14a) shows the orientation of the carbonate groups in the structure. (4.14b) is a projection on the *bc* plane. (4.14c) shows the distances Ca−O and the 7+2 coordination number of both calcium sites. 171

4.15 (a) Phase I at 787 K. (b) Phase IV at 1151 K. The carbonate groups occupy parital positions O1 and O2. (c) Phase V at 1275 K. The carbonate ion can freely rotate. In order to obtain a similar atom arrangement as phases I and IV, Calcite V has been drawn with $a_V = -a_I$, $b_V = -b_I$ and two units cells along the c axis. Image reproduced from Ishizawa *et al.* [131]. 172

5.1 Energy-volume curves for calcite IIIb (space group 2). By analyzing the symmetry of each volume with the FINDSYM program, a symmetry of P_2/c (space group 13) is observed for the last two points highlighted with magenta arrows. Fig. 5.1b: Removing these last 2 points for calcite IIIb, and showing also S.G. 13.176

5.2 Fig. 5.2a: Energy-volume curves for calcite VI (space group 2). By analyzing the symmetry of each structure with the FINDSYM program, a symmetry of P_2/c (space group 13) is observed for the last 3 points highlighted with magenta arrows. Fig. 5.2b: Removing the last 3 points for calcite VI, and showing also S.G. 13. 176

5.3 5.3a: Distance Ca1-O8 as a function of volume for calcite IIIb, in the reference 000 cell and the nearest 00-1 cell. From 62 to 67 $\mathring{A}^3$, two types of calcium-oxygen distances are observed: 2.6 and 4.1 $\mathring{A}$. From 67.5 $\mathring{A}^3$ onwards, the Ca1-O8 distance in both cells become equivalent. 5.3b: Schematic representation of both scenarios. 177

5.4 Space group 13 ($P2/c$): (5.4a) shows the orientation of the carbonate groups in the structure. (5.4b) shows the packaging of octahedras 177

5.5 Variation of the energy with the `TOLINTEG` and (Fig. 5.5a) `SHRINK` (Fig. 5.5a) thresholds. 178

5.6 Energy-volume curves for calcite IIIb and calcite VI using the pob-TVPZ basis set, and the tighter computational parameters described in the text. For all these volumes, a FINDSYM analysis yields a consistent P-1 space group, despite the fact that some jumps are also being observed. Both calcite IIIb and VI volumes present positive frequencies at the Γ point. 179

6.1 Three resonants forms of the carbonate group in gas phase. The charge of -2 is delocalized in the four atoms. 181

6.2 Fig. 6.2a shows the 110 plane, and 6.2b shows the electron density map projected on this plane. 6.2c shows the 3D isosurface. 6.2d shows a 3D orthoslice of the electron density parallel to the c axis. 182

6.3 Fig. 6.3a: Electronic band structure for Calcite I. In the y axis, the difference in energy between the absolute value of energy of each band and the energy of the Fermi level. The selected path of **K** points chosen contains the higher symmetry **K** points from the First Brillouin Zone shown in Fig. 4.5. The conduction band starts at band 51. The GAP energy, defined as the energy difference between the Fermi energy and the minimum value reached by band 51, is is found to be 0.1942 Hartree for the PBE-D3 level of theory. In the graph it has been identified a set of bands: Peak 1−Peak 2, which correspond to the homologous peaks shown in the density of states (Fig. 6.3b). 184

6.4 Density of states of calcite I, in which each set of peaks 1 - 7 shown in Fig. 6.3b is magnified. 185

7.1 Temperature - pressure experimental data for calcite I (triangles), calcite II (circles) obtained by Merlini *et al.* and Suito *et al.*, together with the calcite I - calcite II phase boundary represented with diamonds (Wang *et al.*, Hess *et al.*) and by a line (Bridgman) with the experimental error bars associated. 188

7.2 Electronic energy as a function of volume for calcite I, calcite II and the space group 161 found. Calcite I volumes that present imaginary frequencies are shown with empty red triangles. Stable calcite I volumes are represented with filled red triangles. All data is fitted to a cubic polynomial and PBE-D3 level of theory. . 190

7.3 (a): Energy-volume data for calcite I, calcite II and space group 161. (b): Energy as a function of the displacement for the soft phonon mode that leads to space group 14 (calcite II). (c): Eigenvectors for the distortion that leads to space group 14 and 161. An animation of both eigenvectors represented in (c) can be found in Ref. [173] 191

7.4 Calcite I in the Landau supercell representation (Fig. 7.4a) shows two pathways of transformation via imaginary phonon modes: towards space group 161 (Fig. 7.4b) through the softening of a phonon mode at Γ, or towards space group 14 (Fig. 7.4c) through the softening of a phonon mode at the F k-point. 193

7.5 Fig. 7.5a, upper panel: Energy-volume curves for calcite I, II and space group 161. The structure of each of the calcite II volumes highlated with an arrow (54.7, 56.2 and 60.9 $\mathring{A}^3$) are shown in Fig. 7.5a, lower panel, together with the calcite I structure at the same $V = 60.9\mathring{A}^3$. Fig. 7.5b: evolution of θ and Δ as a function of the athermal pressure, for the four levels of theory studied: PBE-D3, PBE, B3LYP and B3LYP-D3. 194

7.6 Electronic energy as a function of volume for calcite I, calcite II and the space group 161 found, for the PBE level of theory. 197

7.7 Electronic energy as a function of volume for calcite I, calcite II and the space group 161 found, for the B3LYP level of theory. 197

7.8 Electronic energy as a function of volume for calcite I, calcite II and the space group 161 found, for the B3LYP-D3 level of theory. 197

7.9 $E(V)$, $(E + E_{ZP})(V)$ and $F(V)$ (at two temperatures: 150.71 and 311.52 K), including volumes with imaginary phonons in the fit (7.9a) and excluding them (7.9b). The same color code has been used: red triangles for calcite I (filled: stable; empty: unstable), and filled green circles for calcite II. The space group 161 has been omitted for the sake of clarity. In the athermal limit (both with and without zero point motion, the inclusion of metastable volumes for calcite I does not have a significant effect on the quality of the fit. When studying $F(V)$ at finite temperature (e.g. 311.52 K) the equation that fits the stable volumes of calcite I does not describe well these volumes near the phase transition (e.g. the volume marked with an arrow color magenta). On the other hand, if the metastable calcite I volumes are not considered in the fit, the model produces a better description of calcite I near the phase transition (the equivalent volume is now closer to the fitting equation). All PBE-D3 level of theory. 201

7.10 Energy-volume and volume-pressure curves at 0 K, 150.71 K and 311.52 K, for the PBE-D3 level of theory. 202

7.11 Energy-volume and volume-pressure curves at 0 K, 150.71 K and 311.52 K, for the PBE level of theory. 203

7.12 Energy-volume and volume-pressure curves at 0 K, 150.71 K and 311.52 K, for the B3LYP level of theory. 204

7.13 Energy-volume and volume-pressure curves at 0 K, 150.71 K and 311.52 K, for the B3LYP-D3 level of theory. 205

7.14 The intersection between two surfaces (α and β) give us a curve, whose projection in the PT plane yields the temperature-pressure phase boundary we are looking for. Figure adapted from Ref. [178] 206

7.15 $G(P, T)$ scattered surface constructed either via summing directly over the frequencies (red circles), or by the derivative of the Hemholtz free energy (blue circles). All PBE-D3 level of theory. 209

7.16 Energetics for the PBE-D3 level of theory 213

7.17 Energetics for the PBE level of theory 214

7.18 Energetics for the B3LYP-D3 level of theory 215

7.19 Energetics for the B3LYP level of theory 216

7.20 Theoretical result for the calcite I - calcite II phase boundary, using B3LYP, B3LYP-D3, PBE and PBE-D3. The experimental phase boundaries are also reported: Bridgman [113], Wang *et al.* [158] Hess *et al.* [119], ... 217

7.21 Evolution of $\Delta\overline{V}_{\mathrm{trs}}$, $\Delta\overline{S}_{\mathrm{trs}}$, and $\Delta\overline{H}_{\mathrm{trs}}$ with temperature and pressure across the temperature-pressure phase boundary shown in Fig. 7.20, for the B3LYP-D3 and PBE-D3 levels of theory. 218

7.22 PDOS and cumulated entropy for the equilibrium volume of calcite I. The supercells studied are integer multiples of the Landau supercell. 222

7.23 PDOS and cumulated entropy for the equilibrium volume of calcite II, at the volume of 56.948 $\AA^3$/F.U. The supercells studied are integer multiples of the diagonal supercell (Eq. 7.6). 223

7.24 Electronic energy as a function of volume for calcite I, calcite II and the space group 2 found, for the PBE-D3 level of theory. 224

7.25 Electronic energy as a function of volume for calcite I, calcite II and the space group 2 found, for the PBE level of theory. 224

7.26 Electronic energy as a function of volume for calcite I, calcite II and the space group 2 found, for the B3LYP-D3 level of theory. 225

7.27 Electronic energy as a function of volume for calcite I, calcite II and the space group 2 found, for the B3LYP level of theory. 225

7.28 (a) Electronic energy vs volume curves for calcite I and II. In addition, the space group 2 is also shown, as a consecuence of distorting the atomic coordinates of the most compressed volume of calcite II. (b) Scanmode over the -21.18 cm^{-1} imaginary phonon mode encountered over the calcite II structure at 54.66 $\AA^3$. The depth of this minimum is very low. (c) Eigenvectors for this phonon mode. An animation for this eigenvector is shown in Ref. [183]. 226

7.29 Transformation from the $n = 2$ diagonal supercell of calcite II at the most compressed volume (56.66 Å^3) to the space group 2. 227

7.30 Energetics for the expanded supercells in the PBE-D3 level of theory. 229

7.31 Energetics for the expanded supercells in the PBE level of theory. 230

7.32 Temperature-pressure calcite I- calcite II phase diagram for the PBE-D3 level of theory, by considering the Landau supercell for calcite I and the primitive cell for calcite II (dark green), and two times the Landau supercell and the $n = 2$ diagonal supercell for calcite II (light green). 231

7.33 All PBE level of theory, with calcite II using the $n = 2$ supercell (light green circles) or the primitive cell (dark green circles). Fig. 7.33a shows the temperatures; For the same reason as explained before, there is a critical temperature for which the Gibbs free energy curves coincide in a broad pressure range. This critical temperature is 673.33 K in this case. Fig. 7.33b is showing the same plot, but without temperatures. 231

7.34 Electronic energy - volume curves for the three times the Landau supercell for calcite I and the $n = 3$ diagonal supercell for calcite II. Only one calcite II volume does not present imaginary frequencies. 232

7.35 (Previous page). $G(P)$ curves at four different temperatures for calcite I and calcite II, where a cubic (left panel) and linear fit (right panel) has been adopted. For 311.52 K, a linear fit to the last volumes of calcite I and II has been studied as well. 236

7.36 $G(P)$ curves at four different temperatures for calcite I and calcite II. The range of pressures within a pink frame are those for which both curves are almost coincident. The mean value of pressure is also shown in this region. 236

7.37 Temperature-pressure phase boundary obtained with the following approaches: cubic, linear, linear restricted to last 3 volumes and the approach based on the mean value of pressure located beteween the highest pressure of calcite I and the lowest pressure for calcite II. 237

7.38 Temperature-pressure phase boundary using a linear approach, for the PBE-D3, PBE, B3LYP-D3 and B3LYP levels of theory. The error bar has been calculated according to Eq. 7.8. 238

7.39 Evolution of $V(P)$ at 10.0, 90.40, 311.52, 532.63, 693.43 and 753.74 K for the PBE-D3 level of theory. At each temperature, the pressure of transition for a linear fit apporach and the error bar associated is shown, respectively, with orange line and a light blue shadow. 240

7.40 Evolution of ΔV with temperature for PBE-D3, B3LYP-D3, B3LYP and PBE levels of theory. The error on ΔV at each temperature has been calculated according to Eq. 7.14. The temperature at which $\Delta V = 0$ is the critical temperature, T_c, and corresponds to the temperature at which there is a change in the order of the transition. The lower bound error for this T_c is given by the temperature at which the error bar on ΔV crosses the $\Delta V = 0$ line. 241

7.41 Temperature-pressure phase boundary using a linear approach, for the PBE-D3, PBE, B3LYP-D3 and B3LYP levels of theory. The error bar has been calculated according to Eq. 7.8. The experimental phase boundaries are also reported: Bridgman [113], Wang *et al.* [158] Hess *et al.* [119], as well as the critical point proposed by Barnett *et al.* [159] in thick dashed lines. The lower bound critical temperature obtained for PBE-D3 and B3LYP-D3 are shown with, respectively, dashed horizontal red and blue lines. 242

7.42 $E(V)$ curves for calcite I and II in the athermal limit (neglecting zero-point motion). The slope of the common tangent is shown, which is an equation that passes through points $[V_1, E_1(V_1)]$ and $[V_2, E_2(V_2)]$ Fig 7.42b is just the zoomed version of 7.42a. 244

7.43 Common tangent for calcite I and II $E(V)$, $(E + E_{ZP})(V)$ and $F(V)$ curves, across temperatures. 245

7.44 Temperature-pressure phase boundary obtained via intersection of Gibbs free energy curves (cubic fits) and by the common tangent procedure. All PBE-D3 level of theory. 247

7.45 Summarized version of Fig. 2.35. In this figure, only the evolution of $G(P)$ and $V(P)$ are shown for a first and second order phase transition. 248

7.46 Evolution of $V(P)$ for several temperatures below and at the critical temperature (T_c = 331.62 K), according to the cubic approach, for the PBE-D3 level of theory. The pressure of transition P_{trs} indicated in each case is just the pressure of intersection at each temperature according to the cubic fit. For 0, 10.00 and 90.40 K, the volumes for calcite I and II are interpolated on the $V(P)$ curves. An extrapolation is needed in the calcite I branch at 150.71, 311.52 and 331.52 K. 249

7.47 Evolution of $V(P)$ for several temperatures above the critical temperature (T_c = 331.62 K), according to the cubic approach, for the PBE-D3 level of theory. The pressure of transition P_{trs} indicated in each case is the pressure at which both $V(P)$ curves for calcite I and II meet. For temperatures close to T_c, e.g. 351.72, 452.22 or 552.72 K this meeting point arises from an extrapolation on the calcite I curve. 250

7.48 With circles: first order phase boundary corresponding to a first order phase transition. The cubic fit approach has been conducted. With crosses: a second order pressure-temperature phase boundary that corresponds to a second order phase transition. The pressure of transition at each temperature has been determined following the approach presented in Section 7.16. 251

7.49 Fig. 7.49a: $F(V)$ curve, and Fig. 7.49b: $V(P)$ curve at 854.24 K. 251

8.1 Energy-volume curves for aragonite and calcite I for B3LYP and B3LYP-D3 (8.1a) and PBE and PBE-D3 (8.1b). The inclusion of dispersion yields a stabilization of Aragonite respect to calcite I. 253

8.2 Broken symmetry structures found in the first set of imaginary phonon modes. All PBE level of theory 256

8.3 Broken symmetry structures found in the second set of imaginary phonon modes. All PBE level of theory. 257

8.4 Electronic energy-volume curves for aragonite, calcite I and the broken symmetry structures found, at 0 K and at different temperatures for the PBE level of theory. See text for complete description on the evolution of the stability with temperature. All PBE level of theory. 259

8.5 Calcite I - aragonite and aragonite - space group 19 phase boundaries. 260

9.1 9.1a: $G(P)$ for calcite I and aragonite at 311.52 K, for the PBE level of theory. The value of Gibbs free energy for both phases at 1 bar is shown. 9.1b: $G(P)$ for calcite I and II at 311.52 K, for the PBE-D3 level of theory. The value of Gibbs free energy for both phases at 1.28 GPa is shown. 264

10.1 $E(V)$, $P(V)$, $B(V)$ and $B(P)$ plots for the athermal limit, without zero point motion (10.1a - 10.1d), with zero point motion (10.1e - 10.1h), and at a finite temperature of 291.41 K (10.1i - 10.1l). 269

Chapter 1

Introduction

Calcium carbonate ($CaCO_3$) is one of the most abundant rock-forming minerals in the Earth's crust [1], occurring as the principal component of limestone and chalk cliffs [2]. Limestone, sand and gravel constitute the raw materials for the production of the largest volume manufactured solid on earth, concrete [3]. Concrete has been the building block for constructions over centuries. Most historic buildings in Europe are made of limestone, which are noticeably damaged by salt crystallization processes [4, 5]. Investment in finding healing solutions to this deterioration is among one of the European government priorities in order to preserve cultural patrimony.

$CaCO_3$ is one of the subproducts generated in the production of ordinary Portland cement [6], one of the most common cements in concrete, whose production contributes about 5% of global anthropogenic CO_2 emissions. More than 60% of these emissions have a fossil origin, mainly coming from the limestone rock. Hence, there is an important need to replace Portland cement with a greener alternative; e.g. several studies report the use of "low CO_2" concretes with different chemistry and mechanical properties [3, 7]. Not only is the cement industry interested in calcium carbonate, but also other industrial activities benefit from the application of this material, e.g. it forms part of optical devices [8], fillers and pigments in papers [9, 10], acts as a catalyst in the diamond formation at high pressures and temperatures [11, 12], and is the cause of calcareous scale depositions from hard water leading to lower heat transfer efficiency and a considerable increase of energy consumption specially in oil, gas and desalination industries [13], which causes a substantial economical loss.

Calcium carbonate is considered a candidate for carbon dioxide sequestration [14], which represents a promising alternative natural solution for the problem of the accumulation of carbon dioxide in the atmosphere. Carbon dioxide sequestration can be achieved via either a natural or an artificial path. A natural path is accomplished as a consequence of the important role calcium carbonate plays in the geochemical Carbon cycle in the Earth [15, 16], which highly affects the climate on our planet [17]. Subduction processes are responsible for supplying this Carbon into a deep Earth level [18], containing more than three quarters of Earth's Carbon [19, 20]. Since carbon solubility in mantle silicates such as olivine is extremely low [21], the majority of this carbon is to be hosted as carbonate minerals [22]. The high pressure polymorphs of calcite are possible host structures of CO_2 in the Earth's mantle [17], where pressures of 13-23 GPa (upper mantle) and 23-135 GPa (lower mantle) are reached [23] (see Fig. 1.1b).

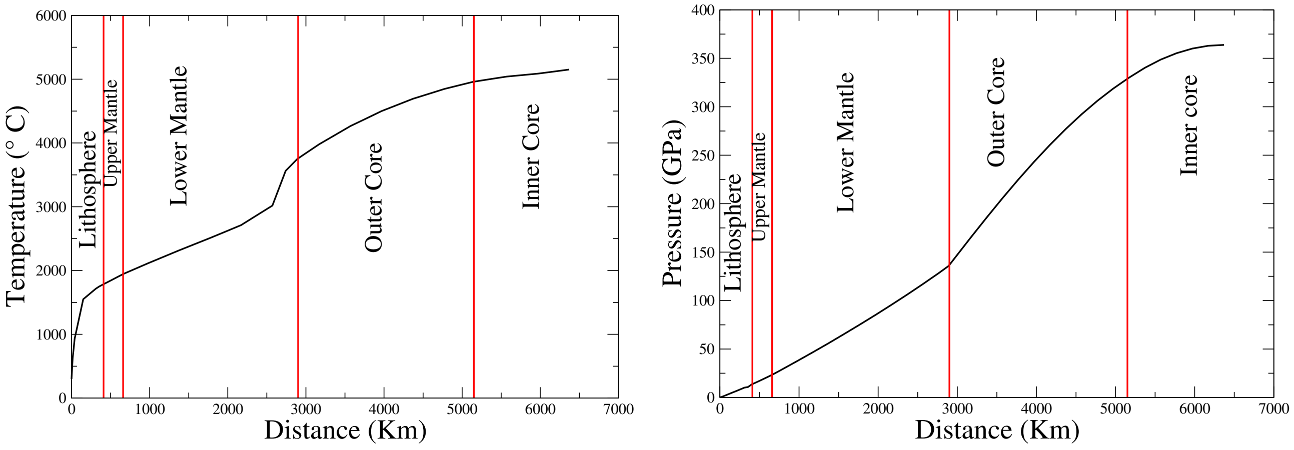

(a) **(b)**

Figure 1.1: (1.1a) and (1.1b) show, respectively, the profile of temperature and pressure versus the distance from the surface of the earth. Figure adapted from Refs. [23].

Artificial CO_2 sequestration can be conducted as well. Experts in enhanced oil recovery (EOR) processes claim that carbonate rocks constitute one of the largest oil reservoirs [24]. Because this gas strongly binds to the carbonate rocks, these are considered as excellent candidates for injection of CO_2. This allows for the possibility of large scale CO_2 storage. Not only does this material attract considerable geological and environmental interest, it is also involved in biological processes, as it plays a key role in self-healing processes, i.e. biomineralization of skeletons and shells of marine organisms [25]. A clear example of these are Scleractinian corals, one of the fastest marine mineralizing organisms [26], where their skeleton is a composite structure of organic components and aragonite, a polymorph of calcium carbonate. In these corals, the calcification process occurs in a biological confined environment, under the control of biological macromolecules [27]. Other examples found in nature are the case of organic-mineral bio-composite materials such as Abalone nacre, which is a composite of aragonite grains glued together by biopolymers. This material has a fracture toughness 1000 times higher than aragonite [28]. Something as relevant as the mineralization of artificial bone can be guided by developing self-assembled materials that mimic these natural self-healing processes [29].

From a fundamental physics point of view, most recent studies suggest that calcium carbonate nucleation pathways do not follow classical nucleation theory [30, 31], which presents an opportunity to a development of new theories on heterogeneous nucleation.

1.1 The Temperature-Pressure phase diagram of $CaCO_3$

Pressure and temperature significantly affect the structure of calcite ($CaCO_3$), resulting in a rich polymorphism: 10 distinct solid phases have indeed been reported so far [17, 15]. In fact, no other compound exhibits polymorphic variation as commonly and abundantly in nature as does $CaCO_3$ [32]. Beside calcite I that is the most stable at ambient conditions, the others (calcite II, III, IIIb, IV, V, VI, aragonite and vaterite) are high temperature and/or high pressure phases. In Fig. 1.2 we have assembled the experimental stability data available so far, which will be explained with much more detail in Chapter 4. It is apparent that the phase boundaries between polymorphs are not clearly defined experimentally. In this respect, the accurate characterization of the structural and energetic transformations occurring in calcite as a function of both temperature and pressure represents a challenge to the state of the art experimental and theoretical techniques, is of great interest and is yet to be fully accomplished. For instance, the pressure-temperature phase diagram of the seemingly simple calcite I to calcite II phase transition has not yet been obtained theoretically. The study of this phase transition is of great interest in order to better understand any other phase transformation on calcite, since this is the very first transformation that occurs when applying pressure on this material.

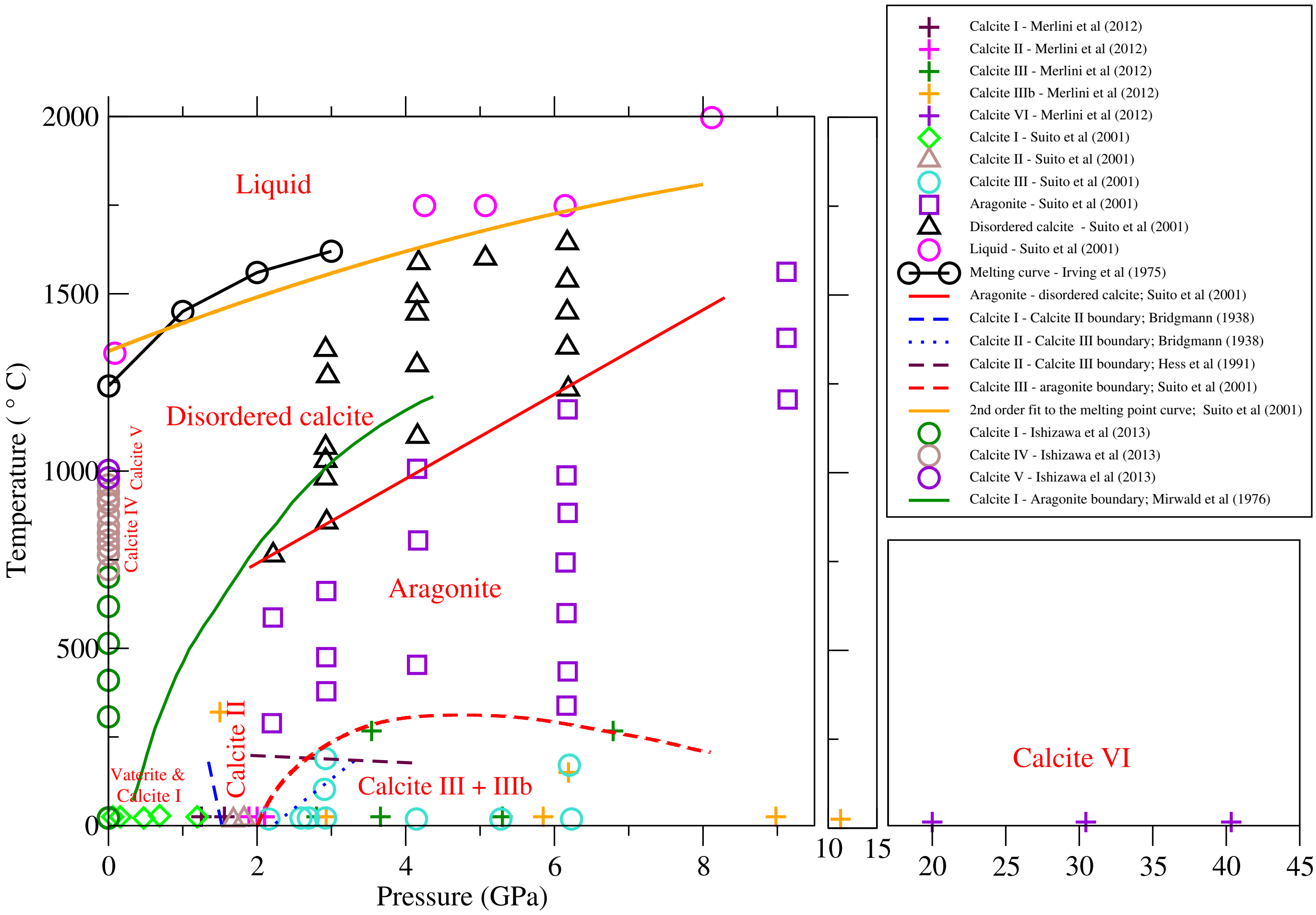

Figure 1.2: Experimental phase diagram of $CaCO_3$ gathering all the available information so far for this material.

1.2 Core motivation, research question and thesis outline

As has already been shown, this TP phase diagram is a complex one. The main purpose of this project is to successfully compute the phase diagram of calcium carbonate, and understand the mechanism of phase transitions involved using first principles simulation techniques. Standard *ab initio* techniques account for the energy at zero kelvin and zero pressure. The simultaneous effect of both temperature and pressure is something that can be computed by state of the art techniques, such as *ab intio molecular dynamics* [33, 34, 35]. Unfortunately, this approach is computationally very expensive. As will be thoroughly explained in Chapter 3, the sole effect of pressure can be taken into account if the geometry optimization is performed at several volume constraints. On the other hand, the unique effect of temperature can be addressed by computing the vibrations, or phonons in a periodic system.

My personal interest and motivation for this project comes from my education in Theoretical Chemistry, and my concern how to include a simultaneous effect of pressure and temperature in an *ab initio* simulation, and then to extend this formalism to a solid state system, to obtain something as relevant as the TP phase diagram. As has been presented earlier in this chapter, calcium carbonate is an ubiquitous material with obvious polymorphism, which makes it a perfect candidate to study and unravel the unknown phase transition mechanisms that lead to each of those polymorphs presented in Fig. 4.1.

The aim of this thesis is to understand the phase stability and phase transition mechanisms occurring in calcium carbonate at finite temperature and pressure in order to generate the computed temperature-pressure phase boundary.

The overall structure of this thesis is as follows: Chapter 2 contains a background theory used throughout this thesis, followed by a more concise Methodology Chapter 3. The experimentally known polymoprhs are described in Chapter 4. The benchmarking of accurate computational thresholds is discussed in Chapter 5. The electronic structure of calcite I is studied in Chapter 6. Special attention has been given to the calcite I to calcite II phase transition, are covered in Chapter 7. Phase transitions occurring in Aragonite, as well as the calcite I to Aragonite phase transition are summarized in Chapter 8. Special emphasis is given to the effect of the DFT functional used, as well as the inclusion of dispersion interactions. Finally, Chapter 9 gives the conclusions and identification of limitations and ideas that deserve further investigation.

Chapter 2

Background Theory

2.1 Elements of Crystallography

The aim of this section is to present essential concepts of crystallography needed to gain a better understanding of the crystal structures considered in this thesis.

2.1.1 Bravais Lattices

A **lattice** is a regular periodic arrangement of points in space. The Bravais lattice specifies the periodic array in which the repeated units of the crystal are arranged. A three dimensional Bravais Lattice consists of the set of all lattice points with position vectors **g** or **R** of the form:

$$\mathbf{g} = \mathbf{R} = n_1\,\mathbf{a}_1 + n_2\,\mathbf{a}_2 + n_3\,\mathbf{a}_3 \tag{2.1}$$

where n_i are integers (0, 1, 2 ...). This vector is called the translational vector. Thus, the point $\sum_i n_i\mathbf{a}_i$ is reached by moving n_i steps of length a_i in the direction of $\mathbf{a}_i$ for $i = 1, 2, 3$. The vectors $\mathbf{a}_i$ appearing in the definition of a Bravais lattice are called *primitive vectors*, that generate or span the lattice:

$$\mathbf{a}_1 = (a_{1x}\,,\, a_{1y}\,,\, a_{1z}) \qquad \mathbf{a}_2 = (a_{2x}\,,\, a_{2y}\,,\, a_{2z}) \qquad \mathbf{a}_3 = (a_{3x}\,,\, a_{3y}\,,\, a_{3z}) \tag{2.2}$$

There are several Bravais lattices:

- **Simple cubic (sc)** lattice.

It consists of three perpendicular primitive vectors of equal length (Fig. 2.1a):

$$\mathbf{a}_1 = a\,\hat{x} \qquad \mathbf{a}_2 = a\,\hat{y} \qquad \mathbf{a}_3 = a\,\hat{z} \tag{2.3}$$

- **Body-centered cubic (bcc)** lattice.

It is formed by adding to the simple cubic lattice an additional point, at the center of the cube (Fig. 2.1b). The most symmetric set of lattice vectors is:

$$\mathbf{a}_1 = \frac{a}{2}\,(\hat{y}+\hat{z}-\hat{x}) \qquad \mathbf{a}_2 = \frac{a}{2}\,(\hat{z}+\hat{x}-\hat{y}) \qquad \mathbf{a}_3 = \frac{a}{2}\,(\hat{x}+\hat{y}-\hat{z}) \tag{2.4}$$

- **Face-centered cubic (fcc)** lattice.

Formed by adding to the simple cubic lattice an additional point in the center of each square face (Fig. 2.1c). A symmetric set is:

$$\mathbf{a}_1 = \frac{a}{2}\,(\hat{y}+\hat{z}) \qquad \mathbf{a}_2 = \frac{a}{2}\,(\hat{z}+\hat{x}) \qquad \mathbf{a}_3 = \frac{a}{2}\,(\hat{x}+\hat{y}) \tag{2.5}$$

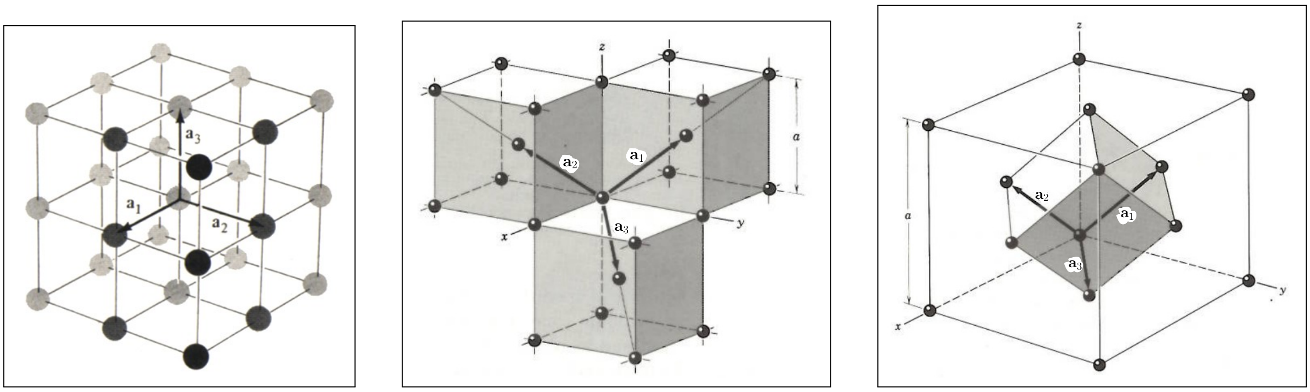

(a) simple cubic (sc) **(b)** body-centered cubic (bbc) **(c)** face-centered cubic (fcc)

Figure 2.1: Three types of Bravais lattices with the most symmetric disposition of the three lattice vectors in each case: simple cubic (sc), body-centered cubic (bbc) and face-centered cubic (fcc) with coordination numbers of 6, 8 and 12 respectively. Figure adapted from Ref. [36]

- **Simple hexagonal (sh)** lattice.

This Bravais lattice is the building block for the hexagonal lattice of Calcite I. For this reason, we will explain it in closer detail in Section 4.1.1.

2.1.2 The Unit cell

The unit cell is a parallelepiped-shaped volume cell that gives the whole Bravais lattice when reproduced in 3D. The volume of a cell is defined by the lattice vectors $\mathbf{a}_1$, $\mathbf{a}_2$ and $\mathbf{a}_3$ as:

$$V = |\mathbf{a}_1 \cdot (\mathbf{a}_2 \times \mathbf{a}_3)| \tag{2.6}$$

There are two main unit cells: the **primitive**, which is a minimum-volume cell and contains only one lattice point (there are lattice points at the eight corners of the parallelepiped, but each is shared among the eight neighbour cells), and the **conventional**, which contains more than one lattice point. Because the bcc and fcc lattices contain two and four lattice points, these can be conceived as conventional unit cells. For example, the body-centered cubic cell and the face-centered cubic cell have, respectively, 2 times and 4 times the volume of the primitive cell embedded inside the conventional lattice (Fig. 2.2a and 2.2b). The sc unit cell can be considered either primitive or conventional since the two are equivalent. The shape of the unit cell is completely defined by the lattice parameters $a = |\mathbf{a}_1|$, $b = |\mathbf{a}_2|$ and $c = |\mathbf{a}_3|$, and the angles α, β and γ. Another way of choosing a cell of equal volume V is by (a) drawing lines that connect a given lattice point to all neighbour lattice points, and (b) at the midpoint and normal to these lines, draw new perpendicular lines. The smallest volume enclosed in this way is the **Wigner-Seitz** primitive cell (Figure 2.3).

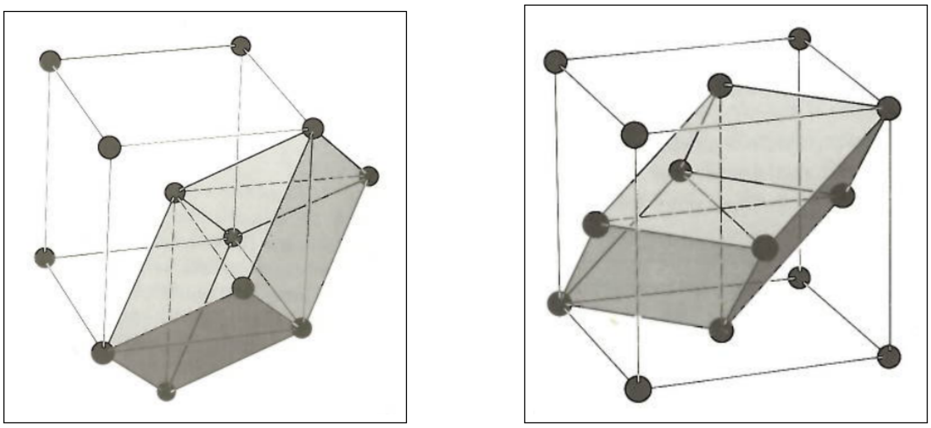

(a) Body-centered cubic (bcc) **(b)** Face-centered cubic (fcc)

Figure 2.2: Primitive (grey) and conventional (white) unit cells for the bcc (2.2a) and fcc (2.2b) Bravais lattices. The primitive cell for the bcc has half the volume of the conventional cubic cell. The primitive cell for the fcc has one quarter the volume of the conventional cubic cell. Figure reproduced from Ref. [36].

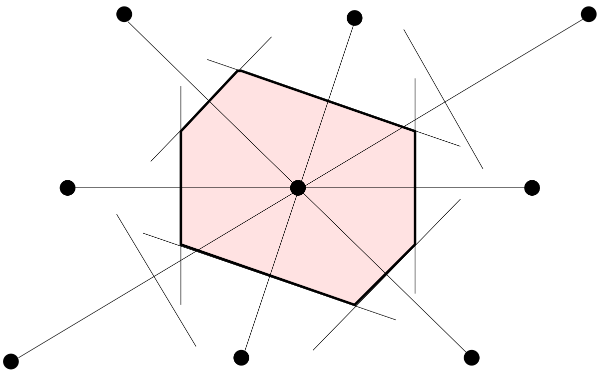

Figure 2.3: Wigner-Seitz primitive cell for a two dimensional lattice.

2.1.3 Fractional coordinates

The atomic positions are specified by the use of **fractional coordinates**:

$$\mathbf{r} = f_1\,\mathbf{a}_1 + f_2\,\mathbf{a}_2 + f_3\,\mathbf{a}_3 \tag{2.7}$$

where f_i are the fractional coordinates of the atom inside a given cell. These are obtained by dividing the absolute atomic coordinates x_i in a particular direction by the length of the lattice parameter in that direction, i.e.

$$f_i = \frac{x_i}{|\mathbf{a}_i|} \tag{2.8}$$

In this way, the coordinates of the atom located in the body center are $(\frac{1}{2}, \frac{1}{2}, \frac{1}{2})$. The atomic position for the face centers are $(\frac{1}{2}, \frac{1}{2}, 0)$, $(0, \frac{1}{2}, \frac{1}{2})$, $(\frac{1}{2}, 0, \frac{1}{2})$. We can generalize this situation and conclude that the atomic position of any atom in a periodic system is given by the vector $\mathbf{R} + \mathbf{r}$ (Fig. 2.4).

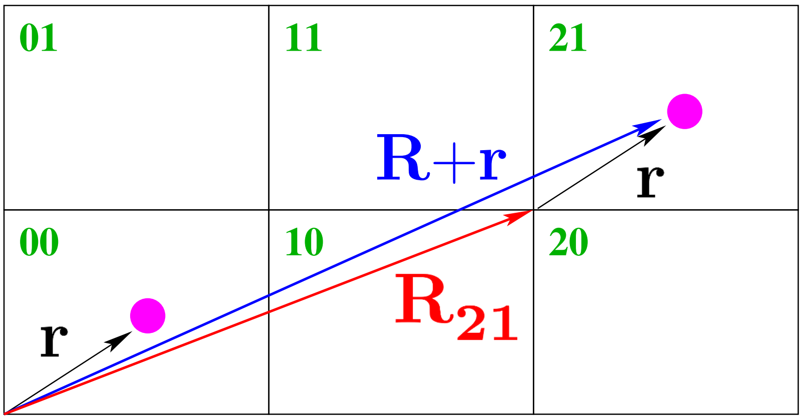

Figure 2.4: Any atomic position in space is given by $\mathbf{R} + \mathbf{r}$. This situation is applicable in 3D.

2.1.4 The crystal structure

The **basis** consists of a single or groups of atoms, molecules, groups of molecules or ions. The **crystal structure** is formed only when the **basis** of atoms is attached to each lattice point:

$$\text{lattice } + \text{basis } = \text{crystal structure}$$

In other words, a crystal structure is formed by the addition of a basis to every lattice point, as shown in Fig. (2.5). A symmetry transformation or symmetry element is a rigid operation that transforms the lattice into itself. The set of all symmetry transformations of a crystal structure or Bravais lattice is known as the **symmetry group** or **space group** of the crystal structure or Bravais lattice. We will consider a single unit cell that presents the same symmetry elements of the entire Bravais lattice. This unit cell is usually a conventional and not primitive unit cell. We can consider two symmetry operations: translation through a Bravais lattice vector $\mathbf{R}$ and a point operation, which includes all symmetry operations that are not translations. The types of point operations are Inversion, Reflection, Rotation and Rotation-Inversion. All symmetry operations of a given Bravais lattice form part of a set known as the **point group** of the Bravais lattice. It turns out to be **seven** different point groups that a Bravais lattice can have, known as **crystal systems**: triclinic, monoclinic, orthorhombic, tetragonal, cubic, trigonal and hexagonal. (Figure 2.6, in which lattice points are connected by lines). For instance, if there is no symmetry, the three lattice parameters have different module, and the three angles are different from each other and from 90° (triclinic system).

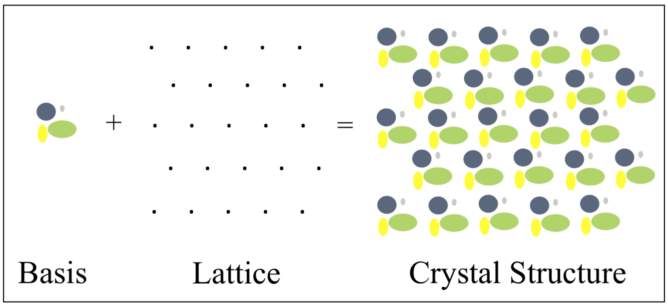

Figure 2.5: A basis and a lattice gives the crystal structure. Figure reproduced from Ref. [37].

If the translational symmetry is considered, then it turns out to be **14** different symmetry groups that a given Bravais lattice can adopt, shown entirely in Figure 2.6.

If we no longer consider the individual lattice points but also the basis, we now have to consider

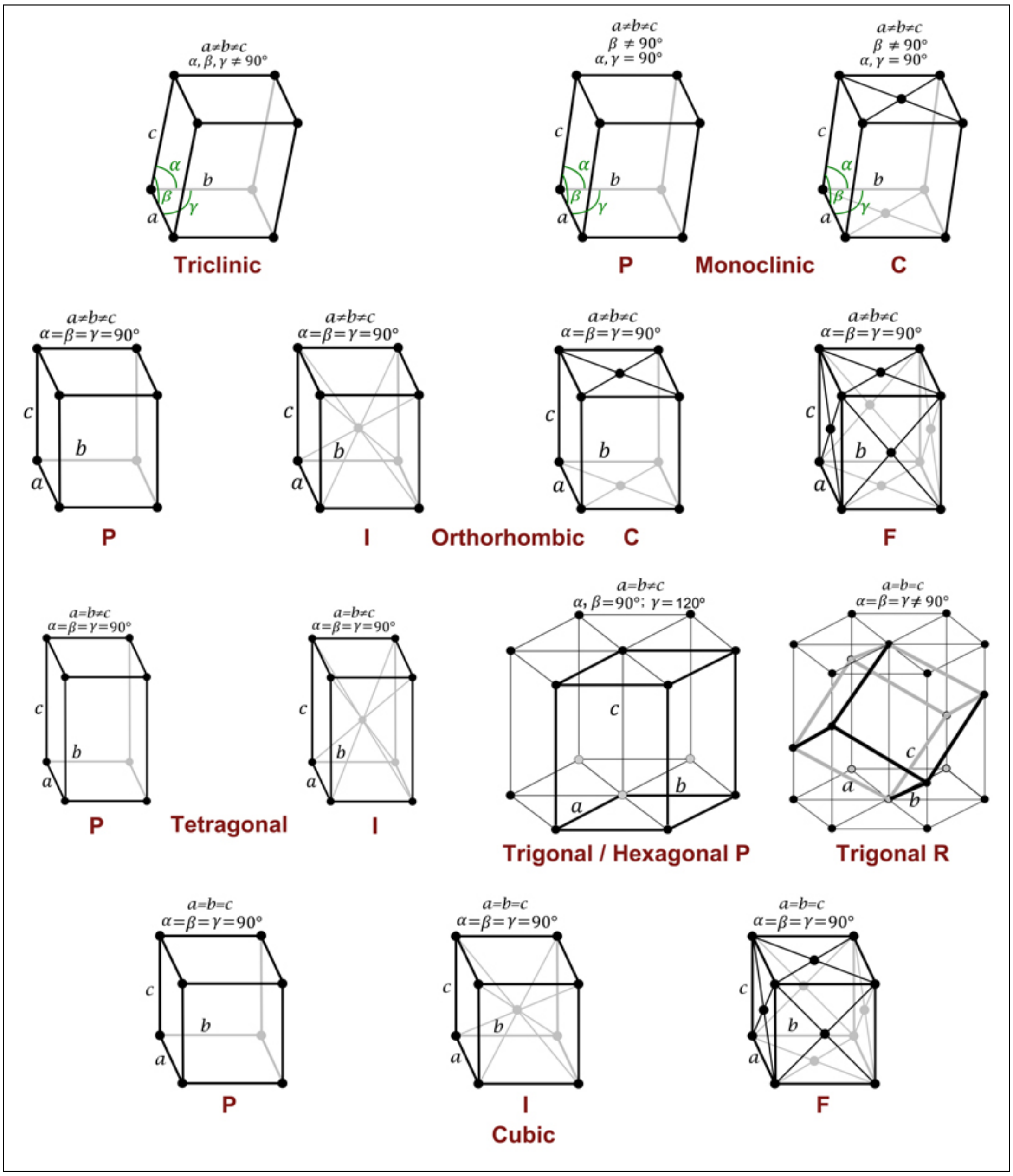

Figure 2.6: The seven crystal systems and 14 Bravais lattices. The lattice points (black and gray points) do not represent atoms. They represent places in space that are indistinguishable from each other. Symbols P, C, I, F and R refer to different lattice types: $P =$ primitive; $C =$ centered in the faces perpendicular to the c axis; $I =$ centered in the body of the cell; $F =$ centered in all faces of the cell; $R =$ primitive, identical cell axes and cell angles. Figure reproduced from Ref. [38].

not only the symmetry of the underlying Bravais lattice, but also the internal symmetry of the basis (say, the molecule or ions). In other words, in most of the cases the basis is formed of objects that do not have the maximum spherical symmetry of the individual lattice points of a Bravais lattice. The number of symmetry transformations and possible symmetry groups that transform the crystal structure into itself is enormously increased, i.e. **230** different space groups that a crystal structure can have.

2.1.5 The reciprocal lattice

There are two lattices for a given crystal structure: the direct and the reciprocal lattices. The first one is a lattice in real or ordinary space, while the second one is in Fourier space. A diffraction pattern of a crystal is a map of the reciprocal lattice of the crystal. On the other hand, a microscope image is a map of the direct lattice.

Given the direct lattice vectors $\mathbf{a}_1$, $\mathbf{a}_2$ and $\mathbf{a}_3$, we can define the corresponding reciprocal lattice vectors $\mathbf{b}_1$, $\mathbf{b}_2$ and $\mathbf{b}_3$ as:

$$\begin{aligned} \mathbf{b}_1 &= 2\pi\frac{\mathbf{a}_2 \times \mathbf{a}_3}{\mathbf{a}_1 \cdot (\mathbf{a}_2 \times \mathbf{a}_3)} \\ \mathbf{b}_2 &= 2\pi\frac{\mathbf{a}_3 \times \mathbf{a}_1}{\mathbf{a}_1 \cdot (\mathbf{a}_2 \times \mathbf{a}_3)} \\ \mathbf{b}_3 &= 2\pi\frac{\mathbf{a}_1 \times \mathbf{a}_2}{\mathbf{a}_1 \cdot (\mathbf{a}_2 \times \mathbf{a}_3)} \end{aligned} \tag{2.9}$$

where $\mathbf{b}_1$, $\mathbf{b}_2$ and $\mathbf{b}_3$ are the basis vectors of the **reciprocal lattice**. These vectors form an infinite set of $\mathbf{G}$ vectors:

$$\mathbf{G} = h\mathbf{b}_1 + k\mathbf{b}_2 + l\mathbf{b}_3, \tag{2.10}$$

$\mathbf{G}$ is a vector from the origin to any point in this reciprocal lattice, and h, k, l are integers named the **Miller indices**. Normally the plane normal to $\mathbf{G}$ is represented by the notation (hkl).

The three $\mathbf{b}_i$ satisfy $\mathbf{b}_i \cdot \mathbf{a}_j = 2\pi\delta_{ij}$, where δ_{ij} is the Kronecker delta symbol:

$$\begin{aligned} \delta_{ij} &= 0, \qquad i \neq j; \\ \delta_{ij} &= 1, \qquad i = j. \end{aligned} \tag{2.11}$$

Vectors in the crystal lattice have dimensions of [length], as opposed to dimensions of $[\text{length}]^{-1}$ for vectors in the reciprocal lattice. When the crystal is rotated, both the direct and reciprocal lattices are rotated. A **Brillouin zone** (BZ) is defined as a Wigner-Seitz cell in the reciprocal lattice. The first Brillouin zone is the smallest volume entirely enclosed by planes that are the perpendicular bisectors of the reciprocal lattice vectors drawn from the origin (Figure 2.7, for an oblique lattice in two dimensions). The first Brillouin zone also contains one lattice point. The volume of the BZ can be calculated as follows:

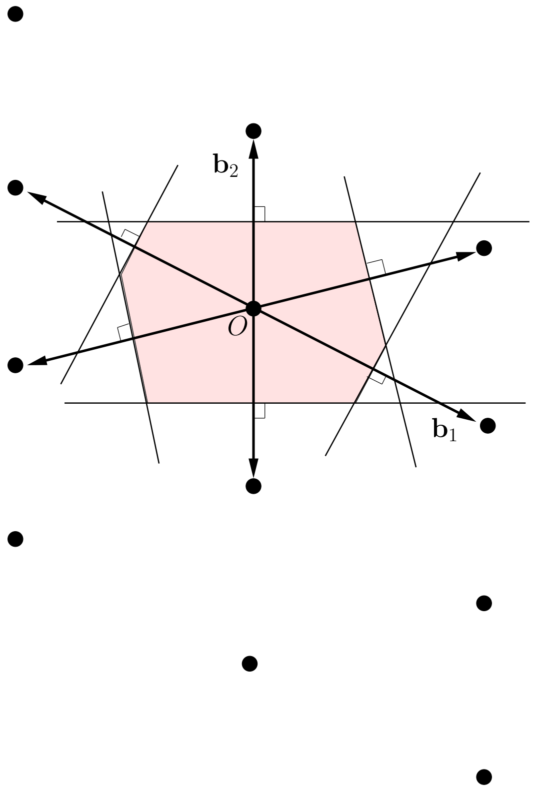

Figure 2.7: First Brillouin zone for an oblique lattice in two dimensions. From O we draw a set of vectors to the nearby points in the reciprocal lattice. Then we construct lines perpendicular to these vectors at their midpoints. The first Brillouin zone is the smallest enclosed area.

$$\begin{aligned} V_b &= \mathbf{b}_1 \cdot (\mathbf{b}_2 \times \mathbf{b}_3) \\ &= \left(\frac{2\pi}{V}\right)^3 \{(\mathbf{a}_2 \times \mathbf{a}_3) \cdot (\mathbf{a}_3 \times \mathbf{a}_1) \cdot (\mathbf{a}_1 \times \mathbf{a}_2)\} \end{aligned} \tag{2.12}$$

Using the definition of the vector quadruple product:

$$\begin{aligned} (\mathbf{A} \times \mathbf{B}) \cdot (\mathbf{C} \times \mathbf{D}) &= [\mathbf{A}, \mathbf{B}, \mathbf{D}]\, \mathbf{C} - [\mathbf{A}, \mathbf{B}, \mathbf{C}]\, \mathbf{D} \\ &= [\mathbf{A} \cdot (\mathbf{B} \times \mathbf{D})] \cdot \mathbf{C} - [\mathbf{A} \cdot (\mathbf{B} \times \mathbf{C})] \cdot \mathbf{D} \end{aligned} \tag{2.13}$$

and applying this to Eq. (2.12), we get:

$$\begin{aligned}
V_b &= \left(\frac{2\pi}{V_a}\right)^3 \left\{ (\mathbf{a}_2 \times \mathbf{a}_3) \cdot \left[\underbrace{[\mathbf{a}_3 \cdot (\mathbf{a}_1 \times \mathbf{a}_2)]}_{=V_a} \cdot \mathbf{a}_1 - \left[\mathbf{a}_3 \cdot \underbrace{(\mathbf{a}_1 \times \mathbf{a}_1)}_{=0} \right] \cdot \mathbf{a}_2 \right] \right\} \\
&= \left(\frac{2\pi}{V_a}\right)^3 \{ (\mathbf{a}_2 \times \mathbf{a}_3) \cdot V_a \cdot \mathbf{a}_1 \} \\
&= V_a \left(\frac{2\pi}{V_a}\right)^3 \underbrace{\{ (\mathbf{a}_2 \times \mathbf{a}_3) \cdot \mathbf{a}_1 \}}_{=V_a} \\
&= V_a^2 \left(\frac{2\pi}{V_a}\right)^3 \\
&= \frac{8\pi^3}{V_a} \qquad (2.14)
\end{aligned}$$

2.2 Elements of Quantum Mechanics

The most relevant aspects of Quantum Mechanics used to produce the results presented in this thesis are reviewed in this section.

2.2.1 The Electronic Problem

One of the problems in quantum chemistry is to describe the motion of N electrons in the field of M nuclear point charges. The position of the M nuclei can be specified by the $3M$ spatial coordinates $\{\mathbf{R}_A\} = \{\mathbf{R}_1, \mathbf{R}_2, ..., \mathbf{R}_M\}$. However, to completely describe an electron, not only is necessary to specify its spatial coordinates, but also its *spin*. Within a non-relativistic approach, this is accomplished by introducing two spin functions $\alpha(s)$ and $\beta(s)$, corresponding to spin up and spin down respectively. These are functions of an spin variable s. For the electron, the spin coordinates can only assume the values $\pm 1/2$. The possible values of the spin functions $\alpha(s)$ (spin up) and $\beta(s)$ (spin down) are:

$$\alpha(1/2) = \beta(-1/2) = 1 \qquad (2.15a)$$

$$\alpha(-1/2) = \beta(1/2) = 0 \qquad (2.15b)$$

Given two basis vectors $\mathbf{e}_1$ and $\mathbf{e}_2$, they are *orthonormal* when they are mutually perpendicular (orthogonal) and have unit length (normalized). This orthonormality is represented by the Kronecker delta symbol δ_{ij}:

$$\mathbf{e}_1 \cdot \mathbf{e}_2 = \delta_{ij} = \delta_{ji} = \begin{cases} 1, & \text{if } i = j \\ 0, & \text{otherwise} \end{cases} \tag{2.16}$$

The two spin functions are complete and orthonormal[1]:

$$\int \mathrm{d}s\ \alpha^*(s)\alpha(s) = \int \mathrm{d}s\ \beta^*(s)\beta(s) = 1 \tag{2.17a}$$

$$\langle\alpha|\alpha\rangle = \langle\beta|\beta\rangle = 1 \tag{2.17b}$$

and

$$\int \mathrm{d}s\ \alpha^*(s)\beta(s) = \int \mathrm{d}s\ \beta^*(s)\alpha(s) = 0 \tag{2.18a}$$

$$\langle\alpha|\beta\rangle = \langle\beta|\alpha\rangle = 0 \tag{2.18b}$$

In this way, an electron is described not only by the three spatial coordinates $\mathbf{r}$, but also by one spin coordinate s. We denote these four coordinates collectively by $\mathbf{x}$,

$$\mathbf{x} = \{\mathbf{r}, s\} \tag{2.19}$$

The collective term $\{\mathbf{x}_i\} = \{\mathbf{x}_1, \mathbf{x}_2, ..., \mathbf{x}_N\}$ for the electrons denotes the $3N$ spatial coordinates and the N spin coordinates.

The time-independent, non-relativistic Schrödinger equation reads like:

$$\hat{H}\Psi\left(\mathbf{x}_1, \mathbf{x}_2, ..., \mathbf{x}_N, \mathbf{R}_1, \mathbf{R}_2, ..., \mathbf{R}_M\right) = E\Psi\left(\mathbf{x}_1, \mathbf{x}_2, ..., \mathbf{x}_N, \mathbf{R}_1, \mathbf{R}_2, ..., \mathbf{R}_M\right) \tag{2.20}$$

where Ψ stands for the wavefunction of a particular state of the system. The wavefunction Ψ contains all the information that can be known about the system. E is the value of the energy of the state described by Ψ.

---

[1] We are using Bra-ket notation, in which Ψ^* is the complex-conjugate of Ψ: $\langle\Psi| \equiv \Psi^*$; $|\Psi\rangle \equiv \Psi$; $\langle\Psi|\Psi\rangle = \int d\tau\ \Psi^*\Psi$; $\langle\Psi|A|\Psi\rangle = \int d\tau\ \Psi^*\hat{A}\Psi$

$\hat{H}$ is the Hamilton operator for a system formed of M nuclei and N electrons:

$$\hat{H} = \hat{T}_e + \hat{T}_n + \hat{V}_{ee} + \hat{V}_{nn} + \hat{V}_{ne} + \hat{V}_{ee} \tag{2.21}$$

where the first term is the operator for the kinetic energy of the electrons, the second term is the operator for the kinetic energy of the nuclei, the third term represents the coulomb attraction between electrons and nuclei (also named external potential $\hat{V}_{\text{ext}}$ in density functional theory), the fourth and fifth terms represent the repulsion between electrons and between nuclei, respectively. The kinetic operator of a particle a and the Coulomb operator between a particle a and b can be obtained as follows:

$$\hat{T}_a = \frac{\hat{p}_a^2}{2m_a} = -\frac{\hbar^2}{2m_a}\nabla_a^2 = -\frac{\hbar^2}{2m_a}\left(\frac{\partial^2}{\partial x_a^2} + \frac{\partial^2}{\partial y_a^2} + \frac{\partial^2}{\partial z_a^2}\right) \tag{2.22}$$

$$\hat{V}_{ab} = \frac{q_a q_b}{4\pi\varepsilon_0 r_{ab}} \tag{2.23}$$

where m_a is the mass of the particle, q_a the charge of the particle, $\hbar$ the reduced Planck's constant and $1/4\pi\varepsilon_0$ the Coulomb constant. From now on, we will work on atomic units, where the mass of an electron, the absolute value of its charge, $\hbar$ and $4\pi\varepsilon_0$ are all set to unity.

If we define the distance between the ith electron and Ath nucleus as $r_{iA} = |\mathbf{r}_{iA}| = |\mathbf{r}_i - \mathbf{R}_A|$, the distance between the ith and jth electron as $r_{ij} = |\mathbf{r}_{ij}| = |\mathbf{r}_i - \mathbf{r}_j|$, and the distance between the Ath and Bth nucleus as $r_{AB} = |\mathbf{R}_{AB}| = |\mathbf{R}_A - \mathbf{R}_B|$, using atomic units on the Equations (3.22) and (3.7), we can write Eq. (2.21) as:

$$\hat{H} = -\sum_{i=1}^{N}\frac{1}{2}\nabla_i^2 - \sum_{A=1}^{M}\frac{1}{2M_A}\nabla_A^2 - \sum_{i=1}^{N}\sum_{A=1}^{M}\frac{Z_A}{r_{iA}} + \sum_{i=1}^{N}\sum_{j>i}^{N}\frac{1}{r_{ij}} + \sum_{A=1}^{M}\sum_{B>A}^{M}\frac{Z_A Z_B}{R_{AB}} \tag{2.24}$$

where M_A is the ratio of the mass of nucleus A to the mass of an electron, and Z_A is the atomic number of nucleus A. The Laplacian operators ∇_i^2 and ∇_A^2 involve differentiation with respect to the $\{\mathbf{x}_i\}$ coordinates of the ith electron and the $\{\mathbf{R}_A\}$ coordinates of the Ath nucleus.

The wavefunction is not an observable, and a physical interpretation can only be found when considering the square of the wave function, that represents the probability that electrons $1, 2, ..., N$ are found simultaneously with spin given by s within the volume elements $\mathrm{d}\mathbf{r}_1, \mathrm{d}\mathbf{r}_2, ... \mathrm{d}\mathbf{r}_N$.

In other words, in terms of the collective term $\{\mathbf{x}_i\}$:

$$P = |\Psi(\mathbf{x}_1, \mathbf{x}_2, ..., \mathbf{x}_N)|^2 \, \mathrm{d}\mathbf{x}_1, \mathrm{d}\mathbf{x}_2, ... \, \mathrm{d}\mathbf{x}_N \tag{2.25}$$

The integral of Eq. (2.25) over all the variables, or in other words, the probability of finding the N electrons anywhere in space, must equal one:

$$\int ... \int |\Psi(\mathbf{x}_1, \mathbf{x}_2, ..., \mathbf{x}_N)|^2 \, \mathrm{d}\mathbf{x}_1, \mathrm{d}\mathbf{x}_2, ..., \mathrm{d}\mathbf{x}_N = 1 \tag{2.26}$$

Because electrons are indistinguishable, this probability must be the same if the coordinates of any two electrons i and j are switched:

$$P = |\Psi(\mathbf{x}_1, \mathbf{x}_2, ..., \mathbf{x}_i, \mathbf{x}_j, ..., \mathbf{x}_N)|^2 = |\Psi(\mathbf{x}_1, \mathbf{x}_2, ..., \mathbf{x}_j, \mathbf{x}_i, ..., \mathbf{x}_N)|^2 \tag{2.27}$$

The two wavefunctions can only differ by a unimodular complex number $\exp(i\phi)$. In order to Eq. (2.27) to hold true, there are two possibilities:

a) Ψ is a antisymmetrical wave function, which means that the interchange leads to a sign change:

$$\Psi(\mathbf{x}_1, \mathbf{x}_2, ..., \mathbf{x}_i, \mathbf{x}_j, ..., \mathbf{x}_N) = -\Psi(\mathbf{x}_1, \mathbf{x}_2, ..., \mathbf{x}_j, \mathbf{x}_i, ..., \mathbf{x}_N) \tag{2.28}$$

These particles are called *fermions*, and have spin half-integral. Electrons are fermions with spin 1/2, and the wavefunction must be antisymmetric with respect to the spatial and spin coordinates of any two electrons.

b) Ψ is a symmetrical wave function, which means that the interchange does not lead to a sign change. These particles are called *bosons*, which have an integer spin, including zero.

2.2.2 The Born-Oppenheimer Approximation

Nuclei are much heavier than electrons. Even the lightest of all nuclei, the proton ^{1}H, weighs 1800 times more than an electron. Therefore, the nuclei move much slower than the electrons. A good approximation is to consider that the electrons are moving in the field of fixed nuclei. Within this approximation, the kinetic energy of the nuclei (term $\hat{T}_n$ in Eq. (2.21)) a can be neglected, and the potential energy due to nucleus-nucleus repulsion (term $\hat{V}_{nn}$ in Eq. (2.21)) can be considered to be constant. A constant added to an operator has no effect on the operator eigenfunctions and only adds to the operator eigenvalues. The electronic Hamiltonian describes the motion of N electrons in the filed of M point charges:

$$\begin{aligned}\hat{H}_{\text{elec}} &= \hat{T}_e + \hat{V}_{ne} + \hat{V}_{ee} \\ &= -\sum_{i=1}^{N} \frac{1}{2}\nabla_i^2 - \sum_{i=1}^{N}\sum_{A=1}^{M} \frac{Z_A}{r_{iA}} - \sum_{i=1}^{N}\sum_{j>i}^{N} \frac{1}{r_{ij}}\end{aligned} \tag{2.29}$$

The solution of the Schrödinger equation with $\hat{H}_{\text{elec}}$:

$$\hat{H}_{\text{elec}}\Psi_{\text{elec}} = E_{\text{elec}}\Psi_{\text{elec}} \tag{2.30}$$

is the electronic wave function:

$$\Psi_{\text{elec}} = \Psi_{\text{elec}}\left(\{\mathbf{r}_i\};\{\mathbf{R}_A\}\right) \tag{2.31}$$

which describes the motion of the electrons. Ψ_{elec} depends *explicitly* on the electronic coordinates and *parametrically* on the nuclear coordinates, as does the electronic energy:

$$E_{\text{elec}} = E_{\text{elec}}\left(\{\mathbf{R}_A\}\right) \tag{2.32}$$

The concept of parametric dependence means that, for different arrangements of the nuclei, Ψ_{elec} is a different function of the electronic coordinates. In other words, the nuclear coordinates do not appear explicitly in Ψ_{elec}. The total energy for fixed nuclei must also include the constant nuclear repulsion:

$$E_{\text{tot}} = E_{\text{elec}} + \sum_{A=1}^{M}\sum_{B>A}^{M} \frac{Z_A Z_B}{R_{AB}} \tag{2.33}$$

In quantum mechanics, given an observable $\hat{O}$, we define the expectation value of this observable as

$$\left\langle \hat{O} \right\rangle = \frac{\langle\Psi|\hat{O}|\Psi\rangle}{\langle\Psi|\Psi\rangle} \tag{2.34}$$

where the denominator equals to 1 if Ψ is normalised. For instance, the electronic energy will be obtained as $E_{\text{elec}} = \langle \Psi | \hat{H}_{\text{elec}} | \Psi \rangle$. If we now define the operator $\hat{O}$ as:

$$\hat{O} = -\sum_{i=1}^{N} \frac{1}{2} \nabla_i^2 - \sum_{i=1}^{N} \sum_{A=1}^{M} \frac{Z_A}{r_{iA}} - \sum_{i=1}^{N} \sum_{j>i}^{N} \frac{1}{r_{ij}} \tag{2.35}$$

then the expectation value of this particular operator is just $E_{\text{elec}}\left(\{\mathbf{R}_A\}\right)$, the electronic energy for a given fixed position of the nucleii:

$$\begin{aligned} \left\langle \hat{O} \right\rangle &= \left\langle -\sum_{i=1}^{N} \frac{1}{2} \nabla_i^2 - \sum_{i=1}^{N} \sum_{A=1}^{M} \frac{Z_A}{r_{iA}} - \sum_{i=1}^{N} \sum_{j>i}^{N} \frac{1}{r_{ij}} \right\rangle \\ &= \langle \Psi | \hat{O} | \Psi \rangle \\ &= E_{\text{elec}}\left(\{\mathbf{R}_A\}\right) \end{aligned} \tag{2.36}$$

In order to solve the motion of the nuclei, starting from Eq. (2.24), we can obtain an expression of the nuclear Hamiltonian, replacing the electronic coordinates by their average values, averaged over the electronic wave function. This generates a nuclear Hamiltonian for the motion of the nuclei in the average field of the electrons:

$$\begin{aligned} \hat{H}_{\text{nucl}} &= -\sum_{A=1}^{M} \frac{1}{2M_A} \nabla_A^2 + \left\langle -\sum_{i=1}^{N} \frac{1}{2} \nabla_i^2 - \sum_{i=1}^{N} \sum_{A=1}^{M} \frac{Z_A}{r_{iA}} - \sum_{i=1}^{N} \sum_{j>i}^{N} \frac{1}{r_{ij}} \right\rangle + \sum_{A=1}^{M} \sum_{B>A}^{M} \frac{Z_A Z_B}{R_{AB}} \\ &= -\sum_{A=1}^{M} \frac{1}{2M_A} \nabla_A^2 + E_{\text{elec}}\left(\{\mathbf{R}_A\}\right) + \sum_{A=1}^{M} \sum_{B>A}^{M} \frac{Z_A Z_B}{R_{AB}} \\ &= -\sum_{A=1}^{M} \frac{1}{2M_A} \nabla_A^2 + E_{\text{tot}}\left(\{\mathbf{R}_A\}\right) \end{aligned} \tag{2.37}$$

The total energy $E_{\text{tot}}\left(\{\mathbf{R}_A\}\right)$ is the Potential Energy Surface. The solution to the nuclear Schrodinger equation:

$$\hat{H}_{\text{nucl}} \Psi_{\text{nucl}} = E \Psi_{\text{nucl}} \tag{2.38}$$

gives:

a) E, which is the Born-Oppenheimer approximation to the total energy of Eq. (2.20). This includes electronic, vibrational, rotational and translational energy.

b) Ψ_{nucl}, which describes the vibration, rotation translation of a molecule. As opposed to

Eq. (2.31), Ψ_{nucl} depends only *explicitly* on the nuclear coordinates:

$$\Psi_{\text{nucl}} = \Psi_{\text{nucl}}\left(\{\mathbf{R}_A\}\right) \tag{2.39}$$

The corresponding approximation to the total wave function of Eq. (2.20) is:

$$\Psi \equiv \Psi\left(\{\mathbf{r}_i\}\,;\{\mathbf{R}_A\}\right) = \Psi_{\text{elec}}\left(\{\mathbf{r}_i\}\,;\{\mathbf{R}_A\}\right)\Psi_{\text{nucl}}\left(\{\mathbf{R}_A\}\right) \tag{2.40}$$

From now on, we will only consider electronic Hamiltonians and electronic wave functions because we will concentrate on the electronic problem, not considering the vibrational-rotational problem. When convenient, a distinction will be made between the electronic energy of Eq. (2.32) and the total energy of Eq. (2.33), which includes nuclear-nuclear repulsion.

2.2.3 The Variational Principle

The exact solution for the Scrödinger equation cannot be obtained with the exception of the most trivial systems like the hydrogen atom. The variational principle is an approach to obtain Ψ_0, the wave function of the ground state, the state that has the lowest energy, E_0. For any guessed Ψ_{trial}, the expectation value of the Hamilton operator $\hat{H}$ will give an energy E_{trial}, that will be an upper bound to the true energy of the ground state:

$$\langle\Psi_{\text{trial}}|\hat{H}|\Psi_{\text{trial}}\rangle = E_{\text{trial}} \geqslant E_0 = \langle\Psi_0|\hat{H}|\Psi_0\rangle \tag{2.41}$$

where the equality holds if and only if Ψ_{trial} is identical to Ψ_0. At this stage, it is important to distinguish between the concepts of *function* and *functional*:

a) A function $f(x)$ is a rule that, given a number x as input, returns a number y: $x \xrightarrow{f(x)} y$

b) A functional $F[f(x)]$ is a rule that, given a function $f(x)$ as input, returns also a number y: $f(x) \xrightarrow{F[f(x)]} y$.

In our case, we have a function Ψ_{trial} as input, that returns a number E_{trial}. Thus, this is the case of a functional. The rule that converts the first to the last one is represented schematically by$E_{\text{trial}}[\Psi_{\text{trial}}] = \langle\Psi_{\text{trial}}|\hat{H}|\Psi_{\text{trial}}\rangle$.

In order to find the ground state energy and wave function, we need to minimize the functional $E_{\text{trial}}[\Psi_{\text{trial}}]$ by searching through all eligible (continuous and quadratic integrable) N-electron wave functions. The function which gives the lowest energy will be $\Psi_{0,\text{trial}}$ and the energy will be the ground state energy $E_{0,\text{trial}}$:

$$E_{0,\text{trial}} = \min_{\Psi_{\text{trial}} \to N} E_{\text{trial}}[\Psi_{\text{trial}}] = \min_{\Psi_{\text{trial}} \to N} \langle \Psi_{\text{trial}} | \hat{T}_e + \hat{V}_{ne} + \hat{V}_{ee} | \Psi_{\text{trial}} \rangle \tag{2.42}$$

where $\Psi_{\text{trial}} \to N$ means that Ψ_{trial} is an eligible N-electron many body wave function.

2.2.4 Spin Orbitals and Slater determinant

Given the fact that the electrons are described by three spatial coordinates and one spin coordinate (Eq. 2.19), we can describe the spatial distribution of an electron as a *spatial orbital* $\phi(\mathbf{r})$, which is a function of the position vector $\mathbf{r}$. It is usually assumed to be orthonormal: $\int \mathrm{d}\mathbf{r}\ \phi_i^*(\mathbf{r})\phi_j(\mathbf{r}) = \delta_{ij}$. The spin is described by two orthonormal functions: $\alpha(s)$ and $\beta(s)$, which are also orthonormal (Equations 2.15a - 2.15b). A *spin orbital* $\chi(\mathbf{x})$ is a wave function for an electron that describes both its spatial distribution and its spin. From each spatial orbital, $\phi(\mathbf{r})$, one can form two different spin orbitals by multiplying the spatial orbital by the α or *beta* spin function:

$$\chi(\mathbf{x}) = \begin{cases} \phi(\mathbf{r})\alpha(s) \\ \text{or} \\ \phi(\mathbf{r})\beta(s) \end{cases} \tag{2.43}$$

If the spatial and spin orbitals are orthonormal, so are the spin orbitals: $\int \mathrm{d}\mathbf{x}\ \chi_i^*(\mathbf{x})\chi_j(\mathbf{x}) = \delta_{ij}$. We could think as a model wave function the simple product:

$$\Psi = \chi_1(\mathbf{x}_1)\chi_2(\mathbf{x}_2)...\chi_i(\mathbf{x}_i)\chi_j(\mathbf{x}_j)...\chi_N(\mathbf{x}_N) \tag{2.44}$$

This is known as the *Hartree Product.* However, this wave function violates the fact that electrons are indistinguishable because it assigns a particular one-electron function (for example χ_1) to a particular electron ($\mathbf{x}_1$). Moreover, this product is not antisymmetric with respect to the interchange of any two electrons:

$$\chi_1(\mathbf{x}_1)\chi_2(\mathbf{x}_2)...\chi_i(\mathbf{x}_i)\chi_j(\mathbf{x}_j)...\chi_N(\mathbf{x}_N) \neq -\chi_1(\mathbf{x}_1)\chi_2(\mathbf{x}_2)...\chi_i(\mathbf{x}_i)\chi_j(\mathbf{x}_j)...\chi_N(\mathbf{x}_N) \tag{2.45}$$

Because of these two reasons, the Hartree Product is not an acceptable wave function. An acceptable candidate for the wave function is the so called Slater determinant:

$$\Psi_0 \approx \Phi_{\mathrm{SD}}(\mathbf{x}_1, \mathbf{x}_2, \ldots, \mathbf{x}_N) = \frac{1}{\sqrt{N!}} \begin{vmatrix} \chi_1(\mathbf{x}_1) & \chi_2(\mathbf{x}_1) & \cdots & \chi_N(\mathbf{x}_1) \\ \chi_1(\mathbf{x}_2) & \chi_2(\mathbf{x}_2) & \cdots & \chi_N(\mathbf{x}_N) \\ \vdots & \vdots & \ddots & \vdots \\ \chi_1(\mathbf{x}_N) & \chi_2(\mathbf{x}_N) & \cdots & \chi_N(\mathbf{x}_N) \end{vmatrix} \tag{2.46}$$

where the prefactor $(N!)^{-\frac{1}{2}}$ is a normalization constant. This Slater determinant meets all the requirements:

a) Satisfies the Pauli exclusion principle: no more than one electron can occupy a spin orbital. Having two electrons occupying the same spin orbital corresponds to having two columns of the determinant equal, which makes the determinant zero.

b) Satisfies the antisymmetry principle. The rows are labelled by electrons: first row ($\mathbf{x}_1$), second row ($\mathbf{x}_2$), etc., and the columns are labelled by spin orbitals: first column (χ_1), second row (χ_2), etc. Interchanging the coordinates of two electrons corresponds to interchanging two rows of the Slater determinant, which changes the sign of the determinant.

2.2.5 Hartree-Fock Approximation

Using the variational principle, The Hartree-Fock approach varies the spin orbitals χ_i under the constraint that they remain orthonormal, such that the energy obtained from the Slater determinant is minimal:

$$E_{\mathrm{HF}} = \min_{\Psi_{\mathrm{SD}} \to \Phi_{\mathrm{SD}}} E[\Phi_{\mathrm{SD}}] \tag{2.47}$$

It can be shown that the HF energy is given by:

$$E_{\mathrm{HF}} = \langle \Phi_{\mathrm{SD}} | \hat{H} | \Phi_{\mathrm{SD}} \rangle = \sum_i^N (i|\hat{h}|i) + \frac{1}{2} \sum_i^N \sum_j^N (ii|jj) - (ij|ji) \tag{2.48}$$

where $(i|\hat{h}|i)$ contains the contribution due to the kinetic energy and the electron-nucleus attraction:

$$(i|\hat{h}|i) = \int \chi_i(\mathbf{x}_1) \left[-\frac{1}{2}\nabla - \sum_A^M \frac{Z_A}{r_{1A}} \right] \chi_i(\mathbf{x}_1) \ \mathrm{d}\mathbf{x}_1 \tag{2.49}$$

The interaction between two electrons is described by two integrals:

a) The *Coulomb* integral:

$$(ii|jj) = \iint |\chi_i(\mathbf{x}_1)|^2 \frac{1}{r_{12}} |\chi_j(\mathbf{x}_2)|^2 \ \mathrm{d}\mathbf{x_1}\mathrm{d}\mathbf{x_2} \tag{2.50}$$

b) The *exchange* integral:

$$(ij|ji) = \iint \chi_i(\mathbf{x}_1)\chi_j^*(\mathbf{x}_1)\frac{1}{r_{12}}\chi_j(\mathbf{x}_2)\chi_i^*(\mathbf{x}_2) \ \mathrm{d}\mathbf{x_1}\mathrm{d}\mathbf{x_2} \tag{2.51}$$

It is obvious from Eq. (2.48) that E_{HF} is a functional of the spin orbitals: $E_{\mathrm{HF}} = E[\chi_i]$. Those χ_i are minimized with the constraint that they remain orthonormal. This constraint is mathematically implemented by introducing *Lagrangian multipliers*, ε_i in the following equations. These equations represent the *Hartree-Fock* equations:

$$\hat{f}\chi_i = \varepsilon_i\chi_i \qquad i = 1, 2, ..., N \tag{2.52}$$

These N equations are eigenvalue equations, where the Lagrangian multipliers ε_i are the eigenvalues of the operator $\hat{f}$, and are essentially the orbital energies. The Fock operator $\hat{f}$ is a one-electron operator:

$$\hat{f}_i = -\frac{1}{2}\nabla_i^2 - \sum_A^M \frac{Z_A}{r_{iA}} + V_{\mathrm{HF}}(i) \tag{2.53}$$

where the first two terms are respectively the kinetic energy and the potential energy due to the electron-nucleus attraction. The complicated electron-electron repulsion represented by the $1/r_{ij}$ operator in the Hamiltonian is replaced by $V_{\mathrm{HF}}(i)$, the *Hartree-Fock potential*, an average repulsive potential experienced by the ith electron due to the remaining $N-1$ electrons:

$$V_{\mathrm{HF}}(\mathbf{x}_1) = \sum_j^N \left[\hat{J}_j(\mathbf{x}_1) - \hat{K}_j(\mathbf{x}_1) \right] \tag{2.54}$$

Hence, the electron-electron repulsion problem is solved by considering this repulsion in an average way. V_{HF} has two components:

a) The Coulomb operator $\hat{J}$ is defined as:

$$\hat{J}_j(\mathbf{x}_1) = \int |\chi_j(\mathbf{x}_1)|^2 \frac{1}{r_{12}} \, \mathrm{d}\mathbf{x}_2 \tag{2.55}$$

Given a reference electron at position $\mathbf{x}_1$ and another one at position $\mathbf{x}_2$, the Coulomb repulsion between the reference electron and electron 2 is weighted by the probability to find electron 2 in the volume element $\mathrm{d}\mathbf{x_2}$. This probability is integrated over all space and spin coordinates.

b) The operator $\hat{K}$ is defined as the exchange operator:

$$\hat{K}_j(\mathbf{x}_1)\chi_i(\mathbf{x}_1) = \int \chi_j^*(\mathbf{x}_2)\frac{1}{r_{12}}\chi_i(\mathbf{x}_2) \, \mathrm{d}\mathbf{x_2} \; \chi_j(\mathbf{x}_1) \tag{2.56}$$

which has no classical interpretation, and can only be defined through its effect when operating on a spin orbital. This effect has to do with exchanging the variables in the two spin orbitals.

In the double summation in Eq. (2.48), the term $i = j$ is allowed. This means that if $i = j$, the Coulomb integral (Eq. 2.50) would be describing the Coulomb interaction of the charge distribution of one electron with itself. Consequently, in a system with only one electron, even though there is no electron-electron repulsion, the Coulomb integral is non-zero. This problem is called *self-interaction*. However, HF solves this problem in a very elegant way: if $i = j$, the Coulomb and exchange integrals are identical and both reduce to $\int\int |\chi_i(\mathbf{x}_1)|^2 \frac{1}{r_{12}} |\chi_i(\mathbf{x}_2)|^2 \; \mathrm{d}\mathbf{x}_1\mathrm{d}\mathbf{x}_2$. Both integrals enter Eq. (2.48) with opposite sign and the self-interaction is exactly cancelled.

In order to solve Eq. (2.52), we need to know the expression of the Fock operator, and this depends on the HF potential (Eq. 2.54), which depends on the spin-orbitals, in other words, on the solutions of the eigenvalue that needs to be solved. Thus, this has to be solved iteratively, through a technique called *self-consistent field* (SCF): we start with a “guessed” set of orbitals, solve the HF equations, and the resulting set of orbitals used in the next iteration until the input and output orbitals differ by less than a threshold.

It can be easily shown that a Slater determinant is an eigenfunction of a Hamilton operator defined as the sum of the Fock operators of equations (2.52):

$$\hat{H}_{\mathrm{HF}}\Phi_{\mathrm{SD}} = E^{0}_{\mathrm{HF}}\Phi_{\mathrm{SD}} = \sum_{i}^{N} \hat{f}_i \Phi_{\mathrm{SD}} = \varepsilon_i \Phi_{\mathrm{SD}} \tag{2.57}$$

The difference between the HF energy and the exact ground state energy is called the electron correlation energy. Post HF methods go beyond the assumption that the solution is a single Slater determinant, for instance, those based on many body perturbation theory (MP methods formulated by Møller and Plesset [39]), configuration interaction (CI) [40], and coupled-cluster (CC) methods [41]. These methods are extremely accurate, but computationally expensive.

2.2.6 Density Functional Theory

The foundation for Density Functional Theory (DFT) is the electron density, designated by $\rho(\mathbf{r})$ [42], which is the number of electrons per unit volume in a given state:

$$\rho(\mathbf{r}) = N \int \cdots \int \left|\Psi\left(\mathbf{r}, \mathbf{r}_2, \ldots, \mathbf{r}_N\right)\right|^2 \mathrm{d}\mathbf{r}_2 \ldots \mathrm{d}\mathbf{r}_N \tag{2.58}$$

By integrating this function is possible to get the total number of electrons:

$$\int \rho(\mathbf{r})\,\mathrm{d}\mathbf{r} = N \tag{2.59}$$

In DFT, $\hat{V}_{\mathrm{ne}}$, the Coulomb interaction between electrons and nuclei, is commonly referred to as $\hat{V}_{\mathrm{ext}}$, the external potential, which can also be written as a sum over all the N electrons, of each attraction:

$$\hat{V}_{\mathrm{ext}} = \sum_{i=1}^{N} v_{\mathrm{ext}}\left(\mathbf{r}_i\right) \tag{2.60}$$

where $v_{\mathrm{ext}}\left(\mathbf{r}_i\right)$, the external potential acting on each electron, is just:

$$v_{\mathrm{ext}}\left(\mathbf{r}_i\right) = -\sum_{A=1}^{M} \frac{Z_A}{r_{iA}} \tag{2.61}$$

DFT is constructed upon two theorems, described herein.

2.2.6.1 The First Hohenberg-Kohn Theorem

The first theorem states that:

"*Given two external potentials* $v(\mathbf{r})$ *and* $v'(\mathbf{r})$*, if their difference* $v(\mathbf{r}) - v'(\mathbf{r})$ *is a constant, they will not give rise to the same ground-state density distribution* $\rho(\mathbf{r})$*.*"

We will prove this theorem by assuming that it is possible to find two external potentials, that differing by a constant, they separately give the same electron density.
Given two Hamiltonians $\hat{H}$ and $\hat{H}'$, which they only differ in the external potential:

$$\hat{H} = \hat{T} + \hat{V}_{ee} + \hat{V}_{\text{ext}} \tag{2.62}$$

$$\hat{H}' = \hat{T} + \hat{V}_{ee} + \hat{V}'_{\text{ext}} \tag{2.63}$$

The two Hamiltonians belong to two different ground state wave functions, Ψ and $\Psi^{'}$, and to two corresponding ground state energies E_0 and $E_0^{'}$ respectively, with $E_0 \neq E_0^{'}$. However, because the density is constructed from a wave function by quadrature (Eq. (2.58)), it is very well possible that both wave functions give the same electron density, i.e.

$$\hat{V}_{\text{ext}} \Rightarrow \hat{H} \Rightarrow \Psi \Rightarrow \qquad \rho(\mathbf{r}) \qquad \Leftarrow \Psi' \Leftarrow \hat{H}' \Leftarrow \hat{V}'_{\text{ext}} \tag{2.64}$$

Using the variational principle:

$$\begin{aligned} E_0 <\ \langle\Psi'|\hat{H}|\Psi'\rangle &=\ \langle\Psi'|\hat{H}'|\Psi'\rangle +\ \langle\Psi'|\hat{H} - \hat{H}'|\Psi'\rangle \\ &= E_0' +\ \langle\Psi'|\hat{T}' + \hat{V}_{\text{ext}} + \hat{V}_{ee} - \hat{T} - \hat{V}'_{\text{ext}} - \hat{V}_{ee}|\Psi'\rangle \\ &= E_0' +\ \langle\Psi'|\hat{V}_{\text{ext}} - \hat{V}'_{\text{ext}}|\Psi'\rangle \\ &= E_0' +\ \langle\Psi'|\sum_{i=1}^{N} v_{\text{ext}}(\mathbf{r}_i) - \sum_{i=1}^{N} v'_{\text{ext}}(\mathbf{r}_i)|\Psi'\rangle \end{aligned} \tag{2.65}$$

Since electrons are indistinguishable, $\hat{V}_{\text{ext}} = \sum_{i=1}^{N} v_{\text{ext}}(\mathbf{r}_i) = v_{\text{ext}}(\mathbf{r}_1) + v_{\text{ext}}(\mathbf{r}_2) + \cdots + v_{\text{ext}}(\mathbf{r}_N) = N v_{\text{ext}}(\mathbf{r}_1) \equiv N v_{\text{ext}}(\mathbf{r})$. Thus,

$$\begin{aligned} E_0 <\ \langle\Psi'|\hat{H}|\Psi'\rangle &= E_0' +\ \langle\Psi'|N\left[v_{\text{ext}}(\mathbf{r}) - v'_{\text{ext}}(\mathbf{r})\right]|\Psi'\rangle \\ &= E_0' + \int \Psi'\Psi'^{*} N\left[v_{\text{ext}}(\mathbf{r}) - v'_{\text{ext}}(\mathbf{r})\right] \mathrm{d}\tau \end{aligned} \tag{2.66}$$

From Eq. (2.58) and Eq. (2.64):

$$\int \Psi' \Psi'^{*} N \mathrm{d}\mathbf{r} = \rho'(\mathbf{r}) \equiv \int \Psi \Psi^{*} N \mathrm{d}\mathbf{r} = \rho(\mathbf{r}) \tag{2.67}$$

Therefore,

$$E_0 < \langle \Psi' | \hat{H} | \Psi' \rangle = E_0' + \int \rho(\mathbf{r}) \left[v_{\text{ext}}(\mathbf{r}) - v_{\text{ext}}'(\mathbf{r}) \right] \mathrm{d}\mathbf{r} \tag{2.68}$$

where E_0 and E_0' are the ground state energies for $\hat{H}$ and $\hat{H}'$ respectively. Similarly, taking Ψ as a trial function for the $\hat{H}'$ problem:

$$\begin{aligned} E_0' < \langle \Psi | \hat{H}' | \Psi \rangle &= \langle \Psi | \hat{H} | \Psi \rangle + \langle \Psi | \hat{H}' - \hat{H} | \Psi \rangle \\ &= E_0 - \int \rho(\mathbf{r}) \left[v_{\text{ext}}(\mathbf{r}) - v_{\text{ext}}'(\mathbf{r}) \right] \mathrm{d}\mathbf{r} \end{aligned} \tag{2.69}$$

Adding (2.68) and (2.69) we obtain $E_0 + E_0' < E_0' + E_0$. This is a contradiction, so there cannot be two different external potentials that give the same ground state electron density. In other words, the ground state density uniquely specifies the external potential V_{ext}. Due to the fact that the ground state energy is a functional of the ground state electron density, so must be its individual components:

$$E_0[\rho_0] = T[\rho_0] + V_{ee}[\rho_0] + V_{ne}[\rho_0] \tag{2.70}$$

where we write $V_{ne}[\rho_0]$ to specify that the external potential is fully determined by the attraction to the nuclei. This term can be obtained as:

$$V_{ne}[\rho_0] = \int \rho_0(\mathbf{r})\, v_{\text{ext}}(\mathbf{r})\, \mathrm{d}\mathbf{r} \tag{2.71}$$

and its value depends on the system. However, the other two terms are universal, in the sense that they do not depend on N, Z_A or R_A:

$$E_0[\rho_0] = \underbrace{\int \rho_0(\mathbf{r})\, v_{\text{ext}}(\mathbf{r})\, \mathrm{d}\mathbf{r}}_{\text{system dependent}} + \underbrace{T[\rho_0] + V_{ee}[\rho_0]}_{\text{universally valid}} \tag{2.72}$$

Gathering the system independent parts into a new quantity, the *Hohenberg-Kohn functional* $F_{\text{HK}}[\rho_0]$, one gets to:

$$E_0[\rho_0] = \int \rho_0(\mathbf{r})\, v_{\text{ext}}(\mathbf{r})\, \mathrm{d}\mathbf{r} + F_{\text{HK}}[\rho_0] \tag{2.73}$$

If we give as an input some arbitrary density $\rho(\mathbf{r})$, the Hohenberg-Kohn functional will allow us to calculate the expectation value $\langle\Psi|\hat{T}+\hat{V}_{ee}|\Psi\rangle$, which is the sum of the kinetic energy and the electron-electron repulsion operator with the ground state wave function Ψ associated with this arbitrary chosen density $\rho(\mathbf{r})$:

$$F_{\mathrm{HK}}[\rho] = T[\rho] + V_{ee}[\rho] = \langle\Psi|\hat{T}+\hat{V}_{ee}|\Psi\rangle \tag{2.74}$$

Because $F_{\mathrm{HK}}[\rho]$ contains the functional of the kinetic energy $T[\rho]$ and the electron-electron interaction $V_{ee}[\rho]$, it is completely independent of the system. However, the explicit form of these two functionals is not known exactly. $V_{ee}[\rho_0]$ can be written as a sum of classical and non-classical contributions:

$$V_{ee}[\rho] = J[\rho] + V_{\text{non-classsical}}[\rho] \tag{2.75}$$

The first term $J[\rho]$ represents the classical electrostatic energy of a charge distribution with itself:

$$J[\rho] = \frac{1}{2}\iint \frac{\rho(\mathbf{r}_1)\rho(\mathbf{r}_2)}{r_{12}}\mathrm{d}\mathbf{r}_1\mathrm{d}\mathbf{r}_2 \tag{2.76}$$

This term contains the unphysical self-interaction: if we consider a system formed of only one electron, there cannot be any electron-electron Coulomb interaction, and unfortunately in this case we obtain $J[\rho] \neq 0$.

$E_{\text{non-classical}}[\rho]$ is the energy of interaction between the charge density and the charge distribution of the exchange-correlation hole. It includes the correction for the self interaction as well as all contributions of quantum-mechanical correlation effects. It is important to know at this stage that hole functions are very useful for discussing exchange and correlation effects.

2.2.6.2 The Second Hohenberg-Kohn Theorem

This theorem reads: *For any density $\rho'(\mathbf{r})$ that satisfies the necessary boundary conditions such as $\rho'(\mathbf{r}) \geqslant 0$, $\int \rho'(\mathbf{r})\mathrm{d}\mathbf{r} = N$, and which is associated with some external potential v_{ext}, the energy functional is an upper bound to E_0, the true ground state energy*:

$$E_0 \leqslant E_0[\rho'] = T[\rho'] + V_{ee}[\rho'] + V_{ne}[\rho'] \tag{2.77}$$

E_0 results only if and only if the exact ground state density is inserted into Eq. (2.73). This theorem is a consequence of the variational principle. If we rewrite Eq. (2.41) with Ψ' as a trial function:

$$\langle \Psi' | \hat{H} | \Psi' \rangle = E'_0 \geqslant E_0 = \langle \Psi_0 | \hat{H} | \Psi_0 \rangle \tag{2.78}$$

and if we work with the exact and trial functionals $E_0[\rho_0]$ and $E_0[\rho']$ we arrive at:

$$\langle \Psi_0 | \hat{H} | \Psi_0 \rangle = E_0 \equiv E_0[\rho_0] = \underbrace{T[\rho_0] + V_{ee}[\rho_0]}_{= F_{\text{HK}}[\rho_0]} + V_{ne}[\rho_0] \tag{2.79}$$

where $V_{ne}[\rho_0] = \int \rho_0(\mathbf{r}) v_{\text{ext}}(\mathbf{r})\, \mathrm{d}\mathbf{r}$. Similarly,

$$\langle \Psi' | \hat{H} | \Psi' \rangle = E'_0 \equiv E'_0[\rho'] = \underbrace{T[\rho'] + V_{ee}[\rho']}_{= F_{\text{HK}}[\rho']} + V_{ne}[\rho'] \tag{2.80}$$

where since we are using a Hamiltonian $\hat{H}$ and not $\hat{H}'$, the external potential corresponds to $v_{\text{ext}}(\mathbf{r})$ so that $V_{ne}[\rho'] = \int \rho'(\mathbf{r}) v_{\text{ext}(\mathbf{r})} \mathrm{d}\mathbf{r}$.

In Density Functional Theory, the functional $E[\rho]$ contains an explicit prescription for how to uniquely map an electron density onto an energy, neglecting the complicated N-particle wave function. The variational principle as proven above, applies to the exact functional only. Many conventional wave function based theories (Hartree-Fock or configuration interaction approaches) are strictly variational and the expectation value $E = \langle \Psi' | \hat{H} | \Psi' \rangle$ is an indicator of the quality of the trial function (the lower E, the better approximation is Ψ' to Ψ). However, the energy value obtained by a trial functional has absolutely no meaning in that respect: it can well occur that the energies obtained from DFT are lower than the exact ones. The reason for these results is that in DFT, by using an approximation for the functional, consequently we are using an approximated Hamiltonian rather than the exact one. Therefore, if we change $\hat{H}$ and use something which is an approximation to it, the variational principle does not hold any more.

2.2.6.3 The Kohn-Sham Approach

As showed in Hartree-Fock, the Fock operator (Eq. 2.53) is an effective one-electron operator, and hence, the Hartree-Fock equations (Eq. (2.57)) describe a system of N electrons which do not interact among themselves but experience an effective potential V_{HF}. In other words, the Slater determinant describes the wave function of N non-interacting fermions moving in the field of the effective potential V_{HF}.

In a Kohn-Sham approach, it is again possible to set up a non-interacting reference system by introducing a Hamiltonian $\hat{H}_{\mathrm{S}}$ that contains an effective, local potential $V_{\mathrm{S}}(\mathbf{r})$:

$$\hat{H}_{\mathrm{S}} = -\frac{1}{2}\sum_{i=1}^{N}\nabla_i^2 + \sum_{i=1}^{N} V_{\mathrm{S}}(\mathbf{r}_i) \tag{2.81}$$

In addition, the ground state wave function is represented by a Slater determinant Θ_{S}:

$$\Theta_{\mathrm{S}} = \frac{1}{\sqrt{N!}}\begin{vmatrix} \varphi_1(\mathbf{x}_1) & \varphi_2(\mathbf{x}_1) & \cdots & \varphi_N(\mathbf{x}_1) \\ \varphi_1(\mathbf{x}_2) & \varphi_2(\mathbf{x}_2) & \cdots & \varphi_N(\mathbf{x}_N) \\ \vdots & \vdots & \ddots & \vdots \\ \varphi_1(\mathbf{x}_N) & \varphi_2(\mathbf{x}_N) & \cdots & \varphi_N(\mathbf{x}_N) \end{vmatrix} \tag{2.82}$$

where the spin orbitals φ_i are named Kohn-Sham orbitals, and are determined by:

$$\hat{f}^{\mathrm{KS}}\varphi_i = \varepsilon_i\varphi_i \tag{2.83}$$

and the Khon-Sham operator $\hat{f}^{\mathrm{KS}}$ is defined as:

$$\hat{f}^{\mathrm{KS}} = -\frac{1}{2}\nabla^2 + V_{\mathrm{S}}(\mathbf{r}_i) \tag{2.84}$$

Hence,

$$\left[-\frac{1}{2}\nabla^2 + V_{\mathrm{S}}(\mathbf{r}_i)\right]\varphi_i = \varepsilon_i\varphi_i \tag{2.85}$$

It can be shown that $\rho_{\mathrm{S}}(\mathbf{r})$, the electron probability density of an N-particle system whose wave function is a Slater determinant of the spin-orbitals (Eq. (2.82)), is given by $\sum_{i=1}^{N}|\varphi_i|^2$. Thus, the effective potential $V_{\mathrm{S}}(\mathbf{r}_i)$ is then chosen such that the density $\rho_{\mathrm{S}}(\mathbf{r})$ exactly equals $\rho_0(\mathbf{r})$, the ground state density of our real target system of interacting electrons:

$$\rho(\mathbf{r}) \equiv \rho_{\mathrm{S}}(\mathbf{r}) = \sum_{i=1}^{N}|\varphi_i(\mathbf{x})|^2 = \rho_0(\mathbf{r}) \tag{2.86}$$

From now on, we will use ρ as if we were talking about ρ_{S}, for simplicity. The kinetic energy of the non-interacting system will be calculated exactly:

$$T_{\text{S}}[\rho] = -\frac{1}{2}\sum_{i=1}^{N} \langle\varphi_i|\nabla^2|\varphi_i\rangle \tag{2.87}$$

$T_{\text{S}}[\rho]$, the non-interacting kinetic energy is not equal to $T[\rho]$, the kinetic energy of the interacting system. This is accounted for by introducing $T_{\text{C}}[\rho]$, a residual part of the part of the true kinetic energy:

$$T[\rho] = T_{\text{C}}[\rho] + T_{\text{S}}[\rho] \tag{2.88}$$

The non-classical contribution of $V_{ee}[\rho]$ (Eq. (2.75)) is also not known. Both $V_{\text{non-classsical}}[\rho]$ and $T_{\text{C}}[\rho]$ are gathered onto the so called *exchange-correlation energy*:

$$E_{\text{XC}}[\rho] = (T[\rho] - T_{\text{S}}[\rho]) + (E_{ee}[\rho] - J[\rho]) = T_{\text{C}}[\rho] + V_{\text{non-classsical}}[\rho] \tag{2.89}$$

In this way, the exchange-correlation energy contains everything that is unknown: not only the non-classical effects of self-interaction correction, exchange and correlation, which are the contributions to the potential energy of the system, but also a portion belonging to the kinetic energy. Having introduced E_{XC}, $[\rho]$ $F[\rho]$ now reads like:

$$F[\rho] = T_{\text{S}}[\rho] + J[\rho] + E_{\text{XC}}[\rho] \tag{2.90}$$

Using the expression for $T_{\text{S}}[\rho]$ (Eq. 2.87), $J[\rho]$ (Eq. 2.76), $V_{ne}[\rho]$ (Eq. 2.71), we find that the expression for the energy is the following:

$$\begin{aligned} E[\rho] &= \underbrace{T_{\text{S}}[\rho] + V_{ee}[\rho]}_{=F[\rho]} + V_{ne}[\rho] \\ &= T_{\text{S}}[\rho] + J[\rho] + E_{\text{XC}}[\rho] + V_{ne}[\rho] \\ &= -\frac{1}{2}\sum_{i=1}^{N} \langle\varphi_i|\nabla^2|\varphi_i\rangle + \frac{1}{2}\iint \frac{\rho(\mathbf{r}_1)\rho(\mathbf{r}_2)}{r_{12}}\mathrm{d}\mathbf{r}_1\mathrm{d}\mathbf{r}_2 + E_{\text{XC}}[\rho] + \int \rho\left(\mathbf{r}\right) v_{\text{ext}}\left(\mathbf{r}\right)\mathrm{d}\mathbf{r} \end{aligned} \tag{2.91}$$

By inserting Eq. (2.61) into Eq. (2.71), we get that $V_{ne}[\rho]$ can be expressed as:

$$V_{ne}[\rho] = \int -\sum_{A=1}^{M} \frac{Z_A}{r_{1A}}\rho\left(\mathbf{r}_1\right)\mathrm{d}\mathbf{r}_1 \tag{2.92}$$

where, using Eq. (2.86) we can replace $\rho(\mathbf{r}_1)\,\mathrm{d}\mathbf{r}_1$ by the Kohn-Sham orbitals:

$$\begin{aligned} V_{ne}[\rho] &= \int -\sum_{A=1}^{M} \frac{Z_A}{r_{1A}} \sum_{i=1}^{N} |\varphi_i(\mathbf{x}_1)|^2\,\mathrm{d}\mathbf{r}_1 \\ &= -\sum_{i=1}^{N} \int \sum_{A=1}^{M} \frac{Z_A}{r_{1A}} |\varphi_i(\mathbf{x}_1)|^2\,\mathrm{d}\mathbf{r}_1 \end{aligned} \tag{2.93}$$

Similarly, $J[\rho]$ (Eq. 2.76) in terms of Khon-Sham orbitals gives:

$$J[\rho] = \frac{1}{2}\sum_{i=1}^{N}\sum_{j=1}^{N} \iint |\varphi_i(\mathbf{r}_1)|^2 \frac{1}{r_{12}} |\varphi_j(\mathbf{r}_2)|^2\,\mathrm{d}\mathbf{r}_1\mathrm{d}\mathbf{r}_2 \tag{2.94}$$

Gathering all this together the final expression of $E[\rho]$ reads like:

$$\begin{aligned} E[\rho] = &-\frac{1}{2}\sum_{i=1}^{N} \langle\varphi_i|\nabla^2|\varphi_i\rangle + \frac{1}{2}\sum_{i=1}^{N}\sum_{j=1}^{N} \iint |\varphi_i(\mathbf{r}_1)|^2 \frac{1}{r_{12}} |\varphi_j(\mathbf{r}_2)|^2\,\mathrm{d}\mathbf{r}_1\mathrm{d}\mathbf{r}_2 \\ &+ E_{\mathrm{XC}}[\rho] - \sum_{i=1}^{N}\int\sum_{A=1}^{M} \frac{Z_A}{r_{1A}} |\varphi_i(\mathbf{x}_1)|^2\,\mathrm{d}\mathbf{r}_1 \end{aligned} \tag{2.95}$$

This scheme is summarized in Fig. 2.8. Just as one can show that the orthonormal orbitals that minimize the Hartree-Fock expression for the energy are those that satisfy Equations (2.52), one can show that the Kohn-Sham orbitals that minimize the expression (2.95) for the ground state energy are:

$$\begin{aligned} &\left(-\frac{1}{2}\nabla^2 + \left[\int \frac{\rho(\mathbf{r}_2)}{r_{12}}\,\mathrm{d}\mathbf{r}_2 + V_{\mathrm{XC}}(\mathbf{r}_1) - \sum_{A=1}^{M}\frac{Z_A}{r_{1A}}\right]\right)\varphi_i \\ &= \left(-\frac{1}{2}\nabla^2 + V_{\mathrm{eff}}(\mathbf{r}_1)\right)\varphi_i = \varepsilon_i^{\mathrm{KS}}\varphi_i \end{aligned} \tag{2.96}$$

By comparing Eq. (2.85) with Eq. (2.96), it is possible to see that V_{eff} is exactly the same as $V_{\mathrm{S}}(\mathbf{r})$:

$$V_{\mathrm{S}}(\mathbf{r}) \equiv V_{\mathrm{eff}}(\mathbf{r}) = \int \frac{\rho(\mathbf{r}_2)}{r_{12}}\,\mathrm{d}\mathbf{r}_2 + V_{\mathrm{XC}}(\mathbf{r}_1) - \sum_{A=1}^{M}\frac{Z_A}{r_{1A}} \tag{2.97}$$

Once each of the contributions in Eq. (2.97) are known, the potential $V_{\mathrm{S}}(\mathbf{r})$ is then casted into the one-electron particle equations (Eq. 2.96), from which we obtain the orbitals, and therefore the ground state density. By using Eq. (2.95), we can determine the ground state energy. However, we encounter an already known problem here: $V_{\mathrm{S}}(\mathbf{r})$ depends on the density, and thus on the orbitals. Therefore, just like the Hartree-Fock equations (2.52), the Kohn-Sham one-electron equations (2.96) also have to be solved iteratively.

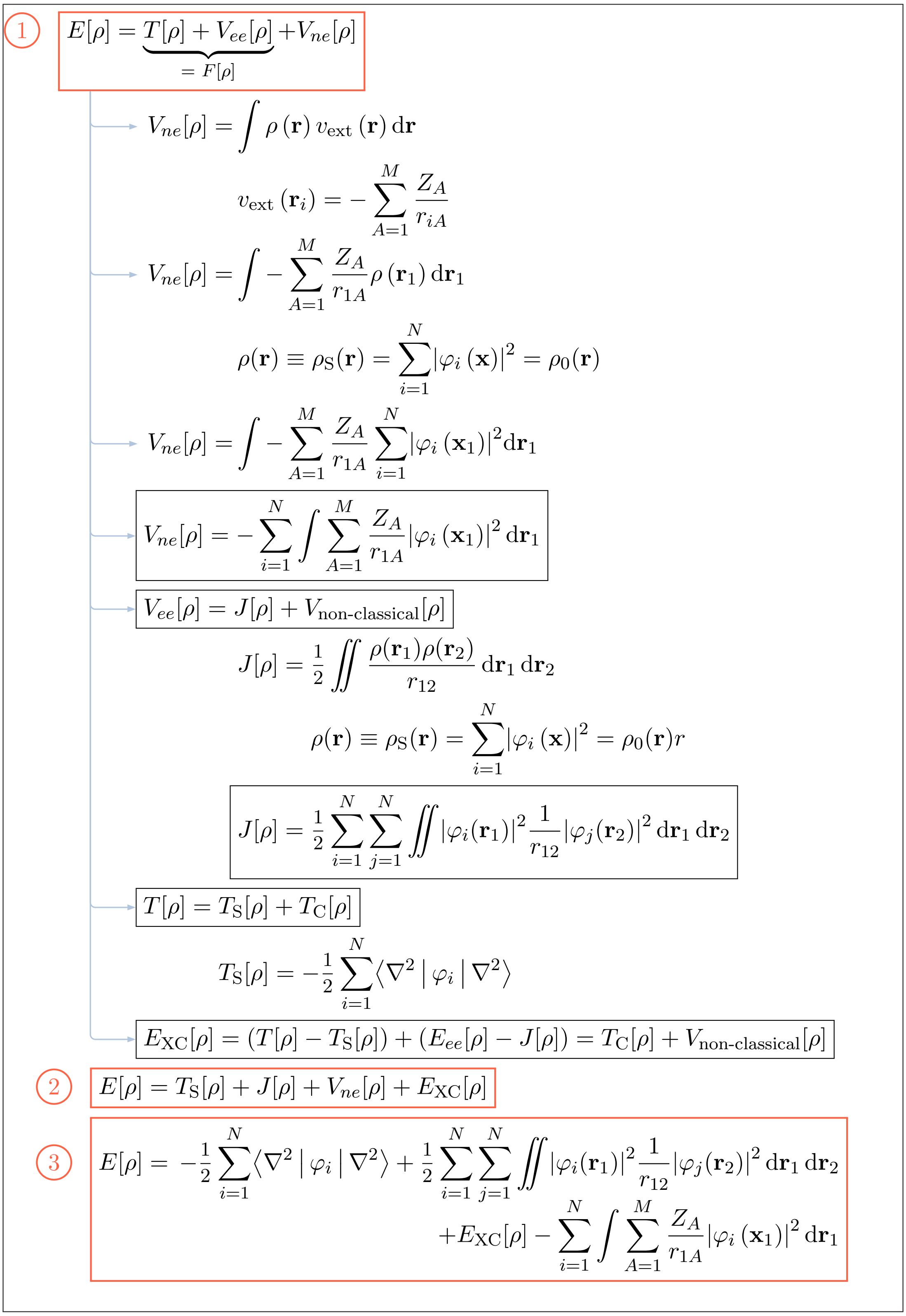

①
$$\boxed{E[\rho] = \underbrace{T[\rho] + V_{ee}[\rho]}_{=F[\rho]} + V_{ne}[\rho]}$$

$$V_{ne}[\rho] = \int \rho\left(\mathbf{r}\right) v_{\text{ext}}\left(\mathbf{r}\right) \mathrm{d}\mathbf{r}$$

$$v_{\text{ext}}\left(\mathbf{r}_i\right) = -\sum_{A=1}^{M} \frac{Z_A}{r_{iA}}$$

$$V_{ne}[\rho] = \int -\sum_{A=1}^{M} \frac{Z_A}{r_{1A}} \rho\left(\mathbf{r}_1\right) \mathrm{d}\mathbf{r}_1$$

$$\rho(\mathbf{r}) \equiv \rho_{\mathrm{S}}(\mathbf{r}) = \sum_{i=1}^{N} \left|\varphi_i\left(\mathbf{x}\right)\right|^2 = \rho_0(\mathbf{r})$$

$$V_{ne}[\rho] = \int -\sum_{A=1}^{M} \frac{Z_A}{r_{1A}} \sum_{i=1}^{N} \left|\varphi_i\left(\mathbf{x}_1\right)\right|^2 \mathrm{d}\mathbf{r}_1$$

$$\boxed{V_{ne}[\rho] = -\sum_{i=1}^{N} \int \sum_{A=1}^{M} \frac{Z_A}{r_{1A}} \left|\varphi_i\left(\mathbf{x}_1\right)\right|^2 \mathrm{d}\mathbf{r}_1}$$

$$\boxed{V_{ee}[\rho] = J[\rho] + V_{\text{non-classical}}[\rho]}$$

$$J[\rho] = \frac{1}{2} \iint \frac{\rho(\mathbf{r}_1)\rho(\mathbf{r}_2)}{r_{12}} \mathrm{d}\mathbf{r}_1 \, \mathrm{d}\mathbf{r}_2$$

$$\rho(\mathbf{r}) \equiv \rho_{\mathrm{S}}(\mathbf{r}) = \sum_{i=1}^{N} \left|\varphi_i\left(\mathbf{x}\right)\right|^2 = \rho_0(\mathbf{r}) r$$

$$\boxed{J[\rho] = \frac{1}{2} \sum_{i=1}^{N} \sum_{j=1}^{N} \iint \left|\varphi_i(\mathbf{r}_1)\right|^2 \frac{1}{r_{12}} \left|\varphi_j(\mathbf{r}_2)\right|^2 \mathrm{d}\mathbf{r}_1 \, \mathrm{d}\mathbf{r}_2}$$

$$\boxed{T[\rho] = T_{\mathrm{S}}[\rho] + T_{\mathrm{C}}[\rho]}$$

$$T_{\mathrm{S}}[\rho] = -\frac{1}{2} \sum_{i=1}^{N} \left\langle \nabla^2 \,\middle|\, \varphi_i \,\middle|\, \nabla^2 \right\rangle$$

$$\boxed{E_{\mathrm{XC}}[\rho] = (T[\rho] - T_{\mathrm{S}}[\rho]) + (E_{ee}[\rho] - J[\rho]) = T_{\mathrm{C}}[\rho] + V_{\text{non-classical}}[\rho]}$$

②
$$\boxed{E[\rho] = T_{\mathrm{S}}[\rho] + J[\rho] + V_{ne}[\rho] + E_{\mathrm{XC}}[\rho]}$$

③
$$\boxed{\begin{aligned} E[\rho] = -\frac{1}{2} \sum_{i=1}^{N} \left\langle \nabla^2 \,\middle|\, \varphi_i \,\middle|\, \nabla^2 \right\rangle + \frac{1}{2} \sum_{i=1}^{N} \sum_{j=1}^{N} \iint \left|\varphi_i(\mathbf{r}_1)\right|^2 \frac{1}{r_{12}} \left|\varphi_j(\mathbf{r}_2)\right|^2 \mathrm{d}\mathbf{r}_1 \, \mathrm{d}\mathbf{r}_2 \\ + E_{\mathrm{XC}}[\rho] - \sum_{i=1}^{N} \int \sum_{A=1}^{M} \frac{Z_A}{r_{1A}} \left|\varphi_i\left(\mathbf{x}_1\right)\right|^2 \mathrm{d}\mathbf{r}_1 \end{aligned}}$$

Figure 2.8: Summary of the DFT formulation

Since we do not know the exchange correlation energy E_{XC}, we also do not know the explicit form of the *exchange-correlation potential*, V_{XC} in Eq. (2.96). Therefore, it is simply defined as the functional derivative of E_{XC} with respect to ρ:

$$V_{\mathrm{XC}} = \frac{\delta E_{\mathrm{XC}}}{\delta \rho} \tag{2.98}$$

The Kohm-Sham approach is in principle exact. The approximation only enters when deciding on an explicit form of the unknown functional for the exchange-correlation energy E_{XC} and the corresponding potential V_{XC}.

2.2.6.4 Approximate Exchange-Correlation Functionals

There are several proposed approximate exchange-correlation functionals, e.g. LDA, GGA and Hybrid functionals, described herein.

- **Local density approximation**

The Local Density Approximation (LDA) assumes that E_{XC} can be written as:

$$E_{\mathrm{EX}}^{\mathrm{LDA}}[\rho] = \int \rho(\mathbf{r})\epsilon_{\mathrm{XC}}\left(\rho(\mathbf{r})\right) \mathrm{d}\mathbf{r} \tag{2.99}$$

where $\epsilon_{\mathrm{XC}}\left(\rho(\mathbf{r})\right)$ is the exchange-correlation energy per particle of a uniform electron gas of density $\rho(\mathbf{r})$, and can be splitted into exchange and correlation contributions:

$$\epsilon_{\mathrm{XC}}\left(\rho(\mathbf{r})\right) = \epsilon_{\mathrm{X}}\left(\rho(\mathbf{r})\right) + \epsilon_{\mathrm{C}}\left(\rho(\mathbf{r})\right) \tag{2.100}$$

The exchange part ϵ_{X} represents the exchange energy of an electron in a uniform electron gas of a particular density, determined by Bloch and Dirac:

$$\epsilon_{\mathrm{X}}\left(\rho\left(\mathbf{r}\right)\right) = -\frac{3}{4}\left(\frac{3}{\pi}\right)^{1/3}\left(\rho\left(\mathbf{r}\right)\right)^{1/3} \tag{2.101}$$

No explicit expression is known for ϵ_{C}, the correlation part. It has instead been derived from highly accurate quantum Monte Carlo simulations of the homogeneous electron gas. On the basis of these results, some authors have obtained analytical expressions of ϵ_{C}, giving rise to widely used LDA functionals such as the Vosko-Wilk and Nusair (VWN) [43] and the Perdew-Wang (PW92) [44] functionals.

Since the LDA functional is based on the uniform electron gas model, this situation resembles the model of an idealized metal consisting of a perfect crystal of valence electrons and positive cores. For this reason, this functional reproduces fairly well the geometries of simple metals e.g. sodium. However, it underestimates band gaps. In addition, this model is far from any realistic situation in atoms or molecules, which are usually characterized by varying densities.

- **Generalised gradient approximation**

In order to account for the non-homogeneity of the true electron density, a possible solution is not only to use the information about the density $\rho(\mathbf{r})$, but also the gradient of the charge density, $\nabla\rho(\mathbf{r})$. This idea gives birth to the Generalised Gradient Approximation (GGA) functionals.

Functionals like Perdew-Wang (PW91) [45], Becke88 (B) [46] are based on scaling relations and sum rules. Others, like Perdew-Burke-Ernzerhof (PBE) [47] are parametrised by numerical fitting procedures in order to reproduce the experimental value of some molecular properties.

GGA functionals lead to a better description of energy barriers and atomisation energies. However, like LDA, it fails to describe van der Waals interactions and also underestimates band gaps. One explanation for this last effect is because of the unresolved problem of the self-interaction in DFT, which makes the occupied levels to be pushed up in energy, leading to an underestimation of band gaps.

Meta-GGA functionals such as PKZB and VS98 [48, 49, 50] include higher order derivatives of the electron density and lead to an improvement in atomisation and binding energies.

- **Hybrid functionals**

These functionals arise from the idea of introducing some percentage of HF exchange energy. This percentage is chosen such that the experimental atomization, ionization energies and proton affinities are optimally reproduced. The best example is the Becke 3 parameter Lee-Yang- Parr (B3LYP) hybrid functional [51, 52]:

$$E_{\mathrm{XC}}^{\mathrm{B3LYP}} = E_{\mathrm{XC}}^{\mathrm{LDA}} + 0.2\left(E_{\mathrm{X}}^{\mathrm{HF}} - E_{\mathrm{X}}^{\mathrm{LDA}}\right) + 0.72\left(E_{\mathrm{X}}^{\mathrm{B88}} - E_{\mathrm{X}}^{\mathrm{LDA}}\right) + 0.81\left(E_{\mathrm{C}}^{\mathrm{PW91}} - E_{\mathrm{C}}^{\mathrm{LDA}}\right) \quad (2.102)$$

where $E_{\mathrm{X}}^{\mathrm{B88}}$ is the B88 exchange functional and $E_{\mathrm{C}}^{\mathrm{PW91}}$ the PW91 correlation functional. These coefficients are determined by fitting to observed atomisation energies, ionisation potentials, proton affinities and total atomic energies [52].

Hybrid functionals are more accurate in atomisation enthalpies, geometries and vibrational frequencies. Band gaps are as accurate as those obtained with correlated methods [53]. B3LYP is considered to be the functional mostly used [54]. Other hybrid functionals include PBE0 [55, 56] and Heyd-Scuseria-Ernzerhof (HSE) [57].

2.2.6.5 Dispersion correction

Even in the absence of charges or permanent electric moments, two non-interacting molecules or atoms present long range attractive forces, also referred to as London forces due to the electron density of both units. At an intermediate distance, the motion of electrons in one unit induces slight perturbations in the electron density of the neighbour unit, generating a induced dipole moment that induces a charge polarization in the first unit. The result is an attractive force between the two systems that decays with the inverse sixth power of the intermolecular distance. [2] These dispersion interactions play an important role in all organic or metallo-organic systems, in terms of the optimized geometry, lattice energy, frequencies, and reactivities. Because of the organic nature of the carbonate group (CO_3^{2-}), dispersion interactions need to be taken into account in the determination of the phase boundary of calcium carbonate. Within this formalism, the total energy is given by:

$$E_{\mathrm{DFT-D}} = E_{\mathrm{KS-DFT}} + E_{\mathrm{disp}} \tag{2.103}$$

where E_{disp}, the empirical dispersion correction, is given by

$$E_{\mathrm{disp}} = -s_6 \sum_{i=1}^{N_{\mathrm{at}}-1} \sum_{j=i+1}^{N_{\mathrm{at}}} \frac{C_6^{ij}}{R_{ij}^6} f_{\mathrm{dmp}}(R_{ij}) \tag{2.104}$$

N_{at} is the number of atoms in the system, C_6^{ij} denotes the dispersion coefficient for atom pair ij, s_6 is a global scaling factor that only depends on the functional used, and R_{ij} is an interatomic

---

[2] An estimation of the strength of the dispersion energy is the following: two atoms or small molecules in contact at $r = \sigma \approx 0.3$ nm, with $\alpha_0/4\pi\epsilon_0 \approx 1.5 \cdot 10^{-30}$ m^3 and $I = h\nu \approx 10^{-18}$J (a typical ionization potential in the UV), yield a dispersion interacting energy of $-4.6 \cdot 10^{-21}$J $\approx 1k_BT$ (at 298K) [58]. Large molecules such as hexane or higher molecular weight hydrocarbons are liquids or solids namely because they are held together solely by dispersion forces.

distance. In order to avoid near-singularities for small R, a damping function f_{dmp} must be used, which is given by

$$f_{\mathrm{dmp}}(R_{ij}) = \frac{1}{1 + \exp\left[-d\left(R_{ij}/R_r - 1\right)\right]} \tag{2.105}$$

Dispersion corrections were initially developed by Grimme [59], and have been progressively being improved by collaborators [60, 61, 62], and implemented in the CRYSTAL code [63], e.g. D2 or the most recent D3 corrections for dispersion interactions.

2.2.7 From Atomic Orbitals to Bloch Functions

In a periodic system there are infinite number of orbitals. To tackle with this situation it is necessary to exploit the translational symmetry.

We will start by developing the orbitals within the unit cell and then extend this situation to a periodic system using Bloch functions.

2.2.7.1 One-dimensional chain of atoms

For a one-dimensional chain of atoms like the one shown in Fig. 2.9, the basis vector in the reciprocal lattice is $\mathbf{b}$, of length:

$$|\mathbf{b}| = \frac{2\pi}{|\mathbf{a}|} = \frac{2\pi}{a} \tag{2.106}$$

The shortest reciprocal lattice vectors from the origin O are $\mathbf{b}$ and $-\mathbf{b}$. The perpendicular bisector of these vectors at their midpoints define the boundaries of the first Brillouin zone. Thus, the boundaries are at:

$$\text{Boundaries: } \pm\frac{|\mathbf{b}|}{2} = \pm\frac{2\pi}{a} = \pm\frac{\pi}{a} \tag{2.107}$$

The region of $\mathbf{k}$ values between π/a and $-\pi/a$ is referred to as the first Brillouin zone. The variation in energy as a function of the wavevector $\mathbf{k}$ is called the ***dispersion band***. It can be shown that the diagram energy vs $\mathbf{k}$ has a mirror symmetry about $\mathbf{k} = 0$, so it is sufficient just

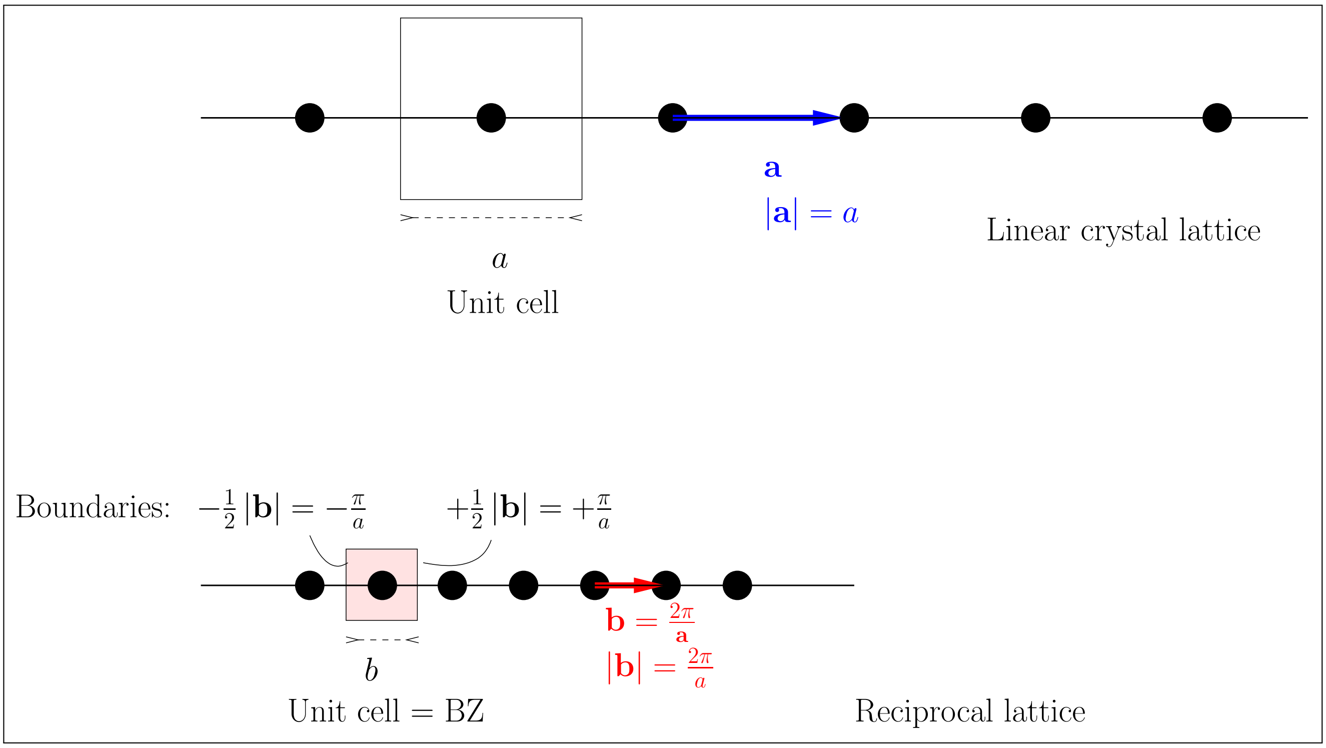

Figure 2.9: Direct (upper panel) and reciprocal (lower panel) lattices for a one-dimensional chain of atoms.

to use one-half of this diagram. We will choose the right-hand half that corresponds to positive $\mathbf{k}$. The point $\mathbf{k} = \pi/a$ is called the zone edge and $\mathbf{k} = 0$ the zone center.

The electrons of each of these atoms are described by an orbital φ_μ centered on each atom. Each unit cell of length a contains one atom and is labelled as $n = 0, 1, 2...$ (Figure 2.10).

The origin of the Cartesian coordinate system is located in the bottom left corner of cell $n = 0$. The position of each atom inside each nth cell is described by the vector $\mathbf{A}_\mu$. The translational vector respect to the cell $n = 0$ is described by $\mathbf{g}_n = n\mathbf{a}$. In this way, we can define the position of any atom in by summing two vectors: $\mathbf{A}_\mu + \mathbf{g}_n$:

$$\text{Position of atom in } n = 0: \quad \mathbf{g}_0 + \mathbf{A}_\mu = \mathbf{A}_\mu$$

$$\text{Position of atom in } n = 1: \quad \mathbf{g}_1 + \mathbf{A}_\mu = \mathbf{a} + \mathbf{A}_\mu$$

$$\text{Position of atom in } n = 2: \quad \mathbf{g}_2 + \mathbf{A}_\mu = 2\mathbf{a} + \mathbf{A}_\mu$$

In order to implement correctly the Bloch Theorem, it is necessary to change the origin of the Cartesian coordinate system: each nth orbital φ_μ will be now referred to the left bottom corner

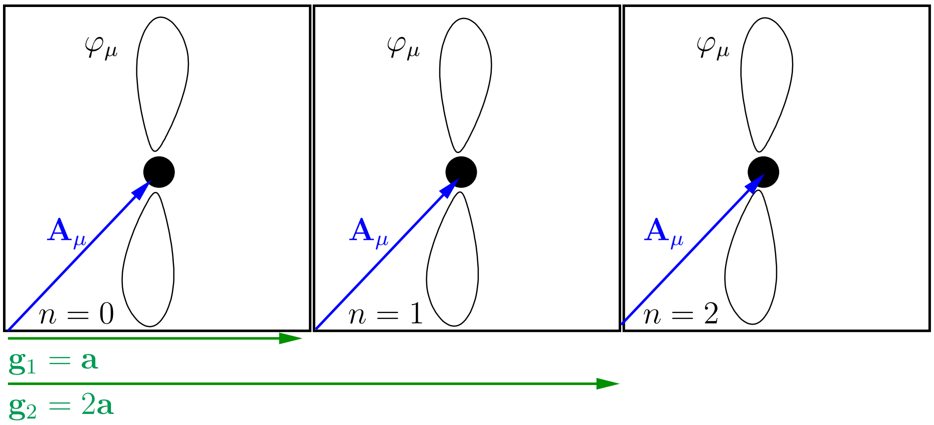

Figure 2.10: One-dimensonal chain of atoms described by an orbital φ_μ centered on each atom. The position of each atom inside each nth cell is described by the vector $\mathbf{A}_\mu$.

of each nth cell[3]

$$\begin{aligned}
&\text{Position of the orbital in } n = 0: \quad \varphi_\mu(\mathbf{A}_\mu - \mathbf{g}_0) = \varphi_\mu(\mathbf{A}_\mu) \\
&\text{Position of the orbital in } n = 1: \quad \varphi_\mu(\mathbf{A}_\mu - \mathbf{g}_1) = \varphi_\mu(\mathbf{A}_\mu - \mathbf{a}) \\
&\text{Position of the orbital in } n = 2: \quad \varphi_\mu(\mathbf{A}_\mu - \mathbf{g}_2) = \varphi_\mu(\mathbf{A}_\mu - 2\mathbf{a})
\end{aligned}$$

It can be proved that the symmetry adapted linear combination of these φ_μ atomic orbitals under the action of translational symmetry is given by Bloch functions:

$$\phi(\mathbf{k}) = \sum_{\mathbf{g}} \varphi_\mu(\mathbf{A}_\mu - \mathbf{g}) \exp[i\mathbf{k} \cdot \mathbf{g}] \tag{2.108}$$

Since we are solving the electronic structure of a periodic system, we need to take into account the position of each electron in the system. Thus, if we denote as $\mathbf{r}$ the position of an electron in orbital $\mathbf{A}_\mu$, we redefine the problem by using a new vector $\mathbf{m}$, as shown in Figure (2.11).

It is satisfied that: $\mathbf{r} = \mathbf{A}_\mu + \mathbf{m}$, so that $\mathbf{m} = \mathbf{r} - \mathbf{A}_\mu$. In this way, we now define the atomic orbital as $\varphi_\mu(\mathbf{m} - \mathbf{g}) = \varphi_\mu(\mathbf{r} - \mathbf{A}_\mu - \mathbf{g})$:

---

[3] Notice that if we maintain the previous coordinate system in which there is only one origin, located in the bottom left corner of the cell $n = 0$, the orbitals on each nth cell will then be given by $\varphi_\mu(\mathbf{A}_\mu + \mathbf{g}_n)$. It is generally agreed by convention to stick to the $\varphi_\mu(\mathbf{A}_\mu - \mathbf{g}_n)$ notation in the construction of Bloch functions. In order to use this notation, there must be n origins, located at the bottom left of each nth cell. In other words, the original coordinate system is translated n times per cell, by a quantity a, $2a$, $3a$, etc.

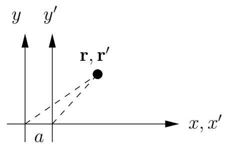

where $\begin{aligned} x' &= x - a \\ y' &= y \end{aligned}$

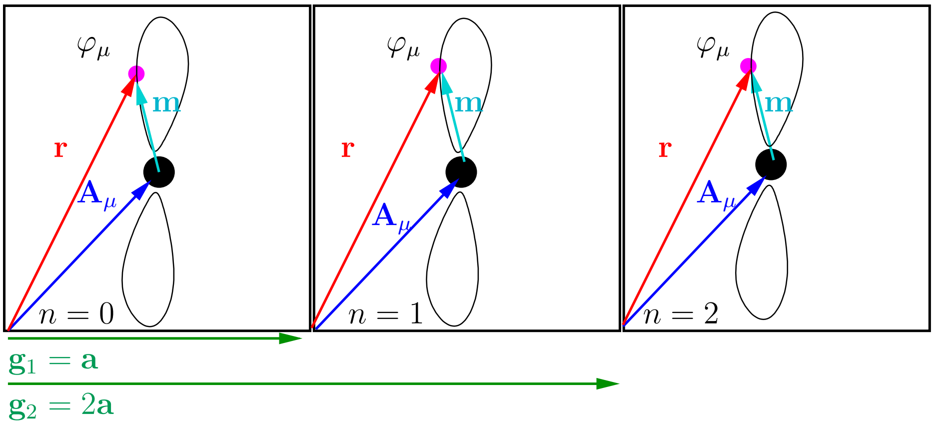

Figure 2.11: One-dimensonal chain of atoms described by an orbital φ_μ centered on each atom. $\mathbf{r}$ is the position of an electron in orbital φ_μ. The position of each atom inside each nth cell is described by the vector $\mathbf{A}_\mu$, so that $\mathbf{r} = \mathbf{A}_\mu + \mathbf{m}$.

$$\boxed{\phi(\mathbf{r};\mathbf{k}) = \sum_{\mathbf{g}} \varphi_\mu\left(\mathbf{r} - \mathbf{A}_\mu - \mathbf{g}\right) \exp\left[i\mathbf{k}\cdot\mathbf{g}\right]} \tag{2.109}$$

The functions $\phi(\mathbf{r};\mathbf{k})$ are called Bloch functions and represent the symmetry adapted linear combination of atomic orbitals, under the action of translational symmetry. BFs are periodic functions with respect to $\mathbf{k}$, and have the same value when equivalent $\mathbf{k}$ points are considered. This property allows to analyze only the $\mathbf{k}$ points of the origin cell, that corresponds to the first Brillouin Zone.

Each atomic orbital is expressed as a linear combination of normalized Gaussian type functions (GTFs), with fixed coefficients d_j and exponents α_j:

$$\boxed{\varphi_\mu\left(\mathbf{r} - \mathbf{A}_\mu - \mathbf{g}\right) = \sum_{j}^{n_G} d_j G\left(\alpha_j; \mathbf{r} - \mathbf{A}_\mu - \mathbf{g}\right)} \tag{2.110}$$

The collection of all atomic orbitals is referred to as the basis set.

We will now proceed to obtain the dispersion band for the case of a 1D chain of atoms in which the unit cell of lenght a contains only one atom.

According to what has been discussed, each nth atom is described by an orbital $\varphi_\mu\left(\mathbf{r} - \mathbf{A}_\mu - n\mathbf{a}\right)$, as shown in Fig. 2.12.

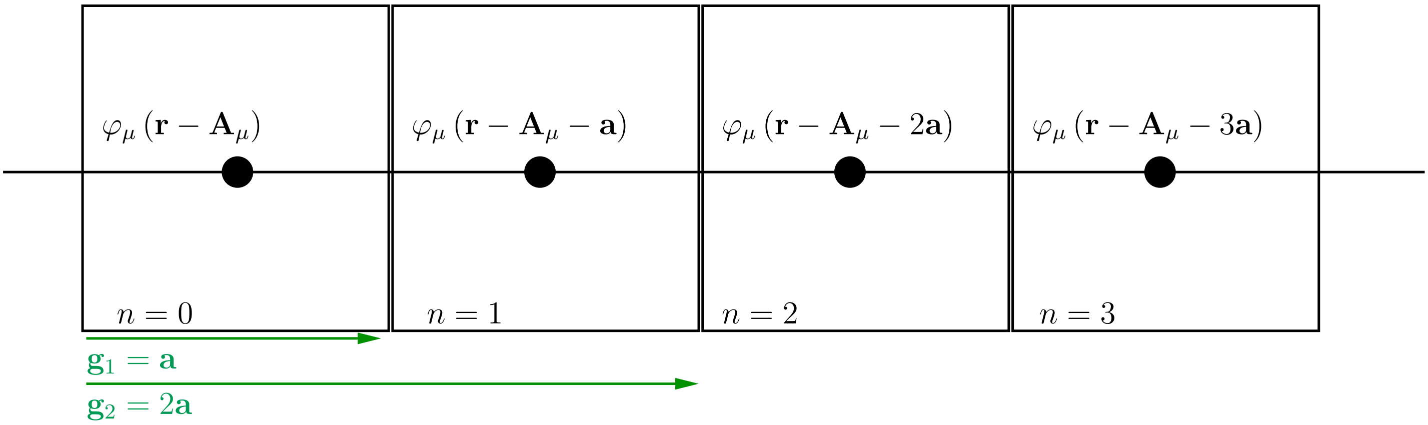

Figure 2.12: Four unit cells of length a, each of them containing one atom represented by a black dot. $\varphi_\mu(\mathbf{r})$ is some arbitrary orbital located on some atom in the chain; $\varphi_\mu(\mathbf{r}-\mathbf{A}_\mu-\mathbf{a})$ lies at a distance $\mathbf{a}$ along the chain, $\varphi_\mu(\mathbf{r}-\mathbf{A}_\mu-2\mathbf{a})$ at a distance $2\mathbf{a}$, and so on, from $\varphi_\mu(\mathbf{r}-\mathbf{A}_\mu)$. For simplicity, the shape of the orbitals is omitted, but is to be considered as an arbitrary orbital.

For this situation, for a general value of $\mathbf{k}$, Eq. (2.109) may be written as[4]:

$$\boxed{\phi(\mathbf{r};\mathbf{k})=\varphi_\mu(\mathbf{r}-\mathbf{A}_\mu)+\varphi_\mu(\mathbf{r}-\mathbf{A}_\mu-\mathbf{a})\exp[i\mathbf{k}\cdot\mathbf{a}]+\varphi_\mu(\mathbf{r}-\mathbf{A}_\mu-2\mathbf{a})\exp[i\mathbf{k}\cdot 2\mathbf{a}]+...} \tag{2.111}$$

By implementing Eq. (2.111) on the boundary conditions:

a) If $\mathbf{k}=0$, $\exp[i\mathbf{k}\cdot\mathbf{g}]=1$ so that:

$$\phi(\mathbf{r};\mathbf{k}=0)=\varphi_\mu(\mathbf{r}-\mathbf{A}_\mu)+\varphi_\mu(\mathbf{r}-\mathbf{A}_\mu-\mathbf{a})+\varphi_\mu(\mathbf{r}-\mathbf{A}_\mu-2\mathbf{a})+\varphi_\mu(\mathbf{r}-\mathbf{A}_\mu-3\mathbf{a})+... \tag{2.112}$$

b) If $\mathbf{k}=\pi/a$:

$$\phi(\mathbf{r};\mathbf{k}=\pi/a)=\varphi_\mu(\mathbf{r}-\mathbf{A}_\mu)-\varphi_\mu(\mathbf{r}-\mathbf{A}_\mu-\mathbf{a})+\varphi_\mu(\mathbf{r}-\mathbf{A}_\mu-2\mathbf{a})-\varphi_\mu(\mathbf{r}-\mathbf{A}_\mu-3\mathbf{a})+... \tag{2.113}$$

In order to visualize in a simple way both wavefunctions (2.112) and (2.113), we will consider each $\varphi_\mu(\mathbf{r}-\mathbf{A}_\mu-n\mathbf{a})$ orbital to be a spheric s type orbital, represented as circles in Figure

---

[4] The first term of this summation on Eq. (2.109) corresponds to $\mathbf{g}=0$, so that this first term reads like: $\varphi_\mu\left(\mathbf{r}-\mathbf{A}_\mu-\underbrace{\mathbf{a}}_{=0}\right)\exp\left[i\mathbf{k}\cdot\underbrace{\mathbf{a}}_{=0}\right]=\varphi_\mu(\mathbf{r}-\mathbf{A}_\mu)$

(2.13): Wavefunction (2.112) found at the zone center ($\mathbf{k} = 0$) corresponds to a maximum bonding, and therefore a maximum stabilization. On the other hand, wavefunction (2.113) at the zone edge ($\mathbf{k} = \pi/a$) is the maximum antibonding situation (Figure (2.13)).

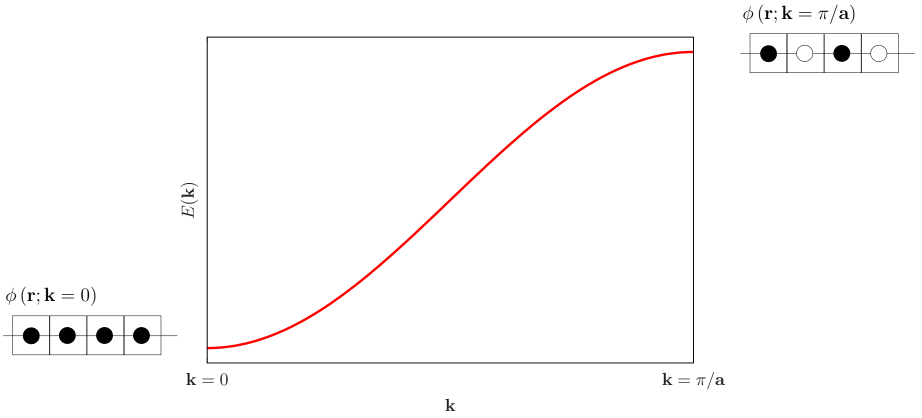

Figure 2.13: Dispersion $E(\mathbf{k})$ versus $\mathbf{k}$ band for a situation described in Figure (2.12), where there is only one atom per unit cell, described by an orbital $\mathbf{A}_\mu$. For simplicity, this orbital is described in this figure as a spheric s type orbital.

In Figure (2.12) we chose a repeating unit for our calculation that contained a single orbital. If we choose a two-atom repeat unit as in Fig. (2.14), where $\mathbf{a}' = 2\mathbf{a}$, the $E(\mathbf{k})$ versus $\mathbf{k}$ diagram will be now different: at each value of $\mathbf{k}$ there will now be two energy levels because there are now two orbitals per unit cell. To tackle with this problem, we first need to develop Bloch functions for each of the two orbitals in the unit cell.

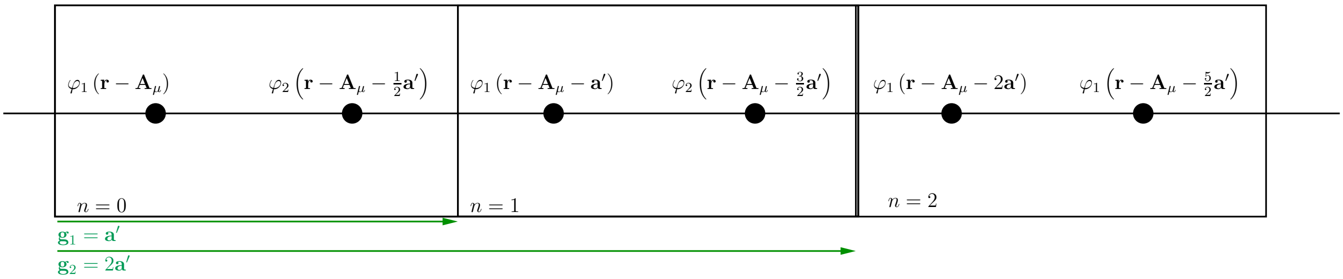

Figure 2.14: Four unit cells of length a, each of them containing two atoms. The labels represent the same as in 2.12, where $\mathbf{a}' = 2\mathbf{a}$.

As shown in Figure (2.14), we will locate φ_1 and φ_2 on the left and right hand side atoms of any given unit cell. Starting with $\varphi_1(\mathbf{r}-\mathbf{A}_\mu)$, this orbital is sent to $\varphi_1(\mathbf{r}-\mathbf{A}_\mu-\mathbf{a}')$ by a translation $\mathbf{a}'$ and to $\varphi_1(\mathbf{r}-\mathbf{A}_\mu-2\mathbf{a}')$ by a translation $2\mathbf{a}'$. φ_1 and φ_2 are translationally separated by $\mathbf{a}'/2$. Using Eq. (2.111), on each of the two orbitals,

$$\begin{aligned}\phi_1(\mathbf{r};\mathbf{k}) &= \varphi_1\left(\mathbf{r}-\mathbf{A}_\mu\right)+\varphi_1\left(\mathbf{r}-\mathbf{A}_\mu-\mathbf{a}'\right)\exp\left[i\mathbf{k}\cdot\mathbf{a}'\right]+\\ &+\varphi_1\left(\mathbf{r}-\mathbf{A}_\mu-2\mathbf{a}'\right)\exp\left[i\mathbf{k}\cdot 2\mathbf{a}'\right]+...\end{aligned} \tag{2.114a}$$

$$\begin{aligned}\phi_2(\mathbf{r};\mathbf{k}) &= \varphi_2\left(\mathbf{r}-\mathbf{A}_\mu-\frac{1}{2}\mathbf{a}'\right)\exp\left[i\mathbf{k}\cdot\frac{1}{2}\mathbf{a}'\right]+\varphi_2\left(\mathbf{r}-\mathbf{A}_\mu-\frac{3}{2}\mathbf{a}'\right)\exp\left[i\mathbf{k}\cdot\frac{3}{2}\mathbf{a}'\right]+\\ &+\varphi_2\left(\mathbf{r}-\mathbf{A}_\mu-\frac{5}{2}\mathbf{a}'\right)\exp\left[i\mathbf{k}\cdot\frac{5}{2}\mathbf{a}'\right]+...\end{aligned} \tag{2.114b}$$

Now there are two orbitals for each value of $\mathbf{k}$. The best way to acquire an intuitive picture of this situation is the following. We will describe the diatomic unit by an orbital ξ, from a linear combination of the φ orbitals:

$$\xi_1(\mathbf{r}) = \varphi_1\left(\mathbf{r}-\mathbf{A}_\mu\right)+\varphi_2\left(\mathbf{r}-\mathbf{A}_\mu-\frac{1}{2}\mathbf{a}'\right) \tag{2.115}$$

$$\xi_2(\mathbf{r}) = \varphi_1\left(\mathbf{r}-\mathbf{A}_\mu\right)-\varphi_2\left(\mathbf{r}-\mathbf{A}_\mu-\frac{1}{2}\mathbf{a}'\right) \tag{2.116}$$

Similarly,

$$\xi_1(\mathbf{r}-\mathbf{a}') = \varphi_1\left(\mathbf{r}-\mathbf{A}_\mu-\mathbf{a}'\right)\exp[i\mathbf{k}\cdot\mathbf{a}']+\varphi_2\left(\mathbf{r}-\mathbf{A}_\mu-\frac{3}{2}\mathbf{a}'\right)\exp[i\mathbf{k}\cdot\mathbf{a}'] \tag{2.117}$$

$$\xi_2(\mathbf{r}-\mathbf{a}') = \varphi_1\left(\mathbf{r}-\mathbf{A}_\mu-\mathbf{a}'\right)\exp[i\mathbf{k}\cdot\mathbf{a}']-\varphi_2\left(\mathbf{r}-\mathbf{A}_\mu-\frac{3}{2}\mathbf{a}'\right)\exp[i\mathbf{k}\cdot\mathbf{a}'] \tag{2.118}$$

and

$$\xi_1(\mathbf{r}-2\mathbf{a}') = \varphi_1\left(\mathbf{r}-\mathbf{A}_\mu-2\mathbf{a}'\right)\exp[i\mathbf{k}\cdot 2\mathbf{a}']+\varphi_2\left(\mathbf{r}-\mathbf{A}_\mu-\frac{5}{2}\mathbf{a}'\right)\exp[i\mathbf{k}\cdot 2\mathbf{a}'] \tag{2.119}$$

$$\xi_2(\mathbf{r}-2\mathbf{a}') = \varphi_1\left(\mathbf{r}-\mathbf{A}_\mu-2\mathbf{a}'\right)\exp[i\mathbf{k}\cdot 2\mathbf{a}']-\varphi_2\left(\mathbf{r}-\mathbf{A}_\mu-\frac{5}{2}\mathbf{a}'\right)\exp[i\mathbf{k}\cdot 2\mathbf{a}'] \tag{2.120}$$

All these wavefunctions Eq.(2.115) - Eq. (2.120) are represented on Figure (2.15). We can now construct Bloch functions as:

$$\boxed{\begin{aligned}\Phi_1\left(\mathbf{r};\mathbf{k}\right) &= \xi_1(\mathbf{r}) + \xi_1(\mathbf{r}-\mathbf{a}') + \xi_1(\mathbf{r}-2\mathbf{a}') + \ldots \qquad (2.121a)\\ \Phi_2\left(\mathbf{r};\mathbf{k}\right) &= \xi_2(\mathbf{r}) + \xi_2(\mathbf{r}-\mathbf{a}') + \xi_2(\mathbf{r}-2\mathbf{a}') + \ldots \qquad (2.121b)\end{aligned}}$$

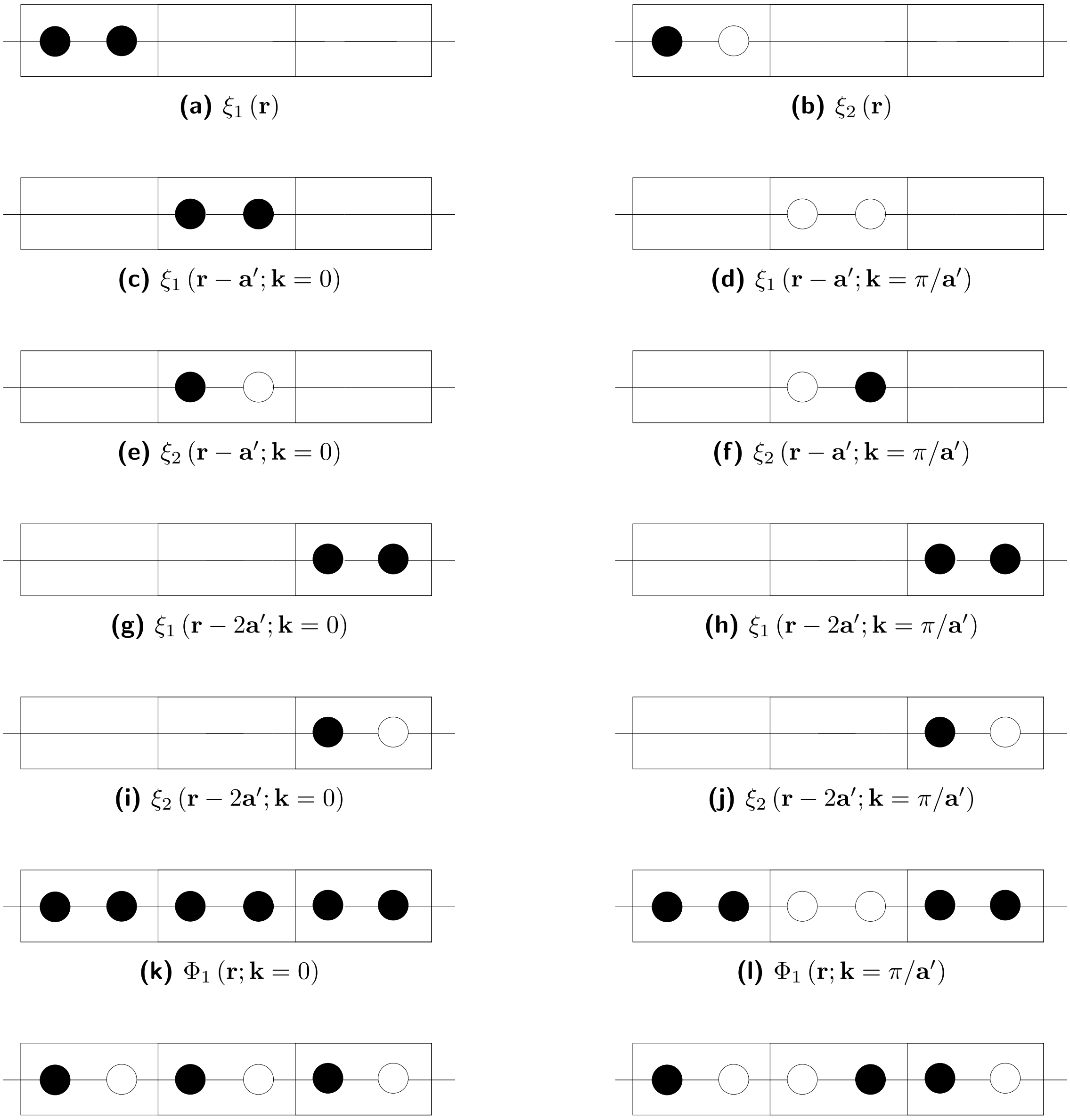

(a) $\xi_1\left(\mathbf{r}\right)$

(b) $\xi_2\left(\mathbf{r}\right)$

(c) $\xi_1\left(\mathbf{r}-\mathbf{a}';\mathbf{k}=0\right)$

(d) $\xi_1\left(\mathbf{r}-\mathbf{a}';\mathbf{k}=\pi/\mathbf{a}'\right)$

(e) $\xi_2\left(\mathbf{r}-\mathbf{a}';\mathbf{k}=0\right)$

(f) $\xi_2\left(\mathbf{r}-\mathbf{a}';\mathbf{k}=\pi/\mathbf{a}'\right)$

(g) $\xi_1\left(\mathbf{r}-2\mathbf{a}';\mathbf{k}=0\right)$

(h) $\xi_1\left(\mathbf{r}-2\mathbf{a}';\mathbf{k}=\pi/\mathbf{a}'\right)$

(i) $\xi_2\left(\mathbf{r}-2\mathbf{a}';\mathbf{k}=0\right)$

(j) $\xi_2\left(\mathbf{r}-2\mathbf{a}';\mathbf{k}=\pi/\mathbf{a}'\right)$

(k) $\Phi_1\left(\mathbf{r};\mathbf{k}=0\right)$

(l) $\Phi_1\left(\mathbf{r};\mathbf{k}=\pi/\mathbf{a}'\right)$

(m) $\Phi_2\left(\mathbf{r};\mathbf{k}=0\right)$

(n) $\Phi_2\left(\mathbf{r};\mathbf{k}=\pi/\mathbf{a}'\right)$

Figure 2.15: Wavefunctions for the one-dimensional lattice (Equations (2.115) to (2.121b)).

The dispersion band for both $\Phi_1\left(\mathbf{r};\mathbf{k}\right)$ and $\Phi_2\left(\mathbf{r};\mathbf{k}\right)$ Bloch functions is represented in Figure (2.16).

From this Figure we can deduce that:

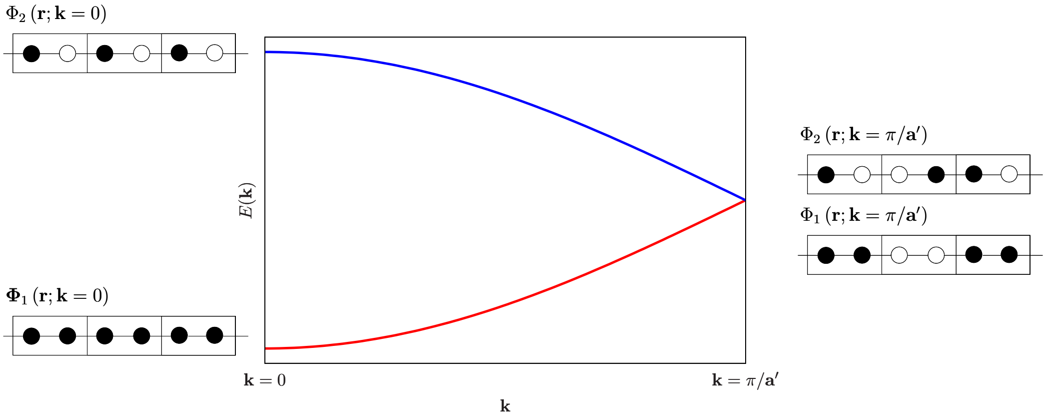

Figure 2.16: Dispersion $E(\mathbf{k})$ versus $\mathbf{k}$ band for a situation described in Figure (2.14), where there are two atoms per unit cell, each of them described by an orbital $\mathbf{A}_\mu$. For simplicity, this orbital is described in this figure as a spheric s type orbital.

a) At the zone center, the most bonding ($\Phi_1\,(\mathbf{r};\mathbf{k}=0)$) and most antibonding ($\Phi_2\,(\mathbf{r};\mathbf{k}=0)$) levels can be found.

b) At the zone edge, the nonbonding levels $\Phi_1\,(\mathbf{r};\mathbf{k}=\pi/\mathbf{a}')$ and $\Phi_2\,(\mathbf{r};\mathbf{k}=\pi/\mathbf{a}')$ are found.

Recall that $\mathbf{a}'$ in Figure 2.14 is twice the value of $\mathbf{a}$ in Figure 2.12. Thus, there is a direct relationship between Figures 2.16 and 2.13. The $E(\mathbf{k})$ versus $\mathbf{k}$ diagram of the two-atom cell is just that of the one-atom cell but the levels have been folded back along $\mathbf{k}=\pi/2\mathbf{a}$ (Figure 2.17).

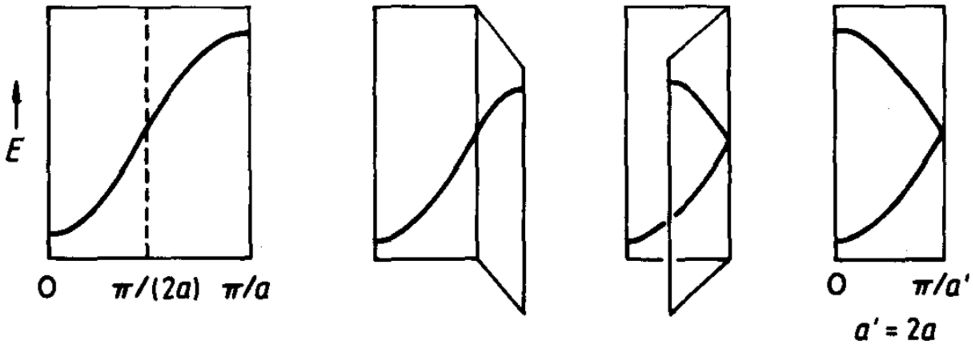

Figure 2.17: Process by which the "folding back" of the dispersion curve for the one orbital cell results in the dispersion curve for the two orbital cell. Image obtained from Ref. [64].

The process can be continued. If the unit cell is tripled or quadrupled the band will fold as in Figure 2.18a or 2.18b respectively.

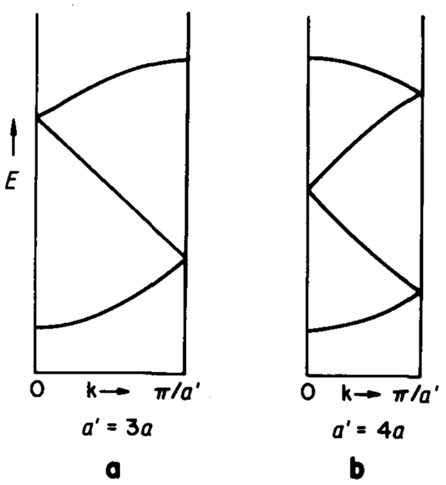

Figure 2.18: Dispersion curve for the three (a) and four (b) orbital cell. Image obtained from Ref. [64].

2.2.7.2 Two-dimensional crystal

Because materials are also two- or three-dimensional, we must extend this formalism to higher dimensionality. In two dimensions, we shall treat $\mathbf{k}$ as a vector:

$$\mathbf{k} = \mathbf{k}_x + \mathbf{k}_y = k_x\hat{x} + k_y\hat{y} \tag{2.122}$$

For example, for a square lattice defined by the translation vectors $\mathbf{a}_1$ and $\mathbf{a}_2$, where $a = |\mathbf{a}_1| = |\mathbf{a}_2|$ (Figure 2.19), we will consider that the range of each vector is $0 \leqslant |\mathbf{k}_x|, |\mathbf{k}_y| \leqslant \pi/a$.

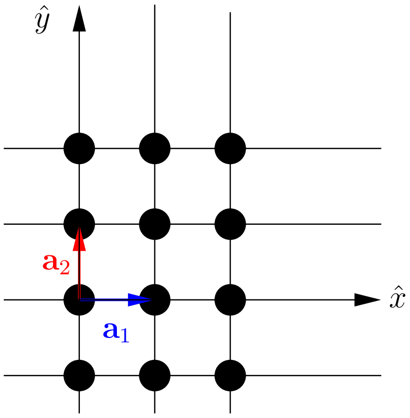

Figure 2.19: Square 2D lattice described by the translation vectors $\mathbf{a}_1$ and $\mathbf{a}_2$.

The reciprocal space here is defined by two vectors $\mathbf{b}_1$ and $\mathbf{b}_2$, and the Brillouin zone is a square (Figure 2.20).

It is very frequent to identify a point on the first Brillouin zone by a set of 2 coordinates (or

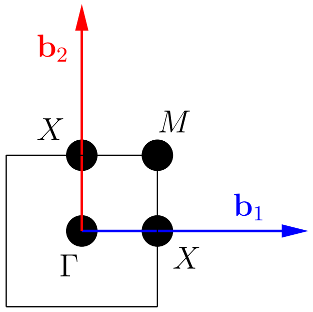

Figure 2.20: First Brillouin zone of a 2D square lattice. The points X, M and Γ are points in reciprocal space.

3 in 3D). This is a common practice in dispersion curves and electronic band structure plots. Therefore, it is important to explain clearly how it is used. These coordinates $(\pm m1, \pm m2)$ are given by the fractional number that multiplies each reciprocal lattice vector. For instance, if we are asking for the point $(\frac{1}{2}, \frac{1}{2})$ in reciprocal space, this would mean:

$$\frac{1}{2}\mathbf{b}_1 = \mathbf{k}_x \qquad \frac{1}{2}\mathbf{b}_2 = \mathbf{k}_y \tag{2.123}$$

So that:

$$\frac{1}{2}|\mathbf{b}_1| = \frac{1}{2}\frac{2\pi}{|\mathbf{a}_1|\,|\mathbf{a}_2|}|\mathbf{a}_2| = \frac{\pi}{a} = k_x \tag{2.124}$$

$$\frac{1}{2}|\mathbf{b}_2| = \frac{1}{2}\frac{2\pi}{|\mathbf{a}_1|\,|\mathbf{a}_2|}|\mathbf{a}_1| = \frac{\pi}{a} = k_y \tag{2.125}$$

This situation corresponds to the wavefunction shown on Fig. (2.21c). Certain special values of k_x and k_y are given names,

1. Point Γ refers to the position $(0, 0)$, wavefunction shown on Fig. 2.21a.

2. Point X refers to 4 equivalent positions: $(\frac{1}{2}, 0)$; $(-\frac{1}{2}, 0)$; $(0, \frac{1}{2})$ and $(0, -\frac{1}{2})$. These points correspond respectively to $(\mathbf{k}_x, \mathbf{k}_y) = (\frac{\pi}{a}, 0)$, wavefunction shown on Fig. 2.21b; $(\mathbf{k}_x, \mathbf{k}_y) = (-\frac{\pi}{a}, 0)$; $(\mathbf{k}_x, \mathbf{k}_y) = (0, \frac{\pi}{a})$, wavefunction shown on Fig. 2.21d; $(\mathbf{k}_x, \mathbf{k}_y) = (0, -\frac{\pi}{a})$.

3. Point M refers to 4 equivalent positions: $(\frac{1}{2}, \frac{1}{2})$; $(\frac{1}{2}, -\frac{1}{2})$; $(-\frac{1}{2}, \frac{1}{2})$; $(-\frac{1}{2}, -\frac{1}{2})$. These points correspond respectively to $(\mathbf{k}_x, \mathbf{k}_y) = (\frac{\pi}{a}, \frac{\pi}{a})$, wavefunction shown on Fig. 2.21c; $(\mathbf{k}_x, \mathbf{k}_y) = (\frac{\pi}{a}, -\frac{\pi}{a})$; $(\mathbf{k}_x, \mathbf{k}_y) = (-\frac{\pi}{a}, \frac{\pi}{a})$; $(\mathbf{k}_x, \mathbf{k}_y) = (-\frac{\pi}{a}, -\frac{\pi}{a})$.

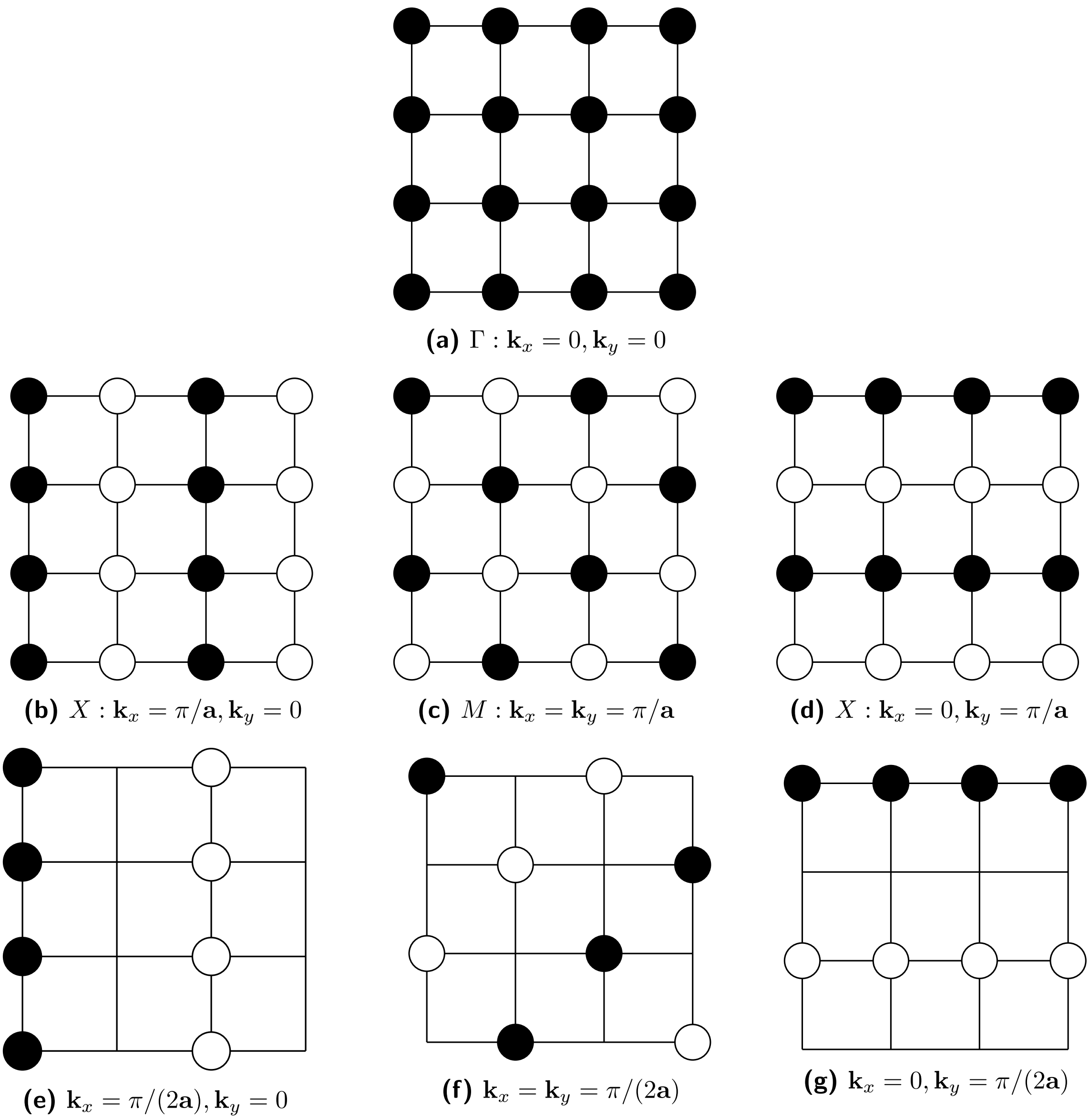

(a) $\Gamma : \mathbf{k}_x = 0, \mathbf{k}_y = 0$

(b) $X : \mathbf{k}_x = \pi/\mathbf{a}, \mathbf{k}_y = 0$

(c) $M : \mathbf{k}_x = \mathbf{k}_y = \pi/\mathbf{a}$

(d) $X : \mathbf{k}_x = 0, \mathbf{k}_y = \pi/\mathbf{a}$

(e) $\mathbf{k}_x = \pi/(2\mathbf{a}), \mathbf{k}_y = 0$

(f) $\mathbf{k}_x = \mathbf{k}_y = \pi/(2\mathbf{a})$

(g) $\mathbf{k}_x = 0, \mathbf{k}_y = \pi/(2\mathbf{a})$

Figure 2.21: Wavefunctions for the two-dimensional lattice

The wavefunctions for the case of a double sized cell shown in Figures 2.21e, 2.21f and 2.21g refer to intermediate solutions, e.g. Fig. 2.21e is halfway point on going from Γ to X, and Fig. 2.21f corresponds to the halfway point on returning from M to Γ.

It would be a complicated task to show the energy levels of $E(\mathbf{k})$ for all $\mathbf{k}$. Typically, the evolution of E along certain lines in the brillouin zone is shown. Some common paths are $\Gamma \to X$, $\Gamma \to M$ or $X \to M$. From Fig. (2.21c) we see that M is the most antibonding situation, and therefore is the highest energy wave function, as opposed to Γ (Fig. (2.21a)), the most bonding interaction. X (Figs. (2.21b, 2.21d)) has a many bonding interactions as it does antibonding ones, so we would be talking about a nonbonding interaction. A band structure corresponding to a square lattice of H atoms with $a = 2.0\mathring{A}$ confirms this behaviour (see Fig.

2.22).

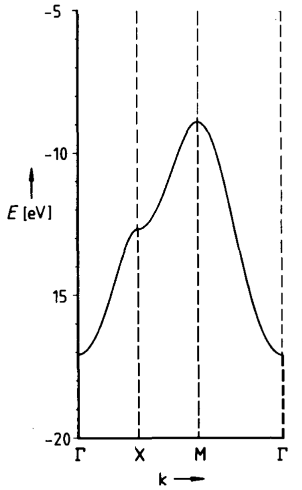

Figure 2.22: Band structure for a square lattice of H atoms. Γ, X and M points correspond to the wavefunctions shown in Fig. 2.21. Image reproduced from Ref. [64].

2.2.7.3 Three-dimensional crystal

In a 3D crystal, the first Brillouin zone is a parallelepiped, whose specific shape and zone boundaries depend on the Bravais lattice considered in direct space. The different case scenarios are described herein.

- **Reciprocal lattice of the simple cubic (sc) lattice**

Given the lattice vectors of the sc lattice (Eq. 2.3), the volume of the cell is $\mathbf{a} \cdot \mathbf{b} \times \mathbf{c} = a^3$. Using the definition (Eq. 2.9), the primitive translation vectors of the reciprocal lattice are found to be:

$$\mathbf{b}_1 = 2\pi \frac{\mathbf{a}_2 \times \mathbf{a}_3}{\mathbf{a}_1 \cdot (\mathbf{a}_2 \times \mathbf{a}_3)} = \frac{2\pi}{a}\,\hat{x}; \qquad \mathbf{b}_2 = \frac{2\pi}{a}\,\hat{y}; \qquad \mathbf{b}_3 = \frac{2\pi}{a}\,\hat{z} \tag{2.126}$$

Thus, the simple cubic reciprocal lattice has lattice constant $2\pi/a$. The boundaries of the first Brillouin zones are the planes normal to the six reciprocal lattice vectors $\pm\mathbf{b}_1$, $\pm\mathbf{b}_2$, $\pm\mathbf{b}_3$ at their midpoints:

$$\text{Boundaries:} \qquad \pm\frac{1}{2}\mathbf{b}_1 = \pm\frac{\pi}{a}\,\hat{x}; \qquad \pm\frac{1}{2}\mathbf{b}_2 = \pm\frac{\pi}{a}\,\hat{y}; \qquad \pm\frac{1}{2}\mathbf{b}_3 = \pm\frac{\pi}{a}\,\hat{z} \tag{2.127}$$

This six planes define a cube of edge $2\pi/a$ and volume $(2\pi/a)^3$. This cube is the first Brillouin zone of the sc crystal lattice.

A point in the first Brillouin zone will be now given by 3 coordinates $(\pm m_1, \pm m_2, \pm m_3)$. These are given by the fractional number that multiplies each reciprocal lattice vector. For instance, if we have in mind the first Brillouin zone for the sc lattice (Fig. 2.23), and we want to refer to a point located in the surface of one of the faces of this cube, we will be asking for the boundary of this first BZ, and therefore the coordinates are normally given as $(\pm\frac{1}{2}, \pm\frac{1}{2}, \pm\frac{1}{2})$. In other words:

1. Point X refers to 6 equivalent positions: $(\pm\frac{1}{2}, 0, 0)$, $(0, \pm\frac{1}{2}, 0)$ and $(0, 0, \pm\frac{1}{2})$.
2. Point M refers to 12 equivalent positions: $(\pm\frac{1}{2}, \pm\frac{1}{2}, 0)$, $(0, \pm\frac{1}{2}, \pm\frac{1}{2})$, and $(\pm\frac{1}{2}, 0, \pm\frac{1}{2})$.
3. Point R refers to 8 equivalent positions: $(\pm\frac{1}{2}, \pm\frac{1}{2}, \pm\frac{1}{2})$,

Roman letters are normally used for points on the surface (boundary) of the BZ. On the other hand, Greek letters are used to refer to points within the zone: Δ for $(\xi, 0, 0)$, Σ for $(\xi, \zeta, 0)$, and Λ for (ξ, ζ, ς). where ξ, ζ and ς are no longer $\frac{1}{2}$. The point $(0, 0, 0)$ is always given the label Γ.

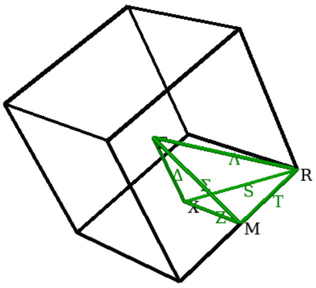

Figure 2.23: First Brillouin zone for a simple cubic lattice. The points R, X, M and Γ are indicated, as explained in the text. Figure obtained from Ref. [65].

- **Reciprocal lattice of the body-centered cubic (bcc) lattice**

Given the lattice vectors of the bcc lattice (Eq. 2.4), the volume of the primitive cell is:

$$\mathbf{a}_1 \cdot (\mathbf{a}_2 \times \mathbf{a}_3) = \frac{1}{2}a^3 \tag{2.128}$$

so that the reciprocal lattice vectors are:

$$\mathbf{b}_1 = \frac{2\pi}{a}\,(\hat{y}+\hat{z})\,; \qquad \mathbf{b}_2 = \frac{2\pi}{a}\,(\hat{x}+\hat{z})\,; \qquad \mathbf{b}_3 = \frac{2\pi}{a}\,(\hat{x}+\hat{y}) \tag{2.129}$$

By comparison with Eq. (2.5), we see that these lattice vectors are just the primitive vectors of an fcc lattice. In other words, an fcc lattice is the reciprocal lattice of the bcc lattice.

According to Eq. (2.10), the infinite set of reciprocal vectors is:

$$\mathbf{G} = h\mathbf{b}_1 + k\mathbf{b}_2 + l\mathbf{b}_3 = \frac{\pi}{a}\,[(h+l)\,\hat{x} + (h+k)\,\hat{y} + (k+l)\,\hat{z}] \tag{2.130}$$

where h, k and l are integers. The shortest vectors are the following 12:

$$\text{Shortest }\mathbf{G}: \qquad \mathbf{G}_1 = \frac{2\pi}{a}(\pm\hat{x}\pm y); \qquad \mathbf{G}_2 = \frac{2\pi}{a}(\pm\hat{y}\pm z); \qquad \mathbf{G}_3 = \frac{2\pi}{a}(\pm\hat{x}\pm z); \tag{2.131}$$

The primitive cell of the reciprocal lattice is the parallelepiped described by the $\mathbf{b}_1$, $\mathbf{b}_2$ and $\mathbf{b}_3$ from Eq. (2.129), and has a volume of $V = |\mathbf{b}_1 \cdot (\mathbf{b}_2 \times \mathbf{b}_3)| = 2(2\pi/a)^3$. Each of the eight corners of the parallelepiped is shared among eight parallelepipeds, so that each parallelepiped contains one-eight of each corner points. The first Brillouin zone is bounded by the planes normal to these 12 vectors of Eq. (2.131) at their midpoints. The zone is a 12-faced solid, a rhombic dodecahedron (Fig. 2.24). The vectors from the origin to the center of each face are:

$$\text{Boundaries: } \frac{1}{2}\,(\text{Shortest }\mathbf{G}): \qquad \frac{1}{2}\mathbf{G}_1 = \frac{\pi}{a}(\pm\hat{x}\pm\hat{y}); \qquad \frac{1}{2}\mathbf{G}_2 = \frac{\pi}{a}(\pm\hat{y}\pm\hat{z}); \qquad \frac{1}{2}\mathbf{G}_3 = \frac{\pi}{a}(\pm\hat{x}\pm\hat{z}) \tag{2.132}$$

For instance, the point N refers to 6 equivalent positions at the surface (boundary): $(\pm\frac{1}{2}, 0, 0)$, $(0, \pm\frac{1}{2}, 0)$ and $(0, 0, \pm\frac{1}{2})$.

- **Reciprocal lattice of the face-centered cubic (fcc) lattice**

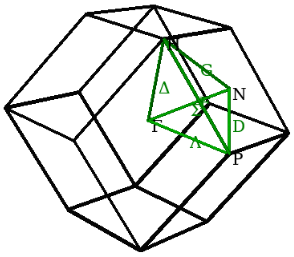

Figure 2.24: First Brillouin zone for a body centered cubic lattice. The points N, is indicated, as explained in the text. Figure reproduced from Ref. [65].

Given the lattice vectors of the fcc lattice (Eq. 2.5), the volume of the primitive cell is:

$$\mathbf{a}_1 \cdot (\mathbf{a}_2 \times \mathbf{a}_3) = \frac{1}{4}a^3 \tag{2.133}$$

and the reciprocal lattice vectors are:

$$\mathbf{b}_1 = \frac{2\pi}{a}\,(\hat{x} + \hat{y} - \hat{z})\,; \qquad \mathbf{b}_2 = \frac{2\pi}{a}\,(-\hat{x} + \hat{y} + \hat{z})\,; \qquad \mathbf{b}_3 = \frac{2\pi}{a}\,(\hat{x} - \hat{y} + \hat{z}) \tag{2.134}$$

The volume of this primitive cell is $|\mathbf{b}_1 \cdot (\mathbf{b}_2 \times \mathbf{b}_3)| = 4(2\pi/a)^3$. These vectors are the primitive vectors of the bcc lattice, so that the bcc lattice is the reciprocal lattice of the fcc lattice.

The infinite set of reciprocal vectors is:

$$\mathbf{G} = h\mathbf{b}_1 + k\mathbf{b}_2 + l\mathbf{b}_3 = \frac{2\pi}{a}\,[(h - k + l)\,\hat{x} + (h + k - l)\,\hat{y} + (-h + k + l)\,\hat{z}] \tag{2.135}$$

The shortest vectors are the following 8:

$$\text{Shortest } \mathbf{G} : \qquad \frac{2\pi}{a}(\pm\hat{x} \pm y \pm z) \tag{2.136}$$

The boundaries are determined by the eight planes normal to these vectors at their midpoints: Thus, the 8 vectors from the origin to the center of each face are:

$$\text{Boundaries: } \frac{1}{2}\,(\text{Shortest } \mathbf{G}) : \qquad \frac{1}{2}\mathbf{G} = \frac{\pi}{a}(\pm\hat{x} \pm \hat{y} \pm z) \tag{2.137}$$

The shape of this BZ is a truncated octahedron (Fig. 2.25) of volume $(4\pi/a)^3$. For instance, the point L refers to 2 equivalent positions at the surface of the BZ: $(\frac{1}{2}, \frac{1}{2}, \frac{1}{2})$ and $(-\frac{1}{2}, -\frac{1}{2}, -\frac{1}{2})$.

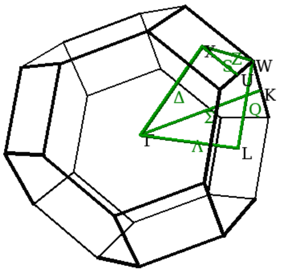

Figure 2.25: First Brillouin zone for a face centered cubic lattice. The points L is indicated, as explained in the text. Figure reproduced from Ref. [65].

The corners of the octahedron are cut by the planes that are perpendicular bisectors of six other reciprocal lattice vectors, so that equivalent lattice vectors can be found:

$$\text{Other shortest } \mathbf{G} : \quad \frac{2\pi}{a}(\pm 2\hat{x}); \quad \frac{2\pi}{a}(\pm 2\hat{y}); \quad \frac{2\pi}{a}(\pm 2\hat{z}) \tag{2.138}$$

2.2.8 From Molecular Orbitals to Crystalline Orbitals

If Molecular Orbitals are linear combinations of AOs, Crystalline orbitals $\psi_i(\mathbf{r};\mathbf{k})$ are expressed as a linear combination of Bloch functions:

$$\psi_i(\mathbf{r};\mathbf{k}) = \sum_{\mathbf{g}} a_{\mu,i}(\mathbf{k})\phi_\mu(\mathbf{r};\mathbf{k}) \tag{2.139}$$

The expansion coefficients of the Bloch functions, $a_{\mu,i}(\mathbf{k})$, are calculated by solving the following matrix equation for each reciprocal lattice vector, $\mathbf{k}$:

$$\mathbf{F}(\mathbf{k})\mathbf{A}(\mathbf{k}) = \mathbf{S}(\mathbf{k})\mathbf{A}(\mathbf{k})\mathbf{E}(\mathbf{k}) \tag{2.140}$$

where all matrices have equal size, and $\mathbf{F}(\mathbf{k})$, $\mathbf{A}(\mathbf{k})$, $\mathbf{S}(\mathbf{k})$, and $\mathbf{E}(\mathbf{k})$ are, respectively, the Fock, eigenvectors, overlap and eigenvalues matrices.

Eq. 2.140 is equivalent to the Roothan-Hall equations, with the only difference that in a periodic system, these equations have to be solved at each $\mathbf{k}$ point of a chosen grid.

By using a BF strategy, the infinite Hamiltonian matrix in the AOs basis becomes an infinite block-diagonal matrix in the BF basis set, with each block referring to one particular **k** point (Fig. 2.26).

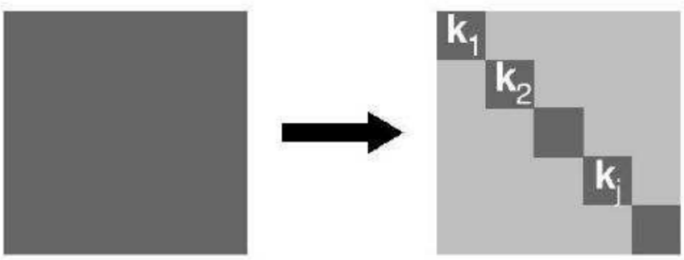

Figure 2.26: The infinite hamiltonian matrix of AOs (left) is transformed to a infinite block-diagonal matrix. Once we set a finite number of **k** points, the matrix becomes finite.

It is convenient to calculate all matrices in the Atomic Orbital representation ("direct space representation"), simply because the Bloch Functions are expressed in terms of a local basis set. After the evaluation of the several integrals has been performed in direct space, all the quantities are transformed to reciprocal space, and Eq. 2.140 is solved for a given number of **k** points.

2.2.9 Building the matrices

Every matrix element is identified by the indices μ and ν. The μ index refers to the atomic orbital centered in the origin cell. The direct lattice vector **g**, labels the cell where the ν-th atomic orbital is centered.

The matrix elements of the overlap matrix are denoted as $S_{\mu\nu}$ and read like:

$$S_{\mu\nu} = \int \phi_\mu(\mathbf{r};\mathbf{k})\,\phi_\nu^*(\mathbf{r};\mathbf{k})d\mathbf{r}, \tag{2.141}$$

Each of the elements of the Fock matrix is calculated as a sum of contributions: kinetic energy (T), electron-nuclear (Z) interactions, electron-electron Coulomb (C) and exchange (X) interactions:

$$F_{\mu\nu}^{\mathbf{g}} = T_{\mu\nu}^{\mathbf{g}} + Z_{\mu\nu}^{\mathbf{g}} + C_{\mu\nu}^{\mathbf{g}} + X_{\mu\nu}^{\mathbf{g}} \tag{2.142}$$

The total energy per cell is given by

$$E_{\text{tot}} = N + \frac{1}{2}\sum_{\mu,\nu}\sum_{\mathbf{g}} P^{\mathbf{g}}_{\mu\nu}\left(T^{\mathbf{g}}_{\mu\nu} + Z^{\mathbf{g}}_{\mu\nu} + F^{\mathbf{g}}_{\mu\nu}\right), \tag{2.143}$$

where $P^{\mathbf{g}}_{\mu\nu}$ are the matrix elements of the density matrix:

$$P^{\mathbf{g}}_{\mu\nu} = \sum_{\mathbf{k}}\sum_{n}^{N_{\text{occ}}} \exp(i\mathbf{k}\cdot\mathbf{g})c^{*}_{\mu n}(\mathbf{k})c_{\nu n}(\mathbf{k}) \tag{2.144}$$

It is more intuitive to rewrite the total energy as a sum of five contributions:

$$E_{\text{tot}} = E_{\text{Nuclear}} + E_{\text{Kinetic}} + E_{\text{Nuc-electron}} + E_{\text{Coulomb}} + E_{\text{Exchange}}, \tag{2.145}$$

where:

$$E_{\text{Kinetic}} = \sum_{\mu\nu}\sum_{\mathbf{g}} K^{\mathbf{g}}_{\mu\nu} \tag{2.146}$$

$$= -\frac{1}{2}\sum_{\mu\nu}\sum_{\mathbf{g}} \overbrace{\langle\varphi^{0}_{\mu}|\nabla^{2}|\varphi^{\mathbf{g}}_{\nu}\rangle}^{T_1} \tag{2.147}$$

$$E_{\text{Nuc-electron}} = \sum_{\mu\nu}\sum_{\mathbf{g}} P^{\mathbf{g}}_{\mu\nu}Z^{\mathbf{g}}_{\mu\nu} \tag{2.148}$$

$$= \sum_{\mu\nu}\sum_{\mathbf{g}} P^{\mathbf{g}}_{\mu\nu}\sum_{\mathbf{h}}\sum_{A}^{N_A} \overbrace{\langle\varphi^{0}_{\mu}|\frac{1}{|\mathbf{r}-\mathbf{R_A}-\mathbf{h}|}|\varphi^{\mathbf{g}}_{\nu}\rangle}^{T_1} \tag{2.149}$$

$$E_{\text{Coulomb}} = \frac{1}{2}\sum_{\mu\nu}\sum_{\mathbf{g}} P^{\mathbf{g}}_{\mu\nu}C^{\mathbf{g}}_{\mu\nu} \tag{2.150}$$

$$= \frac{1}{2}\sum_{\mu\nu}\sum_{\mathbf{g}} P^{\mathbf{g}}_{\mu\nu}\sum_{\sigma,\omega}\sum_{\mathbf{g}'} P^{\mathbf{g}'}_{\sigma\omega}\sum_{\mathbf{h}} \left\langle \overbrace{\varphi^{0}_{\mu}\varphi^{\mathbf{g}}_{\nu}}^{T_1} \middle| \frac{1}{|\mathbf{r_1}-\mathbf{r_2}|} \middle| \overbrace{\varphi^{\mathbf{h}}_{\sigma}\varphi^{\mathbf{h}+\mathbf{g}'}_{\omega}}^{T_1} \right\rangle \tag{2.151}$$

$$E_{\text{Exchange}} = -\frac{1}{4}\sum_{\mu\nu}\sum_{\mathbf{g}} \overbrace{P^{\mathbf{g}}_{\mu\nu}}^{T_4}\sum_{\sigma,\omega}\sum_{\mathbf{g}'} \overbrace{P^{\mathbf{g}'}_{\sigma,\omega}}^{T_5}\sum_{\mathbf{h}} X^{\mathbf{g}}_{\mu\nu} \tag{2.152}$$

$$= -\frac{1}{4}\sum_{\mu\nu}\sum_{\mathbf{g}} \overbrace{P^{\mathbf{g}}_{\mu\nu}}^{T_4}\sum_{\sigma,\omega}\sum_{\mathbf{g}'} \overbrace{P^{\mathbf{g}'}_{\sigma,\omega}}^{T_5}\sum_{\mathbf{h}} \left\langle \overbrace{\varphi^{0}_{\mu}\varphi^{\mathbf{h}}_{\sigma}}^{T_5} \middle| \frac{1}{|\mathbf{r_1}-\mathbf{r_2}|} \middle| \overbrace{\varphi^{\mathbf{g}}_{\nu}\varphi^{\mathbf{h}+\mathbf{g}'}_{\omega}}^{T_3} \right\rangle \tag{2.153}$$

In the case of DFT, E_{Exchange} is the exchange-correlation energy, introduced in Eq. 2.89. These summations are infinite in a periodic system, thus, they require a truncation. A set of five thresholds $T_1 - T_5$ are defined: when the overlap between the two involved functions is smaller than 10^{-T_i}, the integral is disregarded. These thresholds monitor the overlapping of different functions, as can be schematically seen in Eqns. 2.147 - 2.153. All of these thresholds are shown in the above equations with the exception of T_2, which controls the overlap between $\varphi_\nu^{\mathbf{g}}$ and $\varphi_\sigma^{\mathbf{h}}\varphi_\omega^{\mathbf{h}+\mathbf{g}'}$ (more information in Refs. [66, 67, 63, 68]). Running a calculation with these thresholds tight enough is critical in order to obtain correct energies. In CRSYTAL, the `TOLINTEG` keyword followed by 5 numbers, represent each of these thresholds.

2.2.10 The Self Consistent Field

After each matrix element has been introduced, in order to solve Eq. 2.140, one can easily notice that the Fock matrix depends on the Density matrix, which in turn depends on the coefficients, which are not known and are included in the **C** matrix. Thus, this equation has to be solved self-consistently. This iterative process is called Self Consistent Field (SCF), and consists of the following steps:

- **Step 1:** As an iterative method, an initial guess has to be defined: either a density matrix or a Fock matrix guess:

    - The density matrix guess can be either a block-diagonal matrix, obtained as a sum ot atomic densities for each atom, or a density matrix obtained in a previous similar calculation for the same system.
    - If a Fock matrix from a previous calculation is available, this will be used instead of the density matrix. In this case the construction of a first Fock matrix is skipped.

  Typically the SCF method starts with a density matrix guess.

- **Step 2**: Calculate analytically the kinetic, Coulomb and, if required, the exact exchange contributions to the Fock matrix in direct space (atomic orbital) representation, $\mathbf{F}^{\mathbf{g}}$. On the next section we will analyze the time required for each step of the SCF. In the CRYSTAL output, this time is printed in terms of the time consumed by each routine. The routines `MOQGAD` and `SHELLXN` calculate, respectively, the monoelectronic and bielectronic integrals.

- **Step 3**: If the DFT exchange and correlation contribution to $\mathbf{F^g}$ is required, a numerical quadrature is adopted. This operation is performed by the `NUMDFT` routine.

- **Step 4**: Transform $\mathbf{F^g}$ into reciprocal space (or Bloch Function basis): $\mathbf{F}(\mathbf{k})$. This is done by two steps: first a Fourier transform, followed by a similarity transform.

- **Step 5**: At each $\mathbf{k}$ point, diagonalize $\mathbf{F}(\mathbf{k})$. This operation is performed by the `FDIK` routine.

- **Step 6**: Using the eigenvalues from Step 4, calculate the Fermi level as the energy of the highest occupied state. The number of occupied crystalline orbitals at each $\mathbf{k}$ point are obtained.

- **Step 7**: Sum over the occupied eigenvectors to construct a new density matrix, $\mathbf{P}(\mathbf{k})$, that is then back Fourier transformed to give a new "direct space" density matrix $\mathbf{P^g}$ to be used in Step 1. This operation is performed by the `PDIG` routine.

- **Step 6**: The convergence criteria for the SCF can work either on the density matrix, on the Fock matrix or on the value of the energy. This step consists in repeating Steps 1-5 until the energy obtained in the cycle n is the same, within a tolerance, with respect to the one obtained in the previous cycle. The SCF ends when the difference in energy is less than a given threshold, defined in CRYSTAL with the `TOLDEE` keyword. Typically this threshold is 10^{-8} for a geometry optimization or single point calculation. For a frequency calculation, this value is increased to 10^{-10} to ensure a tighter convergence for all the geometries as a result of the displacements.

2.3 Elements of Thermodynamics

2.3.1 Work, Heat and the First Law of Thermodynamics

Heat (q) is a form of energy transfer that leads to a temperature difference between the system and its surroundings. On the other hand, work (w) is transfer of energy between the system of interest and its surroundings, as a consequence of unbalanced forces between those two. The established convention of signs in these two variables is presented in Figure 2.27.

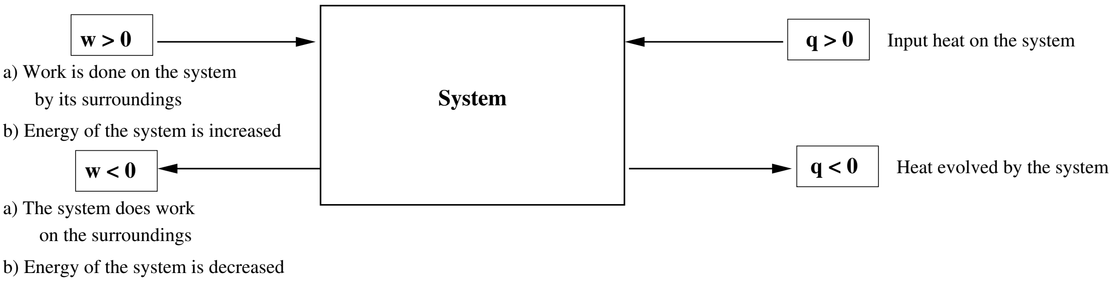

Figure 2.27: Sign convention for work and heat in thermodynamics

If we take a gas with pressure P confined in a cylinder to be our system, the work done on a gas depends upon the pressure P used to compress the gas:

$$w = -\int_{V_i}^{V_f} P\,\mathrm{d}V \tag{2.154}$$

If P is constant during the expansion, $w = -P\,\Delta V$. If the gas is expanding, $\Delta V > 0$ so that $w < 0$, or in other words, the system does work on its surroundings. If the gas is under compression, $\Delta V < 0$ so that $w > 0$ because work is being done on the system when it is compressed.

Work depends on the path taken between the initial and final states 1 and 2. Thus, this is not a state function, but a path function: the differential of work (δw) is an inexact differential, where $\int_1^2 \delta w = w \neq w_2 - w_1$. In its differential form, δw is just:

$$\delta w = -PdV \tag{2.155}$$

Heat is also a path function: the differential of heat (δq) is an inexact differential, where $\int_1^2 \delta q = q \neq q_2 - q_1$. As opposed to δw, the explicit expression of δq will be obtained when the Second Law of Thermodynamics is introduced.

For a process in which energy is transferred both as work and heat, the law of conservation of energy states that the energy of the system follows the equation:

$$dE = \delta q + \delta w \tag{2.156}$$

in differential form, or:

$$\boxed{\Delta E = q + w} \tag{2.157}$$

in integrated form. Equations (2.156) and (2.157) are statements of the **First Law of Thermodynamics**. The static (or internal) energy is an example of a state function, because is a property that depends only upon the state of the system, and not upon how the system was brought to that state. The differential of a state function (dE_{static}) is an exact differential.

2.3.2 Second Law of Thermodynamics

A big picture of a solid (e.g. ice) being an ordered lattice array of its constituent particles and a liquid (e.g. water) being a random structure, directly implies that the melting of the solid ice involves an increase in disorder.

Not only do systems evolve spontaneously in direction that lowers their energy, but also in the direction where they increase their disorder. In general, a compromise between decreasing energy and increasing disorder must be met.

It is at this point where it would be useful to write down the idea of disorder as a state function, just like the static energy, because then it would be a property that would not depend on the previous history of the system. We will relate this state function with δq, which is not a state function.

However, if we divide by T, then $\delta q/T$ is the derivative of a state function. If we denote this state function as S,

$$\mathrm{d}S = \frac{\delta q}{T} \tag{2.158}$$

In this way, the inexact differential δq has been converted to an exact differential by multiplying it by $1/T$. This factor is called known as the *integrating factor* of δq, and the state function we are looking after is called the ***entropy***.

The second law of Thermodynamics states that the entropy of an isolated system increases as a result of a spontaneous process, which we can express mathematically by $\mathrm{d}S > 0$.

2.3.3 Third Law of Thermodynamics

Using Eq. (2.156) (First Law) and the fact that $\delta q = T\mathrm{d}S$ (Second Law), and $\delta w = -P\mathrm{d}V$, we obtain the combination of the First and Second Laws of Thermodynamics:

$$dE = TdS - PdV \tag{2.159}$$

The Third Law of Thermodynamics does not introduce a new state function. If the first law give us the energy, the second law the entropy, the third law presents a numerical scale for the entropy: *"Every substance has a finite positive entropy, but at zero kelvin the entropy may become zero, and does so in the case of a perfectly crystalline substance".* The elegance of this statement will be proved in the derivation of the statistical mechanics definition of entropy (Eq. 2.256), according to which, the entropy of a perfect crystalline solid is mathematically zero at $T = 0$ K.

2.4 Elements of Statistical Mechanics

2.4.1 The Partition Function

Consider a macroscopical system such as a litre of gas, a litre of water or a kilogram of a solid. This system can be described, from a mechanical point of view, by specifying three variables:

- The number of particles, N
- The volume, V
- The forces between the particles.

The Schrödinger equation for this N-body system is:

$$\hat{H}\psi = E_j\psi \qquad\qquad j = 1, 2, 3, \ldots N \tag{2.160}$$

Since the energies depend on N and V, we will write $E_j\left(N, V\right)$. For an ideal gas, the molecules are independent of each other, so that the total energy $E_j\left(N, V\right)$ will be just a sum of individual molecular energies:

$$E_j\left(N, V\right) = \epsilon_1 + \epsilon_2 + \epsilon_3 + \cdots + \epsilon_N \tag{2.161}$$

For instance, in the special case of a monoatomic ideal gas of mass m in a cubic container with sides of length a, if we ignore the electronic states and focus only on the translational states, then the $\epsilon_j s$ are just the translational energies given by

$$\epsilon_{n_x,n_y,n_z} = \frac{h^2}{8ma^2}\left(n_x^2 + n_y^2 + n_z^2\right) \tag{2.162}$$

Note that the number of terms in Eq. (2.161) explains the dependence of $E_j\left(N,V\right)$ on N, and the fact that $a = V^{1/3}$ in Eq. (2.162) explains the dependence of $E_j\left(N,V\right)$ on V. For a more general system in which the particles interact with each other, $E_j\left(N,V\right)$ cannot be expressed as a set of individual particle energies. Instead, a set of allowed macroscopic energies $\{E_j\left(N,V\right)\}$ will be considered.

What is the probability that a system is in state j with energy $E_j\left(N,V\right)$? To answer this question, we will consider an enormous collection of such systems in thermal contact through an infinite heat bath (heat reservoir) at a temperature T (Figure 2.28). Each system has the same values of N, V and T but is likely to be in a different quantum state, consistent with the values of N and V. This collection of systems is called *ensemble.* The number of systems in the state j with energy $E_j\left(N,V\right)$ is denoted by a_j and the total number of systems in the ensemble is denoted by $\mathcal{A}$.

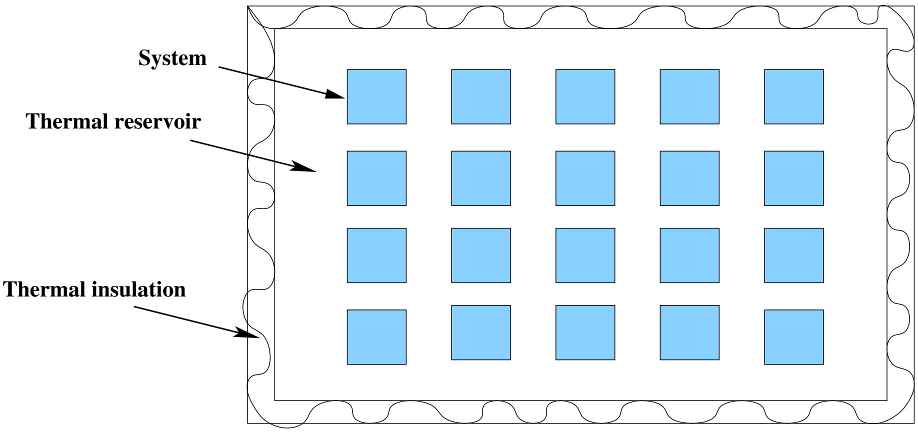

Figure 2.28: An ensemble of $\mathcal{A}$ macroscopic systems in thermal equilibrium provided by a heat bath. a_j is the number of systems in the state j with energy $E_j\left(N,V\right)$. Since an ensemble is a conceptual idea, we shall consider $\mathcal{A}$ to be as large as we want.

Let's focus on two particular states, 1 and 2: a_1 is the number of systems in state 1 with energy $\{E_1\left(N,V\right)\}$ in the ensemble. In the same way, a_2 is the number of systems in state 2 with energy $\{E_2\left(N,V\right)\}$ in the same ensemble. The relative number of systems in the states with energies E_1 and E_2 must depend on E_1 and E_2, so:

$$\frac{a_2}{a_1} = f\left(E_1, E_2\right) \tag{2.163}$$

Since the energy is a quantity that has to be referred to a zero of energy, the dependence on E_1 and E_2 on Eq. (2.163) has to be of the form:

$$f\left(E_1, E_2\right) = f\left(E_1 - E_2\right) \tag{2.164}$$

In this way, any arbitrary zero of energy associated with E_1 nad E_2 will cancel. Therefore,

$$\frac{a_2}{a_1} = f\left(E_1 - E_2\right) \tag{2.165}$$

Eq. (2.165) is equivalent to any two energy states, so we can also write

$$\frac{a_3}{a_2} = f\left(E_2 - E_3\right) \qquad \text{and} \qquad \frac{a_3}{a_1} = f\left(E_1 - E_3\right) \tag{2.166}$$

What is the relation between $f\left(E_1 - E_3\right)$, $f\left(E_1 - E_2\right)$ and $f\left(E_2 - E_3\right)$? Since:

$$\frac{a_3}{a_1} = \frac{a_2}{a_1} \cdot \frac{a_3}{a_2}, \tag{2.167}$$

using Equations 2.164, 2.166 and 2.167, we find that the function f must satisfy

$$f\left(E_1 - E_3\right) = f\left(E_1 - E_2\right) \cdot f\left(E_2 - E_3\right) \tag{2.168}$$

The form of the function f that satisfies this equation may not be obvious, but it is indeed $f\left(E\right) = e^{\beta E}$, where β is an arbitrary constant. To verify that this form for f does satisfy Eq. 2.168, we substitute this functional form of $f\left(E\right)$ into Eq. 2.168:

$$e^{\beta(E_1 - E_3)} = e^{\beta(E_1 - E_2)} e^{\beta(E_2 - E_3)} = e^{\beta(E_1 - E_3)} \tag{2.169}$$

In addition, we find from Eq. 2.165 that

$$\frac{a_2}{a_1} = e^{\beta(E_1 - E_2)} \tag{2.170}$$

which we can write more generally as:

$$\frac{a_n}{a_m} = e^{\beta(E_m - E_n)} \tag{2.171}$$

from which we can obtain an expression for a_n and a_m:

$$a_n = a_m e^{\beta(E_m - E_n)} = a_m e^{\beta E_m} e^{-\beta E_n} = C_m e^{-\beta E_n} \tag{2.172}$$

$$a_m = a_n e^{-\beta(E_m - E_n)} = a_n e^{\beta E_n} e^{-\beta E_m} = C_n e^{-\beta E_m} \tag{2.173}$$

where C_m and C_n are constants. If j represents either a state m or n and C is a constant, we can simplify these last two equations to the following more general expression:

$$a_j = C e^{-\beta E_j} \tag{2.174}$$

These two variables C and β have to be determined. By summing both sides of Eq. 2.174 over all states j, we obtain:

$$\sum_j a_j = C \sum_j e^{-\beta E_j} \tag{2.175}$$

The summation over a_j must equal $\mathcal{A}$, the total number of systems in the ensemble: $\sum_j a_j = \mathcal{A}$. Thus, we can write:

$$C = \frac{\sum_j a_j}{\sum_j e^{-\beta E_j}} = \frac{\mathcal{A}}{\sum_j e^{-\beta E_j}} \tag{2.176}$$

Casting this result into Eq. 2.174, we get:

$$\frac{a_j}{\mathcal{A}} = \frac{e^{-\beta E_j}}{\sum_j e^{-\beta E_j}} \tag{2.177}$$

The ratio $\frac{a_j}{\mathcal{A}}$ is the fraction of systems in our ensemble that will be found in the state j with energy E_j. In principle we can make our ensemble as large as we want, so when $\mathcal{A}$ becomes very large, $\frac{a_j}{\mathcal{A}}$ becomes a probability:

$$\boxed{p_j = \frac{a_j}{\mathcal{A}} = \frac{e^{-\beta E_j}}{\sum_j e^{-\beta E_j}}} \tag{2.178}$$

where p_j is the probability that a randomly chosen system will be in state j with energy $E_j\left(N, V\right)$. Equation 2.178 is one of the most important results of physical chemistry. Typically the denominator of this expression is denoted by Z, and if we include the dependence of E_j on N and V, then we write:

$$\boxed{Q\left(N,V,\beta\right)=\sum_j e^{-\beta E_j(N,V)}} \tag{2.179}$$

Equation 2.178 then becomes:

$$\boxed{p_j\left(N,V,\beta\right)=\frac{e^{-\beta E_j(N,V)}}{Q\left(N,V,\beta\right)}} \tag{2.180}$$

β us defined as:

$$\beta=\frac{1}{k_BT} \tag{2.181}$$

where k_B is the Boltzmann constant and T is the kelvin temperature. Therefore, we can write Equation 2.180 as

$$\boxed{p_j\left(N,V,T\right)=\frac{e^{-E_j(N,V)/k_BT}}{Q\left(N,V,T\right)}} \tag{2.182}$$

Equations 2.180 and 2.182 are equally acceptable. In a theoretical framework, often times β or $1/k_BT$ are more convenient quantities to use than T itself.

The quantity $Q\left(N,V,\beta\right)$ or $Q\left(N,V,T\right)$, is called the canonical ***partition function*** of the system, and is a powerful tool that allows us to calculate macroscopic properties, (e.g., entropy or heat capacity) from the microscopic, quantum behaviour of atoms.

In order to apply the partition function to our system, it is necessary to have the set of eigenvalues $\{E_j\left(N,V\right)\}$ for the N-body Schrödinger equation, which is a very difficult task. However, writing the total energy as a sum of individual energies is a good approximation. This allows to simplify the partition function and obtain important results.

For a system of distinguishable particles, we can denote the individual particle energies by $\left\{\varepsilon_j^a\right\}$, where the superscript labels the particle, and the subscript the energy state of the particle. The total energy of the system can be the expressed as:

$$E_j\left(N,V\right)=\underbrace{\varepsilon_i^a\left(V\right)+\varepsilon_k^b\left(V\right)+\varepsilon_m^c\left(V\right)+...}_{N\text{ terms }\equiv N\text{ particles}} \tag{2.183}$$

Then the system partition function reads like:

$$Q(N,V,\beta)=\sum_j \exp(-\beta E_j)=\sum_{i,k,m...}\exp\left(-\beta\varepsilon_i^a\right)\cdot\exp\left(-\beta\varepsilon_k^b\right)\cdot\exp\left(-\beta\varepsilon_m^c\right)...$$

Since the particles are distinguishable, it is possible to sum over $i,k,m\cdots$ independently, so that $Q(N,V,\beta)$ can be written as a product of individual summations:

$$\begin{aligned}Q(N,V,\beta)&=\sum_i \exp\left(-\beta\varepsilon_i^a\right)\sum_k \exp\left(-\beta\varepsilon_k^b\right)\sum_m \exp\left(-\beta\varepsilon_m^c\right)...\\&=q_a(V,T)\,q_b(V,T)\,q_c(V,T)...\end{aligned}\tag{2.184}$$

If the $\left\{\varepsilon_j^M\right\}$ is a set of molecular energies, thus $q_M(V,T)$ is called a ***molecular partition function***.

Equation (2.184) shows a very important result: If we can write the total energy as a sum of individual, independent terms, and if the atoms or molecules are distinguishable, then the system partition function $Q(N,V,\beta)$ is reduced to a product of molecular partition functions $q(V,T)$. This will allow us to decompose the total partition function into the product of its individual partition functions.

If the energy states of all atoms or molecules are the same, like in a monoatomic system, then Eq. (2.184) becomes:

$$Q(N,V,T)=\left[q(V,T)\right]^N\tag{2.185}$$

where

$$q(V,T)=\sum_j \exp\left(-\beta\varepsilon_j\right)\tag{2.186}$$

However, atoms and molecules are normally not distinguishable. Therefore, Eq. (2.185) cannot be implemented directly. For indistinguishable particles, the total energy is

$$E_j(N,V)=\underbrace{\varepsilon_i(V)+\varepsilon_k(V)+\varepsilon_m(V)+...}_{N\text{ terms }\equiv N\text{ particles}}\tag{2.187}$$

so that:

$$Q\left(N,V,\beta\right)=\sum_{j}\exp\left(-\beta E_j\right)=\sum_{i,k,m...}\exp\left[-\beta\left(\varepsilon_i+\varepsilon_k+\varepsilon_m+...\right)\right] \tag{2.188}$$

Now, the direct evaluation of the summation of Eq. (2.188) has problems for fermions: If we take an example of 2 independent fermions, each of which has states with energies $\varepsilon_1,\varepsilon_2,\varepsilon_3,\varepsilon_4,...$, a direct evaluation of $Q\left(2,V,\beta\right)=\sum_{i,k}^{4}\exp\left[-\beta\left(\varepsilon_i+\varepsilon_k\right)\right]$ will produce the following 16 terms, in which the energies in reverse order have also been taken into account:

$$\begin{array}{llll}
\varepsilon_1+\varepsilon_1 & \varepsilon_1+\varepsilon_2=\varepsilon_2+\varepsilon_1 & \varepsilon_2+\varepsilon_3=\varepsilon_3+\varepsilon_2 & \varepsilon_3+\varepsilon_4=\varepsilon_4+\varepsilon_3 \\
\varepsilon_2+\varepsilon_2 & \varepsilon_1+\varepsilon_3=\varepsilon_3+\varepsilon_1 & \varepsilon_2+\varepsilon_4=\varepsilon_4+\varepsilon_2 & \\
\varepsilon_3+\varepsilon_3 & \varepsilon_1+\varepsilon_4=\varepsilon_4+\varepsilon_1 & & \\
\varepsilon_4+\varepsilon_4 & & &
\end{array} \tag{2.189}$$

each term is represented in Figure (2.29).

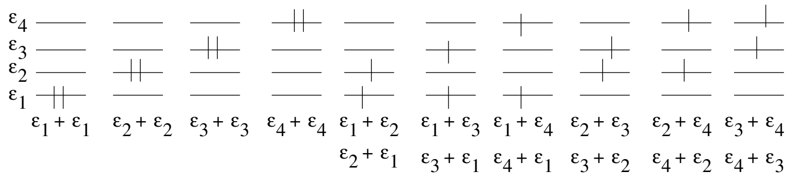

Figure 2.29: Representation of each of the possibilities reported in Eq. 2.189.

The Pauli Exclusion Principle states that no two fermions (particles of spin 1/2, 3/2, 5/2, etc) in an atom can have the same set of four quantum numbers, or in other words, no two electrons in an atom can be in the same quantum state. Therefore, terms like $\varepsilon_1+\varepsilon_1$, $\varepsilon_2+\varepsilon_2$, etc. have to be ignored. If we actually ignore these terms, there would be a total of 12 terms: those shown in the second, third and fourth columns of the set of equations (2.189). Because the particles are indistinguishable, the energies written in reverse order would not have to be taken into account. This means that in the end there are 6 terms. By dividing $Q\left(2,V,\beta\right)$ by 2!, we would obtain the correct number allowed terms. Therefore, we can sum separately over $i,k,m,...$ in

Eq. (2.188), just as we did in Eq. (2.184), as long as we divide by N!:

$$\begin{aligned} Q(N,V,\beta) &= \frac{\sum_i \exp(-\beta\varepsilon_i)\sum_k \exp(-\beta\varepsilon_k)\sum_m \exp(-\beta\varepsilon_m)\ldots}{N!} \\ &= \frac{\left[\sum_j \exp(-\beta\varepsilon_j)\right]^N}{N!} \\ &= \frac{[q(V,T)]^N}{N!} \end{aligned} \tag{2.190}$$

where

$$q(V,T) = \sum_j \exp(-\beta\varepsilon_j) \tag{2.191}$$

2.4.2 The definition of Entropy

Entropy is related to the disorder of a system. The most useful way to define disorder is the following. Lets consider the ensemble shown in Figure (2.30), and maintain the last notation: a_j is the number of systems in the ensemble that are in a state j. If we divide the $\mathcal{A}$ distinguishable systems of the ensemble into j groups, the number of ways of having a_1 systems in state 1, a_2 systems in state 2 or a_j systems in state j is given by:

$$W(a_1,a_2,a_3,\ldots,a_j) = \frac{\mathcal{A}!}{a_1!\,a_2!\,a_3!\ldots a_j!} = \frac{\mathcal{A}!}{\prod_j a_j!} \tag{2.192}$$

with

$$\sum_j a_j = \mathcal{A} \tag{2.193}$$

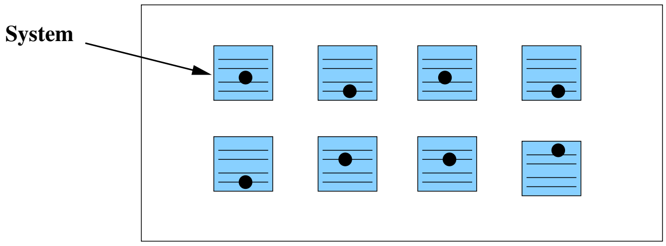

Figure 2.30: This is an ensemble consisted of $\mathcal{A} = 8$ systems. In each system there are 4 states. There are 3 systems in the first state, 2 systems in the second state, 2 systems in the third state and 1 system in the fourth state. Thus, $a_1 = 3, a_2 = a_3 = 2$ and $a_4 = 1$. Note that $\sum_j a_j = 8 = \mathcal{A}$.

Now we consider two extreme cases:

a) If all $\mathcal{A}$ systems are in one particular state, say state 1 (see Figure 2.31), then:

$$a_1 = \mathcal{A} \tag{2.194}$$

$$a_2 = a_3 = ... = a_j = 0 \tag{2.195}$$

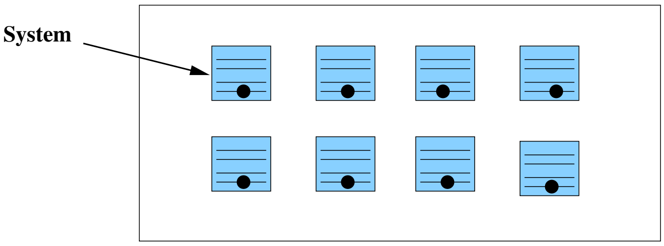

Figure 2.31: This is an ensemble consisted of $\mathcal{A} = 8$ systems. All the systems are in state 1, therefore $W = 1$ (Eq. 2.192), which is the minimum value that W can adopt, and corresponds to a situation of maximum order.

This situation corresponds to a value of $W = \frac{\mathcal{A}!}{a_1!} = \frac{a_1!}{a_1!} = 1$, which is the smallest value of W we can have, and corresponds to a ***totally ordered arrangement***.

b) If all a_j are equal:

$$a_1 = a_2 = ... = a_j, \tag{2.196}$$

it can be shown that W takes its largest value, and corresponds to a ***totally disordered arrangement*** (Figure 2.32).

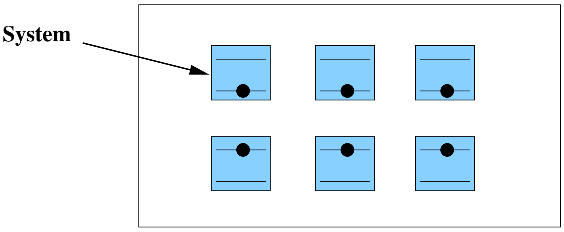

Figure 2.32: This is an ensemble consisted of $\mathcal{A} = 6$ systems. There are only $j = 2$ possible states in each system. In a situation of maximum disorder, $a_1 = a_2 = ... = a_j$, and since $\sum_j a_j = \mathcal{A}$, then $a_j = \frac{\mathcal{A}}{j}$. Thus, $a_1 = a_2 = 6/2 = 3$, which is what is shown in the figure.

Therefore, W can be interpreted as a quantitative measure of the disorder of the system. It would be very useful if we could find a relation between the thermodynamic quantity (entropy) and the statistical quantity (W). This relation is proportional: $S = \text{constant} \cdot W$. This constant is the Boltzmann Constant, and we will not set the entropy proportional to W, but to $\ln W$

according to[5]:

$$\boxed{S = k_B \ln W} \tag{2.197}$$

Even though all the systems have the same energy, they may be in different degenerate quantum states. It would be very convenient if we could find an equivalent expression to (2.197) that takes into account the degeneracy. One of the postulates of statistical thermodynamics states: *"there is no reason to choose one of the Ω degenerate quantum states over any other; each one should occur in an ensemble with equal probability".*

Let the degeneracy associated with the energy be Ω. Now we have to change slightly the formulation of the problem: an ensemble is still made of a_j systems, but instead of having a_j systems in the state j, now we have a set of Ω degenerated quantum states replicated n times in the ensemble. Thus, $\mathcal{A} = n\Omega$, and

$$S_{\text{ensemble}} = \mathcal{A} S_{\text{system}} \tag{2.198}$$

$$= n\Omega S_{\text{system}} \tag{2.199}$$

where

$$S_{\text{ensemble}} = k_B \ln W \tag{2.200}$$

Now it no longer makes sense the definition of each a_j as the number of systems in the ensemble

---

[5] The reason why we set S equal to $\ln W$ rather than W is because we want S to be an extensive state function, that is, that the total entropy of a system is made up of two parts (say A and B): $S_{\text{total}} = S_A + S_B$, and this is only satisfied if S is proportional to $\ln W$. If W_A is the value of W for system A and W_B is the value of W for system B, W_{AB} for the composite system is given by $W_{AB} = W_A W_B$. Then, the entropy of the composite sytem is given by $S_{AB} = k_B \ln W_{AB} = k_B \ln W_A W_B = k_B \ln W_A + k_B \ln W_B = S_A + S_B$

that are in state j; instead, each $a_j = n$. From Eq. 2.192 we can write [6]:

$$\begin{aligned}
\ln W &= \ln A! - \ln \prod_j a_j! \\
&= A \ln A - A - [\ln a_1! + \ln a_2! + \ldots + \ln a_j!] \\
&= A \ln A - A - \sum_{j=1}^{\Omega} [a_j \ln a_j - a_j] \\
&= A \ln A - A - \sum_{j=1}^{\Omega} [a_j \ln a_j] + \underbrace{\sum_{j=1}^{\Omega} a_j}_{=A} \\
&= A \ln A - \sum_{j=1}^{\Omega} [a_j \ln a_j] \\
&= n\Omega \ln (n\Omega) - \sum_{j=1}^{\Omega} [n \ln n] \\
&= n\Omega \ln (n\Omega) - n \ln n \sum_{j=1}^{\Omega} \\
&= n\Omega \ln (n\Omega) - \Omega (n \ln n) \\
&= n\Omega \ln \Omega
\end{aligned} \tag{2.201}$$

By substituting this result in Eq. (2.200):

$$S_{\text{ensemble}} = k_B (n\Omega \ln \Omega) \tag{2.202}$$

Casting Eq. (2.202) into Eq. (2.199):

$$S_{\text{system}} = k_B \ln \Omega \tag{2.203}$$

If we drop the subscript "system":

$$\boxed{S = k_B \ln \Omega} \tag{2.204}$$

Eq. (2.204) is an alternate form of Eq. (2.197) and relates entropy to disorder. Consider for example a system of N distinguishable spins or dipoles that can be oriented in one of two possible directions with equal probability. Then, each spin has a degeneracy of 2 associated

---

[6] The Stirling approximation has been used: $\ln a_j! = a_j \ln a_j - a_j$

with it, $\Omega = 2$, and the degeneracy of the N spins is $\Omega^N = 2^N$. The entropy of the system is $S = k_B \ln 2$.

It is much more useful to express the entropy in terms of the system canonical partition function $Q\left(N, V, \beta\right)$. If we substitute Eq. (2.192) into Eq. (2.200):

$$\begin{aligned}
S_{\text{ensemble}} &= k_B \ln \frac{\mathcal{A}!}{\prod_j a_j!} = k_B \ln A! - k_B \ln \prod_j a_j! \\
&= k_B \mathcal{A} \ln \mathcal{A} - k_B \mathcal{A} - k_B \sum_j a_j \ln a_j + k_B \underbrace{\sum_j a_j}_{=\mathcal{A}} \\
&= k_B \mathcal{A} \ln \mathcal{A} - k_B \sum_j a_j \ln a_j \qquad (2.205)
\end{aligned}$$

Using the fact that the probability of finding a system in the jth quantum state is given by Eq. (2.178), substituting $a_j = \mathcal{A} p_j$ into Eq. (2.205), we obtain:

$$\begin{aligned}
S_{\text{ensemble}} &= k_B \mathcal{A} \ln \mathcal{A} - k_B \sum_j \mathcal{A} p_j \ln\left(\mathcal{A} p_j\right) \\
&= k_B \mathcal{A} \ln \mathcal{A} - k_B \sum_j p_j \mathcal{A} \ln \mathcal{A} - k_B \sum_j \mathcal{A} p_j \ln p_j \\
&= k_B \mathcal{A} \ln \mathcal{A} - k_B \mathcal{A} \ln \mathcal{A} \underbrace{\sum_j p_j}_{=1} - k_B \sum_j \mathcal{A} p_j \ln p_j \\
&= -k_B \sum_j \mathcal{A} p_j \ln p_j \qquad (2.206)
\end{aligned}$$

Using Eq. (2.198):

$$\begin{aligned}
S_{\text{system}} &= \frac{S_{\text{ensemble}}}{\mathcal{A}} \\
&= -k_B \sum_j p_j \ln p_j \qquad (2.207)
\end{aligned}$$

Again, dropping the “system” subscript,

$$\boxed{S = -k_B \sum_j p_j \ln p_j} \qquad (2.208)$$

Note the difference between this result, in which we express the entropy in terms of probability that the system is in a given jth quantum state, and Eq. (2.197) or Eq. (2.204), in which the entropy is given, respectively, as a function of the statistical quantity (W), or as a function of the number of degenerated quantum states (Ω).

Again, we can encounter two extreme cases:

a) If only one p_j is non-zero, say p_1, and the rest are zero, then p_1 must equal unity because $\sum_j p_j = 1$:

$$p_1 = 1 \tag{2.209}$$

$$p_2 = p_3 = ... = p_j = 0 \tag{2.210}$$

This situation means that every system is in the $j = 1$ quantum state, so that the global picture is the one presented in Figure (2.31), and therefore we are in the case of a ***totally ordered arrangement***. Substituting Eq. (2.208),

$$S_{\text{system}} = -k_B[p_1 \ln p_1 + \underbrace{p_2 \ln p_2}_{=0} + ... + \underbrace{p_j \ln p_j}_{=0}] = 0 \tag{2.211}$$

where $S = 0$ for a perfectly ordered system.

b) If all p_j are equal:

$$p_1 = p_2 = ... = p_j, \tag{2.212}$$

it can be shown, through a similar procedure as with W, that S is maximum, and this situation corresponds again to a ***totally disordered arrangement***.

If we substitute Eq. (2.180) into Eq. (2.208) we obtain:

$$\begin{aligned}
S &= -k_B \sum_j p_j \ln p_j \\
&= -k_B \sum_j \frac{e^{-\beta E_j}}{Q} \left[-\beta E_j - \ln Q \right] \\
&= \frac{1}{T} \sum_j \frac{E_j e^{-\beta E_j}}{Q} + k_B \ln Q \cdot \frac{1}{Q} \cdot \underbrace{\sum_j e^{-\beta E_j}}_{=Q} \\
&= \underbrace{\frac{1}{T} \frac{1}{Q} \sum_j E_j e^{-\beta E_j}}_{=k_B T^2 \frac{\partial \ln Q}{\partial T} = U} + k_B \ln Q \\
&= \frac{U}{T} + k_B \ln Q
\end{aligned} \tag{2.213}$$

where in the fourth line we have used this relation:

$$\frac{\partial \ln Q}{\partial T} = \frac{1}{Q} \frac{\partial Q}{\partial T} = \frac{1}{Q} \frac{1}{k_B T^2} \sum_j E_j e^{-E_j / k_B T} \Rightarrow \frac{1}{Q} \sum_j E_j e^{-E_j / k_B T} = k_B T^2 \frac{\partial \ln Q}{\partial T} = U \tag{2.214}$$

Thus,

$$\boxed{S = k_B T \left(\frac{\partial \ln Q}{\partial T} \right)_{N,V} + k_B \ln Q} \tag{2.215}$$

This equation shines by itself: this is the relation between the entropy and the canonical partition function.

2.4.3 The definition of Energy

The average energy of a system in an ensemble of systems is referred to as $\langle E \rangle$. Using Eq. 2.180, this quantity can be calculated as [7]:

$$E \equiv \langle E \rangle = \sum_j p_j \left(N, V, \beta \right) E_j \left(N, V \right) = \sum_j \frac{E_j \left(N, V \right) e^{-\beta E_j (N,V)}}{Q \left(N, V, \beta \right)} \tag{2.216}$$

We can equate $E \equiv \langle E \rangle$, the ensemble average of the energy with the observed energy, E.

---

[7] Suppose that some number x_j is associated with the outcome j. Then we define the *average* of x to be $\langle x \rangle = \sum_{j=1}^{n} x_j p_j = \sum_{j=1}^{n} x_j \, p(x_j)$, where the term $p(x_j)$ means the probability of realizing the number x_j. The average of a quantity is represented by enclosing that quantity in angular brackets.

It would be much more convenient if E could be expressed entirely in terms of $Q(N,V,\beta)$. Using the expression for $Q(N,V,\beta)$ given in Eq. 2.179, first we differentiate $\ln Q(N,V,\beta)$ with respect to β, with N and V held constant:

$$\begin{aligned}\left(\frac{\partial \ln Q(N,V,\beta)}{\partial \beta}\right)_{N,V} &= \frac{1}{Q(N,V,\beta)}\left(\frac{\partial \sum_j e^{-\beta E_j(N,V)}}{\partial \beta}\right)_{N,V}\\ &= \frac{1}{Q(N,V,\beta)}\sum_j \left[-E_j(N,V)\right] e^{-\beta E_j(N,V)}\\ &= -\sum_j \frac{E_j(N,V)\, e^{-\beta E_j(N,V)}}{Q(N,V,\beta)} \qquad (2.217)\end{aligned}$$

By comparison of Eq. (2.216) and (2.217) we see that:

$$E \equiv \langle E\rangle = -\left(\frac{\partial \ln Q}{\partial \beta}\right)_{N,V} \qquad (2.218)$$

We can express this equation as a temperature derivative instead of a β derivative[8]:

$$\boxed{E \equiv \langle E\rangle = k_B T^2 \left(\frac{\partial \ln Q}{\partial T}\right)_{N,V}} \qquad (2.219)$$

2.4.4 The definition of Pressure

Equation (2.216) represents the average energy of an equilibrium system that has the variables N, V and T fixed. If we differentiate Eq. (2.216), we obtain:

$$dE = \sum_j p_j\, dE_j + \sum_j E_j\, dp_j \qquad (2.220)$$

Because $E_j = E_j(N,V,\beta)$, dE_j can be seen as the change in E_j due to a small change in the volume dV, keeping N fixed:

$$dE_j = \left(\frac{\partial E_j}{\partial V}\right)_N dV \qquad (2.221)$$

---

[8] For any given function $f = f(\beta, T)$, the chain rule of differentiation allows us to write: $\frac{\partial f}{\partial T} = \frac{\partial f}{\partial \beta}\cdot\frac{\partial \beta}{\partial T} = \frac{\partial f}{\partial \beta}\cdot\frac{d(1/k_BT)}{dT} = -\frac{1}{k_BT^2}\frac{\partial f}{\partial \beta}$, or in other words, $\frac{\partial f}{\partial \beta} = -k_BT^2\frac{\partial f}{\partial T}$. Using this result with $f = \ln Q$ give us the alternate form.

Substituting this into Eq. (2.220) gives:

$$dE = \sum_j p_j \left(\frac{\partial E_j}{\partial V}\right)_N dV + \sum_j E_j \, dp_j \tag{2.222}$$

The first term in Eq. (2.222) can be interpreted as the average change in energy caused by a small change in its volume, or in other words, the average work. In addition, if this change is done reversibly so that the system remains essentially in equilibrium at each stage, then the p_j in Eq. (2.222) will be given by Eq. (2.180) throughout the entire process. We highlight this by writing:

$$dE = \sum_j p_j(N,V,\beta) \left(\frac{\partial E_j}{\partial V}\right)_N dV + \sum_j E_j(N,V) \, dp_j(N,V,\beta) \tag{2.223}$$

If we compare this result with the macroscopic equation that arises from the First Law of Thermodynamics (Equation 2.156): $dE = \delta q + \delta w$, we see that:

$$\delta w = \sum_j p_j(N,V,\beta) \left(\frac{\partial E_j}{\partial V}\right)_N dV \tag{2.224}$$

which means that the reversible work comes from an infinitesimal change in the allowed energies of a system, without changing the probability distribution of its states. Similarly,

$$\delta q = \sum_j E_j(N,V) dp_j \left(N,V,\beta\right) \tag{2.225}$$

which means that the reversible heat results from a change in the probability distribution of the states of a system, without changing the allowed energies. If we compare Eq. (2.224) with Eq. (2.155) ($\delta w = -PdV$) we can identify the pressure of the gas with:

$$P \equiv \langle P \rangle = -\sum_j p_j(N,V,\beta) \left(\frac{\partial E_j}{\partial V}\right)_N = -\left\langle \left(\frac{\partial E_j}{\partial V}\right)_N \right\rangle \tag{2.226}$$

Just as we equated the ensemble average of the energy with the observed energy, we equate the ensemble average pressure with the observed pressure. Using Equation (2.180) we can write:

$$P \equiv \langle P \rangle = \sum_j p_j(N,V,\beta) \left(-\frac{\partial E_j}{\partial V}\right)_N = \sum_j \left(-\frac{\partial E_j}{\partial V}\right)_N \frac{e^{-\beta E_j(N,V)}}{Q\left(N,V,\beta\right)} \tag{2.227}$$

If we differentiate Eq. (2.179) with respect to V keeping N and β fixed:

$$\left(\frac{\partial Q}{\partial V}\right)_{N,\beta} = -\beta \sum_j \left(\frac{\partial E_j}{\partial V}\right)_N e^{-\beta E_j(N,V)} \tag{2.228}$$

By comparison of this result with the second equality of Eq. (2.227), the following holds true:

$$P \equiv \langle P \rangle = \frac{k_B T}{Q\left(N, V, \beta\right)} \left(\frac{\partial Q}{\partial V}\right)_{N,\beta} \tag{2.229}$$

or equivalently:

$$\boxed{P \equiv \langle P \rangle = k_B T \left(\frac{\partial \ln Q}{\partial V}\right)_{N,\beta}} \tag{2.230}$$

This result offers a deeper understanding of the concept of pressure from a statistical mechanics point of view. Note the slightly difference with respect to the expression for the average energy (Eq. 2.219). However, both equations shine because of its simplicity and elegance: if the partition function Q is known, it is possible to calculate not only the average energy, but also the average pressure.

2.4.5 Decomposition of the total partition function

Say our system is composed of many molecules. The total partition function cannot be obtained directly, it is necessary to break it down into molecular partition functions. If we substitute Eq. (2.190) into Eq. (2.219):

$$\begin{aligned} U \equiv E \equiv \langle E \rangle &= k_B T^2 \left(\frac{\partial \ln Q}{\partial T}\right)_{N,V} \\ &= N k_B T^2 \left(\frac{\partial \ln q}{\partial T}\right)_V \\ &= N \sum_j \varepsilon_j \frac{e^{-\varepsilon_j / k_B T}}{q\left(V, T\right)} \end{aligned} \tag{2.231}$$

If $\langle E \rangle$ is the average energy a system composed of N molecules, then we denote $\langle \varepsilon \rangle$ as the average energy of any one molecule, where

$$\langle E \rangle = N \langle \varepsilon \rangle \tag{2.232}$$

By direct comparison of Eq. (2.231) and (2.232) we get:

$$\langle \varepsilon \rangle = \sum_j \varepsilon_j \frac{e^{-\varepsilon_j / k_B T}}{q\left(V, T\right)} \tag{2.233}$$

Recalling the definition of a probability (Eq. (2.182)), we can conclude that π_j, the probability that a molecule is in its jth molecular energy state, is given by:

$$\pi_j = \frac{e^{-\varepsilon_j / k_B T}}{q\left(V, T\right)} = \frac{e^{-\varepsilon_j / k_B T}}{\sum_j e^{-\varepsilon_j / k_B T}} \tag{2.234}$$

If we assume that the energy of a the jth energy state of a molecule can be written as a sum of the individual contributions:

$$\varepsilon_j = \varepsilon_m^{\text{trans}} + \varepsilon_k^{\text{rot}} + \varepsilon_i^{\text{vib}} + \varepsilon_n^{\text{elec}} \tag{2.235}$$

where each of these terms are, respectively, the mth, kth, ith and nth translational, rotational, vibrational and electronic states of a molecule in the jth molecular state.

Due to the fact that these energy terms are distinguishable, we can apply the reasoning from Eq. (2.184) and write:

$$Q\left(V, T\right) = Q_{\text{trans}}\, Q_{\text{rot}}\, Q_{\text{vib}}\, Q_{\text{elec}} \tag{2.236}$$

where

$$\begin{aligned} q_{\text{trans}} &= \sum_m e^{-\varepsilon_m^{\text{trans}} / k_B T} \\ q_{\text{rot}} &= \sum_k e^{-\varepsilon_k^{\text{rot}} / k_B T} \\ q_{\text{vib}} &= \sum_i e^{-\varepsilon_i^{\text{vib}} / k_B T} \\ q_{\text{elec}} &= \sum_n e^{-\varepsilon_n^{\text{elec}} / k_B T} \end{aligned} \tag{2.237}$$

If we substitute Equations (2.235) and (2.236) into Eq. (2.234) we obtain:

$$\pi_{ikmn} = \frac{e^{-\varepsilon_m^{\text{trans}} / k_B T} e^{-\varepsilon_k^{\text{rot}} / k_B T} e^{-\varepsilon_i^{\text{vib}} / k_B T} e^{-\varepsilon_n^{\text{elec}} / k_B T}}{q_{\text{trans}}\, q_{\text{rot}}\, q_{\text{vib}}\, q_{\text{elec}}} \tag{2.238}$$

where π_{ikmn} is the probability that a molecule is in the mth translational state, the kth rotational state, the ith vibrational state and the nth electronic state.

2.5 Partition Function in a periodic system

With the aim of gaining some simplicity in the formalism, from now on, we will write the partition function as Q instead of $Q(N, V, \beta)$.

Since in a solid there is no translational or rotational degrees of freedom, there are no translational and rotational partition functions Therefore, the total partition function is reduced to the vibrational and electronic contributions:

$$Q = Q_{\text{vib}} Q_{\text{elec}} \tag{2.239}$$

2.5.1 The Vibrational Partition Function

The solution of the Schrödinger equation for the n-th level of an i-th harmonic oscillator reads like:

$$E_{n,i} = (n + 1/2)\, h\nu_i, \tag{2.240}$$

where $E_{n,i}$ is the energy of the n-th level of the i-th harmonic oscillator that has frequency ν_i and n is a quantum number that can take values of 0, 1, 2... Each of these n levels are equivalent to the j quantum states we introduced in the beginning and throughout this Chapter.

To a first approximation, we will assume that the vibrations in a solid are composed of independent harmonic oscillators (a detailed explanation will be given in the next Chapter). By inserting the definition of $E_{n,i}$ (Eq. 2.240) into Eq. 2.179, for a collection of independent oscillators,the partition function for each harmonic oscillator is Q_i:

$$Z_i = \sum_{n=0}^{\infty} \exp\left(\frac{-h\nu_i\,(n + 1/2)}{k_B T}\right) \tag{2.241}$$

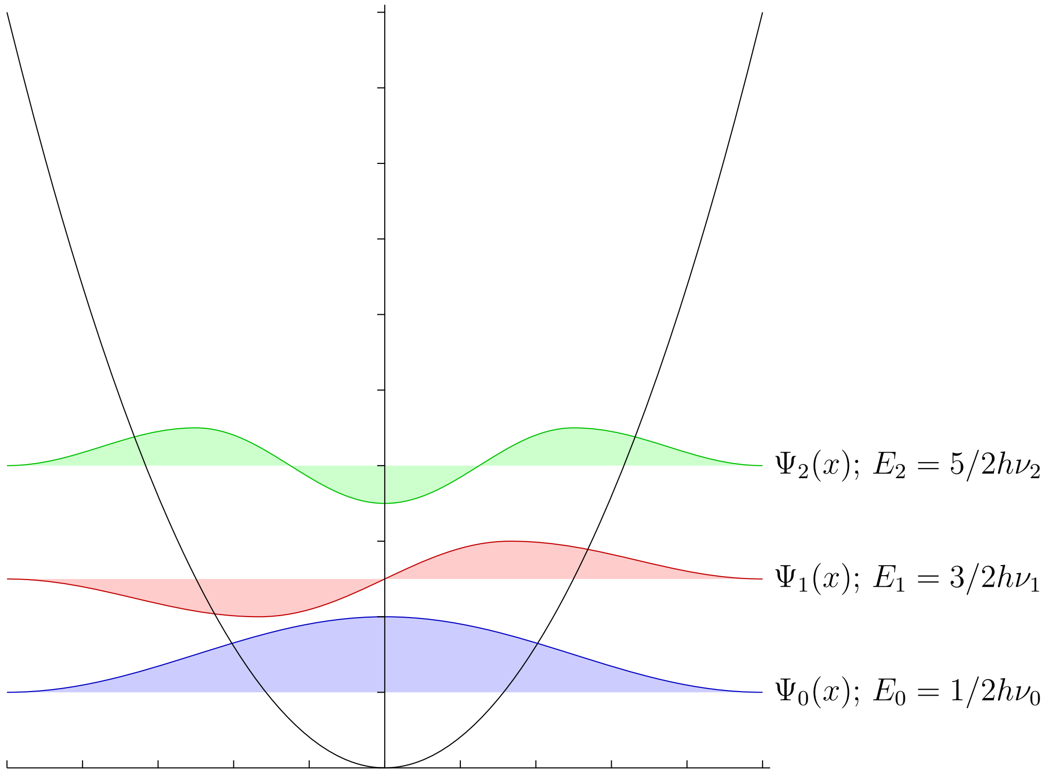

Figure 2.33: First three energy levels for a quantum harmonic oscillator.

By doing $x_i = \frac{1}{k_B T} \cdot h\nu_i$ in Eq. (2.241), Q_i can be written as:

$$\begin{aligned} Z_i &= \sum_{n=0}^{\infty} \exp\left[-x_i\left(n+1/2\right)\right] \\ &= \sum_{n=0}^{\infty} \exp\left[-x_i n - x_i/2\right] \\ &= \sum_{n=0}^{\infty} \exp\left(-x_i n\right) \cdot \exp\left(-x_i/2\right) \\ &= \exp\left(-x_i/2\right) \sum_{n=0}^{\infty} \exp\left(-x_i n\right) \\ &= \exp\left(-x_i/2\right) \sum_{n=0}^{\infty} \left[\exp\left(-x_i\right)\right]^n \end{aligned} \tag{2.242}$$

It is known that:

$$1 + t + t^2 + t^3 + ... = \frac{1}{1-t} \text{ for } |t| < 1, \tag{2.243}$$

or in general terms:

$$\sum_{n=0}^{\infty} t^n = \frac{1}{1-t} \text{ for } |t| < 1. \tag{2.244}$$

In our case, $t = \exp\left(-x_i\right)$. Since $\nu_i > 1$, therefore, $x_i > 1$. The function $y = |\exp\left(-x\right)|$ is plotted in Figure 2.34. It is always satisfied that $|\exp(-x)| < 1$ for $x_i > 1$, and therefore we can use the result of the series in Eq. (2.244).

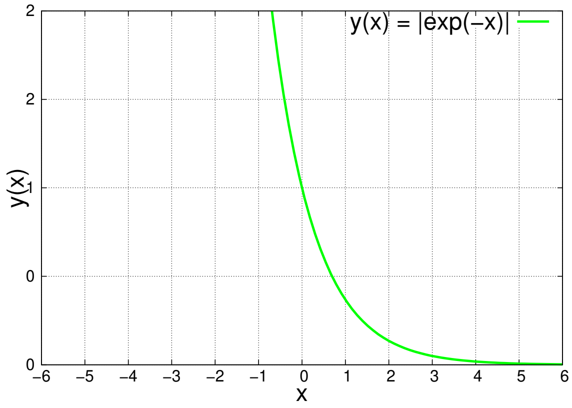

Figure 2.34: Representation of the function $y = |\exp(-x)|$.

$$\begin{aligned}\text{If } t = \exp(-x_i)\,,\ \text{then } Z_i &= \exp\left(-\frac{x_i}{2}\right) \cdot \sum_{n=0}^{\infty} t^n \\ &= \exp\left(-\frac{x_i}{2}\right) \cdot \frac{1}{1-t} \\ &= \exp\left(-\frac{x_i}{2}\right) \cdot \frac{1}{1-\exp(-x_i)}\end{aligned}$$

Since $x_i = \frac{1}{k_B T} \cdot h\nu_i$, therfore we have:

$$\boxed{Q_i = \frac{\exp\left(-\frac{h\nu_i}{2k_B T}\right)}{1-\exp\left(-\frac{h\nu_i}{k_B T}\right)}} \tag{2.245}$$

Q_i is the partition function for each i-th harmonic oscillator, and does not depend on the n vibrational levels of each independent i-th harmonic oscillator.

For each harmonic oscillator, the Helmholtz free energy is defined as:

$$\begin{aligned}F_i &= -k_B T \ln Q_i \\ &= -k_B T\left[-\frac{h\nu_i}{2k_B T}\right] + k_B T\ \ln\left[1-\exp\left(\frac{-h\nu_i}{k_B T}\right)\right].\end{aligned}$$

Therefore:

$$\boxed{F_i = \frac{1}{2}h\nu_i + k_B T\ \ln\left[1-\exp\left(\frac{-h\nu_i}{k_B T}\right)\right]} \tag{2.246}$$

For a molecule with normal vibration frequencies ν_i, $\sum_{i=0}^{\infty} F_i$ gives the part of its free energy due to the vibratory motions.

Since the normal modes are independent and distinguishable, we can apply the same treatment as we did with distinguishable particles (Eq. 2.184), and conclude in the following way: the partition function of a polyatomic molecule is a product of the harmonic oscillator partition functions for each normal coordinate:

$$Q_{\text{vib}} = \prod_{i=1}^{\substack{3N-5\\3N-6}} Q_i = \prod_{i=1}^{\substack{3N-5\\3N-6}} \frac{\exp\left(-\frac{h\nu_i}{2k_BT}\right)}{\left[1-\exp\left(\frac{-h\nu_i}{k_BT}\right)\right]} \qquad \text{for a polyatomic molecule,} \tag{2.247}$$

where ν_i is the vibrational frequency associated with the i-th normal mode and the product is extended to the number of vibrational degrees of freedom ($3N-5$ for a linear molecule and $3N-6$ for a nonlinear molecule, where N is the number of atoms in the molecule).

This idea can be easily extrapolated to a periodic system, where:

$$Q_{\text{vib}} = \prod_{\mathbf{k},i} Q_{i,\mathbf{k}} = \prod_{\mathbf{k},i} \frac{\exp\left(-\frac{h\nu_{i,\mathbf{k}}}{2k_BT}\right)}{1-\exp\left(-\frac{h\nu_{i,\mathbf{k}}}{k_BT}\right)} \qquad \text{for a periodic system,} \tag{2.248}$$

For each $\mathbf{k}$-point in the first Brillouin zone, there are $3N$ harmonic oscillators (i.e., phonons) labelled by a phonon branch index i that runs from 1 to $3N$, where N is the number of atoms in the unit cell. The sum $\sum_{i,\mathbf{k}}$ runs both over all the $i = 1, ..., 3N$ branches of the phonon dispersion curve, and over a finite number of $\mathbf{k}$-points. $\nu_{i,\mathbf{k}}$ is the frequency of vibration for a branch i in a given $\mathbf{k}$-point.

In the same way as Eq. 2.246, the Helmholtz free energy of each harmonic oscillator in a periodic system reads like:

$$\boxed{F_{i,\mathbf{k}} = \frac{1}{2}h\nu_{i,\mathbf{k}} + k_BT\,\ln\left[1-\exp\left(\frac{-h\nu_{i,\mathbf{k}}}{k_BT}\right)\right]} \tag{2.249}$$

The total partition function Q includes the vibrational partition function (Q_{vib}) and the electronic (Q_{elec}). The later can be expressed as:

$$Q_{\text{elec}} = \exp\left(\frac{-E_{\text{static}}}{k_BT}\right) \tag{2.250}$$

where E_{static} is the energy as a result of each lattice particle occupying its mean position. In our calculations, this is the energy that comes from the SCF calculation. Substituting into Eq. 2.239, the total partition function for a periodic system reads like:

$$Q = Q_{\text{elec}} \cdot Q_{\text{vib}} = \exp\left(\frac{-E_{\text{static}}}{k_B T}\right) \cdot \prod_{i,\mathbf{k}} \frac{\exp\left(-\frac{h\nu_{i,\mathbf{k}}}{2k_B T}\right)}{1 - \exp\left(-\frac{h\nu_{i,\mathbf{k}}}{k_B T}\right)} \tag{2.251}$$

2.5.2 The Helmholtz Free energy

According to statistical mechanics, the energy levels of a system completely determine its thermodynamic functions, being the Helmholtz free energy normally given by

$$F = -k_B T \ln Q. \tag{2.252}$$

Using the expression of Q from Eq. 2.251:

$$\begin{aligned}
F &= -k_B T \ln Q \\
&= -k_B T \ln \left\{ \exp\left(\frac{-E_{\text{static}}}{k_B T}\right) \cdot \prod_{i,\mathbf{k}} \frac{\exp\left(-\frac{h\nu_{i,\mathbf{k}}}{2k_B T}\right)}{1 - \exp\left(-\frac{h\nu_{i,\mathbf{k}}}{k_B T}\right)} \right\} \\
&= -k_B T \left\{ \ln\left[\exp\left(\frac{-E_{\text{static}}}{k_B T}\right)\right] + \ln\left[\prod_{i,\mathbf{k}} \frac{\exp\left(-\frac{h\nu_{i,\mathbf{k}}}{2k_B T}\right)}{1 - \exp\left(-\frac{h\nu_{i,\mathbf{k}}}{k_B T}\right)}\right] \right\} \\
&= E_{\text{static}} - k_B T \sum_{i,\mathbf{k}} \ln\left[\frac{\exp\left(-\frac{h\nu_{i,\mathbf{k}}}{2k_B T}\right)}{1 - \exp\left(-\frac{h\nu_{i,\mathbf{k}}}{k_B T}\right)}\right] \\
&= E_{\text{static}} - k_B T \sum_{i,\mathbf{k}} \left\{ \left[-\frac{h\nu_{i,\mathbf{k}}}{2k_B T}\right] - \ln\left[1 - \exp\left(-\frac{h\nu_{i,\mathbf{k}}}{k_B T}\right)\right] \right\}
\end{aligned}$$

$$\boxed{F = E_{\text{static}} + \frac{1}{2}\sum_{i,\mathbf{k}} h\nu_{i,\mathbf{k}} + k_B T \sum_{i,\mathbf{k}} \ln\left[1 - \exp\left(-\frac{h\nu_{i,\mathbf{k}}}{k_B T}\right)\right]} \tag{2.253}$$

From this expression an interesting quantity appears naturally: the **zero point energy**:

$$E_{ZPE} = \frac{1}{2}\sum_{i,\mathbf{k}} h\nu_{i,\mathbf{k}} \tag{2.254}$$

From the free energy F, all the thermodynamical behaviour concerning changes in volume and temperature can be deduced with the help of thermodynamical relations. For instance, the entropy and heat capacity.

2.5.3 The Vibrational Entropy

The entropy is defined as:

$$\begin{aligned} S &= -\left(\frac{\partial F}{\partial T}\right)_V && (2.255) \\ &= -k_B \left\{ \sum_{i,\mathbf{k}} \ln\left[1-\exp\left(\frac{-h\nu_{i,\mathbf{k}}}{k_BT}\right)\right] + T\sum_{i,\mathbf{k}} \frac{-\exp\left(\frac{-h\nu_{i,\mathbf{k}}}{k_BT}\right)}{1-\exp\left(\frac{-h\nu_{i,\mathbf{k}}}{k_BT}\right)} \cdot \frac{\partial}{\partial T}\left[\frac{-h\nu_{i,\mathbf{k}}}{k_BT}\right] \right\} \\ &= -k_B \left\{ \sum_{i,\mathbf{k}} \ln\left[1-\exp\left(\frac{-h\nu_{i,\mathbf{k}}}{k_BT}\right)\right] - \frac{1}{T}\frac{h}{k_B}\sum_{i,\mathbf{k}} \frac{\nu_{i,\mathbf{k}}\exp\left(\frac{-h\nu_{i,\mathbf{k}}}{k_BT}\right)}{1-\exp\left(\frac{-h\nu_{i,\mathbf{k}}}{k_BT}\right)} \cdot \frac{\exp\left(\frac{h\nu_{i,\mathbf{k}}}{k_BT}\right)}{\exp\left(\frac{h\nu_{i,\mathbf{k}}}{k_BT}\right)} \right\} \end{aligned}$$

$$\boxed{S = -k_B\sum_{i,\mathbf{k}} \ln\left[1-\exp\left(\frac{-h\nu_{i,\mathbf{k}}}{k_BT}\right)\right] + \frac{h}{T}\sum_{i,\mathbf{k}} \frac{\nu_{i,\mathbf{k}}}{\exp\left(\frac{h\nu_{i,\mathbf{k}}}{k_BT}\right)-1}} \qquad (2.256)$$

where

$$n\left(\nu_{i,\mathbf{k}},T\right) = \frac{1}{\exp\left(\frac{h\nu_{i,\mathbf{k}}}{k_BT}\right)-1} \qquad (2.257)$$

is the Bose-Einstein distribution, which is an energy distribution function for bosons. Phonons are bosons, and therefore behave according to this distribution. On the contrary, electrons are fermions and follow the Fermi-Dirac statistics. At this point, $hn\left(\nu_{i,\mathbf{k}},T\right)$ has the units of energy, so that is very useful to define $\mathcal{E}$ as:

$$\boxed{\mathcal{E} = \sum_{i,\mathbf{k}} \frac{h\nu_{i,\mathbf{k}}}{\exp\left(\frac{h\nu_{i,\mathbf{k}}}{k_BT}\right)-1}} \qquad (2.258)$$

Having reached to this point, an interesting result appears: plugging in Eq. (2.252) into Eq. (2.255), it is possible to reach to the following expression:

$$\begin{aligned} S &= k_B\ln Q + \frac{k_BT}{Q}\cdot\left(\frac{\partial Q}{\partial T}\right)_V \\ &= k_B\ln Q + k_BT\cdot\left(\frac{\partial \ln Q}{\partial T}\right)_V && (2.259) \end{aligned}$$

Now, Q depends on the static energy, E_{static} (See Eq. 2.251). According to Eq. (2.259) we could think in principle that S depends on the internal energy too. According to Eq. (2.251), we have that:

$$\ln Q = \left(\frac{-E_{\text{static}}}{k_B T}\right) + \ln Q_{\text{vib}} \tag{2.260}$$

Then

$$\frac{\partial \ln Q}{\partial T} = \frac{E_{\text{static}}}{k_B T^2} + \frac{\partial \ln Q_{\text{vib}}}{\partial T} \tag{2.261}$$

Casting (2.260) and (2.261) into Eq. (2.259), we have that

$$\begin{aligned} S &= \frac{-E_{\text{static}}}{T} + k_B \ln Q_{\text{vib}} + \frac{E_{\text{static}}}{T} + k_B T \cdot \frac{\partial \ln Q_{\text{vib}}}{\partial T} \\ &= k_B \ln Q_{\text{vib}} + k_B T \cdot \frac{\partial \ln Q_{\text{vib}}}{\partial T}, \end{aligned} \tag{2.262}$$

which means that the entropy does not depend on the internal energy, only on the vibrations. This is a conclusion that has an important physical relevance. If we obtain the expressions for $\ln Q_{\text{vib}}$ and $\frac{\partial \ln Q_{\text{vib}}}{\partial T}$, we get:

$$\begin{aligned} \ln Q_{\text{vib}} &= \ln \prod_{i,\mathbf{k}} \frac{\exp\left(\frac{-h\nu_{i,\mathbf{k}}}{2k_B T}\right)}{1 - \exp\left(\frac{-h\nu_{i,\mathbf{k}}}{k_B T}\right)} \\ &= \sum_{i,\mathbf{k}} \ln \frac{\exp\left(\frac{-h\nu_{i,\mathbf{k}}}{2k_B T}\right)}{1 - \exp\left(\frac{-h\nu_{i,\mathbf{k}}}{k_B T}\right)} \\ &= \sum_{i,\mathbf{k}} \frac{-h\nu_{i,\mathbf{k}}}{2k_B T} - \sum_{i,\mathbf{k}} \ln \left[1 - \exp\left(\frac{-h\nu_{i,\mathbf{k}}}{k_B T}\right)\right] \end{aligned} \tag{2.263}$$

$$\begin{aligned} \frac{\partial \ln Q_{\text{vib}}}{\partial T} &= \frac{\partial}{\partial T} \ln \prod_{i,\mathbf{k}} \frac{\exp\left(\frac{-h\nu_{i,\mathbf{k}}}{2k_B T}\right)}{1 - \exp\left(\frac{-h\nu_{i,\mathbf{k}}}{k_B T}\right)} \\ &= \frac{\partial}{\partial T} \sum_{i,\mathbf{k}} \ln \frac{\exp\left(\frac{-h\nu_{i,\mathbf{k}}}{2k_B T}\right)}{1 - \exp\left(\frac{-h\nu_{i,\mathbf{k}}}{k_B T}\right)} \\ &= \sum_{i,\mathbf{k}} \frac{\partial}{\partial T} \ln \frac{\exp\left(\frac{-h\nu_{i,\mathbf{k}}}{2k_B T}\right)}{1 - \exp\left(\frac{-h\nu_{i,\mathbf{k}}}{k_B T}\right)} \\ &= \sum_{i,\mathbf{k}} \frac{h\nu_{i,\mathbf{k}}}{2k_B T^2} - \sum_{i,\mathbf{k}} \frac{1}{\exp\left(\frac{h\nu_{i,\mathbf{k}}}{k_B T}\right) - 1} \cdot \frac{h\nu_{i,\mathbf{k}}}{k_B} \frac{1}{T^2} \end{aligned} \tag{2.264}$$

Casting Eq. (2.263) and (2.264) into Eq. (2.262), we get the expression of the entropy obtained previously (Eq. (2.256)).

2.5.4 The Energy at finite temperature

At a given temperature, the energy of the system is given by:

$$E = F + TS \tag{2.265}$$

Casting F (Eq. 2.253) and S (Eq. 2.256) into Eq. 2.265:

$$\boxed{E = E_{\text{static}} + \frac{1}{2}\sum_{i,\mathbf{k}} h\nu_{i,\mathbf{k}} + h\sum_{i,\mathbf{k}} \frac{\nu_{i,\mathbf{k}}}{\exp\left(\frac{h\nu_{i,\mathbf{k}}}{k_B T}\right) - 1}} \tag{2.266}$$

Starting from Eq. 2.219, and inserting the expression of Q given in Eq. 2.251, the same expression as Eq. 2.266 is obtained.

- **For $T = 0\,\mathbf{K}$:** We have that:

$$\exp\left(\frac{h\nu_{i,\mathbf{k}}}{0 \cdot k_B}\right) - 1 = \exp\left(\infty\right) - 1 = \infty - 1 = \infty$$

so that the energy E reduces to the static energy E_{static}, plus the zero-point energy:

$$E = E_{static} + \frac{1}{2}\sum_{i,\mathbf{k}} h\nu_{i,\mathbf{k}} + h\sum_{i,\mathbf{k}} \cancelto{0}{\frac{\nu_{i,\mathbf{k}}}{\infty}}$$

$$\boxed{E = E_{static} + \frac{1}{2}\sum_{i,\mathbf{k}} h\nu_{i,\mathbf{k}}} \tag{2.267}$$

- **For high temperatures:** If we recall $\frac{1}{k_B T} = \beta$ and $h\nu_{i,\mathbf{k}} = \epsilon_{i,\mathbf{k}}$ and redefine Eq. (2.266) as:

$$E = E_{static} + \frac{1}{2}\sum_{i,\mathbf{k}} \epsilon_{i,\mathbf{k}} + h\sum_{i,\mathbf{k}} \frac{\nu_{i,\mathbf{k}}}{\exp\left(\beta\epsilon_{i,\mathbf{k}}\right) - 1}$$

A Taylor expansion of the exponential is: $\exp(\beta\epsilon_{i,\mathbf{k}}) = 1 + \beta\epsilon_{i,\mathbf{k}} + \frac{1}{2}\beta^2\epsilon_{i,\mathbf{k}}^2 + \frac{1}{6}\beta^3\epsilon_{i,\mathbf{k}}^3 + ...$
At high temperatures, $k_BT \gg h\nu_{i,\mathbf{k}} \rightarrow \frac{1}{\beta} \gg \epsilon_{i,\mathbf{k}} \rightarrow \beta\frac{1}{\beta} \gg \beta\epsilon_{i,\mathbf{k}} \rightarrow \boxed{1 \gg \beta\epsilon_{i,\mathbf{k}}}$, and therefore it is a good approximation to truncate the Taylor expansion in the second term. Hence, we get to:

$$\begin{aligned} E &= E_{static} + \frac{1}{2}\sum_{i,\mathbf{k}} \varepsilon_{i,\mathbf{k}} + \frac{1}{\beta} \\ &= E_{static} + \frac{1}{2}\sum_{i,\mathbf{k}} h\nu_{i,\mathbf{k}} + k_BT \end{aligned} \tag{2.268}$$

Since $k_BT \gg h\nu_{i,\mathbf{k}}$, then $\sum_{i,\mathbf{k}} h\nu_{i,\mathbf{k}} + k_BT \approx k_BT$, so:

$$\boxed{E = E_{static} + k_BT} \tag{2.269}$$

This relation express the classical energy partition law: the energy for each vibrational degree of freedom is k_BT. This law holds only when the temperature is so high that the vibratory modes are in such highly excited states, that the quantum effects become insignificant.

There are 3 vibrations for each atom (the total number of normal coordinates is equal to three times the number of particles). In addition, there are the number of Avogadro particles in 1 mol. Therefore, we can express Eq. (2.268) as:

$$E = E_{static} + 3k_BTN_A \tag{2.270a}$$

$$E = E_{static} + 3RT \tag{2.270b}$$

2.5.5 The Heat Capacity

The heat capacity is also a path function, and is defined as the energy as heat required to raise the temperature of a substance by one degree. This energy required depends on the amount of substance, and therefore is an extensive quantity: twice the amount of substance require twice the amount of heat to achieve the same change in temperature.

The heat capacity at a constant volume is obtained by differentiating the energy with respect to the temperature:

$$\begin{aligned} C_V &= \left(\frac{\partial E}{\partial T}\right)_V \\ &= -h\sum_{i,\mathbf{k}} \nu_{i,\mathbf{k}} \left[\exp\left(\frac{h\nu_{i,\mathbf{k}}}{k_BT}\right) - 1\right]^{-2} \cdot \exp\left(\frac{h\nu_{i,\mathbf{k}}}{k_BT}\right) \cdot \frac{h\nu_{i,\mathbf{k}}}{k_B} \cdot (-1) \cdot \frac{1}{T^2} \end{aligned}$$

$$\boxed{C_V = \frac{h^2}{k_BT^2}\sum_{i,\mathbf{k}} \nu_{i,\mathbf{k}}^2 \cdot \frac{\exp\left(\frac{h\nu_{i,\mathbf{k}}}{k_BT}\right)}{\left[\exp\left(\frac{h\nu_{i,\mathbf{k}}}{k_BT}\right) - 1\right]^2}} \tag{2.271}$$

- **For $T = 0\,\mathbf{K}$:**

If we recall $\frac{1}{k_B} = \beta$ and $h\nu_{i,\mathbf{k}} = \epsilon_{i,\mathbf{k}}$ and redefine Eq. (2.271) as:

$$C_V = \frac{1}{\beta T}\sum_{i,\mathbf{k}} \epsilon_{i,\mathbf{k}}^2 \cdot \frac{\exp\left(\epsilon_{i,\mathbf{k}}\beta\right)}{\left[\exp\left(\epsilon_{i,\mathbf{k}}\beta\right) - 1\right]^2} \tag{2.272}$$

A Taylor expansion of the exponential is: $\exp\left(\beta\epsilon_{i,\mathbf{k}}\right) = 1 + \beta\epsilon_{i,\mathbf{k}} + \frac{1}{2}\beta^2\epsilon_{i,\mathbf{k}}^2 + \frac{1}{6}\beta^3\epsilon_{i,\mathbf{k}}^3 + ...$
At low temperatures, $k_BT \ll h\nu_{i,\mathbf{k}} \rightarrow \frac{1}{\beta} \ll \epsilon_{i,\mathbf{k}} \rightarrow \beta\frac{1}{\beta} \ll \beta\epsilon_{i,\mathbf{k}} \rightarrow \boxed{1 \ll \beta\epsilon_{i,\mathbf{k}}}$, and therefore in this case it is not a good approximation to truncate the Taylor expansion in the second term. However, we will still use that approximation:

$$\begin{aligned} C_V &= \frac{1}{\beta T} \cdot \frac{1}{\beta^2}\sum_{i,\mathbf{k}} 1 + \epsilon_{i,\mathbf{k}}\beta \\ &= \frac{1}{\beta T} \cdot \frac{1}{\beta^2} \cdot \beta\sum_{i,\mathbf{k}} \epsilon_{i,\mathbf{k}} \\ &= k_B^2T\sum_{i,\mathbf{k}} h\nu_{i,\mathbf{k}} \end{aligned}$$

$$\boxed{\text{For } T = 0\,K \longrightarrow C_V = 0} \tag{2.273}$$

This is a well known feature in solids; the heat capacity falls to zero on cooling to zero temperature. The origin for this is due to quantum effects.

- **For high temperatures:**

If we recall $\frac{1}{k_B} = \beta$ and $h\nu_{i,\mathbf{k}} = \epsilon_{i,\mathbf{k}}$ and redefine Eq. (2.271) as:

$$C_V = \frac{1}{\beta T} \sum_{i,\mathbf{k}} \epsilon_{i,\mathbf{k}}^2 \cdot \frac{\exp\left(\epsilon_{i,\mathbf{k}}\beta\right)}{\left[\exp\left(\epsilon_{i,\mathbf{k}}\beta\right) - 1\right]^2} \tag{2.274}$$

A Taylor expansion of the exponential is: $\exp\left(\beta\epsilon_{i,\mathbf{k}}\right) = 1 + \beta\epsilon_{i,\mathbf{k}} + \frac{1}{2}\beta^2\epsilon_{i,\mathbf{k}}^2 + \frac{1}{6}\beta^3\epsilon_{i,\mathbf{k}}^3 + ...$
At high temperatures, $k_B T \gg h\nu_{i,\mathbf{k}} \rightarrow \frac{1}{\beta} \gg \epsilon_{i,\mathbf{k}} \rightarrow \beta\frac{1}{\beta} \gg \beta\epsilon_{i,\mathbf{k}} \rightarrow \boxed{1 \gg \beta\epsilon_{i,\mathbf{k}}}$, and therefore it is a good approximation to truncate the Taylor expansion in the second term.

Hence, we reach to:

$$\begin{aligned} C_V &= \beta \cdot \frac{1}{T} \sum_{i,\mathbf{k}} \frac{1 + \beta\epsilon_{i,\mathbf{k}}}{\beta^2} \\ &= \frac{1}{\beta} \cdot \frac{1}{T} \sum_{i,\mathbf{k}} 1 \\ &\boxed{C_V = k_B} \end{aligned} \tag{2.275}$$

This is known as the Dulong-Petit law of specific heat, noted empirically in the 19th century. The specific heat for each vibrational degree of freedom is k_B. Hence, we can express Eq. (2.275) as:

$$\boxed{\begin{aligned} C_V &= 3k_B N_A && (2.276a) \\ C_V &= 3R && (2.276b) \end{aligned}}$$

This law holds only when the temperature is so high that the vibratory modes are in such highly excited states that quantum effects become insignificant. Contrary to the classical result (Dulong-Petit law), the heat capacity falls to zero on cooling to zero temperature.

2.5.6 The Gibbs Free energy

Finally, the Gibbs free energy accounts for pressure and temperature effects on the energy:

$$
\begin{aligned}
G &= F + PV \\
&= E - TS + PV \qquad \text{Plugging in Eq. (2.266) :} \\
&= E_{\text{static}} + \frac{1}{2}\sum_{i,\mathbf{k}} h\nu_{i,\mathbf{k}} + h\sum_{i,\mathbf{k}} \frac{\nu_{i,\mathbf{k}}}{\exp\left(\frac{h\nu_{i,\mathbf{k}}}{k_BT}\right) - 1} - TS + PV
\end{aligned}
$$

$$\boxed{G = E_{\text{static}} + \frac{1}{2}\sum_{i,\mathbf{k}} h\nu_{i,\mathbf{k}} + h\sum_{i,\mathbf{k}} \frac{\nu_{i,\mathbf{k}}}{\exp\left(\frac{h\nu_{i,\mathbf{k}}}{k_BT}\right) - 1} - TS + PV} \tag{2.277}$$

2.6 Classification of phase transitions

Ehrenfest established a classification of phase transitions as follows: the order of a phase transition is the order of the lowest differential of G which shows a discontinuity at the critical temperature T_c or pressure P_c. For instance, if the entropy or the volume (a first differential of G) show a discontinuity (Fig. 2.35), these are first order phase transitions. In addition, the thermal compressibility and heat capacity, both second derivatives of G, show a discontinuity in terms of a sharp spike (Fig. 2.35). Examples of first order phase transitions are the solid-liquid solid-vapour and liquid-vapour transitions. Special interest is the discontinuity observed in the entropy for a liquid-vapour phase transition: In order to change from phase 1 (water) to phase 2 (steam) at a constant temperature T_c, some extra heat is needed, know as latent heat, which is given by:

$$L = \Delta q_{\text{rev}} = T_c(S_2 - S_1), \tag{2.278}$$

where T_c is the critical temperature, corresponding to the boiling point in this liquid-vapour phase transition. S_1 is the entropy of phase 1 and S_2 the entropy of phase 2. Thus, the spike jump observed in the entropy (Fig. 2.35) corresponds to $S_2 - S_1 = L/T_c$

Second order phase transitions are found when the volume (a first derivative of G) is continuous (Fig. 2.35) but the thermal compressibility (a second derivative of G) shows this sharp spike.

In a temperature-pressure phase diagram, for temperatures and pressures along the equilibrium

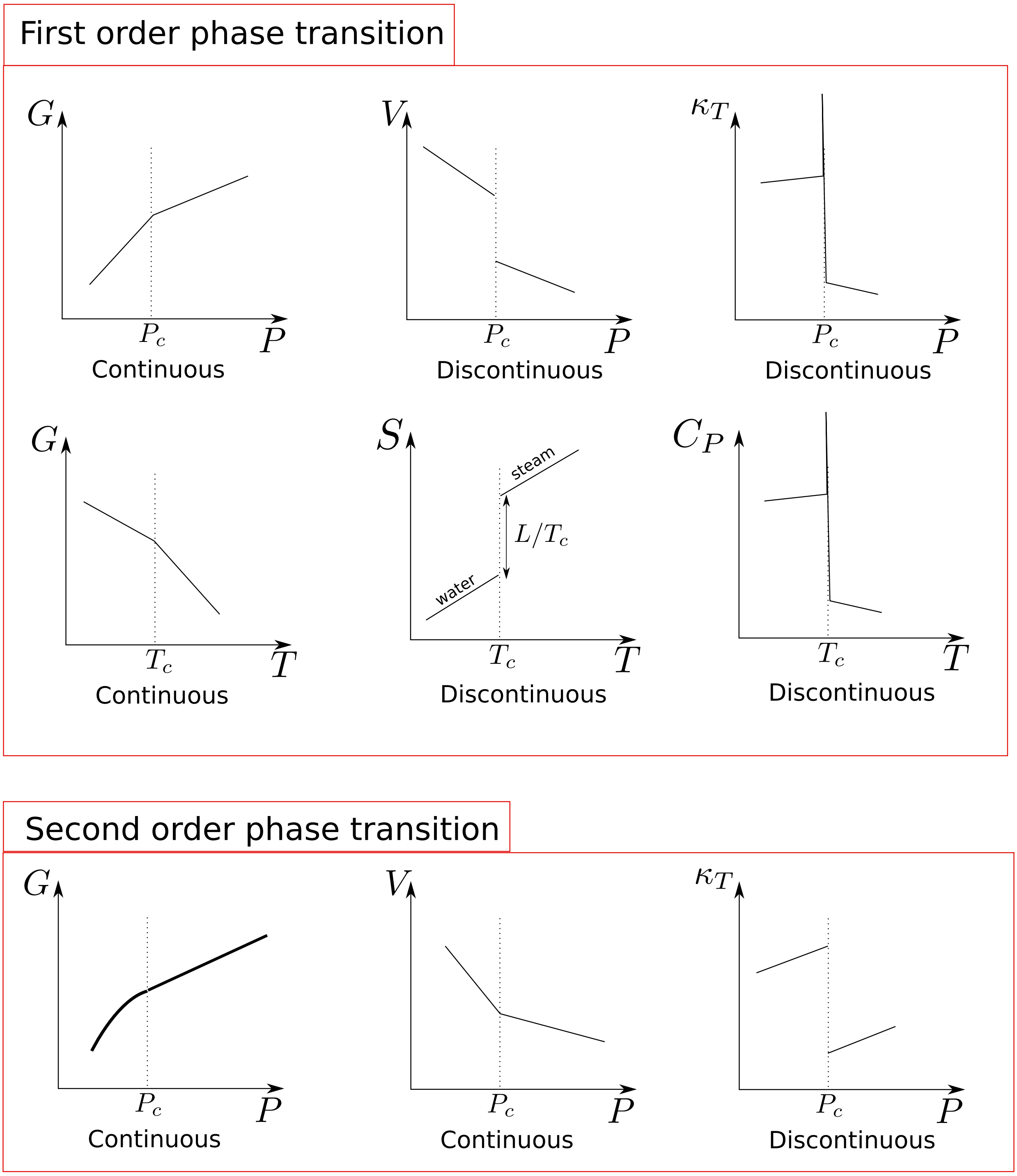

$$V = \left(\frac{\partial G}{\partial P}\right)_T \qquad \kappa_T = -\frac{1}{V}\left(\frac{\partial^2 G}{\partial P^2}\right)_T$$

$$S = -\left(\frac{\partial G}{\partial T}\right)_P \qquad C_P = -T\left(\frac{\partial^2 G}{\partial T^2}\right)_P$$

Figure 2.35: Summary with the shape of the main thermodynamic functions for a first order and second order phase transition.

curve (i.e. phase boundary), both phases exist simultaneously and in contact. The critical point is a pressure-temperature point above which both phases become identical, no difference of phases exists, and the substance is homogeneous.

Chapter 3

Methodology

3.1 Harmonic and quasi-harmonic approximations

In order to successfully compute a situation where temperature and pressure are involved, i.e. the temperature-pressure phase boundary for a phase transition, we need to take into account a combined effect of these two thermodynamic variables in our simulations. Even though usual quantum-chemical DFT *ab initio* techniques allow for a determination of a wide range of ground state structural, electronic, vibrational, elastic, optical and magnetic properties of materials, these are normally calculated at zero temperature and pressure [66, 60, 68, 69]. The effect of pressure can be easily taken into account if the energy-volume data is fitted to a general equation of state [70, 71, 72, 73], or simply to a polynomial fit.

On the contrary, the inclusion of temperature is not so straightforward to implement, i.e., harmonic and quasi-harmonic approximations (HA and QHA) are currently powerful techniques, which are described herein.

3.1.1 Elements of Harmonic Lattice Dyanmics

3.1.1.1 Dimer in one dimension

The vibration of a diatomic molecule is correctly described by a simple harmonic oscillator, i.e., two masses connected by a spring (Figure 3.1). x_1 and x_2 are the position of masses 1 and 2

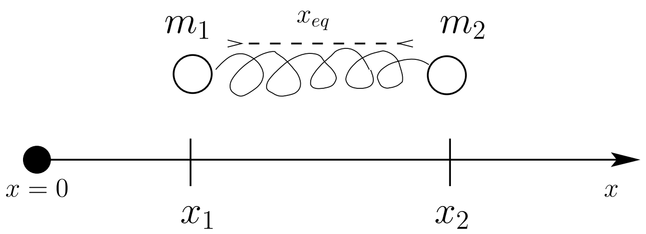

Figure 3.1: Two masses m_1 and m_2 connected by a spring separated by a distance x_{eq}.

respectively, x is the extension of the spring at a given time, and x_{eq} is the natural (equilibrium) length of the spring, and accounts for a separation between both masses so that one does not lie on top of the other.

A Taylor expansion of the potential energy $V(x)$, about the equilibrium bond length $x = x_e$ reads like:

$$V(x) = V(x_e) + \left(\frac{dV}{dx}\right)_{x=x_e} (x - x_e) + \frac{1}{2!}\left(\frac{d^2V}{dx^2}\right)_{x=x_e} (x - x_e)^2 + \frac{1}{3!}\left(\frac{d^3V}{dx^3}\right)_{x=x_e} (x - x_e)^3 + \ldots \tag{3.1}$$

The first term is just a constant and depends upon where we choose the zero of energy. Thus, it is convenient to choose the zero of energy such that $V(x_e) = 0$ and relate $V(x)$ to this convention.

In addition, because x_e denotes the minimum value of $V(x)$, then $\left(\frac{dV}{dx}\right)_{x=x_e} = 0$, so that there is actually no linear term in the expansion. $\frac{dV}{dx}$ is the force acting between the two nuclei, and the fact that $\frac{dV}{dx}$ vanishes at $x = x_e$ means that the force acting between the nuclei is zero at this point. This is why $x = x_e$ is called the equilibrium bond length.

With all these approximations we end up with the following expression:

$$V(x) = \frac{1}{2}\left(\frac{d^2V}{dx^2}\right)_{x=x_e} (x - x_e)^2 \tag{3.2}$$

This is the so called *harmonic approximation*, in which atoms, when slightly disturbed from its equilibrium or rest position, oscillate with simple harmonic motion.

We can consider extensions of the harmonic oscillator model by the higher-order terms in

Equation (3.1). These terms are called *anharmonic terms*, and will make the potential from this model look closer to the true internuclear potential for larger displacements. However, although these corrections can be made, note that if x is close to x_e (vibrations with small amplitudes) then $x - x_e$ is always small. Consequently, the terms on the right hand side of Eq. (3.1) get smaller and smaller.

To calculate the vibrational frequency of a dimer, the only piece of information we need is $\left(\frac{d^2V}{dx^2}\right)_{x=x_e}$. We can obtain a good estimate of the second derivative using a finite-difference approximation:

$$\left(\frac{d^2V}{dx^2}\right)_{x=x_e} \cong \frac{V(x_e+\delta x) - 2V(x_e) + V(x_e-\delta x)}{(\delta x)^2}. \tag{3.3}$$

This expression becomes exact when $\delta x \to 0$. In our simulations, δx is set to 0.003Å.

For this simple case like a diatomic molecule, the term $\left(\frac{d^2V}{dx^2}\right)$ is trivial because the force is trivial: *"A small displacement x from its equilibrium position generates a restoring force which is proportional to x acting in a direction towards the equilibrium position."* This restoring force can be written as:

$$F = -kx \tag{3.4}$$

where k is a constant of proportionality, called the stiffness or restoring force per unit distance (displacement), and has dimensions of

$$[k] \equiv \frac{\text{force}}{\text{distance}} \equiv \frac{ML\ \text{time}^{-2}}{L} \tag{3.5}$$

The negative sign in Eq. 3.4 shows that the force is acting against the direction of increasing displacement and back towards the equilibrium position. This is Hooke's Law of Elasticity.

If we recall that a force can be expressed as a derivative of a potential energy:

$$f(x) = -\frac{dV(x)}{dx}, \tag{3.6}$$

The potential energy is then:

$$V(x) = -\int f(x)dx + \text{constant}. \tag{3.7}$$

Using Eq. (3.4), we have that

$$V(x) = -\int -kx + \text{constant}. \tag{3.8}$$

The constant term is an arbitrary constant that can be used to fix the zero of energy. By choosing the potential energy of the system to be zero when the spring is undistorted ($x = x_{eq}$), we can write the potential energy associated with a simple harmonic oscillator as:

$$V(x) = \frac{k}{2}x^2 \tag{3.9}$$

When the spring is distorted, the potential reads like:

$$\boxed{V(x) = \frac{1}{2}k\left(x - x_e\right)^2} \tag{3.10}$$

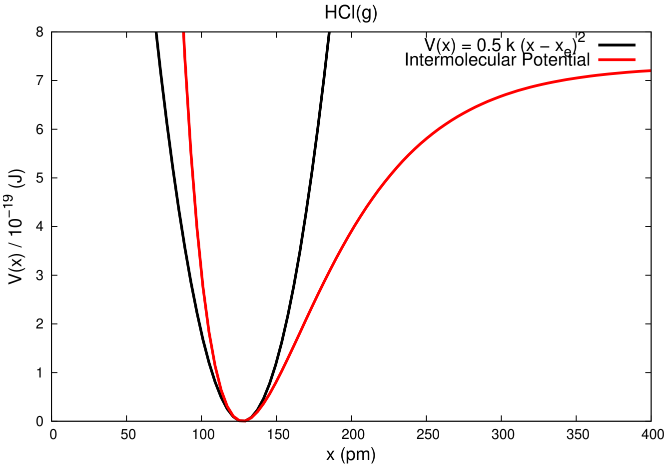

Figure 3.2: For the HCl molecule, the harmonic potential (Eq. 3.10) is shown in black and the experimental intermolecular potential is shown in red. Figure adapted from Ref. [74].

In Fig. 3.2 the harmonic potential (Eq. 3.10) and experimental internuclear potential for HCl(g) is shown, from which we can see that the harmonic oscillator potential is a satisfactory approximation at small displacements.

In this simple system there are two equations of motion, one for each mass:

$$m_1 \frac{\partial^2 x_1}{\partial dt^2} = k \left(x_2 - x_1 - x_{eq} \right) \tag{3.11}$$

$$m_2 \frac{\partial^2 x_2}{\partial dt^2} = -k \left(x_2 - x_1 - x_{eq} \right) \tag{3.12}$$

If $x_2 - x_1 > x_{eq}$, the spring is stretched and the force on mass m_1 is toward the right. This is why the force term in Eq. (3.11) is positive and that in Eq. (3.12) is negative. Note also that the force on m_1 is equal and opposite to the force on m_2, as it should be according to Newton's third law.

We find that $(x_2 - x_1 - x_{eq})$ is the amount by which the spring is stretched or compressed from its natural length. Denoting this quantity simply as x:

$$x = x_2 - x_1 - x_{eq} \tag{3.13}$$

We will use x because the vibrational motion of the two-mass system in Figure (3.1) depend upon only the *relative* separation of the two masses, or upon the *relative coordinate* x.

The two equations of motion are:

$$m_1 \ddot{x}_1 = kx \tag{3.14}$$

$$m_2 \ddot{x}_2 = -kx \tag{3.15}$$

If we divide Eq. (7.15) by m_2 and subtract Eq. (7.16) divided by m_1 we find that:

$$\ddot{x}_1 - \ddot{x}_2 = kx \left(\frac{1}{m_1} + \frac{1}{m_2} \right) \tag{3.16}$$

By differentiating twice Eq. (3.13), we get:

$$\ddot{x} = \ddot{x}_2 - \ddot{x}_1 \tag{3.17}$$

Introducing this result into Eq. (3.16) we get:

$$\ddot{x} = -kx \left(\frac{1}{m_1} + \frac{1}{m_2} \right) \tag{3.18}$$

If we let:

$$\frac{1}{m_1} + \frac{1}{m_2} = \frac{m_1 + m_2}{m_1 m_2} = \frac{1}{\mu} \tag{3.19}$$

the quantity μ that we have defined is called the *reduced mass.* Thus,

$$\boxed{\ddot{x} + \frac{k}{\mu} x = 0} \tag{3.20}$$

where the dimensions of $\frac{k}{\mu}$ are time^{-2}:

$$\left[\frac{k}{\mu} \right] = \frac{[k]}{[\mu]} = \frac{ML \text{ time}^{-2}}{LM} = \text{time}^{-2} \tag{3.21}$$

T is a time, or period of oscillation. Thus,

$$\frac{k}{\mu} = \frac{1}{T^2} \;\Rightarrow\; T = \sqrt{\frac{\mu}{k}} \tag{3.22}$$

The frequency at which the system oscillates is ν, the reciprocal of T, and has units of time^{-1}. Thus, the relation between the frequency and the force constant is the following:

$$\frac{k}{\mu} = \nu^2 \;\Rightarrow\; \nu = \sqrt{\frac{k}{\mu}} \tag{3.23}$$

However, when we solve the equation of motion we shall find that the behaviour of x with time has a sinusoidal or cosinusoidal dependence, and it is more appropiate to consider, not ν, but the angular frequency $\omega = 2\pi\nu$ so that k/μ is now written as ω^2:

$$\boxed{\omega^2 = \frac{k}{\mu} \;\Rightarrow\; \omega = \sqrt{\frac{k}{\mu}}} \tag{3.24}$$

$$\boxed{\nu = \frac{1}{2\pi}\sqrt{\frac{k}{\mu}}} \tag{3.25}$$

and the period now reads like :

$$\boxed{T = 2\pi\sqrt{\frac{\mu}{k}}} \tag{3.26}$$

Thus, Eq. (3.20) becomes:

$$\boxed{\ddot{x} + \omega^2 x = 0} \tag{3.27}$$

Both these solutions

$$x = A\cos(\omega t) \tag{3.28}$$

$$x = B\sin(\omega t) \tag{3.29}$$

satisfy the Equation (3.27) of motion. The general solution for this equation is given by the addition or superposition of both values for x so we have:

$$x = A\cos(\omega t) + B\sin(\omega t) \tag{3.30}$$

with $\ddot{x} = -\omega^2\left(A\cos\omega t + B\sin\omega t\right) = -\omega^2 x$, and where A and B are determined by the values of x and $\dot{x}$ at a specific time. If we rewrite the constants as:

$$A = a\sin\phi \qquad B = a\cos\phi \tag{3.31}$$

where ϕ is a constant angle, then:

$$A^2 + B^2 = a^2(\sin^2\phi + \cos^2\phi) = a^2 \tag{3.32}$$

so that

$$a = \sqrt{A^2 + B^2} \tag{3.33}$$

and

$$\begin{aligned} x &= a\sin\phi\cos(\omega t) + a\cos\phi\sin(\omega t) \\ &\boxed{x = a\sin(\omega t + \phi)} \end{aligned} \tag{3.34}$$

The limiting values of $\sin(\omega t + \phi)$ are ± 1, so the system will oscillate between the values of $\pm a$, known as the *amplitude of displacement.* This amplitude of displacement will be shown in Section 3.2, in which the energy profile along the normal mode coordinate is reported.

The angle ϕ is called the "*phase constant*". The solution $x = a\sin(\omega t)$ defines the displacement that starts from the origin $x = 0$ at time $t = 0$ and the inclusion of ϕ allows the motion to be defined from any starting point in the cycle.

3.1.1.2 Vibrations for a collection of atoms

A more general scenario corresponds to a situation where a collection of multiple atoms can vibrate. This situation is closer to the vibration in a periodic system. We begin by defining a set of N atoms defined by the Cartesian coordinates $\underline{\mathbf{r}}_a, \underline{\mathbf{r}}_b, \ldots \underline{\mathbf{r}}_N$. We need to apply the Taylor expansion for a multi-variable vector-valued functions, i.e., expand $V(\underline{\mathbf{r}}_a, \underline{\mathbf{r}}_b, \ldots \underline{\mathbf{r}}_N)$ around $\underline{\mathbf{r}}_a^{eq}, \underline{\mathbf{r}}_b^{eq}, \ldots \underline{\mathbf{r}}_N^{eq}$:

$$\begin{aligned} V\left(\underline{\mathbf{r}}_a, \underline{\mathbf{r}}_b, \dots \underline{\mathbf{r}}_N\right) &= V\left(\underline{\mathbf{r}}_a^{eq}, \underline{\mathbf{r}}_b^{eq}, \dots \underline{\mathbf{r}}_N^{eq}\right) \\ &+ \sum_{a=1}^{N} \left(\underline{\mathbf{r}}_a - \underline{\mathbf{r}}_a^{eq}\right)^T \nabla_{\underline{\mathbf{r}}_a} V\left(\underline{\mathbf{r}}_a, \underline{\mathbf{r}}_b, \dots \underline{\mathbf{r}}_N\right)\Big|_{\underline{\mathbf{r}}_a=\underline{\mathbf{r}}_a^{eq}} \\ &+ \frac{1}{2} \sum_{a=1}^{N} \sum_{b=1}^{N} \left(\underline{\mathbf{r}}_a - \underline{\mathbf{r}}_a^{eq}\right)^T \nabla_{\underline{\mathbf{r}}_a} \nabla_{\underline{\mathbf{r}}_b}^T V\left(\underline{\mathbf{r}}_a, \underline{\mathbf{r}}_b, \dots \underline{\mathbf{r}}_N\right)\Big|_{\substack{\underline{\mathbf{r}}_a=\underline{\mathbf{r}}_a^{eq} \\ \underline{\mathbf{r}}_b=\underline{\mathbf{r}}_b^{eq}}} \left(\underline{\mathbf{r}}_b - \underline{\mathbf{r}}_b^{eq}\right) + \dots \end{aligned} \tag{3.35}$$

For the same reasons as in the 1D case, the first and second terms become zero, and we do not consider higher order terms. It is more useful to work in terms of displacements:

$$\begin{aligned} \underline{\mathbf{x}}_a &= \underline{\mathbf{r}}_a - \underline{\mathbf{r}}_a^{eq} \\ \underline{\mathbf{x}}_b &= \underline{\mathbf{r}}_b - \underline{\mathbf{r}}_b^{eq} \end{aligned} \tag{3.36}$$

So that:

$$V\left(\underline{\mathbf{r}}_a, \underline{\mathbf{r}}_b, \dots \underline{\mathbf{r}}_N\right) = \frac{1}{2} \sum_{a=1}^{N} \sum_{b=1}^{N} \left(\underline{\mathbf{x}}_a\right)^T \nabla_{\underline{\mathbf{r}}_a} \nabla_{\underline{\mathbf{r}}_b}^T V\left(\underline{\mathbf{x}}_a, \underline{\mathbf{b}}_b, \dots \underline{\mathbf{x}}_N\right)\Big|_{\substack{\underline{\mathbf{x}}_a=0 \\ \underline{\mathbf{x}}_b=0}} \underline{\mathbf{x}}_b \tag{3.37}$$

At this point, we define the Hessian or force constant matrix as:

$$\underline{\underline{\mathbf{H}}}_{a,b} = \nabla_{\underline{\mathbf{r}}_a} \nabla_{\underline{\mathbf{r}}_b}^T V\left(\underline{\mathbf{x}}_a, \underline{\mathbf{b}}_b, \dots \underline{\mathbf{x}}_N\right)\Big|_{\substack{\underline{\mathbf{x}}_a=0 \\ \underline{\mathbf{x}}_b=0}} \tag{3.38}$$

so that:

$$V\left(\underline{\mathbf{r}}_a, \underline{\mathbf{r}}_b, \dots \underline{\mathbf{r}}_N\right) = \frac{1}{2} \sum_{a=1}^{N} \sum_{b=1}^{N} \left(\underline{\mathbf{x}}_a\right)^T \underline{\underline{\mathbf{H}}}_{a,b}\, \underline{\mathbf{x}}_b \tag{3.39}$$

There are N number of Hessian matrices. The matrix elements of each Hessian matrix are calculated as the second derivative of the potential with respect to the displacement of atom a along the ith Cartesian coordinate, and atom b along the j-th Cartesian coordinate.

$$H_{ai,bj} = \frac{\partial^2 V}{\partial x_{ai} \partial x_{bj}}\Big|_{\substack{\underline{\mathbf{x}}_a=0 \\ \underline{\mathbf{x}}_b=0}} \qquad i, j = x, y, z \tag{3.40}$$

The second derivatives are estimated by using finite-difference approximations, in a similar manner as in Eq. 3.3.

The Hessian must first be converted to the equivalent force-constant matrix in *mass-weighted* coordinates. This new matrix is called $\underline{\underline{\mathbf{F}}}_{a,b}$ and reads like:

$$\underline{\underline{\mathbf{F}}}_{a,b} = \underline{\underline{\mathbf{M}}}_{a}^{-1/2}\, \underline{\underline{\mathbf{H}}}_{a,b}\, \underline{\underline{\mathbf{M}}}_{b}^{-1/2} \tag{3.41}$$

where

$$\underline{\underline{\mathbf{M}}}_{a}^{-1/2} = \begin{bmatrix} \frac{1}{\sqrt{m_a}} & 0 & 0 \\ 0 & \frac{1}{\sqrt{m_a}} & 0 \\ 0 & 0 & \frac{1}{\sqrt{m_a}} \end{bmatrix} \tag{3.42}$$

It is necessary to mass weight the force-constant matrix because of the following reason. Say we are modelling the bond between an halogen atom and a deuterium or proton atom, respectively, X−D and X−H. The force constant k_1 and k_2 is roughly the same, to a good approximation. However, the mass of the deuterium is clearly different from the proton, so that the deuterium gives a different motion and a different zero point energy to the X−D compound. Therefore, the masses of the atoms have to be taken into account because a force of a given magnitude will have a different effect upon a larger mass than a smaller one. The use of mass-weighted coordinates takes into account these effects.

We will simplify the notation by dropping the a and b subindices. We then need to obtain the eigenvalues and eigenvectors of $\underline{\underline{\mathbf{F}}}$, being an eigenvector a column matrix, i.e. a vector $\underline{\mathbf{u}}$ such that

$$\underline{\underline{\mathbf{F}}}\, \underline{\mathbf{u}} = \lambda \underline{\mathbf{u}} \tag{3.43}$$

where λ is the associated eigenvalue. The eigenvector problem can be reformulated as follows:

$$\underline{\underline{\mathbf{F}}}\, \underline{\mathbf{u}} = \lambda \underline{\mathbf{u}}\, \underline{\underline{\mathbf{I}}} \Rightarrow \underline{\underline{\mathbf{F}}}\, \underline{\mathbf{u}} - \lambda \underline{\mathbf{u}}\, \underline{\underline{\mathbf{I}}} = 0 \Rightarrow \left(\underline{\underline{\mathbf{F}}} - \lambda \underline{\underline{\mathbf{I}}}\right) \underline{\mathbf{u}} = 0 \tag{3.44}$$

for which the non-trivial solution requires that:

$$\left|\underline{\underline{\mathbf{F}}} - \lambda\underline{\underline{\mathbf{I}}}\right| = 0. \tag{3.45}$$

Expanding the determinant and solving a polynomial in λ is not an efficient way to determine the eigenvalues and eigenvectors of larger matrices. Instead, we will diagonalise the matrix $\underline{\underline{\mathbf{F}}}$, which involves finding a matrix $\underline{\underline{\mathbf{U}}}$ such that:

$$\boxed{\underline{\underline{\mathbf{U}}}^{-\mathbf{1}}\ \underline{\underline{\mathbf{F}}}\ \underline{\underline{\mathbf{U}}} = \underline{\underline{\mathbf{\Lambda}}}} \tag{3.46}$$

where $\underline{\underline{\mathbf{\Lambda}}}$ is the diagonal matrix of eigenvalues and $\underline{\underline{\mathbf{U}}}$ the matrix of eigenvectors.

In a molecule, $\underline{\underline{\mathbf{F}}}$ is always **real** and **symmetric** matrix, as opposed to the periodic system, where this matrix can be complex. The fact that is real means that the eigenvalues and eigenvectors of $\underline{\underline{\mathbf{F}}}$ are always real. In addition, in a molecule the $\underline{\underline{\mathbf{U}}}$ matrix is **orthonormal**, which means that:

a) The eigenvalues are **unit vectors** (i.e. vectors of length 1), and

b) The eigenvalues are **orthogonal** (i.e. the scalar product of all pairs of eigenvectors are zero).

On the contrary, in a periodic system this matrix is unitary (we will see this in Section 3.1.1.3).

Orthogonal matrices satisfy the following relation:

$$\underline{\underline{\mathbf{U}}}^{\mathbf{T}}\ \underline{\underline{\mathbf{U}}} = \underline{\underline{\mathbf{U}}}\ \underline{\underline{\mathbf{U}}}^{\mathbf{T}} = \underline{\underline{\mathbf{I}}} \tag{3.47}$$

Thus, $\underline{\underline{\mathbf{U}}}^{\mathbf{T}} = \underline{\underline{\mathbf{U}}}^{-\mathbf{1}}$. Multiplying Eq. (3.46) by $\underline{\underline{\mathbf{U}}}$ from the left and by $\underline{\underline{\mathbf{U}}}^{-\mathbf{1}}$ from the right, we get:

$$\underline{\underline{\mathbf{U}}}\ \underline{\underline{\mathbf{U}}}^{-\mathbf{1}}\ \underline{\underline{\mathbf{F}}}\ \underline{\underline{\mathbf{U}}}\ \underline{\underline{\mathbf{U}}}^{-\mathbf{1}} = \underline{\underline{\mathbf{U}}}\ \underline{\underline{\mathbf{\Lambda}}}\ \underline{\underline{\mathbf{U}}}^{-\mathbf{1}} \tag{3.48}$$

Since $\underline{\underline{\mathbf{U}}}\ \underline{\underline{\mathbf{U}}}^{-\mathbf{1}} = \underline{\underline{\mathbf{I}}}$:

$$\boxed{\underline{\underline{\mathbf{F}}} = \underline{\underline{\mathbf{U}}}\ \underline{\underline{\mathbf{\Lambda}}}\ \underline{\underline{\mathbf{U}}}^{-\mathbf{1}}} \tag{3.49}$$

We can now write Eq. (3.39) as:

$$\boxed{V\left(\underline{\mathbf{r}}_a, \underline{\mathbf{r}}_b, \dots \underline{\mathbf{r}}_N\right) = \frac{1}{2}\sum_{a=1}^{N}\sum_{b=1}^{N}\left(\underline{\mathbf{x}}_a\right)^T \underline{\underline{\mathbf{U}}}_{a,b}\, \underline{\underline{\mathbf{\Lambda}}}_{a,b}\, \underline{\underline{\mathbf{U}}}^{\mathbf{-1}}_{a,b}\, \underline{\mathbf{x}}_b} \tag{3.50}$$

This equation shines by itself: we have been able to express the potential energy of a system as a function of the eigenvalues and eigenvectors of vibrating atoms.

The frequencies can be obtained from each eigenvalue as:

$$\nu_i = \frac{\sqrt{\lambda_i}}{2\pi} \tag{3.51}$$

3.1.1.3 Periodic system

Extending this formalism to a periodic system, we must consider that in this case the Born-Oppenheimer ground state energy of a crystal is also a well defined function of the equilibrium positions of the $a = 1, 2, \dots N$ nuclei in the reference zero cell. We denote by $\{(\underline{\mathbf{R}}_0)_a\}$ the equilibrium position of all a atoms in the reference zero unit cell. We can write the equilibrium configuration as follows[1]:

$$\mathcal{R}_0 \equiv \{\dots,\ \left[(\underline{\mathbf{R}}_0)_a + \mathbf{g}\right],\ \dots\} \tag{3.52}$$

The translational vector $\mathbf{g}$ was already introduced in Section 2.1.1, accounts for the periodic images of atom a in the neighbour cells, and can be written as:

$$\mathbf{g} = \sum_{m=1}^{3} l_m^g \underline{\mathbf{a}}_m, \tag{3.53}$$

where $\underline{\mathbf{a}}_m$ are the direct lattice vectors and the set of parameters $\{L_m\}$ define the size and shape of the supercell in direct space. For example, if we consider the matrix of lattice vectors of the primitive cell, one possible supercell in which $L_m = 2$ would be the result of multiplying

---

[1] We will denote the translational vector as $\mathbf{g}$ instead of $\underline{\mathbf{g}}$, in order to stick to the standard notation

the matrix of lattice vectors by the matrix 2**I**:

$$\begin{pmatrix} a_{1x} & a_{1y} & a_{1z} \\ a_{2x} & a_{2y} & a_{2z} \\ a_{3x} & a_{3y} & a_{3z} \end{pmatrix} \cdot \begin{pmatrix} 2 & 0 & 0 \\ 0 & 2 & 0 \\ 0 & 0 & 2 \end{pmatrix} = 2 \cdot \begin{pmatrix} a_{1x} & a_{1y} & a_{1z} \\ a_{2x} & a_{2y} & a_{2z} \\ a_{3x} & a_{3y} & a_{3z} \end{pmatrix} \tag{3.54}$$

where the new supercell has double the size of the primitive cell. In this case, there is only one parameter $L_m = 2$ and the integers $l_m^g = 0, 1$. In other words, l_m^g runs from 1 to $L_m - 1$.

By multiplying the matrix of primitive lattice vectors by $2\underline{\underline{\mathbf{I}}}$, we are doubling the three lattice parameters so that the supercell (SC) has the following dimensions: $\left|\underline{\mathbf{a}}_1^{\mathrm{SC}}\right| = 2\left|\underline{\mathbf{a}}_1\right|$, $\left|\underline{\mathbf{a}}_2^{\mathrm{SC}}\right| = 2\left|\underline{\mathbf{a}}_2\right|$ and $\left|\underline{\mathbf{a}}_3^{\mathrm{SC}}\right| = 2\left|\underline{\mathbf{a}}_3\right|$.

If we label as L_n the integer that represents the expansion of the primitive cell in the three directions, we can define the variable L as the variable that defines the size of the supercell:

$$L = \prod_{n=1}^{3} L_n, \tag{3.55}$$

In the previous example, $L_n = 2$, so that $L = 8$ and the size of the supercell is therefore be 8 times bigger than the primitive cell.

When nuclear motion is considered, atoms are displaced by displacement vectors $\underline{\mathbf{x}}_a^{\mathbf{g}}$. Thus, when atoms move, the new configuration $\mathcal{R}$ reads like:

$$\mathcal{R} \equiv \{\ldots,\ [(\underline{\mathbf{R}}_0)_a + \mathbf{g} + \underline{\mathbf{x}}_a^{\mathbf{g}}],\ \ldots\} \tag{3.56}$$

Recalling the derivation of Eq. (3.39):

$$V\left(\underline{\mathbf{r}}_a, \underline{\mathbf{r}}_b, \ldots \underline{\mathbf{r}}_N\right) = \frac{1}{2}\sum_{a=1}^{N}\sum_{b=1}^{N}\left(\underline{\mathbf{x}}_a\right)^T \underline{\underline{\mathbf{H}}}_{a,b}\ \underline{\mathbf{x}}_b \tag{3.39 Previous Section}$$

We can now express $V(\mathcal{R})$ as:

$$\boxed{V(\mathcal{R}) = \frac{L}{2}\sum_{\mathbf{g}}\left(\underline{\mathbf{x}}^{\mathbf{0}}\right)^T \underline{\underline{\mathbf{H}}}^{\mathbf{g}}\ \underline{\mathbf{x}}^{\mathbf{g}}\ +\ \mathcal{O}_3\left(\{\underline{\mathbf{x}}^{\mathbf{g}}\}\right)} \tag{3.57}$$

where we now sum over all the translational **g** vectors, and multiply by L (Eq. 3.55).

For the periodic system we can use the following notation for the Hessian matrix elements:

$$H^{\mathbf{g}}_{ai,bj} = \left(\frac{\partial^2 V}{\partial x^{\mathbf{0}}_{ai} \partial x^{\mathbf{g}}_{bj}} \right) \tag{3.58}$$

where $x^{\mathbf{0}}_{ai}$ represents the displacement of atom a along the i-th Cartesian direction in cell $\mathbf{0}$ (reference cell) and $x^{\mathbf{g}}_{bj}$ represents the displacement of atom b in the $\mathbf{g}$ crystal cell along the j-th Cartesian direction. All the periodic images of atom b in the crystal are displaced in that direction. Indices a and b run from 1 to N, and i and j run from 1 to $3N$. The number of Hessian matrices is equal to L (Eq. 3.55). We will refer to these as the set of Hessian matrices $\{\underline{\underline{\mathbf{H}}}^{\mathbf{g}}\}$.

By neglecting all the $\mathcal{O}_3$ terms, we are still under the formalism of the harmonic approximation.

Like we did in the dimer, we will use a mass-weighted force constant matrix, $\underline{\underline{\mathbf{F}}}$: However, in a periodic system, we need to account for the translational symmetry, and use Bloch functions (Section 2.2.7). Instead of using $\underline{\underline{\mathbf{F}}}$ matrices, we will use $\underline{\underline{\mathbf{W}}}^{\mathbf{k}}$ matrices, called dynamical matrices, and summing over all vectors $\mathbf{g}$ we get:

$$\underline{\underline{\mathbf{W}}}^{\mathbf{k}} = \sum_{\mathbf{g}=1}^{L} \underline{\underline{\mathbf{M}}}^{-\frac{1}{2}}\ \underline{\underline{\mathbf{H}}}^{\mathbf{g}}\ \underline{\underline{\mathbf{M}}}^{-\frac{1}{2}} \exp\left(i\mathbf{k}\cdot\mathbf{g}\right) \tag{3.59}$$

There is a set of L dynamical matrices $\{\underline{\underline{\mathbf{W}}}^{\mathbf{k}}\}$. Each of these has a wave vector associated:

$$\mathbf{k} = \sum_{n=1}^{3} \sum_{m=0}^{L_n - 1} \left(\frac{\kappa_m}{L_n} \right) \mathbf{b}_n \tag{3.60}$$

where $\mathbf{b}_n$ are the reciprocal lattice vectors and the integers m run from 0 to $L_n - 1$. Since there are L Hessian matrices, therefore there are L number of reciprocal lattice vectors $\mathbf{b}_n$. In our previous example, that SC will contain 8 reciprocal lattice vectors $\mathbf{b}_n$. If we constructed a SC from the matrix $3\mathbf{I}$, the frequencies will be calculated over 27 reciprocal lattice vectors. Similarly, if we used $4\mathbf{I}$, the frequencies will be calculated over 64 reciprocal lattice vectors.

Consequently, we can express Eq. (3.57) as:

$$\boxed{V(\mathcal{R}) = \frac{L}{2} \sum_{\mathbf{g}} \left(\underline{\mathbf{x}}^{\mathbf{0}}\right)^T \underline{\underline{\mathbf{W}}}^{\mathbf{k}}\ \underline{\mathbf{x}}^{\mathbf{g}}\ + \mathcal{O}_3\left(\{\underline{\mathbf{x}}^{\mathbf{g}}\}\right)} \tag{3.61}$$

As has been explained in the previously, $\underline{\underline{\mathbf{F}}}$ is a real matrix. However, in a periodic system, $\underline{\underline{\mathbf{W}}}^{\mathbf{k}}$ is a **complex** matrix, meaning that some eigenvalues and eigenvectors are complex. Thus, the diagonalisation is reformulated as:

$$\boxed{\left(\underline{\underline{\mathbf{U}}}^{\mathbf{k}}\right)^{\dagger} \underline{\underline{\mathbf{W}}}^{\mathbf{k}} \; \underline{\underline{\mathbf{U}}}^{\mathbf{k}} = \underline{\underline{\mathbf{\Lambda}}}^{\mathbf{k}}} \tag{3.62}$$

where $\underline{\underline{\mathbf{U}}}^{\mathbf{k}}$ is the matrix of eigenvectors, and has complex entries. $\left(\underline{\underline{\mathbf{U}}}^{\mathbf{k}}\right)^{\dagger}$ is the complex conjugate of the transpose of $\underline{\underline{\mathbf{U}}}^{\mathbf{k}}$, which means that for a given $\underline{\underline{\mathbf{U}}}^{\mathbf{k}}$, we take the transpose of this matrix, $\left(\underline{\underline{\mathbf{U}}}^{\mathbf{k}}\right)^{T}$, and then we take the complex conjugate of each entry.

$\underline{\underline{\mathbf{U}}}^{\mathbf{k}}$ is a **unitary** matrix, meaning that its conjugate transpose $\left(\underline{\underline{\mathbf{U}}}^{\mathbf{k}}\right)^{\dagger}$ satisfies:

$$\left(\underline{\underline{\mathbf{U}}}^{\mathbf{k}}\right)^{\dagger} \; \underline{\underline{\mathbf{U}}}^{\mathbf{k}} = \underline{\underline{\mathbf{U}}}^{\mathbf{k}} \; \left(\underline{\underline{\mathbf{U}}}^{\mathbf{k}}\right)^{\dagger} = \underline{\underline{\mathbf{I}}} \tag{3.63}$$

Since $\left(\underline{\underline{\mathbf{U}}}^{\mathbf{k}}\right)^{-1} \underline{\underline{\mathbf{U}}}^{\mathbf{k}} = \underline{\underline{\mathbf{I}}}$, thus,

$$\left(\underline{\underline{\mathbf{U}}}^{\mathbf{k}}\right)^{-1} = \left(\underline{\underline{\mathbf{U}}}^{\mathbf{k}}\right)^{\dagger} \tag{3.64}$$

Multiplying Eq. (3.62) by $\left(\left(\underline{\underline{\mathbf{U}}}^{\mathbf{k}}\right)^{\dagger}\right)^{-1}$ from the left and by $\left(\underline{\underline{\mathbf{U}}}^{\mathbf{k}}\right)^{-1}$ from the right, we get:

$$\left(\left(\underline{\underline{\mathbf{U}}}^{\mathbf{k}}\right)^{\dagger}\right)^{-1} \left(\underline{\underline{\mathbf{U}}}^{\mathbf{k}}\right)^{\dagger} \underline{\underline{\mathbf{W}}}^{\mathbf{k}} \; \underline{\underline{\mathbf{U}}}^{\mathbf{k}} \; \left(\underline{\underline{\mathbf{U}}}^{\mathbf{k}}\right)^{-1} = \left(\left(\underline{\underline{\mathbf{U}}}^{\mathbf{k}}\right)^{\dagger}\right)^{-1} \underline{\underline{\mathbf{\Lambda}}}^{\mathbf{k}} \; \left(\underline{\underline{\mathbf{U}}}^{\mathbf{k}}\right)^{-1} \tag{3.65}$$

Since $\left(\left(\underline{\underline{\mathbf{U}}}^{\mathbf{k}}\right)^{\dagger}\right)^{-1} \left(\underline{\underline{\mathbf{U}}}^{\mathbf{k}}\right)^{\dagger} = \underline{\underline{\mathbf{I}}}$ and $\underline{\underline{\mathbf{U}}}^{\mathbf{k}} \; \left(\underline{\underline{\mathbf{U}}}^{\mathbf{k}}\right)^{-1} = \underline{\underline{\mathbf{I}}}$:

$$\underline{\underline{\mathbf{W}}}^{\mathbf{k}} = \left(\left(\underline{\underline{\mathbf{U}}}^{\mathbf{k}}\right)^{\dagger}\right)^{-1} \underline{\underline{\mathbf{\Lambda}}}^{\mathbf{k}} \; \left(\underline{\underline{\mathbf{U}}}^{\mathbf{k}}\right)^{-1} \tag{3.66}$$

Using Eq. (3.64),

$$\underline{\underline{\mathbf{W}}}^{\mathbf{k}} = \left(\left(\underline{\underline{\mathbf{U}}}^{\mathbf{k}}\right)^{-1}\right)^{-1} \underline{\underline{\mathbf{\Lambda}}}^{\mathbf{k}} \; \left(\underline{\underline{\mathbf{U}}}^{\mathbf{k}}\right)^{-1} \tag{3.67}$$

So that:

$$\boxed{\underline{\underline{\mathbf{W}}}^{\mathbf{k}} = \underline{\underline{\mathbf{U}}}^{\mathbf{k}} \; \underline{\underline{\mathbf{\Lambda}}}^{\mathbf{k}} \; \left(\underline{\underline{\mathbf{U}}}^{\mathbf{k}}\right)^{\dagger}} \tag{3.68}$$

We can now write Eq. (3.61) as:

$$\boxed{\boxed{V(\mathcal{R}) = \frac{L}{2} \sum_{\mathbf{g}} \left(\underline{\mathbf{x}}^{\mathbf{0}}\right)^{T} \underline{\underline{\mathbf{U}}}^{\mathbf{k}} \; \underline{\underline{\mathbf{\Lambda}}}^{\mathbf{k}} \; \left(\underline{\underline{\mathbf{U}}}^{\mathbf{k}}\right)^{\dagger} \underline{\mathbf{x}}^{\mathbf{g}} \; + \mathcal{O}_3\left(\{\underline{\mathbf{x}}^{\mathbf{g}}\}\right)}} \tag{3.69}$$

As happened with the molecule, we have been able to elegantly express the potential energy of a periodic system as a function of the eigenvalues and eigenvectors of vibrating atoms.

3.1.1.4 Deficencies of the Harmonic approximation

The harmonic approximation presents serious limitations, that arise from the fact that only constant volume quantities can be calculated, so that thermal expansion cannot be explained [75, 76]. In this respect, an effective technique, although computationally expensive, is *ab initio* molecular dynamics [33, 34, 35], which takes into account the simultaneous effect of both temperature and pressure, and intrinsically accounts for anharmonicity. Simpler and less computationally expensive, but still effective techniques can be used based on the so called quasi-harmonic approximation (QHA), which corrects the HA deficiencies, and is described herein.

3.1.2 Framework of the Quasi-Harmonic Approximation

Let's recall the equations derived in the previous sections:

$$dE = TdS - PdV \qquad \text{(Eq. 2.159 from Section 2.3.3)}$$

$$E = F + TS \qquad \text{(Eq. 2.265 from Section 2.5.4)}$$

By differentiating $F = E - TS$ from Eq. 2.265,

$$dF = dE - TdS - SdT \tag{3.70}$$

Plugging in Eq. 2.159, we get:

$$dF = -PdV - SdT \tag{3.71}$$

So that the pressure is defined as:

$$P = -\left(\frac{\partial F}{\partial V}\right)_T \tag{3.72}$$

If we recall Eq. 2.253:

$$F = E_{\text{static}} + \frac{1}{2}\sum_{i,\mathbf{k}} h\nu_{i,\mathbf{k}} + k_B T \sum_{i,\mathbf{k}} \ln\left[1 - \exp\left(-\frac{h\nu_{i,\mathbf{k}}}{k_B T}\right)\right] \qquad \text{(2.253 Previous Chapter)}$$

The quasi-harmonic approximation corrects the HA deficiencies by maintaining the same harmonic expression [77]:

$$F(T) = E_{\text{static}} + E_{ZP} + \mathcal{E}(T) - TS(T), \tag{3.73}$$

but introducing an explicit dependence of both the electronic energy and the vibration phonon frequencies on volume [78, 79]:

$$F(V,T) = E_{\text{static}}(V) + E_{ZP}(V) + \mathcal{E}(V,T) - TS(V,T). \tag{3.74}$$

For the sake of simplicity, from now on the subindex "static" will be dropped, so that:

$$F(V,T) = E(V) + E_{ZP}(V) + \mathcal{E}(V,T) - TS(V,T). \tag{3.75}$$

where $E_{ZP}(V)$, $\mathcal{E}(V,T)$ and $S(V,T)$ are the same expressions derived in Eqns. 2.254, 2.258 and 2.256, but introducing the dependence on the volume and temperature:

$$E_{ZP}(V) = \frac{h}{2}\sum_{i,\mathbf{k}} \nu_{i,\mathbf{k}}(V) \tag{3.76}$$

$$\mathcal{E}(V,T) = \sum_{i,\mathbf{k}} \frac{h\nu_{i,\mathbf{k}}(V)}{\exp\left(\frac{h\nu_{i,\mathbf{k}}(V)}{k_B T}\right) - 1} \tag{3.77}$$

$$S(V,T) = -k_B \sum_{i,\mathbf{k}} \ln\left[1 - \exp\left(\frac{-h\nu_{i,\mathbf{k}}(V)}{k_B T}\right)\right] + \frac{1}{T}\mathcal{E}(V,T). \tag{3.78}$$

It is quite reasonable to think that a better description of the system is obtained when considering that the electronic energy depends on the volume constraint of the cell. In addition, E is to be regarded a well known function of V (by a fit to a cubic polynomial or any of the generally-purposed equation of state, such as the Birch-Murnaghan [71]).Regarding the vibrations, it is reasonable to think that these are affected by the volume constraint, i.e. for a compressed volume, atoms have less room to move, so that frequencies become higher. On the contrary, for expanded volumes, phonons get softer. By casting Eqns. 3.77 and 3.78 into Eq. 2.253, one gets the following expression for the Helmholtz free energy:

$$F(V,T) = E(V) + E_{ZP}(V) + k_B T \sum_{i,\mathbf{k}} \ln\left[1 - \exp\left(\frac{-h\nu_{i,\mathbf{k}}(V)}{k_B T}\right)\right]. \tag{3.79}$$

differentiation of Eq. (3.79) yields the pressure-volume relation at a finite temperature.

$$P(V,T) = -\left(\frac{\partial F(V,T)}{\partial V}\right)_T \tag{3.80}$$

$$= -\frac{\partial E(V)}{\partial V} - \frac{h}{2}\frac{\partial}{\partial V}\left[\sum_{i,\mathbf{k}} \nu_{i,\mathbf{k}}(V)\right] - k_B T \frac{\partial}{\partial V}\left\{\sum_{i,\mathbf{k}} \ln\left[1 - \exp\left(\frac{-h\nu_{i,\mathbf{k}}(V)}{k_B T}\right)\right]\right\} \tag{3.81}$$

The pressure at $T = 0$ K (athermal limit) considering zero-point motion, is just:

$$P(V, T = 0\text{ K, considering zero-point motion}) = -\frac{\partial E(V)}{\partial V} - \frac{h}{2}\frac{\partial}{\partial V}\left[\sum_{i,\mathbf{k}} \nu_{i,\mathbf{k}}(V)\right] \tag{3.82}$$

By neglecting zero-point energy, we get:

$$P(V, T = 0\text{ K, neglecting zero-point motion}) = -\frac{\partial E(V)}{\partial V} \tag{3.83}$$

The derivative over the neperian logarithm from Eq. 3.79 reads like:

$$\begin{aligned}\frac{\partial}{\partial V}\left\{\sum_{i,\mathbf{k}} \ln\left[1 - \exp\left(\frac{-h\nu_{i,\mathbf{k}}(V)}{k_B T}\right)\right]\right\} &= \frac{1}{1 - \exp\left(\frac{-h\nu_{i,\mathbf{k}}(V)}{k_B T}\right)} \frac{\partial}{\partial V}\left[1 - \exp\left(\frac{-h\nu_{i,\mathbf{k}}(V)}{k_B T}\right)\right] \\ &= \frac{\exp\left(\frac{-h\nu_{i,\mathbf{k}}(V)}{k_B T}\right)}{1 - \exp\left(\frac{-h\nu_{i,\mathbf{k}}(V)}{k_B T}\right)} \frac{h}{k_B T} \frac{\partial \nu_{i,\mathbf{k}}(V)}{\partial V}\end{aligned} \tag{3.84}$$

Casting Eq 3.84 into Eq. 3.80, we can obtain the pressure at finite temperature (finite pressure), as a function of the vibrations:

$$\boxed{P(V,T) = -\frac{\partial E(V)}{\partial V} - \sum_{i,\mathbf{k}} \left[\frac{1}{2} + \frac{1}{\exp\left(\frac{h\nu_{i,\mathbf{k}}(V)}{k_B T}\right) - 1}\right] h \frac{\partial \nu_{i,\mathbf{k}}(V)}{\partial V}} \tag{3.85}$$

$\nu_{i,\mathbf{k}}(V)$ is a known function of volume, where a polynomial of degree 2 is generally good approximation:

$$\nu_{i,\mathbf{k}}(V) = c_{i,\mathbf{k}}V^2 + d_{i,\mathbf{k}}V + f_{i,\mathbf{k}} \tag{3.86}$$

so that:

$$\frac{\partial \nu_{i,\mathbf{k}}(V)}{\partial V} = 2c_{i,\mathbf{k}}V + d_{i,\mathbf{k}} \tag{3.87}$$

Eq. 3.85 provides the requisite relation between P, V and T. It is often convenient to introduce, instead of the derivatives of the frequencies, the dimensionless quantities $\gamma_{i,\mathbf{k}}$ called Grüneisen parameters:

$$\gamma_{i,\mathbf{k}} = -\frac{\partial \ln \nu_{i,\mathbf{k}}(V)}{\partial \ln V} = -V\frac{1}{\nu_{i,\mathbf{k}}(V)}\frac{\partial \nu_{i,\mathbf{k}}(V)}{\partial V} \tag{3.88}$$

At this level, the Gibbs free energy can be calculated:

$$G(V,T) = E(V) + E_{ZP}(V) + \mathcal{E}(V,T) - TS(V,T) + P(V,T)V(T) \tag{3.89}$$

$$= F(V,T) + P(V,T)V(T) \tag{3.90}$$

It is more convenient to work in terms of G as a function of P and T so that at this point all these properties become as a function of pressure and no longer volume:

$$G(P,T) = E(P) + E_{ZP}(P) + \mathcal{E}(P,T) - TS(P,T) + P(T)V(P,T) \tag{3.91}$$

$$= F(P,T) + P(T)V(P,T) \tag{3.92}$$

The pressure of transition between two phases at a finite temperature occurs when the following condition is satisfied:

$$G^{I}(P;T) = G^{II}(P;T) \tag{3.93}$$

For the case of 0 K, the Gibbs free energy is reduced to the enthalpy:

$$H(P) = E(P) + E_{ZP}(P) + PV(P), \tag{3.94}$$

and the pressure is

$$P(V) = -\frac{\partial(E(V) + E_{ZP}(V))}{\partial V}. \tag{3.95}$$

For the specific case of the athermal limit without considering zero point motion, the enthalpy is just

$$H(P) = E(P) + PV(P), \tag{3.96}$$

so that the pressure is

$$P(V) = -\frac{\partial E(V)}{\partial V}. \tag{3.97}$$

In both cases the pressure of transition is obtained when $H^{I}(P) = H^{II}(P)$.

3.1.3 Deficiencies of the quasi-harmonic approximation

The QHA allows to study the combined effect of temperature and pressure on materials. This represents an advantage respect to the HA. However, there is still one deficiency not solved by the QHA, and is the fact that we are considering independent harmonic oscillators, which is a simplification, because in nature all vibrations are coupled to each other, e.g. normal mode $i = 1$ affects the vibration of normal mode $i = 2$. If higher order terms are considered in the Taylor expansion, then the vibrations are no longer treated as independent harmonic oscillators, but coupled oscillations. Including higher order terms means considering anharmonic effects, which requires the calculation of phonon-phonon interaction coefficients with techniques such as Vibrational Configuration Interaction (VCI), Vibrational Self-Consistent-Field (VSCF), Vibrational Perturbation Theory (VPT), Transition Optimized Shifted Hermite (TOSH), calculation of higher order interatomic force constants, etc [80, 81, 82, 83, 84, 85]. These calculations are computationally demanding for large systems.

3.2 Distortion of the geometry along a soft phonon mode

In the course of this PhD we have encountered, for some expanded or compressed volumes, negative eigenvalues λ_i, and therefore imaginary frequencies ν_i. From now on the terms "imaginary frequency" and "negative frequency" are used interchangeably throughout this thesis. These are often referred to as soft phonon modes in a periodic system. This means that we are in a transition state, and a phase transition can occur. An example occurs in calcite I when compressed. A soft phonon mode appears at a finite **k** point (details about this phase transition will be given in Chapter 7). In these situations it is very useful to distort the atomic positions along the normal mode coordinate responsible for this imaginary frequency. This provides the natural way of breaking symmetry and induce the correct structural changes for the phase transition to occur. An energy scan along this normal coordinate is shown in Fig. 3.3. The two minima are equivalent to each other, arise from a positive and negative normal mode displacement, and correspond to the distortion that yields to the calcite II structure.

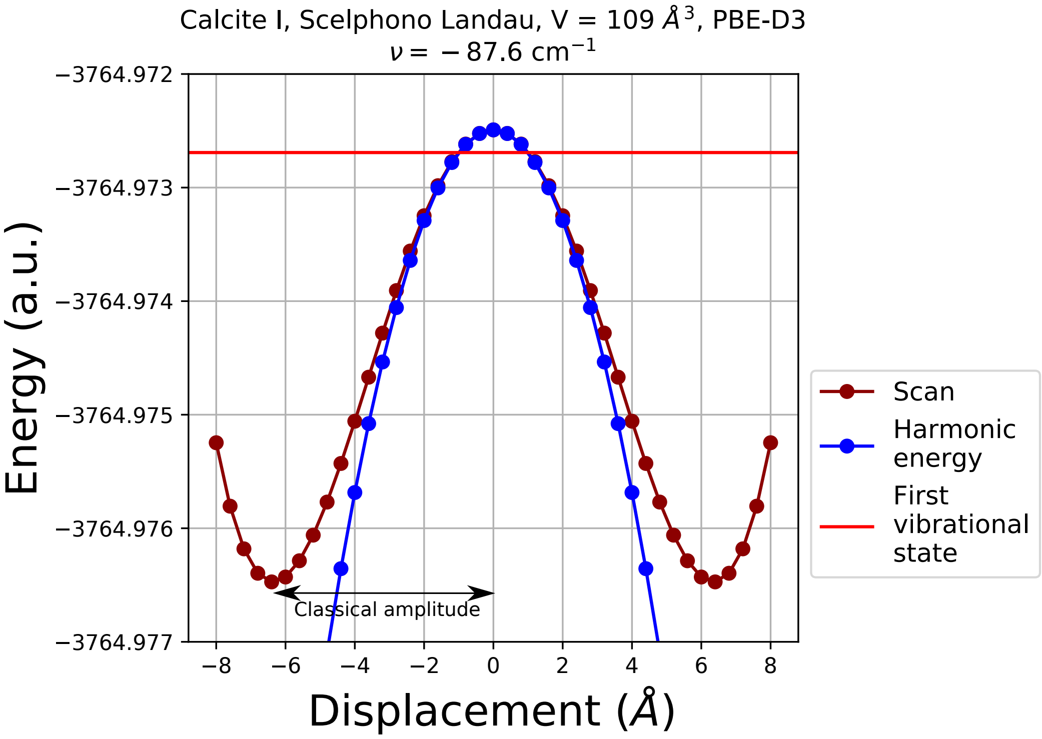

Figure 3.3: Brown circles: energy scan along the soft phonon mode of frequency -87.6 cm^{-1} observed in the calcite I structure for a percentage of compression corresponding to 15% using the PBE-D3 level of theory. A symmetric double well potential is observed (for more details refer to text).

There is available a feature on CRYSTAL named `SCANMODE` that performs this energy scan. Say $|r_0\rangle$ is the equilibrium configuration, then the following $|r_i\rangle$ configurations are explored through this routine:

$$|r_i\rangle = |r_0\rangle + \underbrace{i \underbrace{\Delta}_{\texttt{STEP}}}_{\texttt{DISPLACEMENT}} \underbrace{|u\rangle}_{\text{eigenvector}} \tag{3.98}$$

where $|u\rangle$ is the eigenvector of the selected mode and Δ is the step. This step is chosen in the variable `STEP`, as well as two more variables: `INI` and `IFI`, the initial and final points of the scan. i is a positive or negative integer, that runs from `INI` to `IFI`.

For example, the calculation `INI=-10`; `IFI=10`; `STEP=0.4` will be computing, in a step of 0.4 Å, `IFI - INI` $= 10 - (-10) = 20$ configurations, where $i = \pm 1, \pm 2, \pm 3 \cdots \pm 10$:

$$\begin{array}{ll}
i = 1 \Rightarrow |r_1\rangle = |r_0\rangle + 0.4\ |u\rangle & i = -1 \Rightarrow |r_1\rangle = |r_0\rangle - 0.4\ |u\rangle \\
i = 2 \Rightarrow |r_2\rangle = |r_0\rangle + 0.8\ |u\rangle & i = -2 \Rightarrow |r_2\rangle = |r_0\rangle - 0.8\ |u\rangle \\
i = 3 \Rightarrow |r_3\rangle = |r_0\rangle + 1.2\ |u\rangle & i = -3 \Rightarrow |r_3\rangle = |r_0\rangle - 1.2\ |u\rangle \\
i = 4 \Rightarrow |r_4\rangle = |r_0\rangle + 1.6\ |u\rangle & i = -4 \Rightarrow |r_4\rangle = |r_0\rangle - 1.6\ |u\rangle \\
i = 5 \Rightarrow |r_5\rangle = |r_0\rangle + 2.0\ |u\rangle & i = -5 \Rightarrow |r_5\rangle = |r_0\rangle - 2.0\ |u\rangle \\
i = 6 \Rightarrow |r_6\rangle = |r_0\rangle + 2.4\ |u\rangle & i = -6 \Rightarrow |r_6\rangle = |r_0\rangle - 2.4\ |u\rangle \\
i = 7 \Rightarrow |r_7\rangle = |r_0\rangle + 2.8\ |u\rangle & i = -7 \Rightarrow |r_7\rangle = |r_0\rangle - 2.8\ |u\rangle \\
i = 8 \Rightarrow |r_8\rangle = |r_0\rangle + 3.2\ |u\rangle & i = -8 \Rightarrow |r_8\rangle = |r_0\rangle - 3.2\ |u\rangle \\
i = 9 \Rightarrow |r_9\rangle = |r_0\rangle + 3.6\ |u\rangle & i = -9 \Rightarrow |r_9\rangle = |r_0\rangle - 3.6\ |u\rangle \\
i = 10 \Rightarrow |r_{10}\rangle = |r_0\rangle + 4.0\ |u\rangle & i = -10 \Rightarrow |r_{10}\rangle = |r_0\rangle - 4.0\ |u\rangle
\end{array}$$

All 20 $|r_i\rangle$ configurations in this case would arise from 20 displacements of the atoms along the selected eigenvector. We will denote the product $i\,\Delta$ as `DISPLACEMENT`, which is the x axis in Fig. 3.3. In this figure, we can distinguish:

a) The brown circles represent the DFT energy over all the 20 $|r_i\rangle$ displacements shown in the above list.

b) The blue circles represent the harmonic energy of all these displacements over the selected negative mode. After all the previous derivation, it may be evident now that these points are calculated using the equation derived previously:

$$\boxed{V(\mathcal{R}) = \frac{L}{2} \sum_{\mathbf{g}} \left(\underline{\mathbf{x}}^{\mathbf{0}}\right)^T \underline{\underline{\mathbf{U}}}^{\mathbf{k}} \ \underline{\underline{\mathbf{\Lambda}}}^{\mathbf{k}} \ \left(\underline{\underline{\mathbf{U}}}^{\mathbf{k}}\right)^{\dagger} \underline{\mathbf{x}}^{\mathbf{g}} \ + \mathcal{O}_3\left(\{\underline{\mathbf{x}}^{\mathbf{g}}\}\right)} \qquad \text{(3.69 Previous Section)}$$

In this case, the matrix $\underline{\underline{\mathbf{\Lambda}}}^{\mathbf{k}}$ only contains one eigenvalue, the one that is scanned. Because it is negative, the resulting parabola is inverted. Similarly, the matrix $\underline{\underline{\mathbf{U}}}^{\mathbf{k}}$ only contains one eigenvector.

c) The horizontal red line represents the first vibrational state of this scanned mode, i.e. $\left(0 + \frac{1}{2}\right) h\nu$ (note that the y-axis is the energy of the crystal).

d) The classical amplitude of an harmonic oscillator is indicated. This is the amplitude of displacement introduced in Section 3.1.1.1 as the variable a (Eq. 3.34).

Chapter 4

The polymorphism of the calcite system

In this section we will describe the structure of most of the polymorphs in some detail. In Fig. 4.1 we have assembled the stability data for all the phases to produce a temperature-pressure phase diagram. The most stable phase of calcite at ambient conditions is calcite I. Under these conditions, aragonite and vaterite are metastable polymorphs of calcite I. In solution, the pH is the most important factor that affects the preference of precipitation between calcite I, aragonite and vaterite [86]. However, the influence of this factor is still unclear: while some authors have obtained pure vaterite at pH between 9.3 and 9.9[87], others have shown that pH lower than 9 results in an increase of supersaturation and nuclei formation, improving vaterite crystal growth [88].

Chemical control of phase stability beyond just pH, has been demonstrated as well. For instance, in several experiments it has been observed the deposition of an amorphous calcium carbonate phase when calcium chloride and sodium carbonate salt solutions are mixed [89, 90]. This amorphous phase rapidly transforms to vaterite within minutes. If vaterite remains in contact with the solution, it transforms to calcite I within one day. If kept dry, vaterite is metastable at temperatures up to 670 K [91].

Vaterite is an important ingredient of Portland cement [6] and has been found in gallstones [92] and in oil field drills [6]. As a biomaterial, vaterite can be found in very low proportion in green turtle eggshells [93], coho salmon otoliths [94], freshwater lackluster pearls [95], and

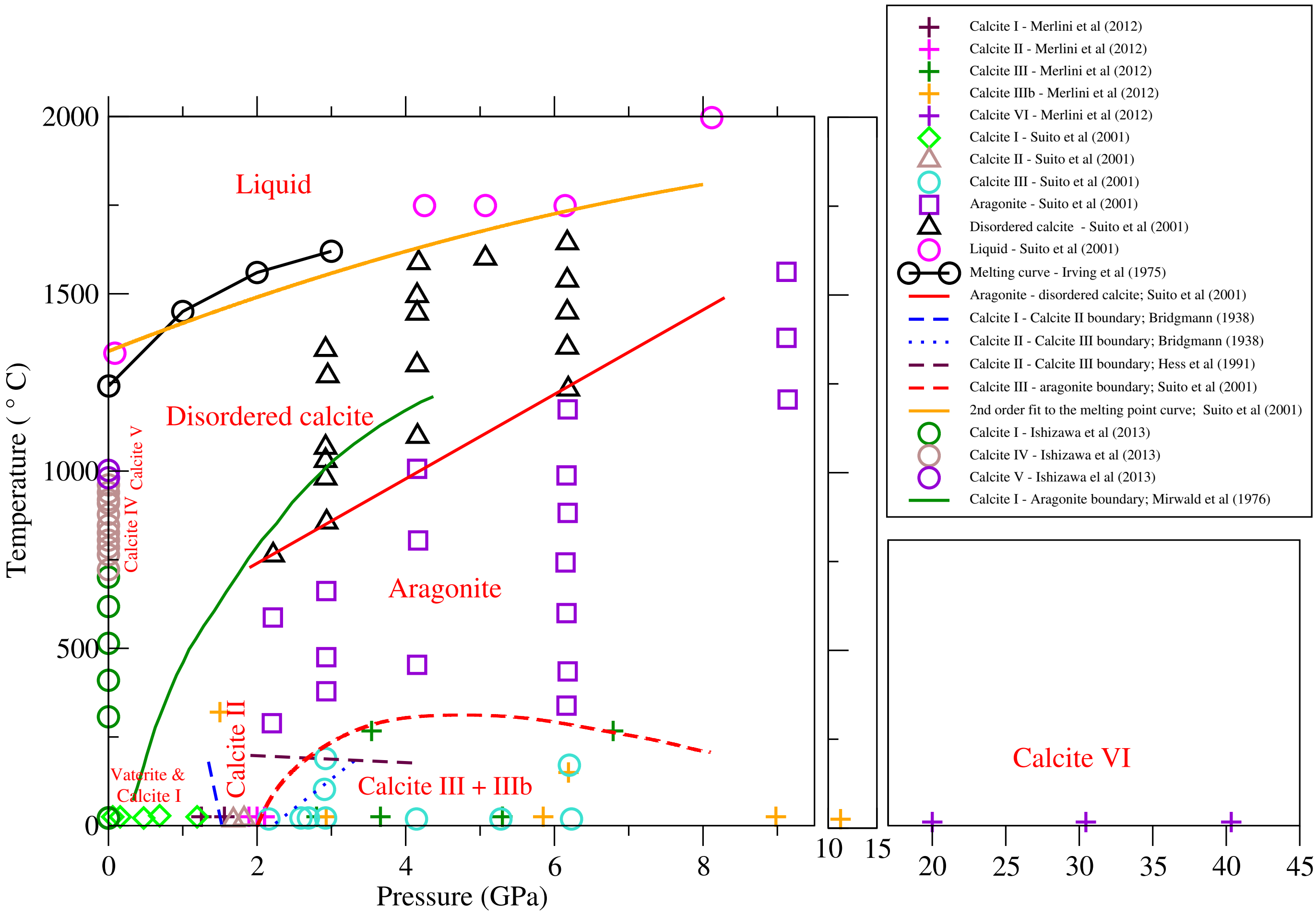

Figure 4.1: Experimental phase diagram of $CaCO_3$ gathering all the available information so far for this material.

in the aberrant growth of mollusk shells repaired after an injury [96]. Vaterite can also be found as the only mineral component in the endoskeleton of the body and tunic spicules of the solitary stolidobranch ascidian *Herdmania momus* [97]. Recent investigations suggest that the nucleation of calcium carbonate does not proceed accordingly to classical nucleation theory and a more complex pathway is involved in the process [30, 31]. As a consequence, in the last few years there has been an increasing interest in vaterite, since it is the metastable phase that appears in the mechanism of nucleation of calcium carbonate. The existence of vaterite in a wide range of biominerals suggests biological control of the nucleation mechanism. Therefore, the study of its initial nucleation and growth offer an opportunity not only to better understand the crystal nucleation and growth of calcium carbonate [98, 99], but also the mechanism of biomineralization. However, it is rather difficult to make further progress in understanding the growth and nucleation because its crystal structure is still controversial, and a matter of ongoing debate [100]. On the other hand, this is a great challenge. Its structure has stymied scientists for over almost a century, and many authors have proposed very different interpretations [101, 102, 103, 104, 105, 106, 94, 107, 108, 97, 90, 100, 109, 110, 111], which will be described in Section 4.3.

Recently, there has been interest in the behaviour and properties of $CaCO_3$ above 1.7 GPa as a potential geological carbon storage pathway. Research in this field is aimed at understanding the carbon cycle on Earth [112]. At ambient temperature and by applying pressure, calcite I evolves from a highly symmetric structure ($R\overline{3}c$) to lower symmetric structures: calcite II (monoclinic), calcite III and calcite VI (both triclinic). In 1938 Bridgman first identified Calcite II and III by applying volumetric measurements [113]. In that study, the calcite I - calcite II and calcite II - calcite III phase boundaries were described. These corresponds, respectively, to the negatively and positively sloped curves shown in Fig. 4.1 with blue dashed lines.

Calcite II and III appear within the accepted stability field of aragonite. They have larger molar volumes and are considered to be metastable with respect to aragonite [114]. On the low temperature (300 to 600 K) and high-pressure side of the phase diagram (Fig. 4.1), aragonite transforms to calcite II and calcite III [113, 115, 116, 114, 117].

As can be seen in Fig. 4.1, the calcite III-aragonite boundary is curved: from 2 to 4.5 GPa, the transition temperature increases with pressure, and from 4.5 GPa, the transition temperature decreases with increasing pressure [12]. One possible interpretation for this bowed boundary could be the fact that there is a change in the transition, from first to second order [118]. According to Suito *et al.* [12], there is no thermodynamic evidence that supports this hypothesis. However, Hess's *et al.* [119] negatively sloped boundary , combined with the already mentioned Bridgman's positively sloped boundary is the best explanation for this bowed behaviour, even though these two boundaries do not meet exactly at the maximum of the curve.

For the last 40 years calcite III has been extensively studied [115, 120, 121, 122, 12, 123], but the determination of its structure has generated considerable controversy. In 2012, Merlini *et al.* first characterized calcite III using single-crystal synchrotron X-ray diffraction [17]. At ambient temperature, they observed this phase above 2.5 GPa and up to 15 GPa, a pressure range that corresponds to that in the upper mantle (Fig. 1.1b). By applying very slow pressure ramps, they revealed a structural modification of calcite III that was named calcite IIIb. This phase is described in more details in the next section.

By performing shock-compression experiments, Tyburczy *et al.* [124] first revealed in 1986 the formation of a denser phase above 15 GPa, named calcite VI. From changes in infrarred spectra, Catalli *et al.* [125] noticed a further phase transition also above 15 GPa. However, it was not until 2012 that this structure was first determined by Merlini *et al.* [17], where high pressure was produced with a membrane type diamond anvil cells (DAC). The authors report that in all these experiments the transitions towards the high pressure polymorphs were reversible, always obtaining calcite I. From this, they concluded that it would be improbable to find these structures directly in nature or as synthetic materials quenched to ambient pressures. However, in 2015 Schaebitz *et al.* [15] found calcite III and calcite IIIb as 50-150 nm sized crystals natural samples several meters from the surface in quaternary loess deposits in Central Asia, characterizing them by TEM. Based on their recent finding, Schaebitz *et al.* [15] suggested that high surface stresses may stabilize the high-pressure phase nanoparticles outside their stability region of bulk phases.

At ambient pressure as upon heating, calcite I undergoes a reversible phase transition to a high-temperature disordered form (space group $R\bar{3}m$) [126, 127, 128, 129, 130] at $\sim$ 967 K (see Fig. 4.1). This phase has been named calcite V. Recent studies by Ishizawa *et al.* [131] over a range of temperatures from 294K to 1275K revealed the following temperature stability field: calcite I (from 294K to 974K), calcite IV (form 995K to 1234K) and calcite V (from 1254K to 1275K). Calcite IV was classified as an intermediate state that bridges phases I and V. The experimental temperature and pressure data at which calcite I, IV and V were observed is shown in Fig. 4.1. These measurements were made in the limited pressure range of 0.1 to 0.44 MPa (more details will be given in the next section). The influence of higher pressures on these phases has yet to be documented.

Suito *et al.* [12] performed three type of experiments for a wide range of pressure and temperature on the stability field of calcite II, III and aragonite: 1) in-situ X-ray diffraction (XRD) using synchrotron radiation to 6 GPa and 1750°C, 2) Raman scattering to 10 GPa at room temperature using a diamond-anvil cell and 3) post-compression XRD on samples retrieved after heat treatment at temperatures to 2000°C and pressures to 9 GPa. These results are displayed in Fig. 4.1. In this study, they described a phase boundary between aragonite and a high temperature "disordered calcite" phase to be a line with a slope of 125 °C/GPa. This "disordered calcite" is just a term to refer to calcite IV and V, due to the orientational disorder of the carbonate groups. Unfortunately these points were presented as a whole set and were not classified into calcite IV or V.

At higher temperatures calcite melts. Irving *et al.* [132] were the first to determine the melting point curve up to 3.6 GPa from the texture of quenched samples. Suito *et al.* [12] reported a melting curve to be T_m (°C)$= 1338 + 82P - 2.9P^2$ (P in GPa) up to 6 GPa. An extrapolation of that curve to 8 GPa gives a T_m of 1800°C, just 200°C less than the minimum temperature required for the synthesis of diamond using $CaCO_3$ as a catalyst.

In the following sections, the structure of each of the polymorphs will be described.

4.1 Calcite I

Calcite I is the most studied polymorph throughout this PhD project, and its careful study and understanding of the structure sets the basis for any other phase transition observed in $CaCO_3$.

4.1.1 The direct lattice

Calcite I has a structure that belongs to the Trigonal Crystal. The periodicity of the structure is represented most efficiently in a rhombohedral (primitive) cell ($a = b = c$ and $\alpha = \beta = \gamma \neq 90°$, Fig. 4.2b), but the symmetry of the structure is revealed best by an hexagonal (conventional) cell ($a = b \neq c$ and $\alpha = \beta = 90°$ and $\gamma = 120°$, Fig. 4.2a).

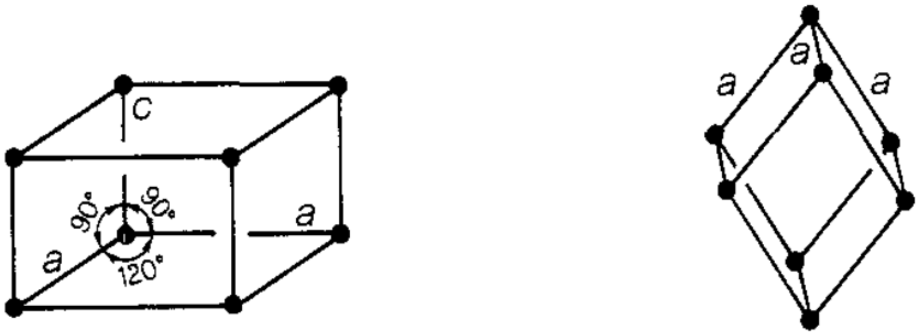

(a) **(b)**

Figure 4.2: (4.2a) Hexagonal cell. (4.2b) rhombohedral cell

The hexagonal cell has three times the volume of the rhombohedral cell (the so called "triple hexagonal representation") as shown in Figure 4.3. Calcite I belongs to the space group $R\bar{3}c$, which in the international tables for crystallography is the 167th space group.

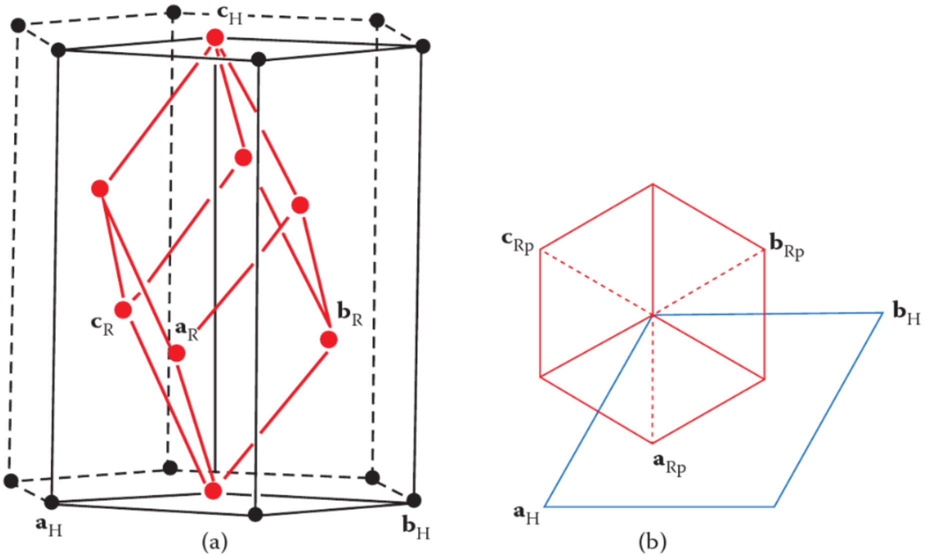

Figure 4.3: (a): The basis of the rhombohedral cell is labelled as $\mathbf{a_R}$, $\mathbf{b_R}$ and $\mathbf{c_R}$. (b): Projection along $\mathbf{c_H}$. The basis of the hexagonal centered cell is labelled as $\mathbf{a_H}$, $\mathbf{b_H}$ and $\mathbf{c_H}$.

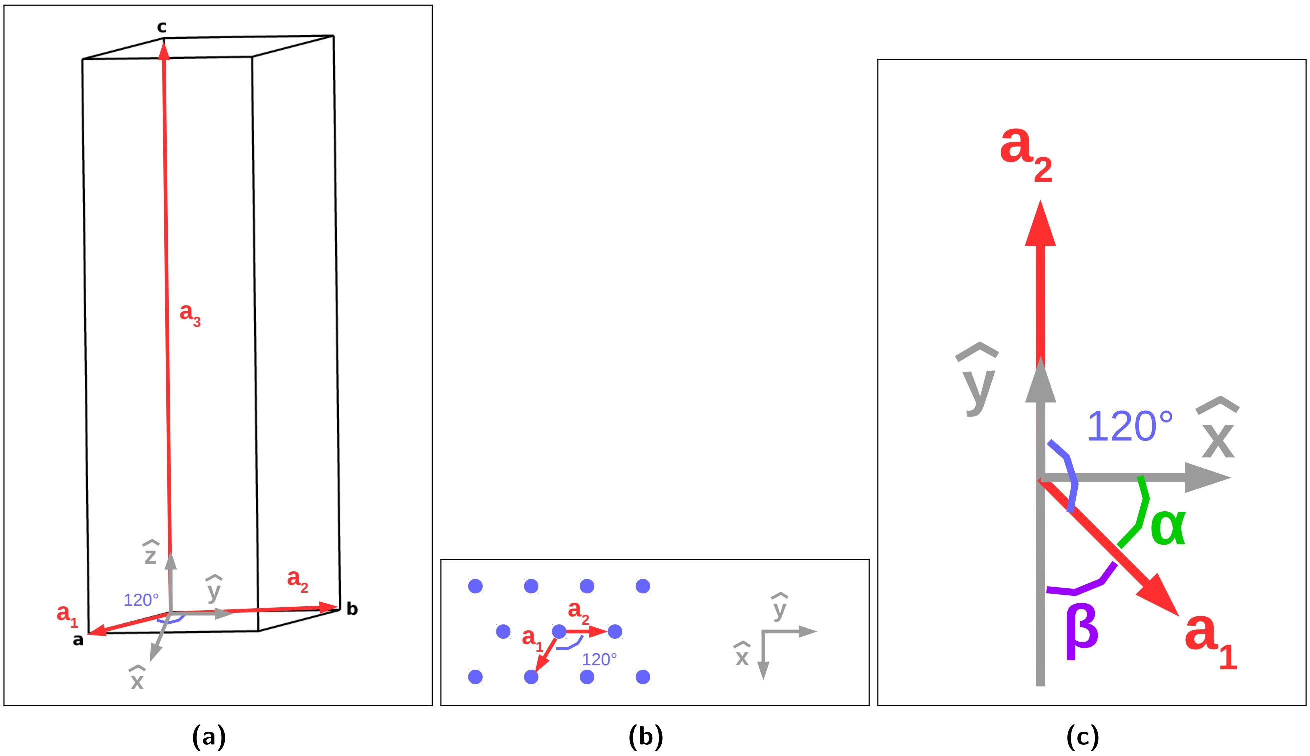

(a) (b) (c)

Figure 4.4: Different projections of an hexagonal Bravais Lattice: 4.6a: three-dimensional projection, where the vectors $\mathbf{a}_1$, $\mathbf{a}_2$, $\mathbf{a}_3$ are shown, as well as the unitary vectors $\hat{x}, \hat{y}$ and $\hat{z}$. 6.4e and 4.4c: two-dimensional representation. The unitary vector $\hat{y}$ and $\hat{z}$ coincide with the $\mathbf{a}_2$ and $\mathbf{a}_3$ vectors respectively. The $\mathbf{a}_1$ vector is at an angle of α with respect to $\hat{x}$, and at an angle of β with respect to $-\hat{y}$

We will describe the hexagonal Bravais Lattice using three lattice vectors: $\mathbf{a}_1$, $\mathbf{a}_2$, $\mathbf{a}_3$, as shown in Fig. 4.4. By using the geometric relations shown on Fig. 4.4c, each lattice vector $\mathbf{a}_i$ and its module $|\mathbf{a}_i|$ can be easily obtained:

$$\begin{aligned}
\mathbf{a}_1 &= a_{1x} \cdot \hat{x} + a_{1y} \cdot (-)\hat{y} + \cancelto{0}{a_{1z}} \cdot \hat{z} \\
&= a_{1x} \cdot \hat{x} - a_{1y} \cdot \hat{y} \\
&= a\cos(\alpha = 30)\,\hat{x} - a\cos(\beta = 60)\,\hat{y} \\
&= \frac{\sqrt{3}a}{2}\hat{x} - \frac{a}{2}\hat{y} \\
|\mathbf{a}_1| &= \sqrt{\frac{3}{4}a^2 + \frac{a^2}{4}} \\
&= \sqrt{\frac{4}{4}a^2} \\
&= a
\end{aligned}$$

$$\begin{aligned}
\mathbf{a}_2 &= \cancelto{0}{a_{2x}} \cdot \hat{x} + a_{2y} \cdot \hat{y} + \cancelto{0}{a_{2z}} \cdot \hat{z} = b\,\hat{y} \\
|\mathbf{a}_2| &= \sqrt{a_{2y}^2} = a_{2y} = b
\end{aligned}$$

$$\begin{aligned}
\mathbf{a}_3 &= \cancelto{0}{a_{3x}} \cdot \hat{x} + \cancelto{0}{a_{3y}} \cdot \hat{y} + a_{3z} \cdot \hat{z} = c\,\hat{z} \\
|\mathbf{a_3}| &= \sqrt{a_{3z}^2} = a_{3z} = c
\end{aligned}$$

The set of lattice vectors can be represented in matrix form:

$$\begin{pmatrix} \mathbf{a}_1 \\ \mathbf{a}_2 \\ \mathbf{a}_3 \end{pmatrix} = \begin{pmatrix} a_{1x} & a_{1y} & a_{1z} \\ a_{2x} & a_{2y} & a_{2z} \\ a_{3x} & a_{3y} & a_{3z} \end{pmatrix} = \begin{pmatrix} a_{1x} & a_{1y} & 0 \\ 0 & a_{2y} & 0 \\ 0 & 0 & a_{3z} \end{pmatrix} = \begin{pmatrix} a_{1x} & a_{1y} & 0 \\ 0 & b & 0 \\ 0 & 0 & c \end{pmatrix} \underset{\text{Calcite I}}{=} \begin{pmatrix} 4.376 & -2.527 & 0 \\ 0 & 5.053 & 0 \\ 0 & 0 & 17.234 \end{pmatrix} \tag{4.1}$$

By direct calculation, the volume of the cell is:

$$
\begin{aligned}
V = |\mathbf{a}_1 \cdot (\mathbf{a}_2 \times \mathbf{a}_3)| &= \left(\frac{\sqrt{3}a}{2}\,\hat{x} - \frac{a}{2}\,\hat{y}\right) \cdot \begin{vmatrix} \hat{x} & \hat{y} & \hat{z} \\ 0 & b & 0 \\ 0 & 0 & c \end{vmatrix} \\
&\underset{\text{a=b}}{=} \left(\frac{\sqrt{3}a}{2}\,\hat{x} - \frac{a}{2}\,\hat{y}\right) \cdot (ac\,\hat{x}) \\
&= \frac{\sqrt{3}a^2c}{2}
\end{aligned}
$$

Other equivalent definition of the volume of the cell is the determinant of the lattice vector matrix:

$$
\begin{aligned}
V &= \begin{vmatrix} a_{1x} & a_{1y} & 0 \\ 0 & b & 0 \\ 0 & 0 & c \end{vmatrix} \\
&= bc\,a_{1x} \\
&\underset{\text{a=b}}{=} \frac{\sqrt{3}a^2c}{2}
\end{aligned}
$$

The hexagonal and rhombohedral lattices can be easily related by a mathematical transformation: the supercell expansion matrix that converts the rhombohedral lattice vectors matrix to the hexagonal is the following:

$$
\underline{\underline{\mathbf{SC}}} = \begin{vmatrix} 1 & -1 & 0 \\ 0 & 1 & -1 \\ 1 & 1 & 1 \end{vmatrix} \tag{4.2}
$$

so that the hexagonal direct lattice vectors matrix ($\underline{\underline{\mathbf{H}}}$) is obtained from the rhombohedral ($\underline{\underline{\mathbf{R}}}$) as:

$$
\underline{\underline{\mathbf{SC}}} \cdot \underline{\underline{\mathbf{R}}} = \underline{\underline{\mathbf{H}}} \tag{4.3}
$$

4.1.2 The reciprocal lattice

Similarly, each reciprocal lattice vector $\mathbf{b}_i$ and its module $|\mathbf{b}_i|$ can be easily obtained:

$$\begin{aligned}
\mathbf{b_1} &= 2\pi \cdot \frac{\begin{vmatrix} \hat{x} & \hat{y} & \hat{z} \\ 0 & b & 0 \\ 0 & 0 & c \end{vmatrix}}{\frac{\sqrt{3}a^2c}{2}} \\
&\underset{\text{a=b}}{=} \frac{4\pi}{\sqrt{3}a}\,\hat{x} \\
|\mathbf{b_1}| &= \frac{4\pi}{\sqrt{3}a}
\end{aligned}$$

$$\begin{aligned}
\mathbf{b_2} &= 2\pi \cdot \frac{\begin{vmatrix} \hat{x} & \hat{y} & \hat{z} \\ 0 & 0 & c \\ \frac{\sqrt{3}a}{2} & \frac{-a}{2} & 0 \end{vmatrix}}{\frac{\sqrt{3}a^2c}{2}} \\
&\underset{\text{a=b}}{=} -2\pi \cdot \frac{1}{\sqrt{3}a}\,\hat{x} - 2\pi \cdot \frac{1}{a}\hat{y} \\
|\mathbf{b_2}| &= \frac{4\pi}{\sqrt{3}a}
\end{aligned}$$

$$\begin{aligned}
\mathbf{b_3} &= 2\pi \cdot \frac{\begin{vmatrix} \hat{x} & \hat{y} & \hat{z} \\ \frac{\sqrt{3}a}{2} & \frac{-a}{2} & c \\ 0 & b & 0 \end{vmatrix}}{\frac{\sqrt{3}a^2c}{2}} \\
&\underset{\text{a=b}}{=} \frac{2\pi}{c}\hat{z} \\
|\mathbf{b_3}| &= \frac{2\pi}{c}
\end{aligned}$$

The First Brillouin Zone of the trigonal crystal of Calcite I is shown in Fig. 4.5. Several of the reciprocal lattice points shown in this figure will play a key role in the phase transitions of calcite I.

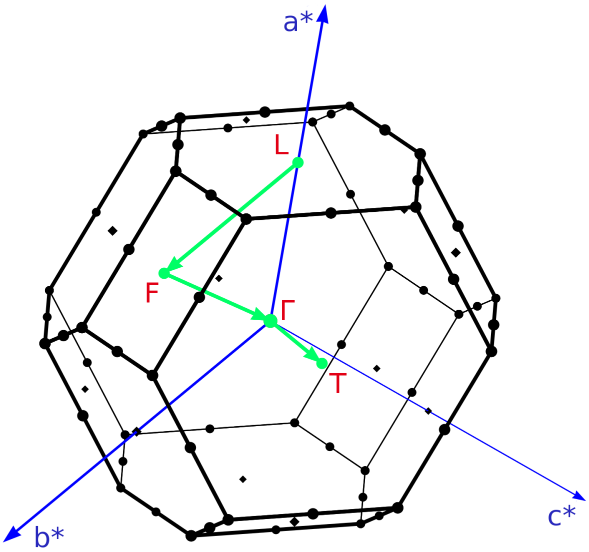

Figure 4.5: First Brillouin Zone of the trigonal crystal of calcite I. On green, a path along several reciprocal lattice points is shown: $\mathbf{L} = [1/2, 0, 0]$, $\mathbf{F} = [1/2, 1/2, 0]$, $\mathbf{\Gamma} = [0, 0, 0]$, $\mathbf{T} = [1/2, 1/2, 1/2]$. The k-point $\mathbf{T}$ can also be labeled as $\mathbf{Z}$. Some of these reciprocal lattice points will be crucial for understanding phase transitions in this material.

4.1.3 Crystal structure

The crystallographic cell of Calcite I is hexagonal, contains 6 formula units and 30 atoms (Fig. 4.6a). The coordinates of the asymmetric unit are the following: one calcium atom at fractional coordinates (0,0,0), and one carbon atom at $(0,0,\frac{1}{4})$. The only positional parameter not constrained by symmetry is the x coordinate for the oxygen atom, which is located at $(x,0,\frac{1}{4})$. The experimental lattice parameters deduced from X-ray diffraction at $T = 293$K are found to be $a = 4.991(2)$Å, $c = 17.062(2)$Å, $V = 368.1(3)$Å^3, $x = 0.2573(2)$, and density of 2.709 g/cm^3[133].

The Ca cation is coordinated with six oxygen ions forming an octahedron which is slightly flattened in the direction of the hexagonal c axis (see Fig. 4.6a). The Ca-O bond distance in the octahedral environment is 2.359 Å, and two types of $O - \widehat{Ca} - O$ angles are identified: 87.435° and 92.575° (Fig. 4.7), which means the octahedron is slightly distorted from a perfect octahedron (all angles equal to 90°). This distortion of a perfect octahedral environment may be caused because of the vertex of the octahedron forms part of a carbonate group, which "pulls" the octahedron in that direction.

The carbonate groups are perpendicular to the c-axis and located at planes parallel to (001), as shown in Fig. 4.6b. These are pointing opposite directions, as shown with different colors,

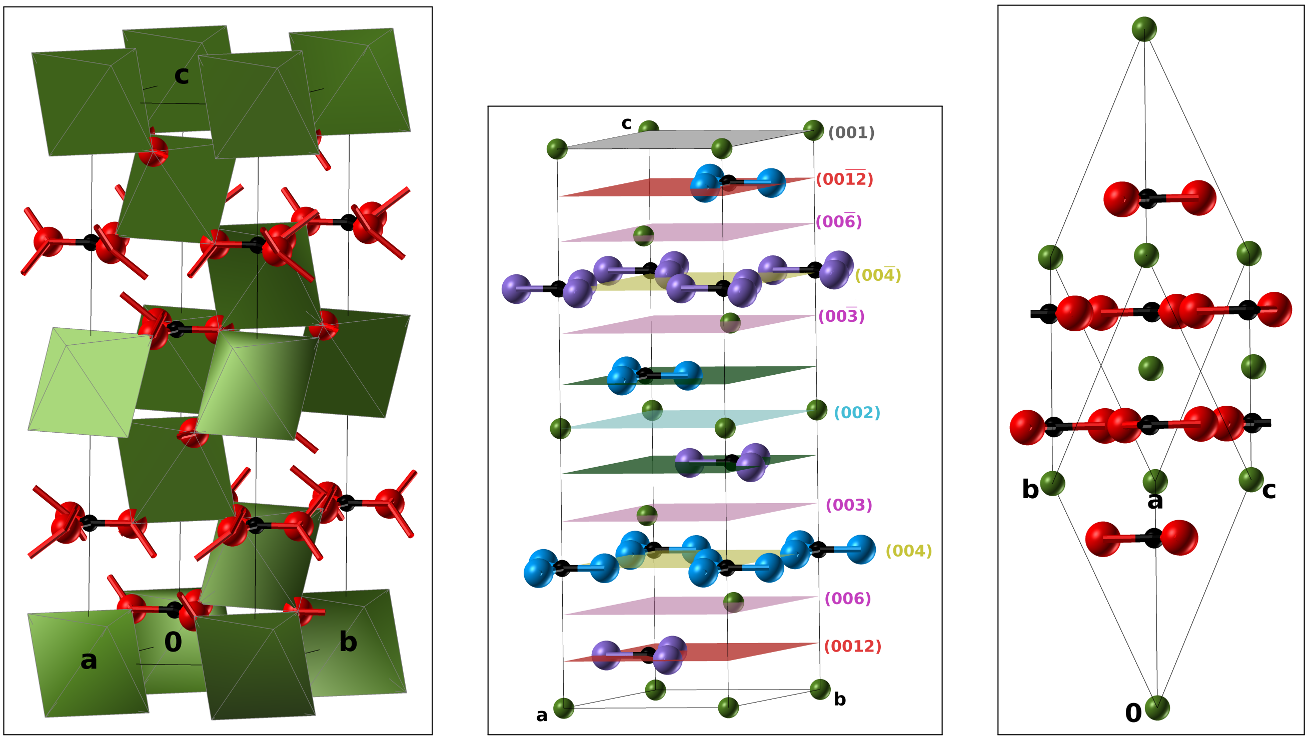

(a) (b) (c)

Figure 4.6: View of the crystallographic (4.6a) and primitive (6.4e) cells of Calcite I. Fig. 4.6b: all carbonate groups are located at planes parallel to (001), pointing to opposite directions, as shown with two different colors: blue and purple.

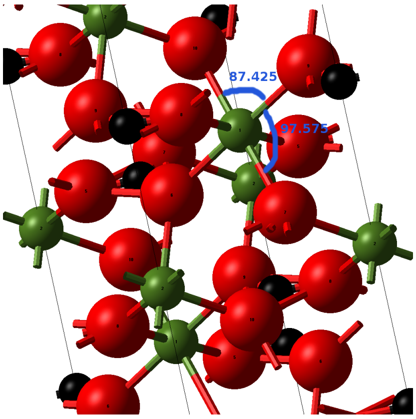

Figure 4.7: Two types of angles are described in the octahedral environment of a calcium ion: 87.425° and 92.575°.

blue and purple.

4.2 Aragonite

Aragonite adopts an orthorhombic lattice with space group *Pmcn* with 20 atoms in the unit cell (4 formula units). The experimental lattice parameters deduced from single-crystal X-ray diffraction are: $a = 4.9616$, $b = 7.9705$, $c = 5.7394$, $\alpha = \beta = \gamma = 90°$, and a density of 2.929 g/cm^3 [134].

The CO_3^{2-} ions are perpendicular to the c-axis, projected on top of each other, in different planes, and pointing in opposite directions (Fig. 4.8a), destroying the trigonal symmetry that is characteristic of Calcite I. The calcium ions are in an hexagonal closest packing, and have a ninefold coordination with the oxygen atoms [135].

In this ninefold polyhedron a very interesting way of coordination appears. We can identify two types of Ca−O bonds (see Fig. 4.8b) :

1. Bonds to 2 Oxygen atoms in each of 3 carbonate groups. There are a total of 6 Ca−O bonds of this type, per calcium atom. These 6 bonds are distributed as follows:
    (a) Two equal d(Ca−O) = 2.541 Å distances to the first carbonate group.
    (b) d(Ca−O) = 2.655 Å and d(Ca−O) = 2.526 Å to the second carbonate group.
    (c) d(Ca−O) = 2.655 Å and d(Ca−O) = 2.526 Å to the third carbonate group.
2. Bonds to 1 Oxygen atom in 3 other carbonate groups. There are a total of 3 Ca−O bonds of this type, per calcium atom. These 3 bonds are distributed as follows:
    (a) A d(Ca−O) = 2.448 Å to the forth carbonate group.
    (b) A d(Ca−O) = 2.411 Å to the fifth carbonate group.
    (c) A d(Ca−O) = 2.448 Å to the sixth carbonate group.

Each oxygen is bonded to three Ca cations, whereas in Calcite I each oxygen was bonded to two Calcium cations.

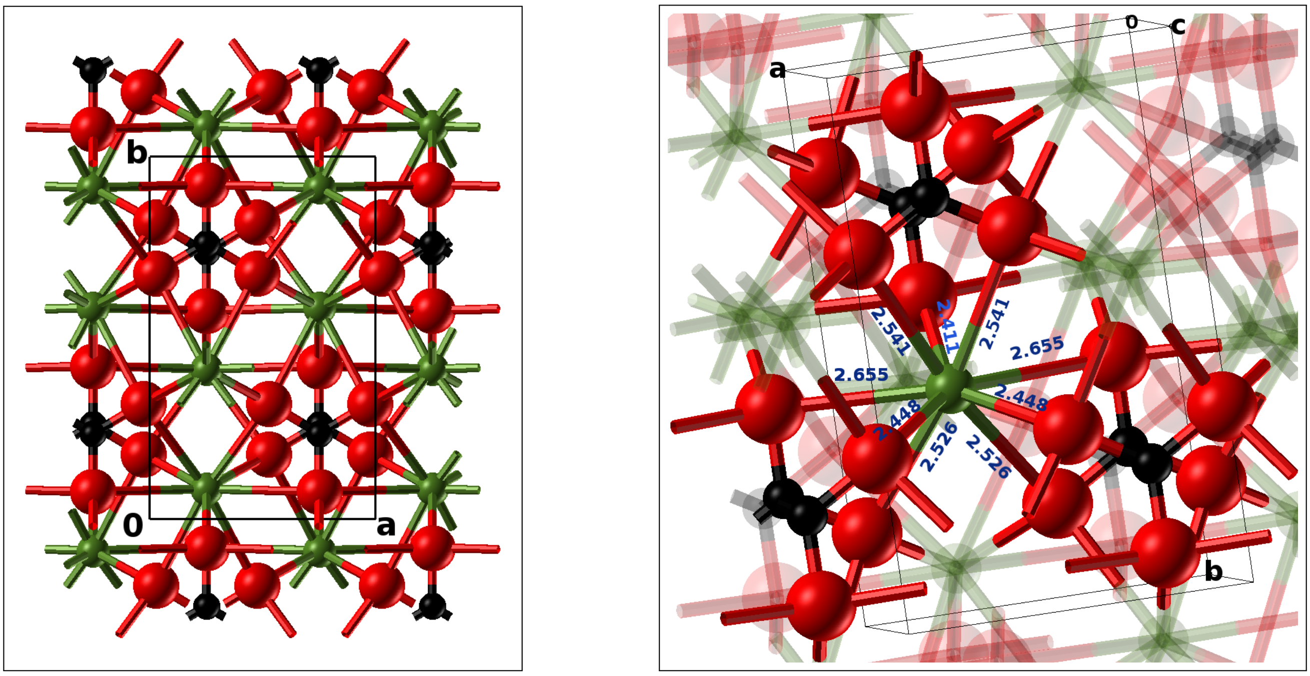

(a)

(b)

Figure 4.8: Structure of Aragonite: 4 formula units in the unit cell, where the carbonate planes are one on top of the other in different planes, oriented in opposite directions. Fig. (4.8a) is a projection on the *ab* plane, showing the ninefold coordination of calcium ion. Fig. (4.8b) highlights a single calcium atom and the 6 types of bonds (bonds to 2 Oxygen atoms in each of 3 carbonate groups) and the 3 types of bonds (bonds to 1 Oxygen atom in 3 other carbonate groups). For more details, refer to text.

4.3 Vaterite

As has been said at the beginning of this chapter, the structure of vaterite is still unknown. Its crystalline state is today a matter of ongoing debate. There are many interpretations of both the experimental data and theoretical calculations. The symmetry and space group, dimensions of the unit cell, orientation and site symmetry of the carbonate groups are controversial. Figure 4.9 is a chart of the proposed vaterite structures available in the literature. They are organized in such a way so as to identify the parent vaterite structures. There are several interpretations, based on a hexagonal, monoclinic, or orthorhombic lattices.

In 1959 Meyer was the first to determine the vaterite crystal structure derived from single-crystal X-ray diffraction experiments, in which an orthorhombic unit cell with a space group *Pnma* was reported [101]. One year later he refined the structure and suggested an orthorhombic cell, but with space group *Pbnm* with partial occupancies of different carbonate sites [102]. From X-ray diffraction experiments, in 1963 Kamhi classified the structure with hexagonal symmetry and space group $P6_3/mmc$ [103], in which the calcium atoms are in eightfold coordination

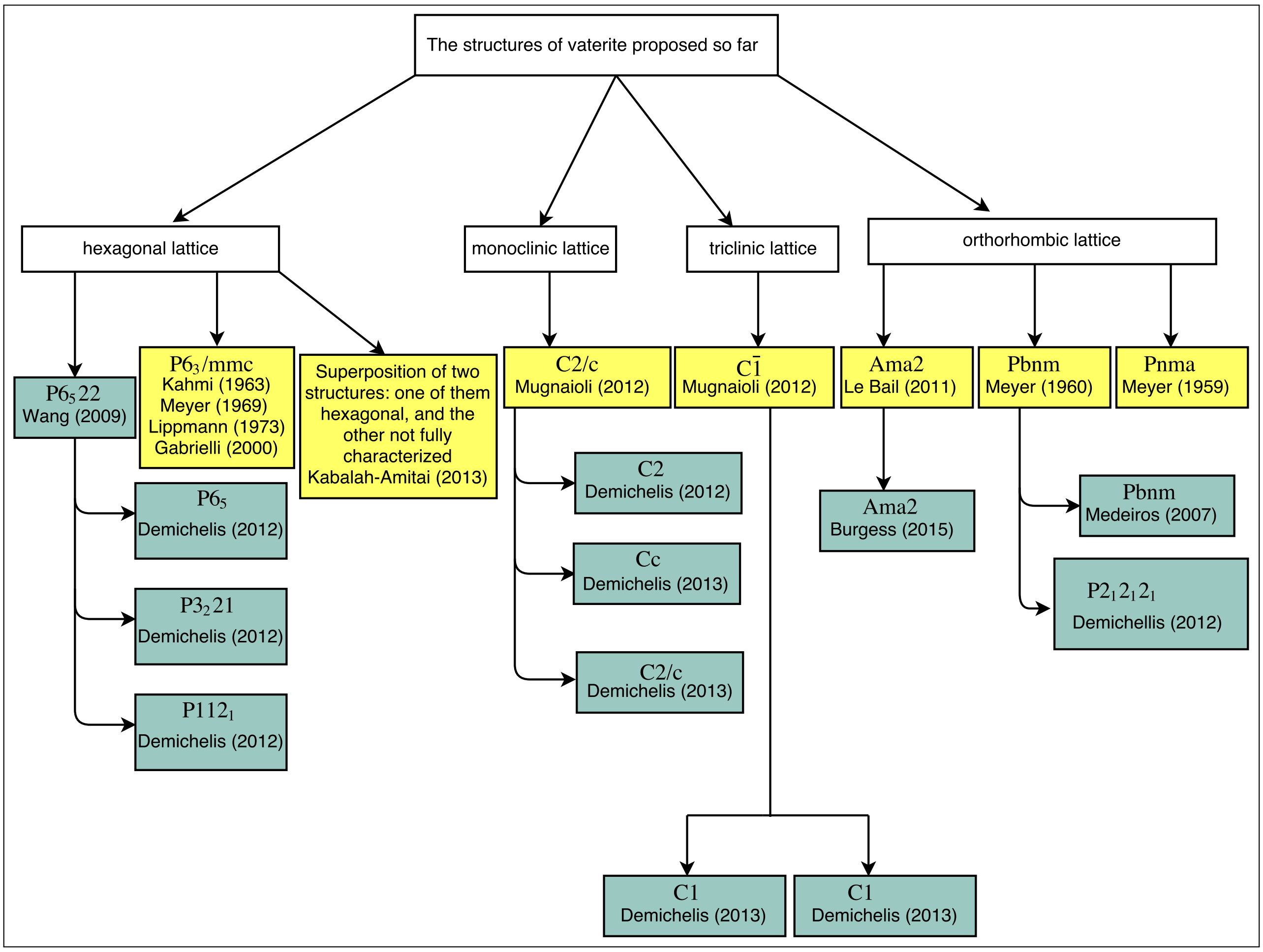

Figure 4.9: Structures of vaterite proposed so far. Models are based on hexagonal, monoclinic, or orthorhombic lattices. Figure updated and inspired from Burgess *et al.* [111]. Rectangles filled in blue and yellow indicate theoretical and experimental studies respectively. For more details refer to text.

with oxygen atoms. In 1969 Meyer [104] and later confirmed by Lippmann [105] proposed an hexagonal lattice with the same space group as Kamhi's model

The Raman spectrum of vaterite performed in carbonically pure water [106] revealed in 2000 that the only structure that is in agreement with the experiment is the one considered by Meyer in 1969. However, a more recent Raman spectrum study of vaterite is inconsistent with either an hexagonal or orthorhombic symmetry [94]. Recently, Le Bail [107] suggested a modified orthorhombic unit cell based on a microtwinning hypothesis. In this study, the ESPOIR code was used to move independently the Ca ions and one or several rigid carbonate groups in the cell, by Monte Carlo approaches. A structure with $Ama2$ space group was the most appropriate candidate based on these simulations. Mugnaioli et al. [108] suggested in 2012 two structures with very low symmetries: a monoclinic unit cell (space group $C2/c$) and a triclinic one (space group $C\bar{1}$) based on automated diffraction tomography (ADT) and electron diffraction experiments done on a transmission electron microscope.

Only one year later Kabalah-Amitai *et al.* [97] concluded that the structure of vaterite consists of an hexagonal structure coexisting with at least another structure not fully characterized. Both of them are rotated by 30° respect to the other, and with a lattice parameter relationship of $a' = \sqrt{3a}$.

Although there is no consensus on the structure, some features regarding the vaterite crystal structure emerge: a) the Ca atoms are in an hexagonal sublattice; b) carbonate groups are parallel to the *c*-axis, as opposed to calcite and aragonite, where the carbonate planes are perpendicular to the c-axis; and c) there is considerable disordering of the carbonate groups in the structure [90].

In order to understand the structure of vaterite, theoretical calculations have also been performed. Medeiros *et al.* [100] conducted DFT calculations (plane-wave basis and ultrasoft Vanderbilt pseudopotentials) of the *Pbnm* orthorhombic cell given by Meyer [102] with LDA and GGA level of theory. In that study the structural, electronic (band gap) and optical properties were investigated. The intensity of optical absorption was predicted to be more pronounced that the experiment only for energies larger than 6.0 eV.

Wang *et al.* [90] performed DFT calculations with the projector-augmented wave method (PAW) and GGA functionals (PW91). The starting point was also the orthorhombic structure of Meyer. Then, Molecular dynamics (MD) simulation with temperature annealing was used to address disordering and to find an ordered superstructure. As a result of an energetic analysis of different hexagonal configurations, a structure with 18 formula units, belonging to the $P6_522$ space group was proposed, in which two Ca sites can be identified: Ca atoms coordinated by six O atoms at distances of about 2.350−2.440 Å (octahedra labelled as **1** in Fig. 4.10) and Ca atoms coordinated by six O atoms at distances of about 2.313−2.460 Å (octahedra labelled as **2** in Fig. 4.10).

Demichelis et al. [109, 110] suggested that the $P6_522$ structure proposed by Wang was a Boltzmann-weighted average structure of three different configurations with space groups $P6_5$, $P3_221$ and $P112_1$, as a consequence of rotations of the carbonate groups. In the $P6_5$ structure the calcium ions are only surrounded by 6 oxygens, whereas in the $P3_221$ structure calcium ions are surrounded by 6 and 7 oxygens. A coordination index of 6, 7 and 8 is observed in the

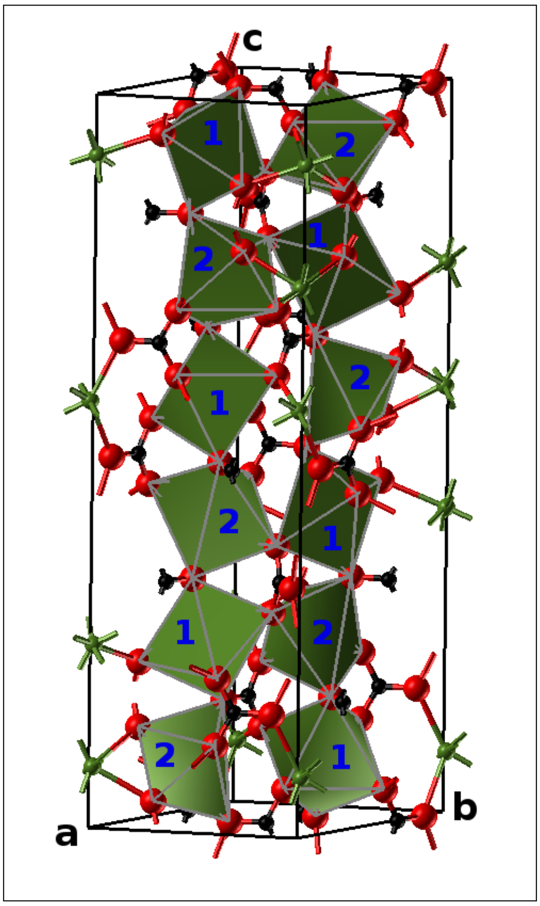

Figure 4.10: Wang's proposed structure for Vaterite, with two types of Ca sites: octahedras **1**(Ca−O distances of about 2.350−2.440 Å) and octahedras **2** (Ca−O distances of about 2.313−2.460 Å).

$P112_1$ structure. These calculations were performed with all-electron localized Gaussian-type functions basis sets, using the GGA (PBEsol functional).

Regarding the $C2/c$ structure described by Mugnaioli *et. al*, Demichelis et al. [109], suggested two more stable monoclinic lattices, again as a result of rotations in the carbonate ions: $C2$ and Cc. Similarly, Demichelis et al. [109] postulated the $C\bar{1}$ structure described by Mugnaioli *et. al* to be two $C1$ structures of very similar energy, in which the difference is a minor rotation of carbonates. In addition, Meyer's $Pbnm$ structure was identified to be $P2_12_12_1$.

PAW DFT calculations of Mugnaioli's $C2/c$ and Le Bail's $Ama2$ structures were performed by Burgess *et al.* [111] , in order to understand ^{43}Ca solid-state nuclear magnetic resonance (SSNMR) experiments on vaterite.

4.4 High-pressure polymorphs

4.4.1 Calcite II

The Bravais Lattice of Calcite II is monoclinic, with symmetry group $P2_1/c$ and experimental lattice parameters $a = 6.334(20)$Å, $b = 4.948(15)$Å, $c = 8.033(25)$Å, $\beta = 107.9°$, $V = 239.57$Å^3, with 20 atoms in the unit cell (4 formula units) and a density of 2.77 g/cm^3. Merril *et al.* [114] obtained these experimental values by applying 1.8 GPa to Calcite I at room temperature. The structure was characterized by single-crystal X-ray diffraction using designed miniature diamond-anvil pressure cell. The Calcium atoms are surrounded by six oxygen atoms(Figures 4.11a and 4.11b). As can be seen in these figures, each calcium atom is coordinated to one oxygen atom of a carbonate group, as opposed to aragonite, where a calcium atom was coordinated to the two oxygens of a single carbonate group. The Ca−O distances in each octahedra are shown in Fig. 4.11a. In addition, all octahedra are not oriented in the same way, and 4 types of octahedra can be defined: $\mathrm{Oh}_1 - \mathrm{Oh}_4$. The relationship between each of them is an inversion symmetry operation between Oh_1 and Oh_3, and similarly between Oh_2 and Oh_4, as is shown in (4.11d).

The Calcite I - Calcite II phase transition is displacive and the sample remains a single crystal in the Calcite II phase. The mechanism proposed for this phase transition was due to a soft phonon instability at the F point of the rhombohedral Brillouin zone boundary [136] (See Fig. 4.5). This mechanism, as well as the temperature-pressure phase diagram for this phase transition has been studied with substantial detail in the course of the PhD, and will be thoroughly explained in Chapter 7.

Biellmann *et al.* [137] performed experiments on Calcite I at 45 GPa and temperatures between 300 and 2000 K in a YAG-laser-heated diamond-anvil cell. In these experiments calcite II was quenched and characterized for the first time by transmission electron microscopy (TEM) at ambient conditions. In that experiment no decomposition reaction was observed ($CaCO_3 \rightarrow CaO + CO_2$), which lead the authors to think that CO_2 may be trapped in carbonates in the upper and lower mantle. The transition calcite I to calcite II results from two displacements: first, an 11° rotation in opposite directions of adjacent carbonate groups along the c axis, and second, a small antiparallel displacement of adjacent rows of Ca in the (104) direction [137].

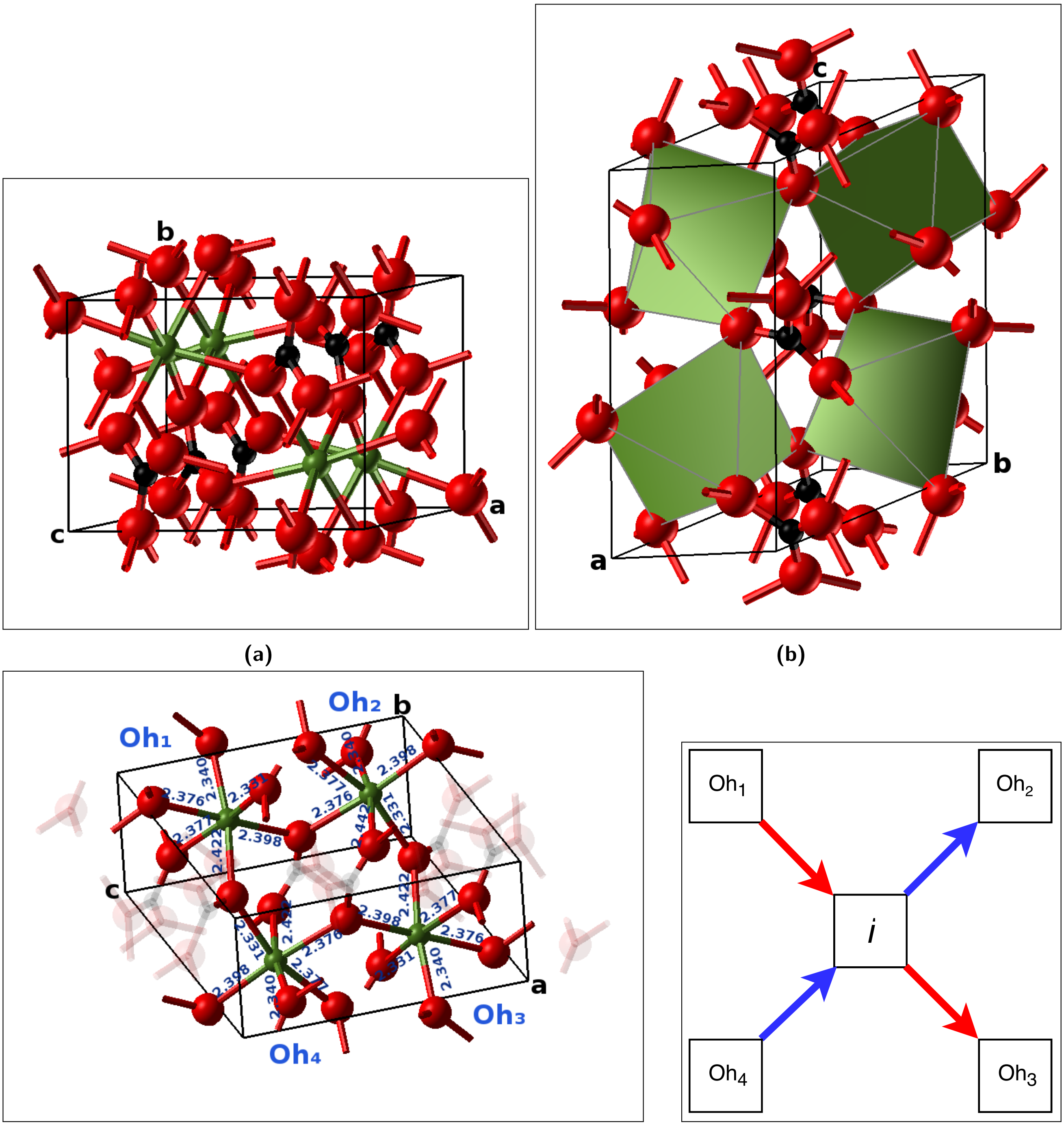

(a)

(b)

(c)

(d)

Figure 4.11: Structure of calcite II: (4.11a) shows the octahedral coordination of the four calcium ions per formula unit, and the carbonate groups pointing alternately in two different directions. (4.11b) shows the polyhedron and again the alternate orientation of the carbonate groups. Unlike in Aragonite, each calcium atom is coordinated to only one oxygen atom of a carbonate group. (4.11c) is a similar projection as (4.11a) but shows only the Ca$-$O distances in each octahedron. From this figure we can define 4 types of octahedrons: $\mathrm{Oh}_1 - \mathrm{Oh}_4$, not oriented in the same way. An inversion symmetry operation relates Oh_1 and Oh_3, and similarly between Oh_2 and Oh_4, as is shown in (4.11d).

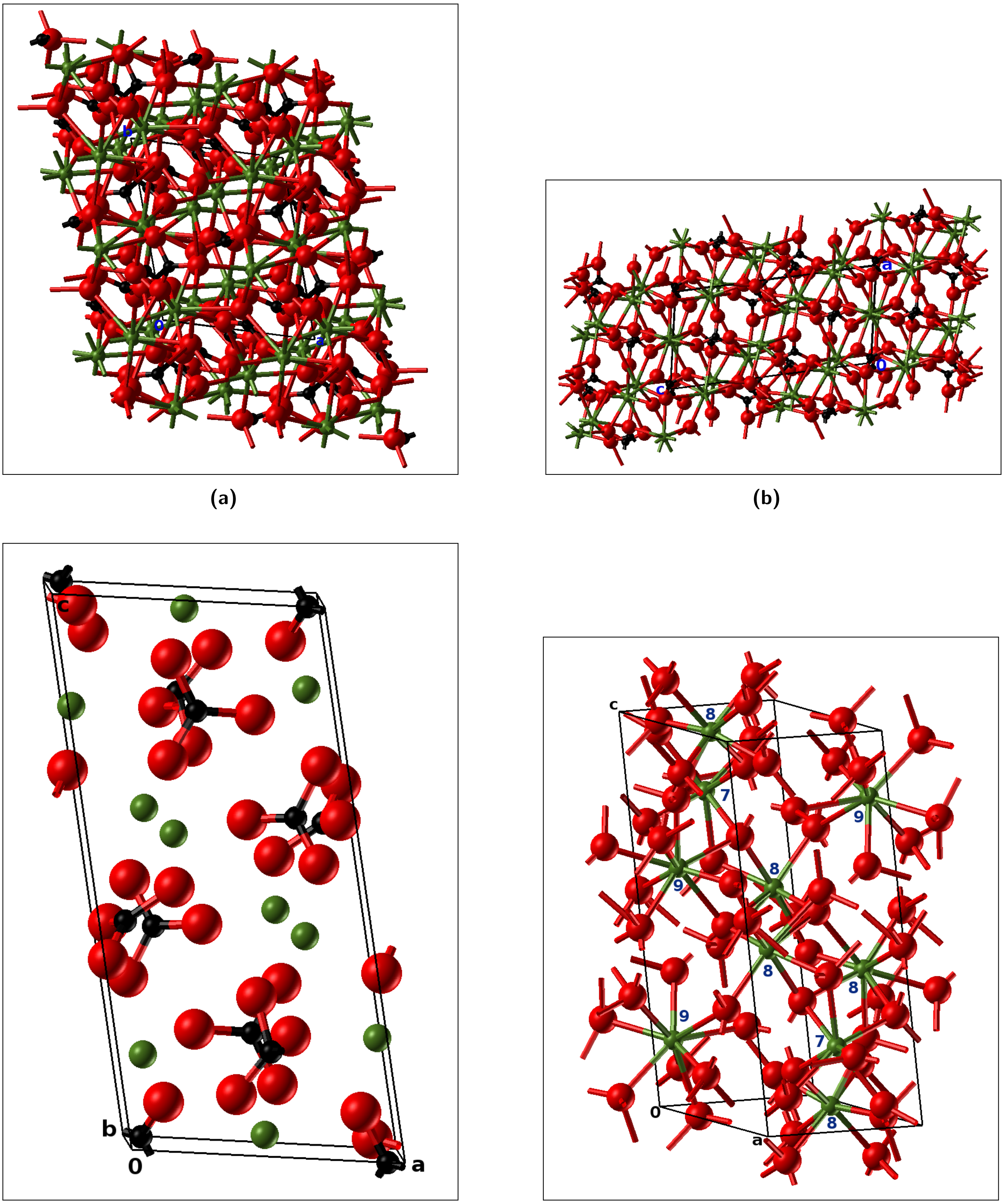

(a) **(b)**

(c) **(d)**

Figure 4.12: Structure of calcite III: (4.12a) and (4.12b) show a projection on the ab and ac plane respectively. (4.12c) shows the unit cell of Calcite III, with 10 formula units. (4.12d) shows the three different sites of the calcium atoms with coordination numbers of 7, 8 and 9.

4.4.2 Calcite III and IIIb

As has been mentioned at the beginning of this Chapter, the most recent characterization of calcite III and IIIb was conducted by Merlini *et al.*[17] in 2012. In that study, they characterized Calcite III as triclinic (space group $P\bar{1}$) in the pressure range 2.5 − 15 GPa, and was presented as a closely related structural modification of Calcite III. Calcite III has 10 formula units (50 atoms in the unit cell), in which the lattice parameters are found to be a = 6.281(1)Å, b = 7.507(2)Å, c = 12.516(3)Å, α = 93.76(2)°, β = 98.95(2)°, γ = 106.49(2)°, V = 555.26(20) Å^3 and a density of 2.99 g/cm^3 at 2.8 GPa. In an attempt to observe more polymorphs, Merlini *et al.*[17] studied in detail the Calcite II−Calcite III stability field by applying very slow pressure ramps (0.01 GPa/min). They were able to observe in two experiments a polymorph that was not Calcite II because it could not be indexed with a monoclinic cell, but with a tricilinc $P\bar{1}$ space group. They called this structure Calcite IIIb, with 4 formula units (20 atoms), a = 6.144(3)Å, b = 6.3715(14) Å, c = 6.3759(15)Å, α = 93.84(2)°, β = 107.34(3)°, γ = 107.16(3)°, V = 224.33(13) Å^3 and a density of 2.96 g/cm^3 at 3.1 GPa. Different pressure-time experimental paths can stabilize one or the other polymorph (more information on Ref. [17]). Both structures are characterized by the presence of non-coplanar CO_3 groups.

In Calcite III the carbonate groups are no longer coplanar with each other as occurs in Calcite II. The coordination number of calcium atom varies from 7, 8 and 9 (see Fig. 4.12). Therefore, the cation sites are not equivalent.

Calcite IIIb has a similar structure as Calcite III: it also contains non coplanar carbonate groups and two non-equivalent Ca coordination polyhedron (Fig. 4.13). Merlini *et al.*[17] did not report the coordination numbers. As can be seen in Fig. (4.13d), the calcium ion has a 7+1 irregular coordination: 7 shorter Ca−O distances (2.3 - 2.6 Å) and one longer one (3.4 Å).

Merlini *et al.*[17] hypothesized that Calcite IIIb should have a higher energy than Calcite III and therefore the first one is thermodynamically metastable with respect to Calcite III In this work we will prove Merlini's hypothesis showing through our calculations that in fact the energy of Calcite IIIb is higher that Calcite III, at least at 0K.

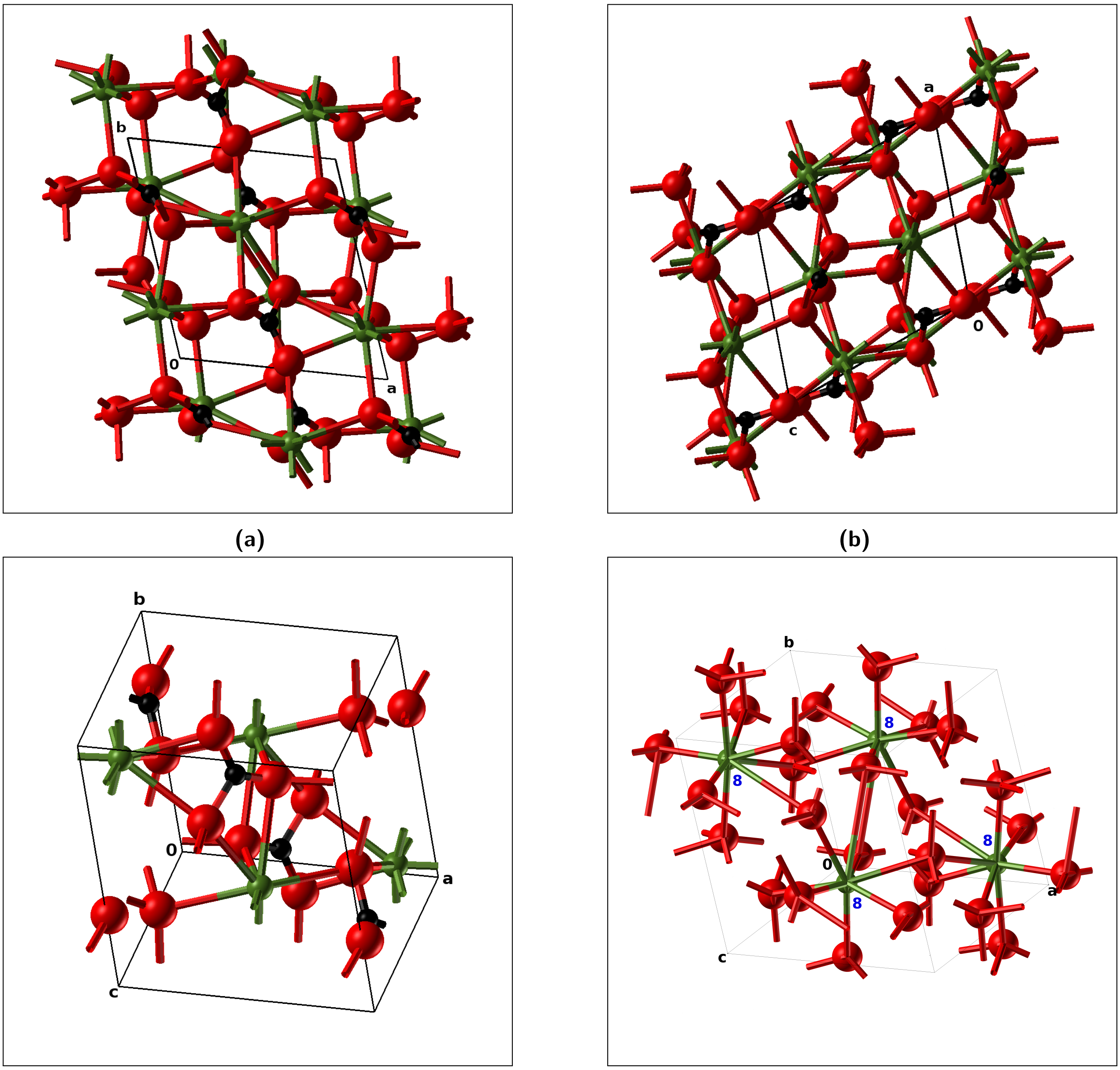

(a) (b)

(c) (d)

Figure 4.13: Structure of Calcite IIIb: (4.13b) and (4.13b) show the projection on the planes ab and ac respectively (the same planes from which Calcite III was visualized in Figures (4.12a) and (4.12b). (4.13c) shows the unit cell of Calcite IIIb, with 4 formula units. (4.13d) shows the the calcium atoms with coordination numbers of 8.

4.4.3 Calcite VI

Merlini *et al.*[17] characterized this phase as triclinic (space group $P\bar{1}$), with 10 atoms (2 formula units) in the unit cell and lattice parameters: $a = 3.3187(12)$Å, $b = 4.8828(14)$Å, $c = 5.5904(14)$Å, $\alpha = 103.30(2)°$, $\beta = 94.73(2)$Å°, $\gamma = 89.21(2)°$, $V = 87.86(20)$Å^3 at 30.4

GPa.

Calcite VI has parallel (coplanar) CO_3 groups (Figures 4.14a and 4.14b), but the structure is no longer layered as in the lower pressure polymorphs. According to Merlini *et al.*[17], the different orientation of the carbonate groups is responsible for a higher density than aragonite: 3.78 g/cm^3 at a pressure of 30.4 GPa. In that study it is suggested that this higher density could result in calcite IIIb replacing aragonite in some regions of the Earth's intermediate mantle.

As can be seen in Fig. 4.14c, the calcium atom has a 7+2 irregular coordination: 7 shorter Ca−O distances (2.301, 2.217, 2.302, 2.316, 2.159, 2.353, 2.324 Å) and 2 longer ones (2.499 and 2.630 Å).

4.5 High temperature polymorphs

4.5.1 Calcite IV and V

Despite many attempts to determine the structure of Calcite V unambiguously [138] a consensus has yet to be reached. This is, in part, because Calcite V is very unstable and decomposes into calcium oxide and carbon dioxide even under a CO_2 atmosphere up to 0.4 MPa. The characterization is also difficult because of thermal vibrations, the oxygen atoms do not sit at rest at the specific atom positions defined by the space group [131].

In 2013 Ishizawa *et al.* [131] performed high-temperature X-ray diffraction experiments on a crystal-sample sealed in a quartz glass capillary with CO_2 gas under ambient pressure and temperature. In that work they came to the conclusion that calcite I has a definite structure (see Fig. 4.15a, with oxygen occupying atomic positions in blue and lime). Under the influence of temperature, at 995K the carbonate group can flip between two orientations (Calcite IV, Fig. 4.15b) and at 1240 K almost free rotation (Calcite V, Fig. 4.15c).

The structure of Calcite IV belongs to $R\bar{3}c$ space group, in which the experimental lattice parameters are: $a = 4.9747(2)$Å, $c = 17.4468(8)$Å, $x = 0.2492(6)$, and $V = 373.91(3)$Å^3 at 995K. The Ca ion is at fractional coordinates (0,0,0) and the C ion at $(0,0,\frac{1}{4})$, just as is Calcite I. However, it contains two different O atom sites partially occupied due to substitutional disorder: O1 at $(x,0,\frac{1}{4})$ and O2 at $(-x,0,\frac{1}{4})$. The two kinds of carbonate molecules in disorder

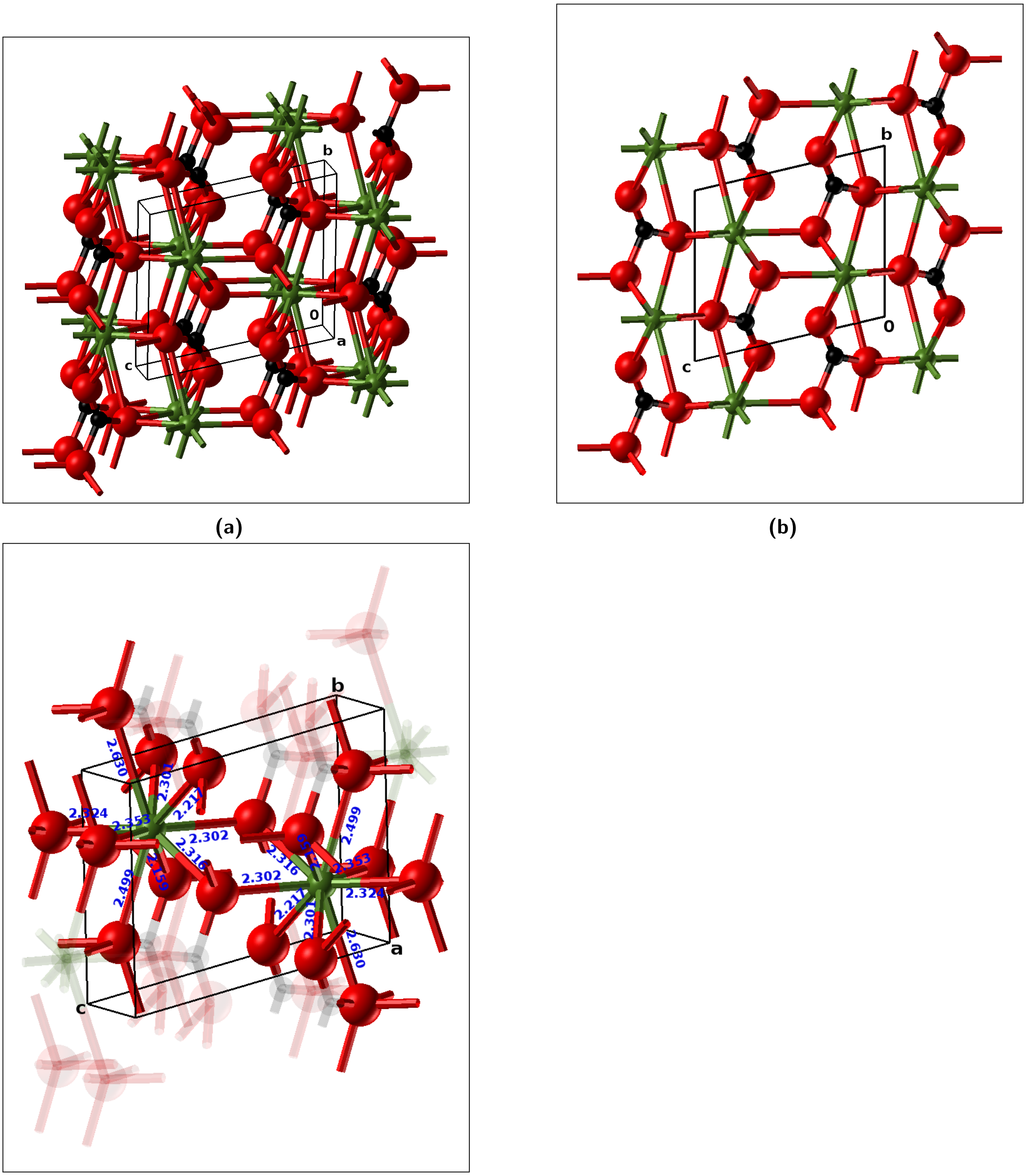

(a)

(b)

(c)

Figure 4.14: Structure of Calcite VI: (4.14a) shows the orientation of the carbonate groups in the structure. (4.14b) is a projection on the bc plane. (4.14c) shows the distances Ca−O and the 7+2 coordination number of both calcium sites.

are not in the 60° or 180° rotation relationships, but related by an inversion symmetry operation at the carbon atom.

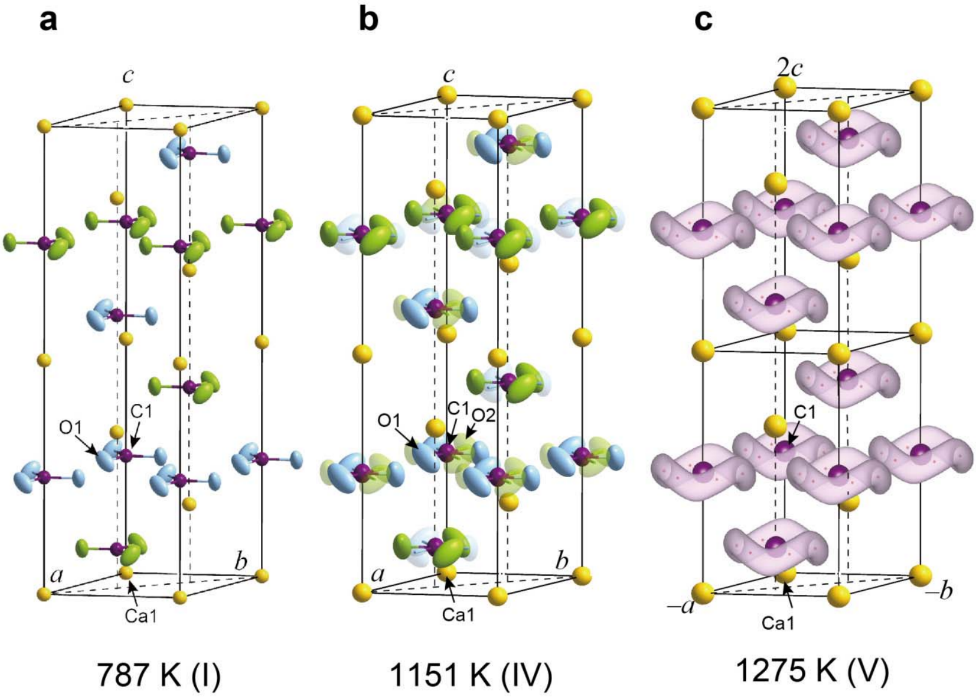

Figure 4.15: (a) Phase I at 787 K. (b) Phase IV at 1151 K. The carbonate groups occupy parital positions O1 and O2. (c) Phase V at 1275 K. The carbonate ion can freely rotate. In order to obtain a similar atom arrangement as phases I and IV, Calcite V has been drawn with $a_V = -a_I$, $b_V = -b_I$ and two units cells along the c axis. Image reproduced from Ishizawa *et al.* [131].

In Calcite V the Ca atom sits at (0,0,0) and the carbon atom at (0,0,$\frac{1}{2}$). The oxygen atom does not sit still at a specific position because the carbonate ion can freely rotate with a very low activation energy (Fig. 4.15c). The experimental parameters given were: $a = 4.9699(8)$Å, $c = 8.9167(18)$Å, $x = 0.2370(14)$ and $V = 190.73(7)$Å^3 at 1254 K.

Chapter 5

Benchmarking accurate thresholds and description of higher symmetry structures found

All calculations are performed with the CRYSTAL17 program [63], which works within periodic boundary conditions and with localized Gaussian-type function basis sets (BSs). Several computational parameters need to be tight enough to ensure accurate calculations. The first of these considerations is the basis set. Initially, the basis set used was the one labelled as BSA [139], which includes a triple-zeta valence with polarization quality for the calcium and oxygen atoms and double-zeta valence with polarization for the carbon atom.

In addition to the Basis set, there are several computational parameters that have to be taken into account as well:

1. Integrals calculated in reciprocal space require an integration over the possible values of $\mathbf{k}$ in the First Brillouin Zone, e.g. a given integral $\bar{g}$ would be defined as:

$$\bar{g} = \frac{V_{\text{cell}}}{8\pi^3} \int_{\text{BZ}} g(\mathbf{k}) d\mathbf{k} \tag{5.1}$$

   The Pack and Monkhorst method [140] is used in CRYSTAL to define the sampling of $\mathbf{k}$ points. A shrinking factor s specifies how many equidistant $\mathbf{k}$ vectors must be taken along each direction of $\mathbf{b}_1$, $\mathbf{b}_2$, and $\mathbf{b}_3$ inside one reciprocal lattice unit cell so that the total number of points in the grid, n_s, is equal to s^n, with n denoting the order of periodicity ($n = 3$ for three dimensional crystals). Because of the symmetry operators, the integrals in reciprocal space do not need to be evaluated using the entire BZ. Instead, they can just be evaluated in a reduced portion of the zone and then be extended without approximation to fill the entire BZ using symmetry. This reduced region is called the **Irreducible Brillouin Zone (IBZ)**.

A Monkhorst-Pack mesh of $6 \times 6 \times 6$ was initially used, which corresponds to the `SHRINK 6` option in CRYSTAL, and 32 k-points in the Irreducible part of the Brillouin Zone (IBZ) for calcite I.

2. The DFT exchange-correlation contribution, which is evaluated by numerical integration over the unit cell volume. A pruned grid with 75 radial (through Gauss-Legendre radial quadrature) and 974 angular points (Lebedev two- dimensional angular point generation) was initially used. This corresponds to the defult `XLGRID` option, as implemented in the CRYSTAL program.

3. The truncation of the Coulomb and exchange sums. As was explained in Section 2.2.9, these sums are infinite for a periodic system, so they must be truncated at some point, in order to perform the calculation effectively. The truncation of these sums is implemented in CRYSTAL via five thresholds ($T_1 - T_5$), through the `TOLINTEG` keyword, set here to the default 6, 6, 6, 6, and 12 respectively. Each threshold T_i is controlling a specific integral, as was thoroughly explained in Section 2.2.9. For the sake of simplicity, since $T_1 = T_2 = T_3 = T_4$, we will refer the `TOLINTEG` settings with two numbers separated by a dash, e.g. 6-12.

These last two thresholds used correspond to the default ones in the CRYSTAL code. Additionally, the energy difference between two optimization steps is controlled through the `TOLDEE` keyword. This was set to 10^{-8} for the geometry optimization.

Working on this basis, we started by performing geometry optimisations of calcite I, III, IIIb, and VI. Since there are several models available for vaterite, the optimization of this structure was not considered in the first place. Kamhi's structure of vaterite is the experimental interpretation most accepted nowdays, however it presents partial occupation, so that it cannot be studied by conventional DFT geometry optimisation approaches. Calcite II becomes calcite I for conditions corresponding to a fully relaxed geometry optimization ($T = 0$ K and $P = 0$ GPa), and this phase transition will be thoroughly explained in Chapter 7. The high temperature polymorphs Calcite IV and V present partial occupation of the oxygen atoms as well (Section 4.5).

After the geometry optimization was conducted, the next step consisted in performing volume constraint optimisations of the calcite I, IIIb and VI polymorphs at different degrees of compression and expansion, as implemented in the CRYSTAL program within the `EOS` (equation of state) routine [141]. Several interesting jumps were observed in the energy-volume curves for calcite IIIb and VI (space group 2, or P-1), as shown in Figs. 5.1a and 5.2a. A search of the symmetry was performed using the FINDSYM program over each of these volumes, in order to verify whether a change of symmetry was occurring in the proximity of those jumps. For the structures highlighted with a magenta arrow in Fig 5.1a (calcite IIIb) and 5.2a (calcite VI), a higher symmetry structure was found (space group of 13, or $P2/c$). A full geometry optimization of this higher symmetry structure, followed by an equation of state run yields the green curves shown in Figs. 5.1b and 5.2b. Similarly, calcite VI presented three expanded volumes (shown with three magenta arrows in Fig. 5.1a), for which a further symmetry search yields space group 13 instead of space group 2. Both structures space group 13 obtained from calcite IIIb and VI have the same energy and neighbour analysis, thus, they are the same structure. This jump observed in the volume has to be reflected in a change in the structure. Hence, a highly detailed analysis of the distances was performed. The Ca-O distances were found to be severely affected by this jump. As an example, we can focus on the distance labelled as Ca1-O8 (Fig. 5.3a)

In the volume range from 62 to 67 $\AA^3$, two types of Ca1-O8 distances are observed: a short one (2.6 Å) and a larger one (4.1 Å, see Fig. 5.3b). On the contrary, only one type of distance is observed (3.5 Å) at volumes higher than 67.5 Å^3. The higher space group found is in agreement with two different distances becoming equivalent. A visualization of this higher symmetry structure is shown in Fig. 5.4.

In order to verify whether these phase transitions in calcite IIIb and VI were indeed physical, a richer basis set was used: triple zeta in all three atoms of calcium, carbon and oxygen, i.e. the pob-TVPZ, a type of TZ basis sets developed by Peintinger, Oliveira, and Bredow [142],

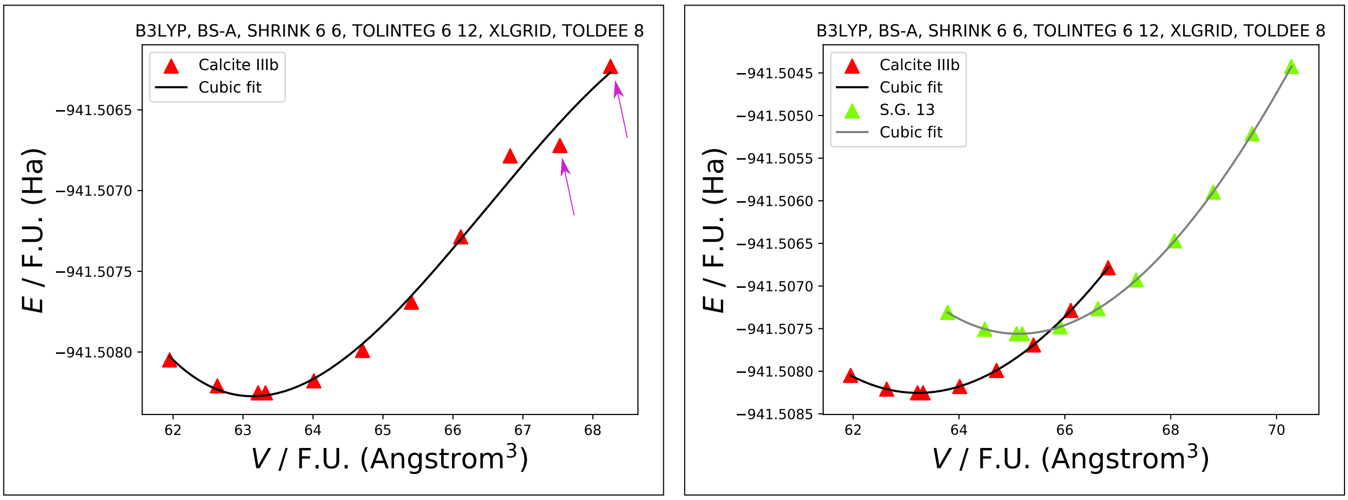

(a) **(b)**

Figure 5.1: Energy-volume curves for calcite IIIb (space group 2). By analyzing the symmetry of each volume with the FINDSYM program, a symmetry of P_2/c (space group 13) is observed for the last two points highlighted with magenta arrows. Fig. 5.1b: Removing these last 2 points for calcite IIIb, and showing also S.G. 13.

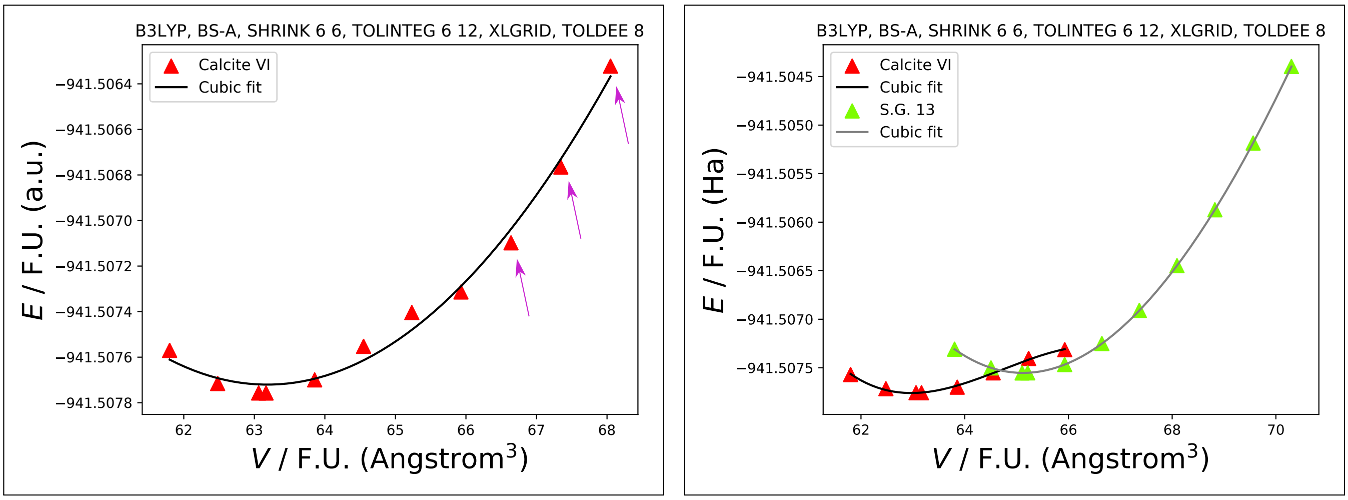

(a) **(b)**

Figure 5.2: Fig. 5.2a: Energy-volume curves for calcite VI (space group 2). By analyzing the symmetry of each structure with the FINDSYM program, a symmetry of P_2/c (space group 13) is observed for the last 3 points highlighted with magenta arrows. Fig. 5.2b: Removing the last 3 points for calcite VI, and showing also S.G. 13.

specially optimized for periodic quantum-chemical solid-state calculations with the crystalline-orbital program CRYSTAL. By maintaining the rest of the thresholds constant, a difference in energy of 0.07 Ha was obtained, between BSA and pob-TVPZ for calcite I. (Table 5.1).

In other words, just by increasing the richness of the basis set, a lower energy was obtained, in agreement with the variational theorem.

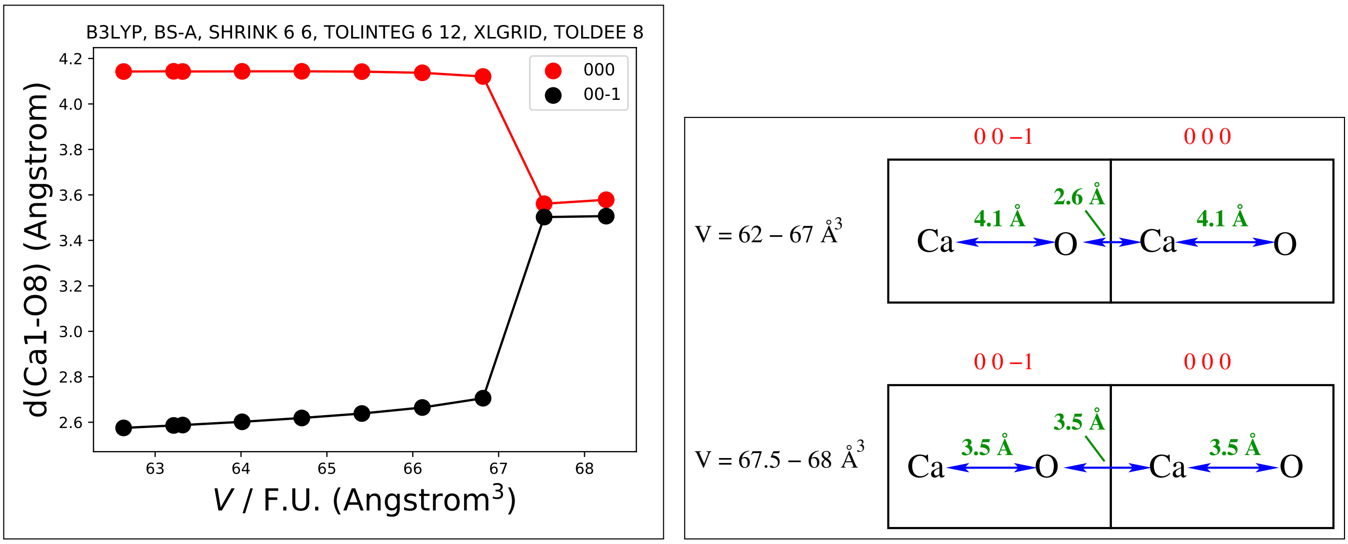

(a) **(b)**

Figure 5.3: 5.3a: Distance Ca1-O8 as a function of volume for calcite IIIb, in the reference 000 cell and the nearest 00-1 cell. From 62 to 67 $\AA^3$, two types of calcium-oxygen distances are observed: 2.6 and 4.1 $\AA$. From 67.5 $\AA^3$ onwards, the Ca1-O8 distance in both cells become equivalent. 5.3b: Schematic representation of both scenarios.

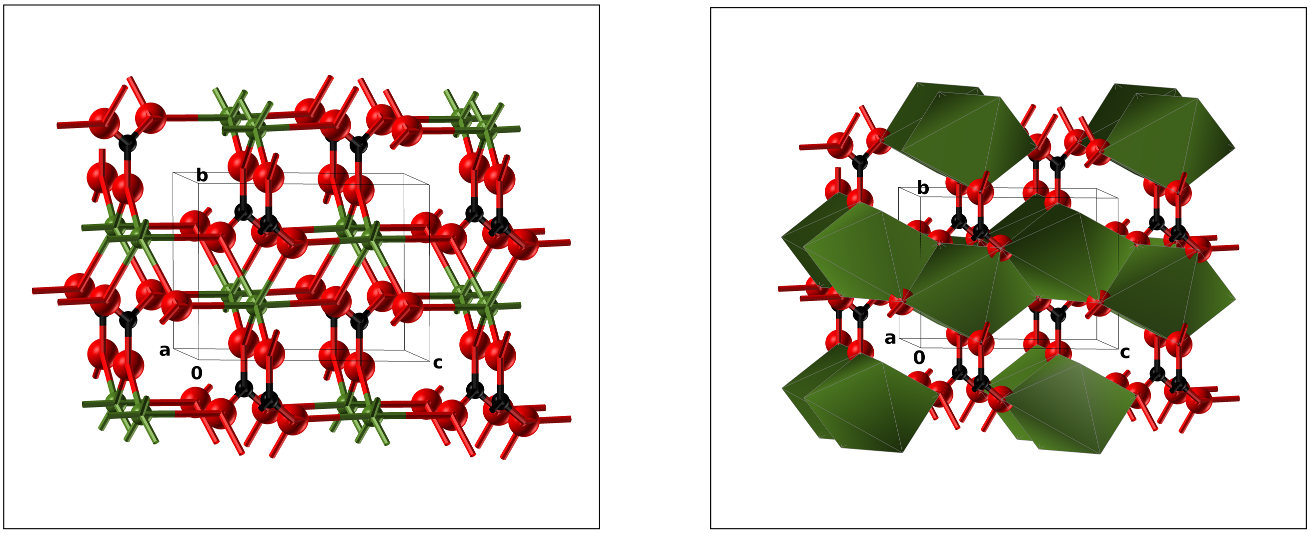

(a) **(b)**

Figure 5.4: Space group 13 ($P2/c$): (5.4a) shows the orientation of the carbonate groups in the structure. (5.4b) shows the packaging of octahedras

Within this basis set, we decided to tighten each of those computational parameters, one at at a time:

1. Firstly, several `TOLINTEG` parameters were studied for the Coulomb and exchange sums, i.e. 6-12, 7-14, 8-16, 9-18, 10-20, 11-21. All these tests were produced keeping constant the rest of the default computational parameters, i.e. `SHRINK` 6 6 and `XLGRID`. As can be displayed in Fig. 5.5a, convergence is reached at 8-16, which yields the same energy as

	Energy (Ha/F.U.)	Δ Energy
BSA, XLGRID, SHRINK 6 6, TOLINTEG 6-12	-941.510819247000	0.036 Ha/F.U. 95.29 KJ/mol
pob, XLGRID, SHRINK 6 6, TOLINTEG 6-12	-941.547122134500	

Table 5.1: A difference in energy of 0.036 Ha/F.U. or 95.29 KJ/mol is observed for calcite I between two different basis sets: BSA (triple-zeta valence with polarization quality for the calcium and oxygen atoms and double-zeta valence with polarization for the carbon atom) and pob-TVPZ (triple zeta in all three atoms of calcium, carbon and oxygen). All computational thresholds are maintained constant for this comparison.

the computationally expensive 10-20.

2. Secondly, the `SHRINK` parameter was tested at 2, 4, 6, 8 and 10. As can be seen in Fig. 5.5b, convergence is reached at `SHRINK 6`.

3. Finally, the DFT grid can be assessed through the error on the numerically integrated density. Since calcite I contains 100 electrons, we find that the default `XLGRID` setup yields an error on the numerically integrated density on the order of $3.25 \cdot 10^{-4}|e|$ out of a total of $100|e|$. On the contrary, a finer DFT grid such as `XXLGRID`, i.e. 99 radial (Gauss-Legendre radial quadrature) and 1454 angular points (two-dimensional angular points generation), yileds an error of $1.42 \cdot 10^{-4}|e|$ (Table 5.2).

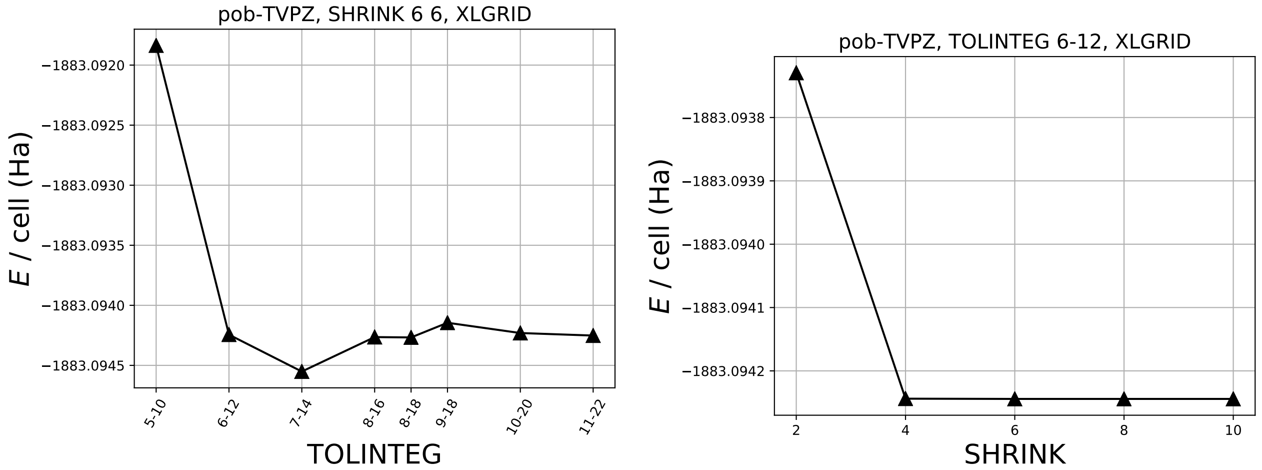

(a) **(b)**

Figure 5.5: Variation of the energy with the `TOLINTEG` and (Fig. 5.5a) `SHRINK` (Fig. 5.5a) thresholds.

As a result of this analysis, we decided to use a `TOLINTEG` 8-18, `SHRINK` 6 6 and the `XXLGRID` parameters.

Under this scheme, no change of symmetry was observed at all compressed and expanded volumes for calcite IIIb and VI. The realisation of this fact allowed us to confirm the urgent

	Numerically integrated density, @pob-TVPZ, TOLINTEG 6-12, SHRINK 6 6 ($\|e\|$)	Δ ($\|e\|$)
XLGRID	100.0003259339	$3.25 \cdot 10^{-4}$
XXLGRID	99.9998579240	$1.42 \cdot 10^{-4}$

Table 5.2: Calcite I numerically integrated density (in units of the charge of one electron). There are 100 electrons in the unit cell of calcite I, thus the exact value is $100|e|$. Using a finer grid (`XXLGRID`), the difference in the integrated density with respect to the exact value is $1.42 \cdot 10^{-4}|e|$.

need to tighten these computational parameters. However, we must highlight that, even though the symmetry is conserved along all the volumes explored, there are some jumps still remaining, as shown in Figs. 5.6a and 5.6b. These might correspond to pathways to phase transitions to other polymorphs. A frequency calculation at Γ was performed al all of these volumes of calcite IIIb and calcite VI shown in Fig. 5.6, and all frequencies were positive.

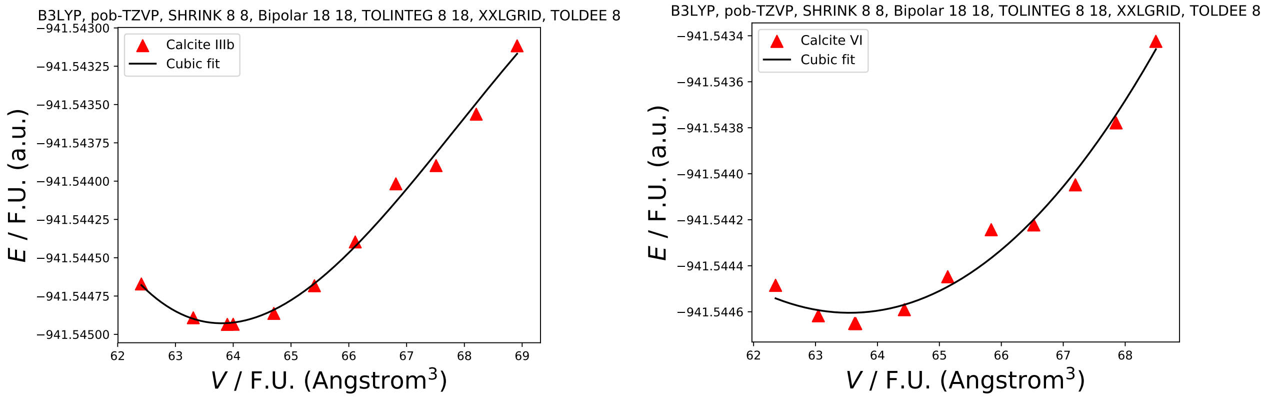

(a) **(b)**

Figure 5.6: Energy-volume curves for calcite IIIb and calcite VI using the pob-TVPZ basis set, and the tighter computational parameters described in the text. For all these volumes, a FINDSYM analysis yields a consistent P-1 space group, despite the fact that some jumps are also being observed. Both calcite IIIb and VI volumes present positive frequencies at the Γ point.

Chapter 6

Electronic structure of Calcite I

6.1 Electronic and charge distribution

When studying the electronic structure of a material, several questions arise, e.g. how are the electrons distributed in the solid, or how does the charge density look like. One way of addressing these questions is by studying the partial charges on atoms. Several methods have been developed for the determination of partial charges on atoms; these can be classified into methods based on the population analysis of wavefunctions (Mulliken [143, 144, 145, 146], Lowdin [147] or natural polulation analyses [148, 149, 150]), or those based on partitioning the electron density distribution, such as the Bader's atoms-in-molecules (AIM) technique [151, 152, 153]. None of the above methods give an accurate atomic charge, but nevertheless these are valid methods that allow us to have a general idea on the charge distribution.

A Mulliken analysis has been performed in the equilibrium volume of calcite I. This method provides a charge on the calcium atom of 18.220 times the charge of one electron, which means that the calcium atom is charged as +1.78 in the calcite I crystal (Table 6.1). Similarly, the Mulliken analysis predicts a charge of -8.851 and -5.227 for the oxygen and carbon atoms respectively. According to this, the carbonate group (CO_3^{2-}) would have a charge of -1.78, which compensates exactly the +1.78 in the calcium ion. The carbonate group in gas phase presents a charge of -2 delocalized over four atoms via three resonant forms (see Fig. 6.1). On the contrary, in a solid, this situation changes, because there is no longer an isolated carbonate group; instead, each oxygen atom is bonded to two calcium atoms (as described in Section 4.1), so that the charge must decrease. According to the Mulliken analysis, this charge is decreased from -2 to -1.78.

		Charge on each ion
$q_{\text{Ca atom}}$	-18.220	$\text{Ca}^{1.78+}$
Z_{Ca}	+20	
$q_{\text{O atom}}$	-8.851	$[\text{CO}_3]^{1.78-}$
Z_O	+8	
$q_{\text{C atom}}$	-5.227	
Z_C	+6	

Table 6.1: The result of the Mulliken Analysis of Calcite I shows that the calcium ion in the solid is charged positively with 1.78 times the charge of the electron and the carbonate group is charged negatively with 1.78 times the charge of the electron.

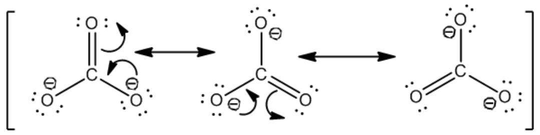

Figure 6.1: Three resonants forms of the carbonate group in gas phase. The charge of -2 is delocalized in the four atoms.

A more qualitatively analysis of the electronic density in the crystal can be obtained by choosing a plane of intersection, e.g. the 110 plane (Fig. 6.2a), and analyzing the electron density map projected on this plane (Fig. 6.2b). An almost spherical electron density can be identified for the calcium atom, as opposed to an elongated shape for the carbonate group due to this 110 plane is cutting the triangular shape of this group. Fig. 6.2c shows the 3D isosurface, and Fig. 6.2d a 3D orthoslice of the electron density parallel to the *c* axis, in which a maximum electron density is identified in the surroundings of the atoms (warm colors) as opposed to neighbour regions where the electronic density decreases (colder colors).

6.2 Electronic band structure and density of states

The purpose of this section is to show the electronic band structure of the calcite I crystal. We would like to show the valence and conduction bands, as well as the band gap obtained with different levels of theory. For the basis set chosen, i.e. pob-TVPZ for calcium, oxygen and carbon atoms, there are a total number of 190 atomic orbitals in the calcite I primitive cell (10 atoms / cell). Since there are a total number of 100 electrons (Table 6.2), and one band is occupied by 2 electrons, there will be 50 bands occupied. Thus, the last valence band

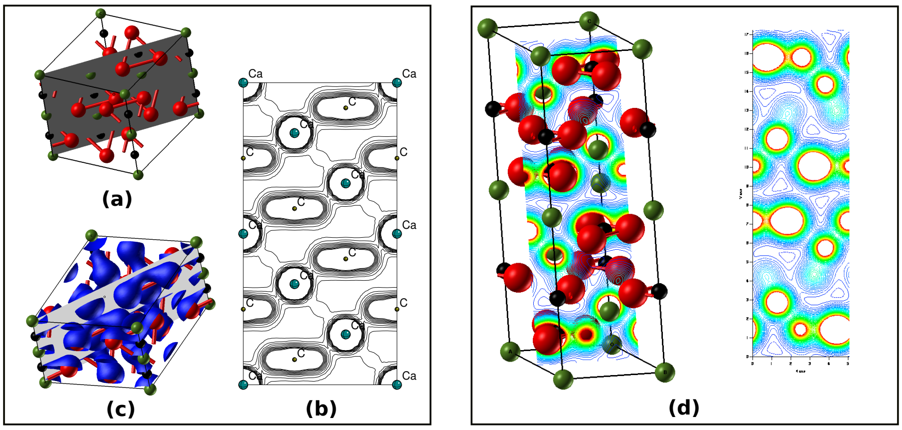

Figure 6.2: Fig. 6.2a shows the 110 plane, and 6.2b shows the electron density map projected on this plane. 6.2c shows the 3D isosurface. 6.2d shows a 3D orthoslice of the electron density parallel to the c axis.

will correspond to the 50th band, and the 51th band will belong to the conduction band (Fig. 6.3a).

The band gap will be then be given by the energy difference between the 50th and 51 bands.

	Total number of e^-/atom	Number of atoms in the primitive cell	Total number of e^-
Ca	20	2	40
C	6	2	12
O	8	6	48
			Total: 100 e^-

Table 6.2: Number of electrons per atom and total number of electrons in the primitive cell. There is a total of 100 electrons for calcite I.

The calculated and experimental band gaps for calcite I are reported in Table 6.3. Reflection electron energy-loss spectroscopy (REELS) experiments reveal a value of 0.2205 ± 0.01 Hartree for the band gap [154]. Our theoretical calculations show that GGA type of functional slightly underestimates this band gap. On the contrary, the hybrid functional clearly overestimates it. The value of the band gap is independent on the inclusion of dispersion. Finally, the LDA approximation yields a significantly lower value, as it is well known for this level of theory to give underestimated band gaps [155]. In any case, this material is undoubtedly an insulator.

Each set of bands has been grouped and labelled as “Peaks” in Fig. 6.3a. Each of these set of bands are displayed in a density of states plot (Fig. 6.3b), where the contribution of each atom is shown in green, black, red for calcium, carbon and oxygen respectively. The total density of states as a sum of the individual contributions is shown in blue. The contribution of each atom to each peak is something that cannot be easily observed in this plot. A zoomed version of each peak is shown in Fig. 6.4. First peak has a major contribution of calcium atom, while third, fifth and sixth contain a major contribution of oxygen atom.

Level of theory	Band Gap (eV)	Band Gap (Ha)
PBE and PBE-D3	5.2855	0.1942
B3LYP and B3LYP-D3	7.5217	0.2764
LDA	4.9238	0.1809
Experimental [154]	6.0 ± 0.35	0.2205 ± 0.01

Table 6.3: Band gaps obtained for calcite I, for PBE and B3LYP (with and without dispersion) and LDA levels of theory, well as the experimental value.

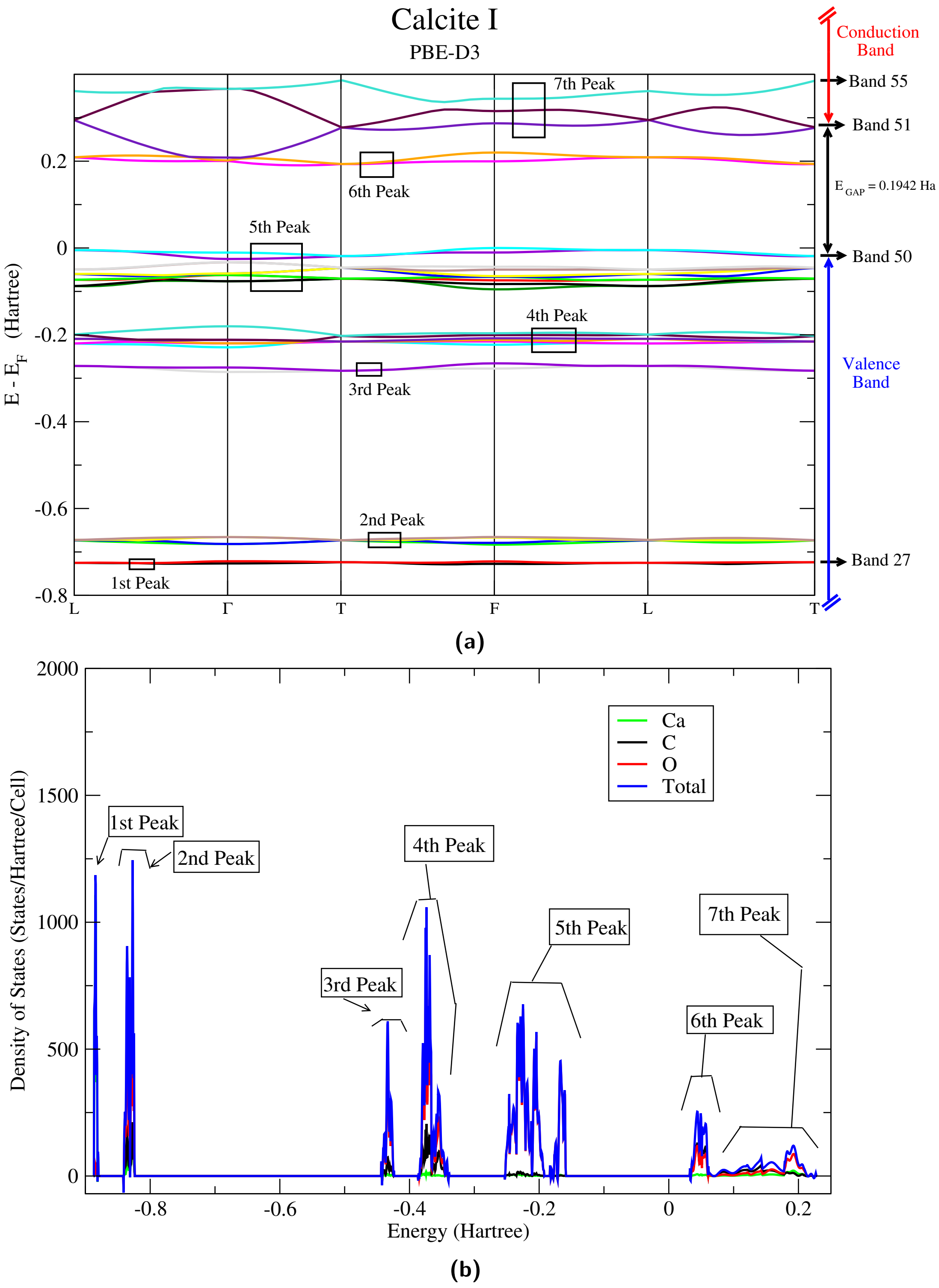

Figure 6.3: Fig. 6.3a: Electronic band structure for Calcite I. In the y axis, the difference in energy between the absolute value of energy of each band and the energy of the Fermi level. The selected path of $\mathbf{K}$ points chosen contains the higher symmetry $\mathbf{K}$ points from the First Brillouin Zone shown in Fig. 4.5. The conduction band starts at band 51. The GAP energy, defined as the energy difference between the Fermi energy and the minimum value reached by band 51, is is found to be 0.1942 Hartree for the PBE-D3 level of theory. In the graph it has been identified a set of bands: Peak 1—Peak 2, which correspond to the homologous peaks shown in the density of states (Fig. 6.3b).

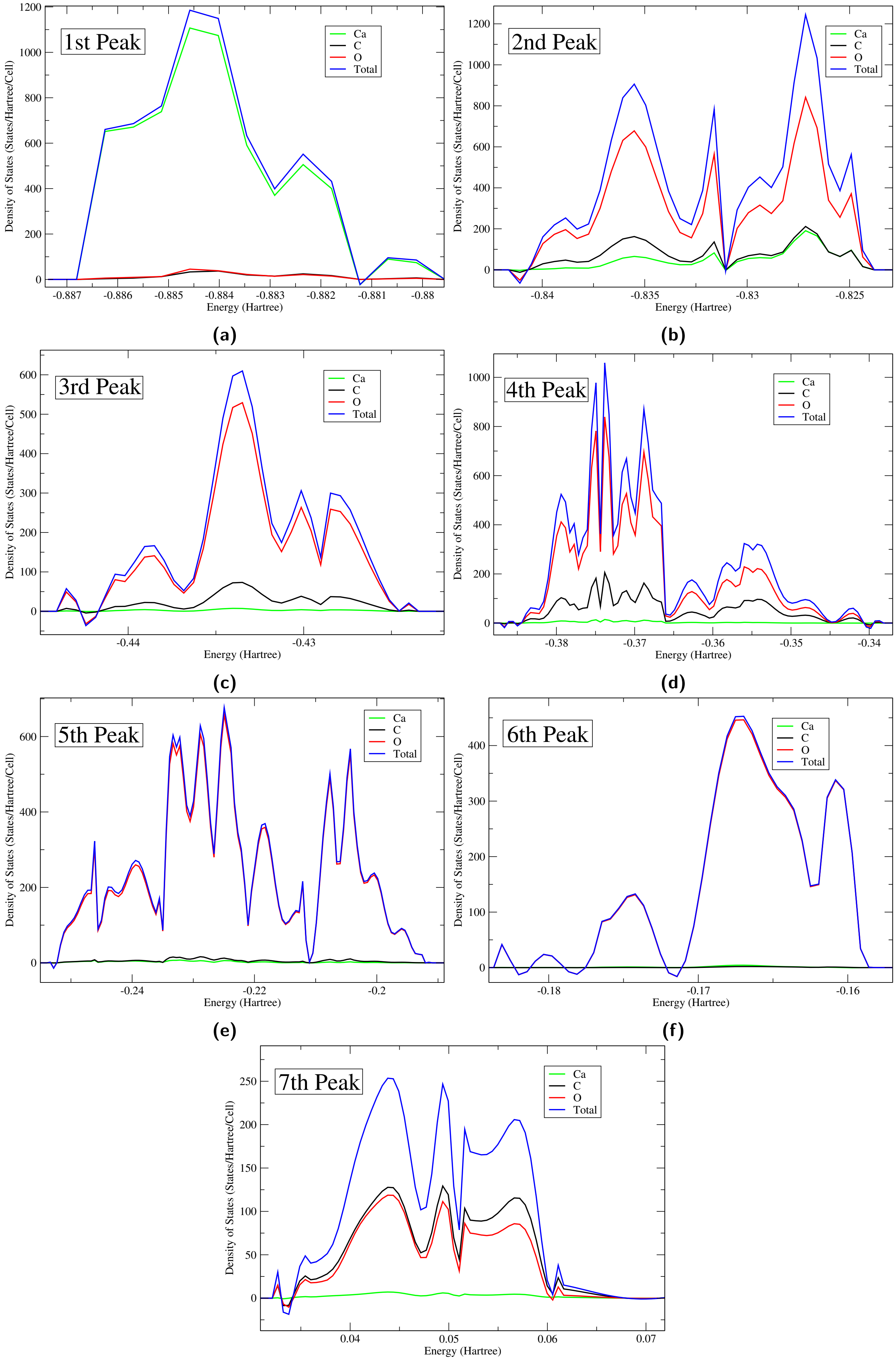

Figure 6.4: Density of states of calcite I, in which each set of peaks 1 - 7 shown in Fig. 6.3b is magnified.

Chapter 7

Calcite I - calcite II phase transition

7.1 Literature review on the CI-CII phase transition

The calcite I - calcite II transformation is an example of a soft phonon mode phase transition. Pioneer works on the understanding of soft phonon modes mechanisms were mainly devoted to perovskites (e.g. $BaTiO_3$ and $SrTiO_3$) where the high symmetry phase is cubic and the low symmetry is tetragonal (e.g. the well known $SrTiO_3$ transition at 104 K and $P = 0$ [156]). The calcite I - calcite II phase transition, even though mechanistically simple (a rotation and a small displacement), it however involves a noncubic, more complex system (the higher symmetry is trigonal and the lower symmetry is monoclinic). In this respect, first principles lattice dynamical simulations of this phase transition are needed. Most studies focused on the sole effect of pressure on the phase transition, while few of them explicitly explored the combined effect of pressure and high temperature. At room temperature, when applying pressure, a first order phase transition is observed, from calcite I (trigonal, $R\overline{3}c$) to calcite II (monoclinic, $P2_1c$), at about 1.5 GPa [113, 119, 12, 157, 136, 158, 17, 114, 159]. Volumetric and compressibility experiments at room temperature were performed by Vaidya *et al.* [160] and Singh *et al.* [161], where a polynomial $V(P)/V_0$ relation was addressed for both polymorphs. Synchrotron X-ray diffraction experiments conducted by Suito *et al.* [12] in 2001 and Merlini *et al.* [17] in 2012 also studied the effect of pressure at ambient temperature, as shown in Fig. 7.1. On the contrary, partially contradicting accounts have been reported as regards the explicit characterization of the corresponding phase boundary as a function of both temperature and pressure. The temperature - pressure phase boundary was first investigated using volumetric measurements by Bridgman in 1938 [113], up to 473 K and 2.8 GPa. A slightly negative slope of the temperature - pressure phase boundary was reported (Fig. 7.1). By studying the velocity of compressional waves of ultrasonic frequencies up to 453 K and 1.5 GPa, Wang *et al.* [158] also reported in 1968 a slightly negative slope, almost parallel to the one reported by Bridgman (Fig. 7.1). Raman spectroscopic techniques were performed by Fong *et al.* [162] and Hess *et al.* [119]. In particular, the latter conducted experiments up to 4 GPa and 623 K, and described a positive slope for the calcite I - calcite II phase transition. Suito *et al.* [12] supported the occurrence of a negative slope by a thermodynamic analysis based on the Clapeyron equation, assuming a negative change in volume and a positive change in entropy upon transition (we will further discuss this point in Section 7.7.) Most of the above mentioned results from the literature are summarized in Fig. 7.1.

A second order phase transition at higher temperatures has been suggested in several studies ([157, 136, 163, 159].) This will be covered thoroughly in Section 7.13.1, in which our findings regarding a change in the order of the transition will be presented.

Clearly, some aspects of the calcite I to calcite II phase boundary are still to be fully understood. In particular, the sign of the slope of the phase boundary as a function of temperature is debated. Experimental measurements with the associated error bars (also shown on Fig. 7.1) might not allow for a definitive conclusion. Several molecular dynamics simulations using empirical interatomic potentials overestimate the transition pressure, i.e., 3.2 GPa [164] or 8.3 GPa [165]. Thus, theoretical first-principles lattice-dynamical simulations could help to clarify and shed new light on this respect, as they allow for an atomistic description and understanding of energetic, structural, mechanical and thermodynamic aspects of phase transitions. Additionally, atomistic simulations are needed to address a possible change in the order of the transition at higher temperatures. While the only such theoretical study previously reported solely addressed the description of the transition pressure at zero kelvin (Ukita *et al.* [166]), an explicit investigation of the combined effect of temperature and pressure on the phase boundary is still to be examined.

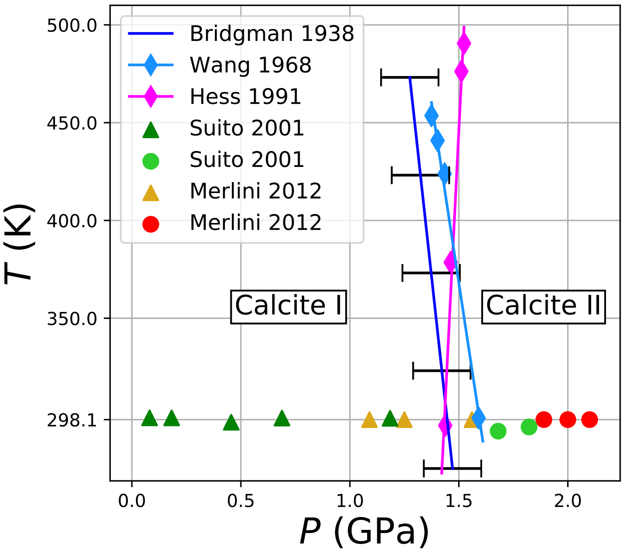

Figure 7.1: Temperature - pressure experimental data for calcite I (triangles), calcite II (circles) obtained by Merlini *et al.* and Suito *et al.*, together with the calcite I - calcite II phase boundary represented with diamonds (Wang *et al.*, Hess *et al.*) and by a line (Bridgman) with the experimental error bars associated.

7.2 The theoretical approach

In order to successfully compute the phase boundary of this phase transition as a function of temperature and pressure, we need to take into account the combined and simultaneous effect of these two thermodynamic variables in our simulations.

The sole effect of pressure can be easily taken into account if the structure is fully relaxed through a volume constraint geometry optimization process. If this process is repeated over a series of equidistant volumes ranging from compression to expansion [141], a energy-volume or pressure-volume relation equation of state is obtained, which describes the behaviour of a solid under compression and expansion in the athermal limit. On the contrary, the inclusion of temperature is not so straightforward to implement. As has been explained in the Methodology Chapter (Chapter 3), different approaches can be considered. The Quasi-harmonic approximation was the method of choice most suitable for our pressure-temperature phase boundary purpose, due to the reasons explained in that chapter.

In this chapter, we will show the results obtained by performing DFT lattice dynamical simulations. These will provide a thermodynamic insight of the phase boundary, in which different functionals from different families have been used: generalized-gradient approximation (Perdew-Burke-Ernzerhof, PBE) and hybrid (Becke-three parameters-Lee-Yang-Parr, B3LYP).

Furthermore, the inclusion of weak dispersion interactions will also be considered in terms of the Grimme's D3 correction. All simulations are performed using all-electron basis sets instead of pseudo-potentials, as it has been recently shown to be of particular relevance since core electrons can participate in the chemical bond when materials are under high pressure conditions [167].

7.3 Mechanism of the phase transition in the athermal limit

Calcite I cell is trigonal, space group 167 ($\mathrm{R\overline{3}c}$), with two formula units per cell, while calcite II is monoclinic, s.g. 14 ($P2_1c$), with four formula units per cell. The phase transition mechanism is driven by the softening of the phonon mode located at the F k-point of the first Brillouin zone [114, 136]. Because of the symmetry of the trigonal crystal, F has several symmetry equivalent k-points in the first Brillouin zone: $[\pm\frac{1}{2}, \pm\frac{1}{2}, 0]$, $[\pm\frac{1}{2}, 0, \pm\frac{1}{2}]$ or $[0, \pm\frac{1}{2}, \pm\frac{1}{2}]$ (see the representation of the First Brillouin Zone for the trigonal crystal shown in Fig. 4.5). Hatch and Merril [136] explained this phase transition in terms of the Landau theory of phase transitions. In that study, the transformation matrix between the trigonal lattice of calcite I to the monoclinic lattice of calcite II has been rationalized to be:

$$\begin{bmatrix} 1 & 0 & 0 \\ 0 & -1 & 1 \\ 1 & -1 & -1 \end{bmatrix} \tag{7.1}$$

This supercell will be labelled as "Landau supercell" from now on throughout this thesis.

We started by performing full structural relaxations of both calcite I and calcite II. The full optimization gives the equilibrium volume in the athermal limit, V_{eq} (no zero point energy effects are considered at this point). An unconstrained geometry optimization of calcite II yields a configuration that is energetically and structurally identical to calcite I because the optimization process is performed at zero pressure and zero temperature, and in those conditions calcite I is the most stable phase. Secondly, we performed volume constraint geometry optimisations of the calcite I structure at different degrees of compression and expansion, as implemented in the

CRYSTAL17 program [141]. The corresponding energy-volume curve is reported in Figure 7.2 for the PBE-D3 level of theory. At that point, in order to check whether or not calcite I was mechanically and energetically stable at different compressed and expanded configurations, we computed harmonic phonons at each volume by sampling the phonon dispersion at both the Γ and F k-points.

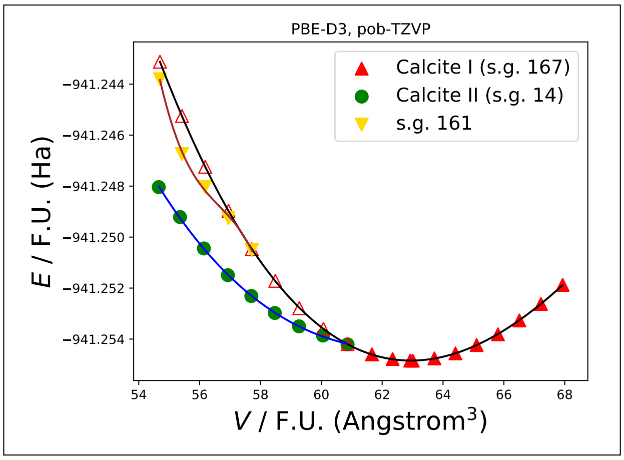

Figure 7.2

Volume / F.U. ($\AA^3$)	% compression	k-point	Imaginary Frequency	S.G. found (0.1. Tol)
54.6958	15.04%	Gamma	-99.0651	161
		[0, 0.5, 0.5]	-87.0462	14
55.4201	13.54%	Gamma	-88.6188	161
		[0, 0.5, 0.5]	-81.3470	14
56.1833	11.99%	Gamma	-73.8666	161
		[0, 0.5, 0.5]	-74.4209	14
56.9484	10.49%	Gamma	-60.6482	161
		[0, 0.5, 0.5]	-67.6441	14
57.7162	9.02%	Gamma	-40.8219	161
		[0, 0.5, 0.5]	-59.9609	14
58.4872	7.58%	[0, 0.5, 0.5]	-52.6922	14
59.2756	6.15%	[0, 0.5, 0.5]	-43.6047	14
60.0669	4.75%	[0, 0.5, 0.5]	-32.6514	14
60.8627	3.38%	[0, 0.5, 0.5]	-16.9922	14

Table 7.1

Fig. 7.2 shows the electronic energy as a function of volume for calcite I, calcite II and the space group 161 found. Calcite I volumes that present imaginary frequencies are shown with empty red triangles. Stable calcite I volumes are represented with filled red triangles. All data is fitted to a cubic polynomial and PBE-D3 level of theory. Table 7.1 summarizes the imaginary frequencies found in all the explored constrained volumes of calcite I for the PBE-D3 level of theory. The space group found is a result of a symmetry search (imposing a low tolerance) over the broken symmetry structure found as a consequence of the distortion of the atomic positions along the phonon eigenvector. Space groups 14 and 161 have no imaginary frequencies at the $\mathbf{\Gamma}$ point

Harmonic phonon frequencies at k-points different from Γ are computed by diagonalizing the dynamical matrix [168, 169], and building a supercell (the one described in eq. 7.1), following a direct-space approach [80, 170, 171, 172].

For all of the expanded configurations, all the frequencies are found to be positive, which is also the case for the equilibrium volume and for all compressions below 3.4% for the PBE-D3 level of theory (Table 7.1). The volumes with positive frequencies are shown with filled red triangles (calcite I). On the contrary, volumes with imaginary frequencies are shown with empty red triangles. For all compressions greater or equal than 3.4%, an imaginary frequency appears at the F k-point in the phonon dispersion (-16.99 cm^{-1} for 3.4% compression, becomes -87.05 cm^{-1} for 15.04% compression for PBE-D3 level of theory, see Table 7.1). Additionally, for compressions greater than 9%, an extra imaginary frequency appears at the $\mathbf{\Gamma}$ point.

Both the normal mode at the F k-point and the one at Γ correspond to a rotation of the carbonate groups and to a small displacement of calcium atoms. The eigenvectors of both phonon modes are shown on Fig. 7.3c. There is a clear difference in the relative displacements: in the phonon mode at the F k-point, calcium atoms and carbonate groups in different planes move in opposite directions, while in the phonon mode at Γ they move in the same direction. An animation for both eigenvectors can be found in Ref. [173]. The normal mode at the F k-point has already been identified through DFT lattice dynamical calculations by Ukita *et al.* [166]. On the contrary, the normal mode at Γ point has not been reported, to our knowledge.

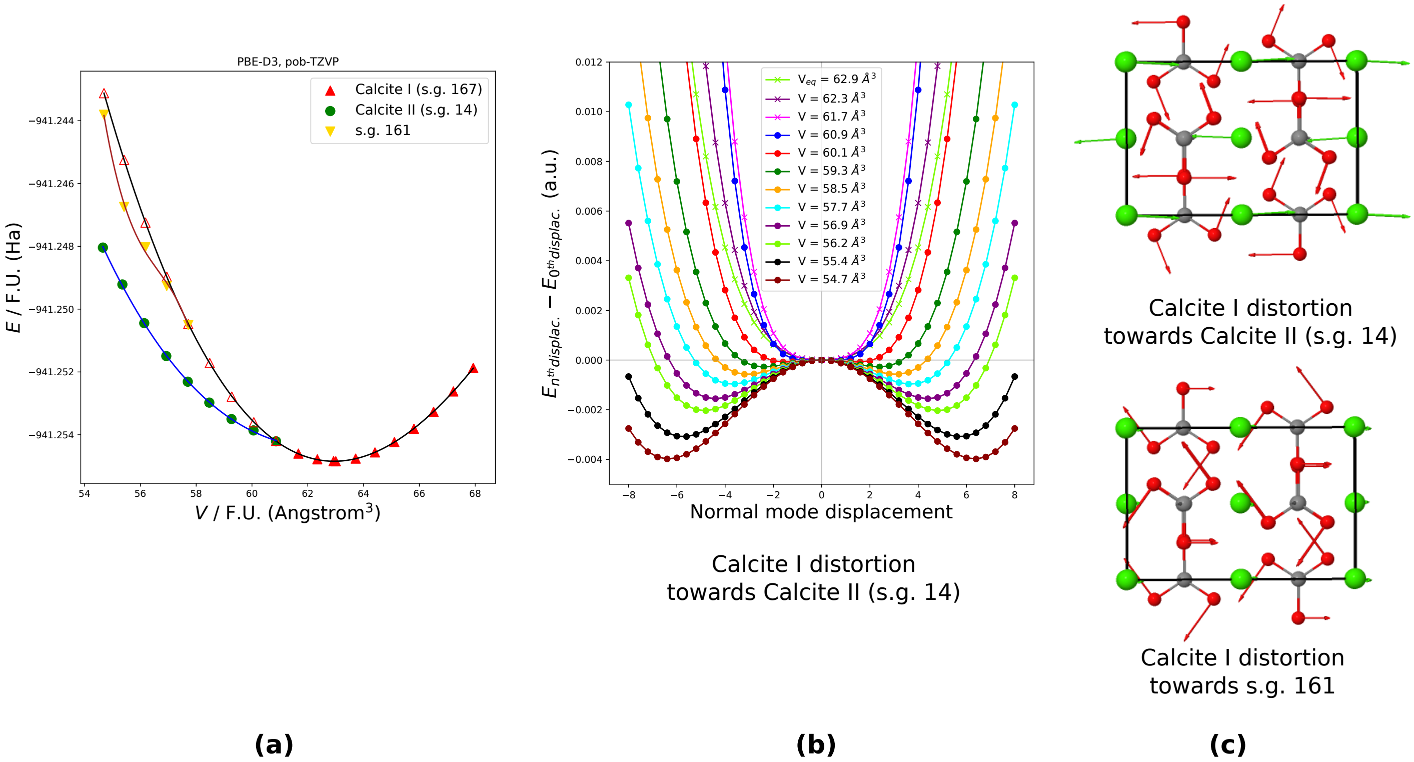

Figure 7.3: (a): Energy-volume data for calcite I, calcite II and space group 161. (b): Energy as a function of the displacement for the soft phonon mode that leads to space group 14 (calcite II). (c): Eigenvectors for the distortion that leads to space group 14 and 161. An animation of both eigenvectors represented in (c) can be found in Ref. [173]

We have performed energy scans along this normal coordinate at all the volumes where we observed the imaginary frequency. The corresponding results are shown on Fig. 7.3b for the eigenvector at the F k-point. The same scan is also performed for the equilibrium volume and for a couple of compressed volumes (2% and 0.92% compression), where that frequency was still positive. We can see that the curves referring to volumes where the frequency is positive show a minimum of the energy at zero normal displacement along the normal mode. On the contrary, for the most compressed volumes, two new broken symmetry minima appear, whose depth increases with compression. These two minima are equivalent to each other, arise from a positive and negative normal mode displacement, and correspond to the distortion that yields to the calcite II structure. The space group of this broken symmetry structure at the minimum has been deduced with the FINDSYM program [174]. When running this program, a threshold corresponding to the accuracy to which dimensions of the unit cell and positions of atoms are known has to be defined. Different space groups can be obtained depending on this parameter: If the threshold is very tight (10^{-6}), almost always the less symmetry space group is obtained, i.e. $P1$ (space group 1), as shown in Table 7.2. If the threshold is less tight (10^{-2}), space group 7 is obtained. Finally, if the threshold is 10^{-1}, the desired space group 14 is obtained. A further constant volume geometry optimization is performed using as an input the coordinates and lattice parameters printed on the CIF file generated with FINDSYM for a tolerance of $1 \cdot 10^{-1}$. This process is repeated at at each volume, so that the calcite II curve is obtained (see green circles in Fig. 7.3a). Similar energy scans were performed for the imaginary frequency at Γ point. In the same way, a FINDSYM analysis of the broken symmetry structure produces the structure labelled as space group 161. A further constant volume geometry optimization of this structure under this space group produces the yellow triangles in Fig. 7.3a. As can be seen in that figure, space group 161 is less stable than calcite II, but slightly more stable than calcite I at the highest pressure studied.

Tolerance ($\mathring{A}$)	S.G. found
$1 \cdot 10^{-6}$	$P1$ (1)
$1 \cdot 10^{-5}$	$P1$ (1)
$1 \cdot 10^{-4}$	$P1$ (1)
$1 \cdot 10^{-3}$	$P1$ (1)
$1 \cdot 10^{-2}$	Pc (7)
$1 \cdot 10^{-1}$	$P2_1/c$ (14)

Table 7.2: Different space groups obtained when analyzing the symmetry of the structure at the bottom of the curve (Fig. 7.3b) of the most compressed calcite I volume ($54.7\mathring{A}^3$). The column "Tolerance" refers to a FINDSYM threshold in $\mathring{A}$ on the lattice parameters and atomic coordinates. Both the symbol and the space group number corresponding to that symbol in parentheses are shown on the second column.

The structural changes that lead to calcite II have been described by an angle θ and a displacement Δ and are graphically introduced in Fig. 7.4. This provides the natural way of breaking symmetry and induce the correct structural changes to transform from calcite I to calcite II. In order to establish a link between the different volumes at which the calculations were performed

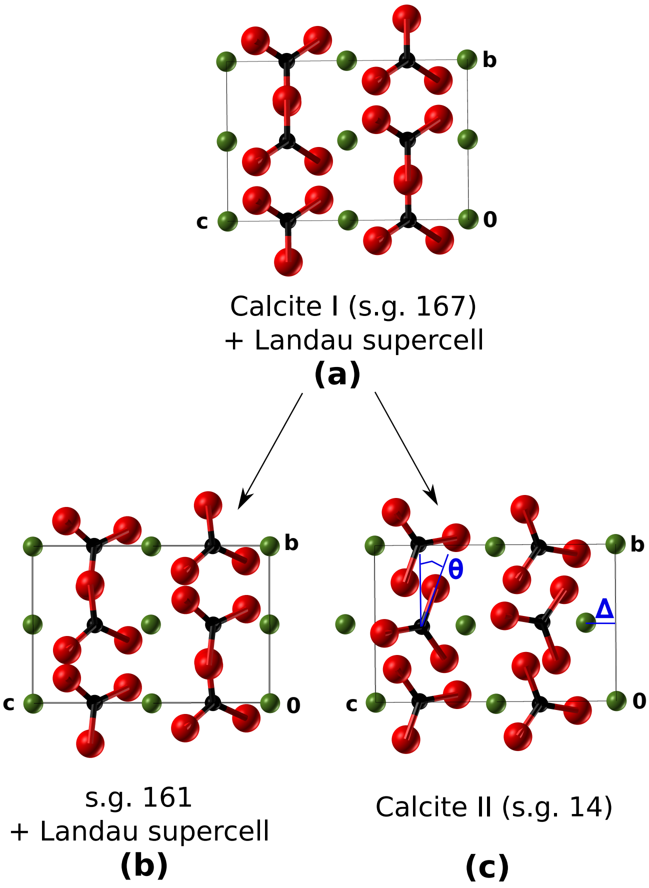

Calcite I (s.g. 167)
+ Landau supercell
(a)

s.g. 161
+ Landau supercell
(b)

Calcite II (s.g. 14)
(c)

Figure 7.4: Calcite I in the Landau supercell representation (Fig. 7.4a) shows two pathways of transformation via imaginary phonon modes: towards space group 161 (Fig. 7.4b) through the softening of a phonon mode at Γ, or towards space group 14 (Fig. 7.4c) through the softening of a phonon mode at the F k-point.

and pressure, the energy-volume data reported in Fig. 7.2a has been fitted to a third order polynomial. The corresponding pressure at 0 K is computed as $P = -\frac{\partial E(V)}{\partial V}$. Fig. 7.5b shows the evolution of θ and Δ as a function of pressure, as determined with the four levels of theory considered (here, data still corresponds to 0 K). At pressures below the transition pressure, both parameters are zero in calcite I. As soon as the transition pressure is reached, a sharp increase is observed, increasing regularly as a function of pressure.

This increase of Δ and θ upon compression is graphically shown on the lower panel of Fig. 7.5a, where the structure of calcite I at the volume constraint of 60.9 $\AA^3$ together with three chosen volumes for calcite II are shown: 54.7, 56.2 and 60.9 $\AA^3$. For a volume constraint of 60.9 $\AA^3$, both calcite I and II structures are identical, which is in agreement with the fact that both structures have the same energy (upper panel Fig. 7.5a). For a volume constraint of 54.7 $\AA^3$, both Δ and θ reach the maximum value studied (0.97 $\AA$ and 19.5° respectively, for the PBE-D3 level of theory). It can also be noted that inclusion of dispersion interactions in the

DFT functionals produces an increase of the structural modifications in calcite II: for instance, the values of Δ and θ are higher in PBE-D3 and B3LYP-D3 compared to PBE and B3LYP.

Merril and Basset [114] reported an experimental 11 degree rotation of the carbonate groups at the transition pressure of 1.5 GPa. The experimental structure provided by these authors corresponds to a pressure of 1.8 GPa, where the angle is 13 degree and the displacement is 0.52 Å. We see that both dispersion corrected functionals, and in particular B3LYP-D3 provide structural changes that are found to agree with these experimental values.

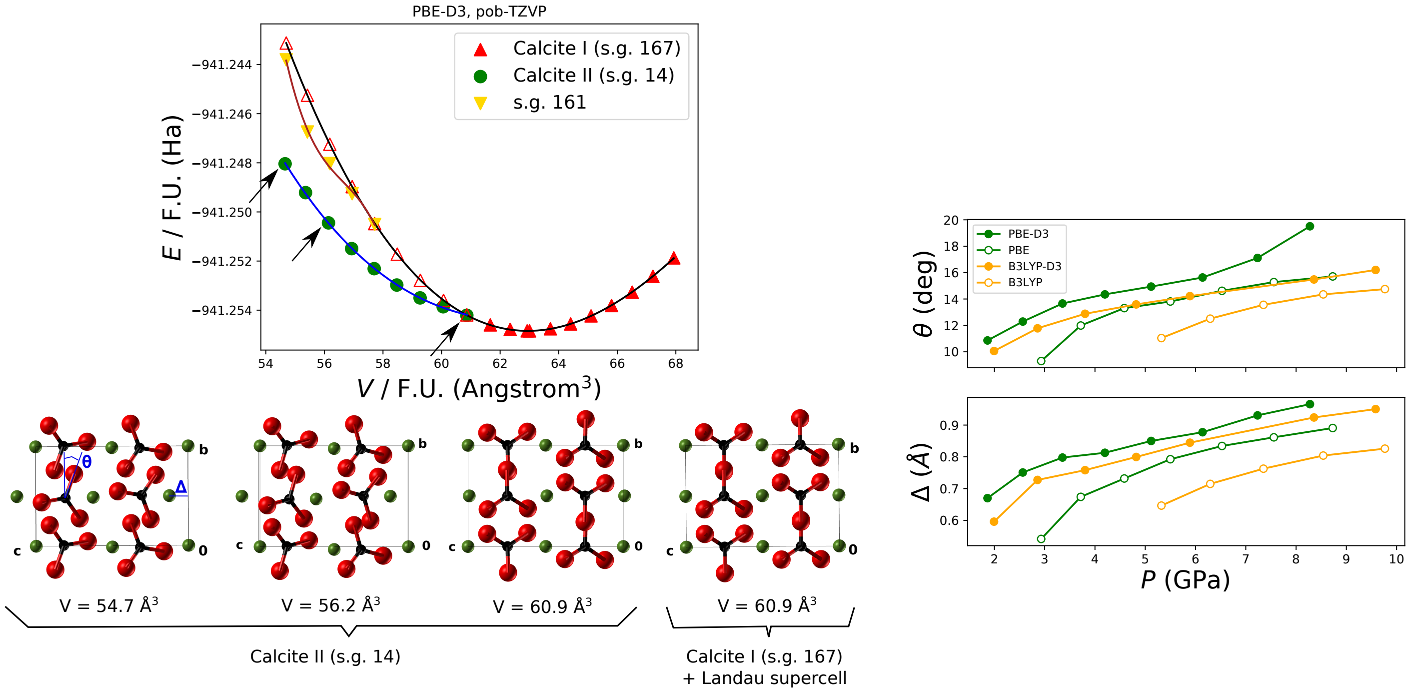

(a) **(b)**

Figure 7.5: Fig. 7.5a, upper panel: Energy-volume curves for calcite I, II and space group 161. The structure of each of the calcite II volumes highlated with an arrow (54.7, 56.2 and 60.9 $\AA^3$) are shown in Fig. 7.5a, lower panel, together with the calcite I structure at the same $V = 60.9 \AA^3$. Fig. 7.5b: evolution of θ and Δ as a function of the athermal pressure, for the four levels of theory studied: PBE-D3, PBE, B3LYP and B3LYP-D3.

A great amount of information can be extracted by studying this phase transition across functionals. For the GGA case, without dispersion (PBE), a greater level of compression is required (5.79%) in order to detect the imaginary phonon mode that leads to calcite II, as shown on Table 7.3 and Fig. 7.6. As said previously, just the inclusion of dispersion (PBE-D3) reduces the level of compression to 3.4% (Table 7.1). This is also true for hybrid functionals: 7% compression is needed for B3LYP (Table 7.4), as opposed to just 4.5% for B3LYP-D3 (Table 7.5). As is clearly shown in Fig. 7.4, this behaviour is intrinsically related with the nature of the calcite I to calcite II phase transition: In calcite I (Fig. 7.4a), carbonate groups are pointing in the same direction, and there is a greater repulsion effect due to electronic clouds being close to each other. When calcite I transforms to calcite II (Fig. 7.4c), the rotation of carbonate groups in opposite direction, as well as the small displacement of calcium atoms contribute to an overall decrease of this esteric effect. The inclusion of dispersion interactions in the functional allow to take into account long range interactions such as those that appear when atoms are at greater distance. In calcite II there is a large number of those long range interactions. Therefore, the inclusion of dispersion effects (PBE-D3 and B3LYP-D3) allows to better capture these interactions on calcite II, which in turn makes the level of compression required to observe calcite II, to be lowered with respect to modelling the transition with a level of theory that does not account for long range interactions (PBE and B3LYP). On the contrary, the level of compression required to observe the instability at Γ that leads to s.g. 161 is roughly the same for PBE and PBE-D3 (around 9% compression). The only explanation for this is again the nature of the phase transition that leads to space group 161, which is slightly different: the carbonate groups rotate in the same direction, which results in s.g. 161 containing carbonate groups slightly rotated, but still facing directly one to each other. Because of this slight rotation in the same direction, a direct comparison of s.g. 161 (Fig. 7.4b) and calcite I (Fig. 7.4a), shows that the amount of repulsion effects is greater in s.g. 161. In other words, the number of short range interactions is greater than the amount of long range. This results in dispersion effects not having such an important effect for describing the calcite I to s.g. 161 phase transition. In summary, we have found that:

- If the soft phonon mode phase transition leads to a structure in which the amount of long range interactions has been increased, i.e. there is an overall decrease of repulsion effects between electronic clouds, the inclusion of dispersion will lower down the level of compression needed in order to start detecting the imaginary frequency. This has been found to occur in the calcite I to calcite II phase transition, where PBE and PBE-D3 require a level of compression of 5.79% and 3.4% respectively. This statement also holds true for hybrid functionals, where B3LYP and B3LYP-D3 require levels of compression of, respectively, 7% and 4%.

- If the soft phonon mode phase transition leads to a structure in which the amount of short range interactions has been increased, i.e. there is an overall increase of repulsion effects between electronic clouds, the inclusion of dispersion, and so the inclusion of long range interactions will not have a significant effect on the level of compression needed in order to start detecting the imaginary frequency. This has been found to occur in the calcite I to s.g. 161 phase transition, where both PBE and PBE-D3 levels of theory require around 9% compression. While this last argument is found to be valid for GGA, on the other hand, this explanation is not so valid for hybrid functionals, since an unequal level of compression has been found for B3LYP and B3LYP-D3: the first one requires a 12% level of compression, as opposed to 8% for the second one.

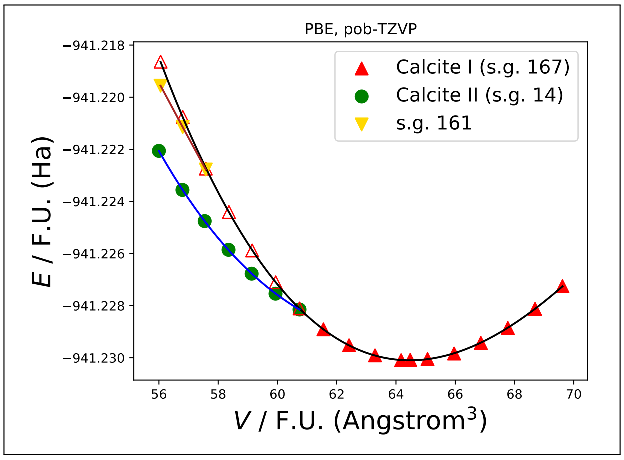

Figure 7.6

Volume / F.U. ($\AA^3$)	% Compression	k-point	Imaginary Frequency	S.G. found (0.1. Tol)
56.0571	13.06%	Gamma	-78.3283	161
		[0, 0.5, 0.5]	-76.5672	14
56.8045	11.90%	Gamma	-64.4728	161
		[0, 0.5, 0.5]	-70.0812	14
57.5820	10.70%	Gamma	-45.5676	161
		[0, 0.5, 0.5]	-62.6908	14
58.3625	9.49%	Gamma	-14.5807	167 [a]
		[0, 0.5, 0.5]	-55.5251	14
59.1467	8.27%	[0, 0.5, 0.5]	-46.8729	14
59.9407	7.04%	[0, 0.5, 0.5]	-37.3304	14
60.7459	5.79%	[0, 0.5, 0.5]	-23.7625	14

Table 7.3

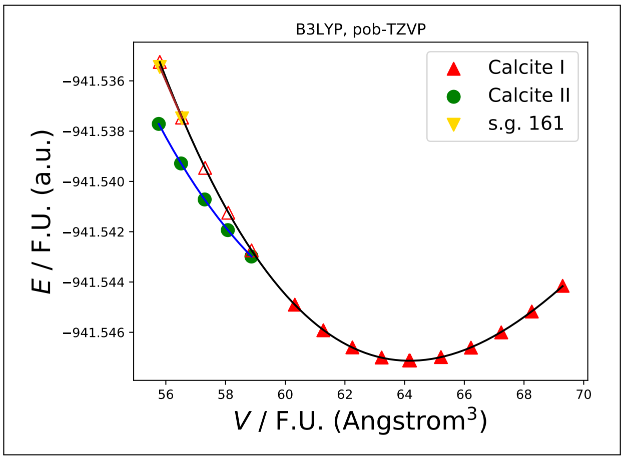

Figure 7.7

Volume	% compression	k-point	Imaginary Frequency	S.G. found (Tol. 0.1)
55.7969	13.06%	Gamma	-51.5206	161
		[0, 0.5, 0.5]	-66.3997	14
56.5438	11.90%	Gamma	-28.1521	161
		[0, 0.5, 0.5]	-59.5391	14
57.3161	10.69%	[0, 0.5, 0.5]	-51.0784	14
58.0920	9.48%	[0, 0.5, 0.5]	-41.0868	14
58.8718	8.27%	[0, 0.5, 0.5]	-28.8782	14
59.6634	7.04%	[0, 0.5, 0.5]	-3.6351	14

Table 7.4

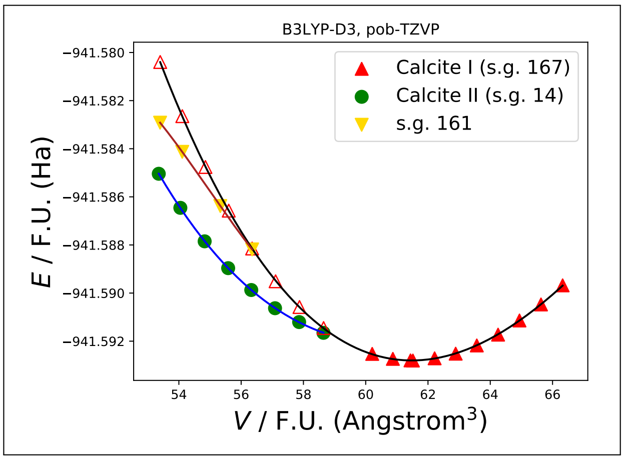

Figure 7.8

Volume / F.U. ($\AA^3$)	% compression	k-point	Imaginary Frequency	S.G. found (Tol. 0.1)	Constant volume optimization, followed by FINDSYM analysis. S.G. found (Tol. 0.1)
53.4001	13.08%	Gamma	-94.0810	161	
		[0, 0.5, 0.5]	-85.3680	14	
54.1105	11.93%	Gamma	-84.1995	161	
		[0, 0.5, 0.5]	-79.9728	14	
54.8531	10.72%	Gamma	-71.1906	7	14[b]
		[0, 0.5, 0.5]	-73.3793	7	14[b]
55.6016	9.50%	Gamma	-55.0033	161	
		[0, 0.5, 0.5]	-66.1821	14	
56.3525	8.28%	Gamma	-32.5851	161	
		[0, 0.5, 0.5]	-58.4583	14	
57.1063	7.05%	[0, 0.5, 0.5]	-49.6819	14	
57.8734	5.80%	[0, 0.5, 0.5]	-40.2551	14	
58.6478	4.54%	[0, 0.5, 0.5]	-28.3388	14	

Table 7.5

(Caption next page)

Figs. 7.2, 7.6, 7.7 and 7.8 show the electronic energy as a function of volume for calcite I, calcite II and the space group 161 found, for the PBE-D3, PBE, B3LYP and B3LYP-D3 levels of theory respectively. Those calcite I volumes that present imaginary frequencies are shown with empty red triangles. Calcite I volumes that do not present imaginary frequencies are represented with filled red triangles. Calcite II is represented with green filled circles. The space group 161 is shown in filled yellow triangles. Tables 7.1, 7.3, 7.4 and 7.5 summarize the imaginary frequencies found in all the explored constrained volumes of calcite I. All data is fitted to a cubic polynomial. Note [a] in Table 7.3: the scanmode over the imaginary frequency -14.5807 cm^{-1} does not yield a minimum, hence, the space group of this structure remains 167 (calcite I). Note [b] in Table 7.5: the scanmode around the imaginary frequencies -71.1906 and -73.3793 cm^{-1} yields space group 7. A constant volume optimization of these two structures, followed by a FINDSYM analysis yields space group 14. These two structures have the same energy. For all levels of theory, the space groups 14 and 161 found have no imaginary frequencies at the $\mathbf{\Gamma}$ point.

7.4 Automation of the process

After having introduced in detail how to isolate a structure coming from a soft-phonon mode phase transition, the following is a summary of the automated steps that one should follow:

1. Generation of the energy-volume curve for the low pressure phase, e.g. calcite I. The `EOS` routine in CRYSTAL is the feature most suitable for this purpose.
2. Perform a frequency calculation over several dispersion k-points, for each of these volumes. The standalone `SCELPHONO` routine in CRYSTAL accounts for this step.
3. The series of python and bash codes available in my GitHub repository named `search_neg_freqs` [175] will scan the frequencies of the entire set of constrained-volume-frequency outputs. This program will output the volumes for which an imaginary frequency has been encountered, and the dispersion k-point at which that negative eigenvalue belongs to.
4. Distortion of the atomic coordinates along the eigenvector of that imaginary frequency. The `SCANMODE` routine built-in CRYSTAL is in charge of this step.
5. Extraction of the geometry corresponding to the minimum energy displacement (the minimum on the curves presented in Fig. 7.3b) The `SCANMODE` routine saves this geometry is in a `.gui` file format.
6. A FINDSYM analysis over this `.gui` file is conducted, in order to determine the space group of this structure. As shown on Table 7.2, a not very tight tolerance has to be set in order to determine the space group we are looking for, e.g. space group 14 (calcite II).

7. The FINDSYM program writes the relevant information in a `.cif` file. In order to automate this process for all the volumes, the program CIF2CELL [176] has been used to generate valid CRYSTAL input files for the next step.

8. A constant volume geometry optimization over this structure by imposing the space group found is required. This is best computed by the `CVOLOPT` routine. The stability of this structure is checked by computing the frequencies at the Γ point at least. The frequency calculation at finite k-points of the broken symmetry structure can also be a matter of study, and will be part of a thorough discussion in the next chapter.

It is possible to automate the series of tasks 1-8 in the high performance computing facilities by using the series of python and bash codes available in my `EOS_2_phonons` [177] GitHub repository.

7.5 Influence of finite temperature

Up to now, all the plots presented correspond to the athermal limit, where the starting point is the energy-volume curve, $E(V)$. A volume range has been identified, for which imaginary frequencies are found in calcite I. We will denote these volumes as metastable volumes for calcite I. The upper and lower bound of this volume range depends on the level of theory.

At 0 K, a small correction due to zero point motion is necessary, i.e. $(E + E_{ZP})(V)$. Finally, at finite temperature the starting point is the Helmholtz free energy-volume curve, $F(V)$, according to the expressions already introduced in the Methodology chapter (Section 3.1.2).

A great amount of useful information can be extracted from the evolution of the $F(V)$ curves with temperature. In particular, for the determination of the temperature-pressure phase boundary, we will be looking for the pressure at which $G^{I}(P,T) = G^{II}(P,T)$, as was extensively explained in Section 3.1.2. For this purpose, it is essential to work with an excellent quality on the $F(V)$ fit because, for instance, the pressure at finite temperature is obtained by a direct differentiation of this fit (Eq. 3.72). If the initial $F(V)$ is poor quality, the consequent thermodynamic analysis derived from here is going to be dramatically affected.

The evolution of $E(V)$, $(E+E_{ZP})(V)$ and $F(V)$ (at two temperatures) are shown in Fig. 7.9a and 7.9b: in the first case, calcite I metastable volumes have been included in the fit; in the second case, these have been neglected. In the athermal limit, the quality of the fit is almost the same independently of the inclusion of calcite I metastable volumes. On the contrary, whenever metastable volumes are included, it can be easily seen that the $F(V)$ fit is very poor, specially at higher temperatures.

Not only we are looking for a good quality of the overall fit, but also this fit has to be exceptional specially in the regions close to the phase transition, which is the region of interest. In particular, at 311.52K the stable calcite I volume highlighted with an arrow color magenta (Fig. 7.9a) is very poorly described by a calcite I fit that includes metastable volumes. On the contrary, just by removing these metastable volumes from the fit, that volume is much better described by the model (Fig. 7.9b at 311.52 K).

From here we conclude that only stable volumes (i.e. those that do not contain soft phonon modes) will be considered in the determination of the phase boundary. In addition, an inclusion of those volumes in the thermodynamic analysis will be physically incorrect, since we will be using a $F(V)$ expression obtained via having considered calcite I volumes out of their stability domain.

Once we have decided not to include calcite I metastable volumes, we can now commence the study about the relative stability of calcite I, calcite II and space group 161 with temperature, as shown in Figs. 7.10, 7.11, 7.12 and 7.13 for the PBE-D3, PBE, B3LYP and B3LYP-D3 levels of theory respectively, in which the pressure as a function of volume is also shown. The motivation behind this study was to address whether space group 161 would become more stable than calcite II at higher temperatures.

There is a remarkable strange behaviour on the $P(V)$ curves for the 161 space group. From these plots we conclude that space group 161 does not become more stable than calcite II for every level of theory studied, at any temperature.

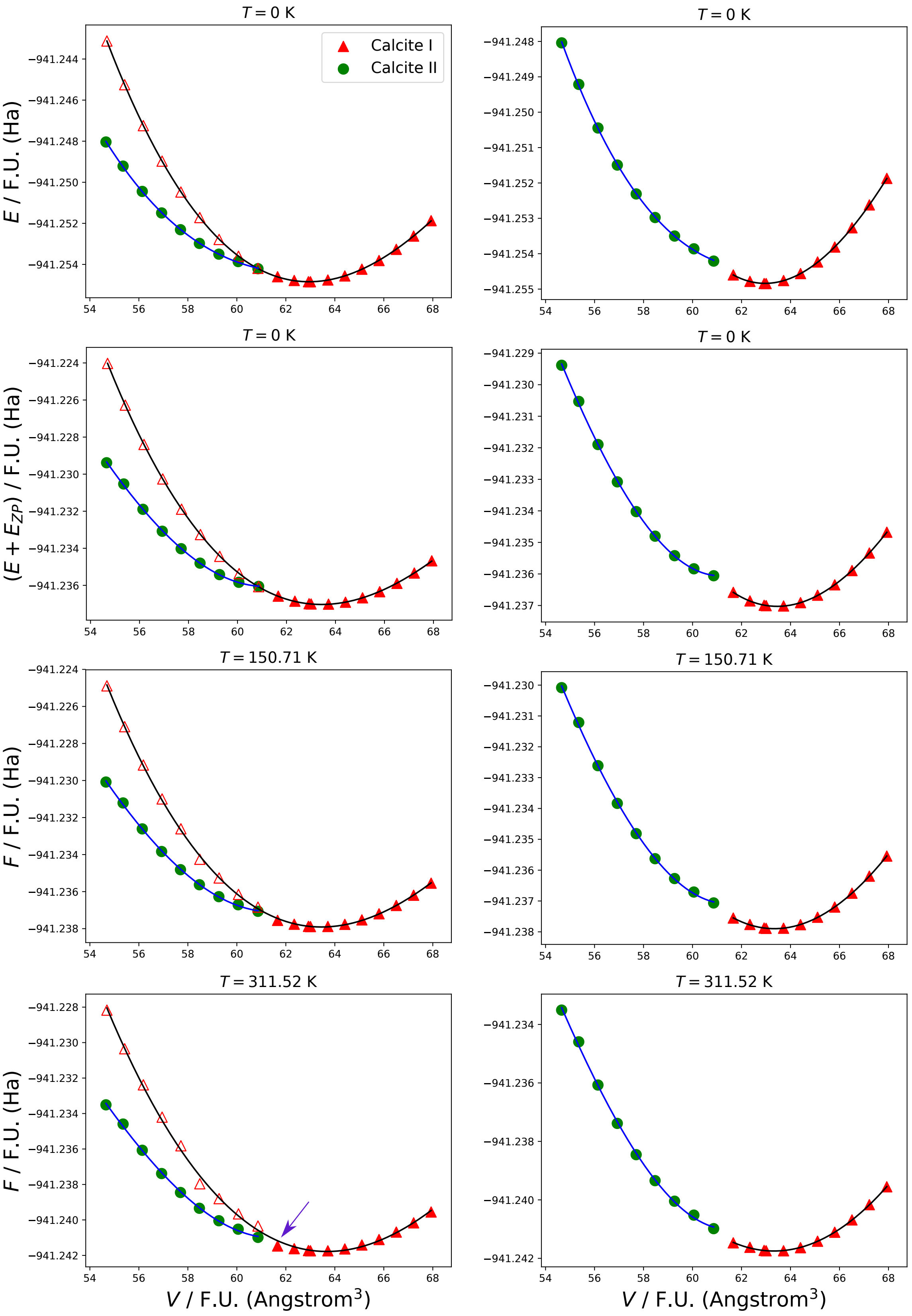

(a) **(b)**

Figure 7.9: $E(V)$, $(E + E_{ZP})(V)$ and $F(V)$ (at two temperatures: 150.71 and 311.52 K), including volumes with imaginary phonons in the fit (7.9a) and excluding them (7.9b). The same color code has been used: red triangles for calcite I (filled: stable; empty: unstable), and filled green circles for calcite II. The space group 161 has been omitted for the sake of clarity. In the athermal limit (both with and without zero point motion, the inclusion of metastable volumes for calcite I does not have a significant effect on the quality of the fit. When studying $F(V)$ at finite temperature (e.g. 311.52 K) the equation that fits the stable volumes of calcite I does not describe well these volumes near the phase transition (e.g. the volume marked with an arrow color magenta). On the other hand, if the metastable calcite I volumes are not considered in the fit, the model produces a better description of calcite I near the phase transition (the equivalent volume is now closer to the fitting equation). All PBE-D3 level of theory.

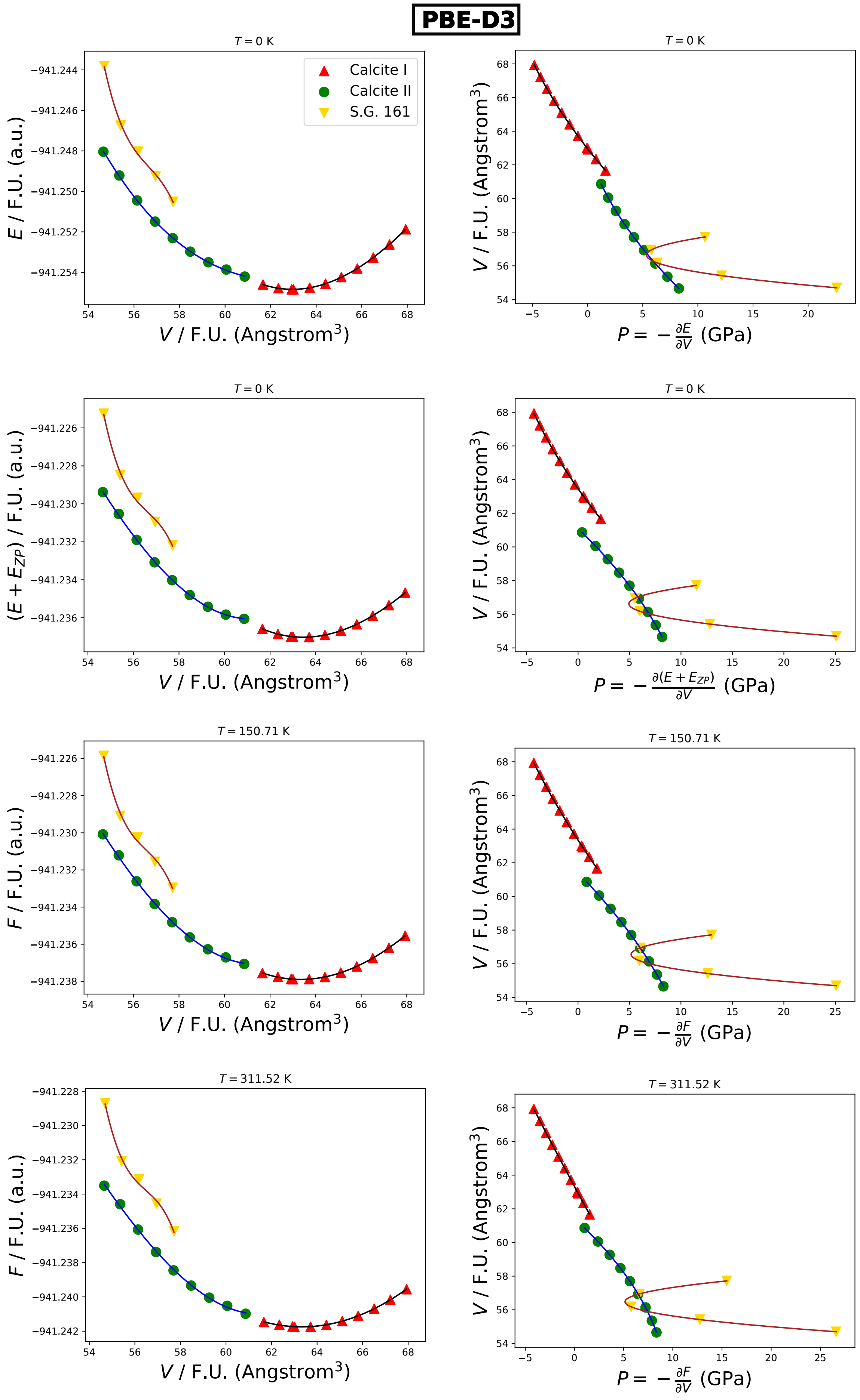
PBE-D3
$T = 0$ K
Calcite I
Calcite II
S.G. 161
E / F.U. (a.u.)
−941.244
−941.246
−941.248
−941.250
−941.252
−941.254
V / F.U. (Angstrom^3)
54
56
58
60
62
64
66
68
$T = 0$ K
V / F.U. (Angstrom^3)
$P = -\frac{\partial E}{\partial V}$ (GPa)
−5
0
5
10
15
20
$T = 0$ K
$(E + E_{ZP})$ / F.U. (a.u.)
−941.226
−941.228
−941.230
−941.232
−941.234
−941.236
V / F.U. (Angstrom^3)
$T = 0$ K
V / F.U. (Angstrom^3)
$P = -\frac{\partial (E + E_{ZP})}{\partial V}$ (GPa)
25
$T = 150.71$ K
F / F.U. (a.u.)
−941.226
−941.228
−941.230
−941.232
−941.234
−941.236
−941.238
V / F.U. (Angstrom^3)
$T = 150.71$ K
V / F.U. (Angstrom^3)
$P = -\frac{\partial F}{\partial V}$ (GPa)
$T = 311.52$ K
F / F.U. (a.u.)
−941.228
−941.230
−941.232
−941.234
−941.236
−941.238
−941.240
−941.242
V / F.U. (Angstrom^3)
$T = 311.52$ K
V / F.U. (Angstrom^3)
$P = -\frac{\partial F}{\partial V}$ (GPa)

Figure 7.10

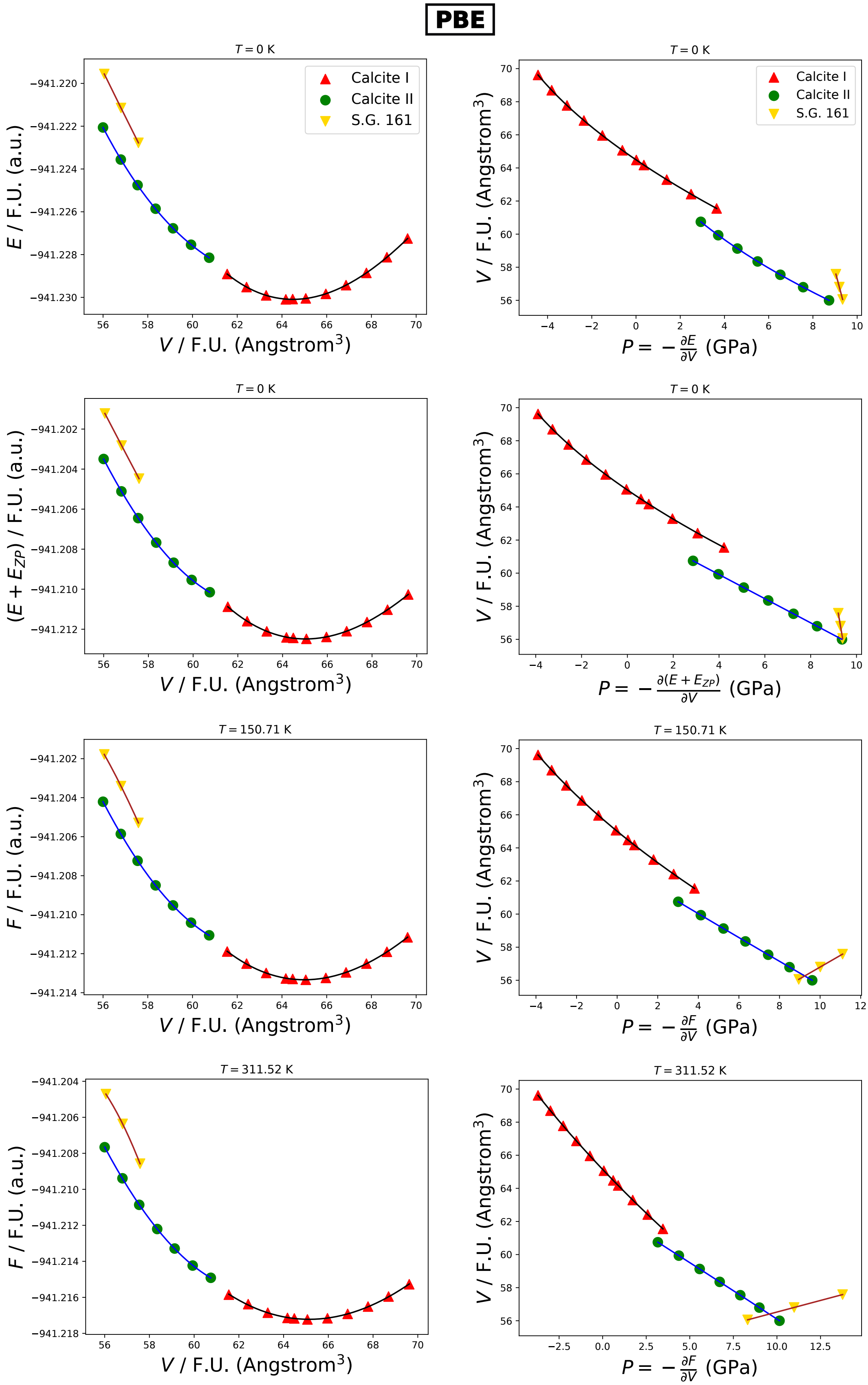
PBE
T = 0 K
Calcite I
Calcite II
S.G. 161
E / F.U. (a.u.)
−941.220
−941.222
−941.224
−941.226
−941.228
−941.230
V / F.U. (Angstrom³)
56
58
60
62
64
66
68
70
V / F.U. (Angstrom³)
P = −∂E/∂V (GPa)
−4
−2
0
2
4
6
8
10
(E + E_ZP) / F.U. (a.u.)
−941.202
−941.204
−941.206
−941.208
−941.210
−941.212
P = −∂(E + E_ZP)/∂V (GPa)
T = 150.71 K
F / F.U. (a.u.)
−941.214
P = −∂F/∂V (GPa)
12
T = 311.52 K
−941.216
−941.218
−2.5
0.0
2.5
5.0
7.5
10.0
12.5

Figure 7.11

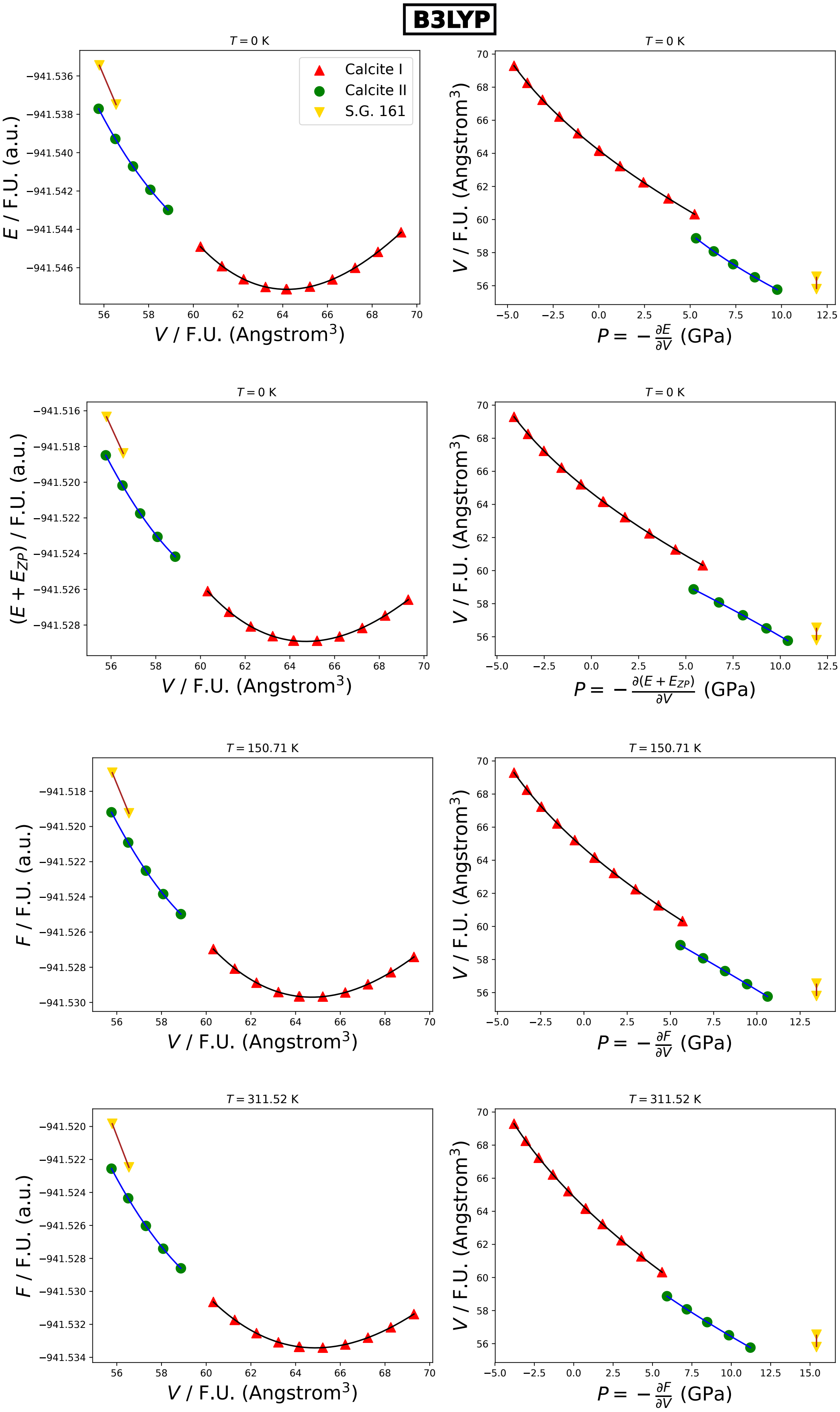
B3LYP
T = 0 K
Calcite I
Calcite II
S.G. 161
E / F.U. (a.u.)
V / F.U. (Angstrom³)
V / F.U. (Angstrom³)
P = −∂E/∂V (GPa)
T = 0 K
(E + E_ZP) / F.U. (a.u.)
V / F.U. (Angstrom³)
P = −∂(E + E_ZP)/∂V (GPa)
T = 150.71 K
F / F.U. (a.u.)
V / F.U. (Angstrom³)
P = −∂F/∂V (GPa)
T = 311.52 K
F / F.U. (a.u.)
V / F.U. (Angstrom³)
P = −∂F/∂V (GPa)

Figure 7.12

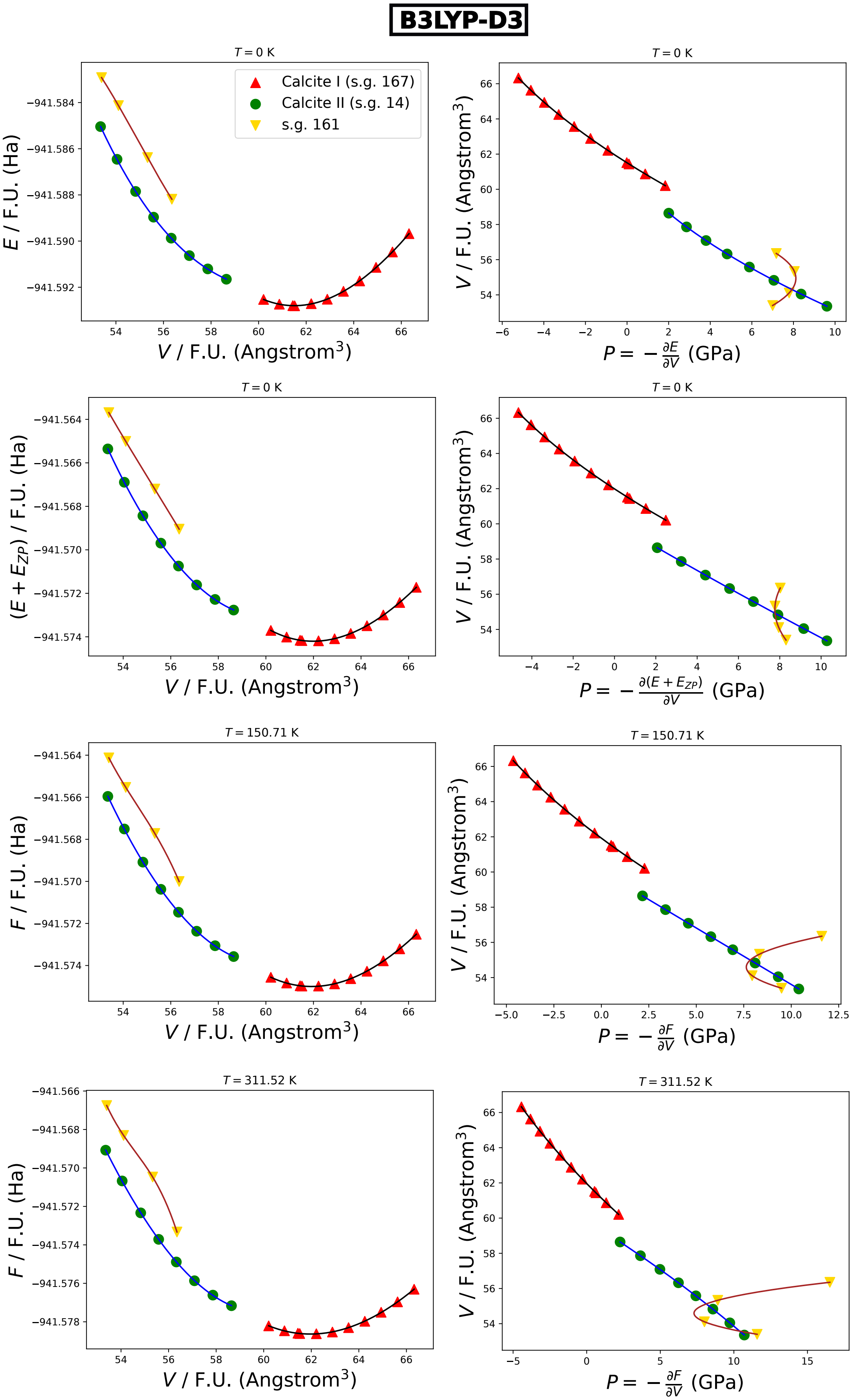
B3LYP-D3
$T = 0$ K
Calcite I (s.g. 167)
Calcite II (s.g. 14)
s.g. 161
E / F.U. (Ha)
V / F.U. (Angstrom^3)
$P = -\frac{\partial E}{\partial V}$ (GPa)
$(E + E_{ZP})$ / F.U. (Ha)
$P = -\frac{\partial (E + E_{ZP})}{\partial V}$ (GPa)
$T = 150.71$ K
F / F.U. (Ha)
$P = -\frac{\partial F}{\partial V}$ (GPa)
$T = 311.52$ K
−941.584
−941.586
−941.588
−941.590
−941.592
−941.564
−941.566
−941.568
−941.570
−941.572
−941.574
−941.576
−941.578
54
56
58
60
62
64
66
−6
−4
−2
0
2
4
6
8
10
−5.0
−2.5
0.0
2.5
5.0
7.5
10.0
12.5
−5
5
15

Figure 7.13

(Caption from previous figures): Figs. 7.10, 7.11, 7.12 and 7.13 show the energy-volume and volume-pressure curves at 0 K, 150.71 K and 311.52 K, for the PBE-D3, PBE, B3LYP and B3LYP-D3 levels of theory respectively. Calcite I, II and space group 161 are shown. Neither for any level of theory nor any temperature space group 161 becomes more stable than calcite II.

7.6 Determination of the phase boundary

In order to successfully determine the temperature-pressure phase boundary, we must recall the following condition introduced in the Methodology Chapter (Section 3.1.2): The pressure of transition between two phases at a finite temperature occurs when the following condition is satisfied:

$$G^{I}(P;T) = G^{II}(P;T) \qquad \text{(3.93 Previous Chapter)}$$

Several approaches have been considered:

7.6.1 Intersection between Gibbs free energy surfaces, $G(P,T)$

If we were able to construct $G(P,T)$ surfaces for calcite I and II, we would find that the intersection between both surfaces is defined by a curve (Fig. 7.14), whose projection in the PT plane yields the temperature-pressure phase boundary.

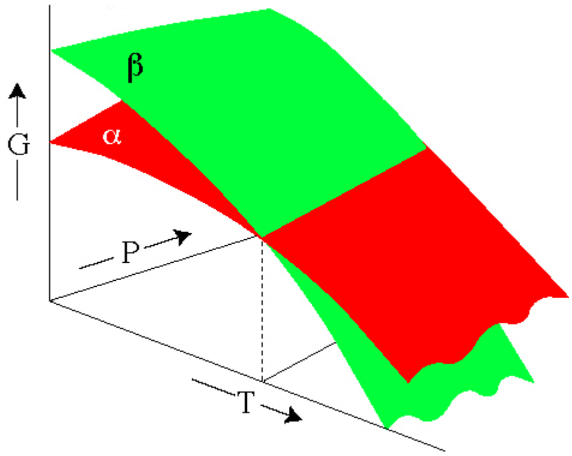

Figure 7.14: The intersection between two surfaces (α and β) give us a curve, whose projection in the PT plane yields the temperature-pressure phase boundary we are looking for. Figure adapted from Ref. [178]

In order to construct a $G(P,T)$ surface, we need to solve the equation introduced in the Methodology Chapter (Section 3.1.2):

$$\begin{aligned} G(P,T) &= E(P) + E_{ZP}(P) + \mathcal{E}(P,T) - TS(P,T) + P(T)V(P,T) && \text{(3.91 Previous Chapter)} \\ &= F(P,T) + P(T)V(P,T) && \text{(3.92 Previous Chapter)} \end{aligned}$$

Because we start working on the basis of independent frequency calculations for each volume, it is more convenient to work in terms of volume, at least as a starting point:

$$\begin{aligned} G(V,T) &= E(V) + E_{ZP}(V) + \mathcal{E}(V,T) - TS(V,T) + P(V,T)V(T) && \text{(3.89 Previous Chapter)} \\ &= F(V,T) + P(V,T)V(T) && \text{(3.90 Previous Chapter)} \end{aligned}$$

All of the quantities $E_{ZP}(V)$,$\mathcal{E}(V,T)$, $S(V,T)$ and $P(V,T)$ have in common that they depend on the sum over phonon modes as a function of volume, i.e. $\sum_{i,\mathbf{k}} \nu_{i,\mathbf{k}}(V)$:

$$\begin{aligned} E_{ZP}(V) &= \frac{h}{2}\sum_{i,\mathbf{k}} \nu_{i,\mathbf{k}}(V) && \text{(3.76 Previous Chapter)} \\ \mathcal{E}(V,T) &= \sum_{i,\mathbf{k}} \frac{h\nu_{i,\mathbf{k}}(V)}{\exp\left(\frac{h\nu_{i,\mathbf{k}}(V)}{k_BT}\right) - 1} && \text{(3.77 Previous Chapter)} \\ S(V,T) &= -k_B \sum_{i,\mathbf{k}} \ln\left[1 - \exp\left(\frac{-h\nu_{i,\mathbf{k}}(V)}{k_BT}\right)\right] + \frac{1}{T}\mathcal{E}(V,T). && \text{(3.78 Previous Chapter)} \\ P(V,T) &= -\left(\frac{\partial F(V,T)}{\partial V}\right)_T && \text{(3.80 Previous Chapter)} \\ &= -\frac{\partial E(V)}{\partial V} - \sum_{i,\mathbf{k}} \left[\frac{1}{2} + \frac{1}{\exp\left(\frac{h\nu_{i,\mathbf{k}}(V)}{k_BT}\right) - 1}\right] h\,\frac{\partial \nu_{i,\mathbf{k}}(V)}{\partial V} && \text{(3.85 Previous Chapter)} \end{aligned}$$

For each volume, an independent frequency calculation has been performed, over two dispersion k-points (Γ and F, as described in Section 7.3). It is more convenient to encompass $E(V)$, $E_{ZP}(V)$, $\mathcal{E}(V,T)$ and $S(V,T)$ into $F(V,T)$, i.e $F(V,T) = E(V) + E_{ZP}(V) + \mathcal{E}(V,T) - TS(V,T)$, for a fixed volume. According to Eq. 3.90, the only term left is $P(V,T)$. Two approaches were pursued to obtain this term: either by a direct sum over the frequencies or by differentiation of the Helmholtz free energy.

7.6.1.1 First approach: calculation of $P(V,T)$ by summing directly over frequencies

According to Eq. 3.85, the $P(V,T)$ term can be obtained by summing directly over phonon modes. When coding Eq. 3.85, special attention has to be paid to the $\nu_{i,\mathbf{k}}(V)$ term, which has been approximated to a polynomial of degree 2:

$$\nu_{i,\mathbf{k}}(V) = c_{i,\mathbf{k}}V^2 + d_{i,\mathbf{k}}V + f_{i,\mathbf{k}} \qquad \text{(3.86 Previous Chapter)}$$

CRYSTAL prints the frequencies in ascending order, for each dispersion k-point considered, for a fixed volume. For instance, the first 8 normal modes appearing at the Γ point for calcite I for two consecutive volumes (61.7 and 62.3 $\mathring{A}^3$) are shown in ascending order in Table 7.6.

	Volume / F.U. = 61.7 ($\mathring{A}^3$)	Volume / F.U. = 62.3 ($\mathring{A}^3$)
	Frequencies (cm^{-1})	Frequencies (cm^{-1})
i=1	80.9187	87.0309
i=2	92.7025	98.2464
i=3	92.7025	98.2464
i=4	160.2778	157.7408
i=5	160.2778	157.7408
i=6	182.0797	176.5630
i=7	241.6601	236.7709
i=8	241.6601	236.7709

Table 7.6: List of the eight first frequencies at the Γ point for calcite I at two of the stable volumes considered in Fig. 7.3a,b. These frequencies are shown in ascending order, so that the i label only accounts for the position of the sorted list of frequencies. It may occur that the frequency labelled as $i = 3$ on both volumes does not correspond to the same eigenvector and thus the same vibration.

As an example, we will work with the $i = 3$ mode. It may occur very frequently that the mode labelled as $i = 3$ for instance in one volume may not correspond to the same normal mode and phonon vibration as the phonon labelled as $i = 3$ for the next volume, since the i label is just referring to the ascending order in which the frequencies are sorted for each volume. For example, the mode labelled as $i = 3$ for $V = 61.7$ ($\mathring{A}^3$) may correspond to the one labelled as $i = 4$ for $V = 62.3$ ($\mathring{A}^3$). Although this issue is less probable to occur at low frequencies, it is much more common at higher frequencies. Therefore, one of the most important requirements of Eq. 3.86 is to ensure that the i-th mode refers to the same eigenvector across volumes, so that the volume dependence $\nu_{i,\mathbf{k}}(V)$ given by that polynomial expression actually monitors the same i-th frequency across all volumes. The only way of checking whether or not we are referring to the same normal mode in two consecutive volumes is by ensuring that the eigenvector for $i = 3$ in both volumes is the same.

Unfortunately, we did not realise about this small detail in the first place, and Eq. 3.89 was coded by extracting each frequency and considering that for example the label $i = 3$ refers to the same normal mode across all the volumes studied. Once $P(V, T)$ has been obtained, then $F(V, T)$ can be calculated. This gives us $G(V, T)$, which in turn allows us to rewrite it to $G(P, T)$ so that we end up with the $G(P, T)$ scattered surface shown in Fig. 7.15 with red circles. The code that allows the construction of Gibbs free energy surfaces following this first approach is available in the GitHub repository named `QHA_3D` [179].

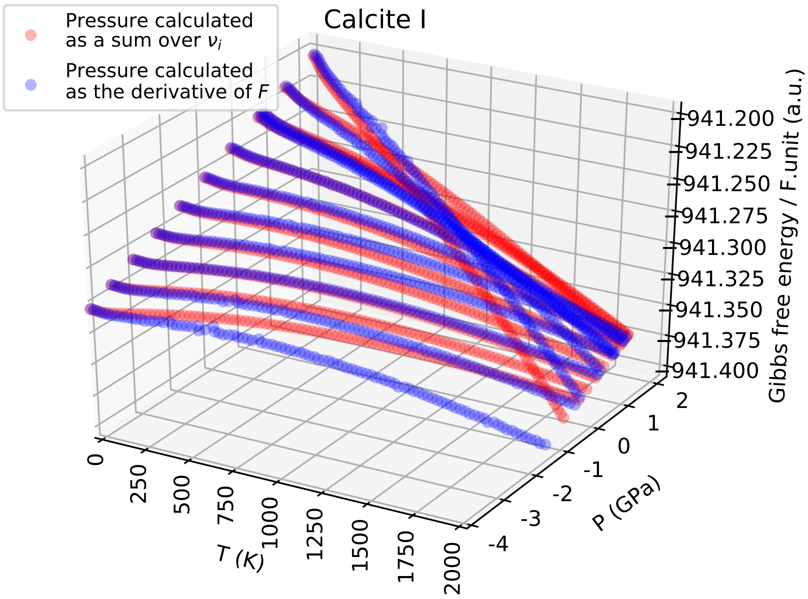

Figure 7.15: $G(P, T)$ scattered surface constructed either via summing directly over the frequencies (red circles), or by the derivative of the Hemholtz free energy (blue circles). All PBE-D3 level of theory.

7.6.1.2 Second approach: calculation of $P(V,T)$ as the derivative of $F(V,T)$

Instead of analyzing the eigenvectors between all the modes across all the volumes, a simpler approach was pursued: since the thermal pressure is the derivative of the Helmholtz free energy (Eq. 3.72), the former can be obtained accurately without the need to sum directly over the frequencies. This approach is more correct than summing directly over the frequencies without checking the eigenvectors. The scattered surface obtained by this strategy is shown in Fig. 7.15 with blue circles.

The code that allows the construction of Gibbs free energy surfaces following this second approach is available in the GitHub repository entitled `QHA_3D_der_F`.

7.6.1.3 Discussion of first and second approaches

The shape of the scattered surface obtained through both approaches 1 and 2 is presented in Fig. 7.15 with red and blue circles respectively. Instead of behaving as a nice flat surface in all the pressure and temperature domain, this surface has been found to be slightly folded in the range of extreme temperatures (1000 - 2000 K) and pressures ≈2 GPa. This behaviour is related to the fact that at these conditions calcite I is no longer stable, so that the $G(P,T)$ surface presents a discontinuity. Both approaches coincide at low temperatures for any given pressure studied, but they start to differ at temperatures higher than 500 K approximately. This certainly can be due to an incorrect thermal pressure constructed by summing the frequencies without checking the eigenvectors. Interestingly, some noise can be appreciated in the blue scattered plot, which might be related to the fact that in the end, the pressure comes from a first derivative of a fitting equation to the Helmholtz free energy. First derivatives of a fitting polynomial are quite sensitive.

7.6.2 Intersection between Gibbs free energy curves, $G(P)$, at a fixed temperature

In order to pursue the approach based on the intersection between two Gibbs free energy surfaces $G(P,T)$, we would have to ensure first that the surfaces produced do not present discontinuities, i.e. restrict the $G(P,T)$ surface to values of pressure and temperature for which calcite I and II are stable.

In practice, we developed a simplified approach, based on a transformation from a three dimensional to a two dimensional problem. The first part of this 2D approach is the same as the method described in Section 7.6.1: firstly, obtain $F(T)$ for a fixed volume, and secondly an expression for $F(V,T)$ across the range of stable volumes. At this point, the experience obtained by the approaches 1 and 2 (section 7.6.1.1 and 7.6.1.2), is enormously useful to realise that the thermal pressure has to be obtained by direct differentiation of the Helmholtz free energy. Having reached to this point, instead of analyzing the intersection between two $G(P,T)$ surfaces, we will fix a temperature instead and sort out the intersection between two $G(P)$ curves at that temperature. For a fixed temperature, the equation to solve now becomes

$$G^{I}(P) - G^{II}(P) = 0, \tag{7.2}$$

so that a pressure of intersection is obtained, for that temperature. A temperature-pressure phase diagram arises quite naturally form this treatment. The code that automates this process and produces the temperature-pressure phase diagram is available in the GitHub repository `QHA_2D` [180].

The energy-volume, volume-pressure and Gibbs free energy-pressure curves for several temperatures are presented in Figs. 7.16, 7.17 7.18 and 7.19 for the PBE-D3, PBE, B3LYP-D3 and B3LYP levels of theory respectively. Regarding the volume-pressure plots, there is a clear discontinuity when passing from calcite I to calcite II, which confirms the fact that this is a first order phase transition (as explained in the Theory Chapter).

In the athermal limit, the pressure of transition is 1.99 GPa and 2.57 GPa for the PBE-D3 and B3LYP-D3 level of theory respectively (see Figs. 7.16 and 7.18).When neglecting zero point motion, the pressure of transition is slightly lower: 1.87 and 2.44 GPa for the PBE-D3 and B3LYP-D3 level of theory respectively. The pressure of transition increases progressively as a function of temperature. Along the pressure-temperature phase boundary there is a coexistence between both phases. The temperature - pressure phase diagram has been obtained through this methodology using PBE and B3LYP functionals, both with and without Grimme's D3 dispersion correction. The results are shown in Fig. 7.20.

For every functional there is a temperature for which $G^I(P)$ and $G^{II}(P)$ are very flat and coincide in a broad pressure range, so that the intersection occurs at very high values of pressure. This corresponds to a value of temperature above which there is no coexistence between calcite I and II.

For both a GGA and hybrid type of functional, a remarkable decrease in the pressure of transition is observed when including dispersion effects: a decrease of 3.2 GPa (when passing from B3LYP to B3LYP-D3) and 1.7 GPa (when passing from PBE to PBE-D3) is observed at 0 K (Fig 7.20). Hybrid functional with dispersion effects (B3LYP-D3) is capable of describing a phase boundary up to 653 K, while this upper bound is increased up to 934 K when dispersion is not included (B3LYP). On the contrary, there is no calcite I - calcite II phase boundary above 331 K for GGA (both PBE and PBE-D3) level of theory. These four Hamiltonians result in a slightly positive TP slope. A decrease in the pressure of transition is observed when passing from hybrid to GGA. The minimum percentage of compression needed in order to detect the imaginary phonon mode responsible for the transition to calcite II is of 7.04% and 4.54% for B3LYP and B3LYP-D3 respectively (As was summarized in Tables 7.4 and 7.5). On the contrary, PBE and PBE-D3 only require 5.79% and 3.38% respectively (Tables 7.3 and 7.1) From these results we conclude that GGA functionals require lower level of compression, which is in agreement with the fact that GGA functionals lead to a greater overestimation of the volume with respect to B3LYP, as has been shown elsewhere [181]. This leads to a lower pressure of transition for PBE and PBE-D3 with respect to B3LYP and B3LYP-D3 (Fig. 7.20).

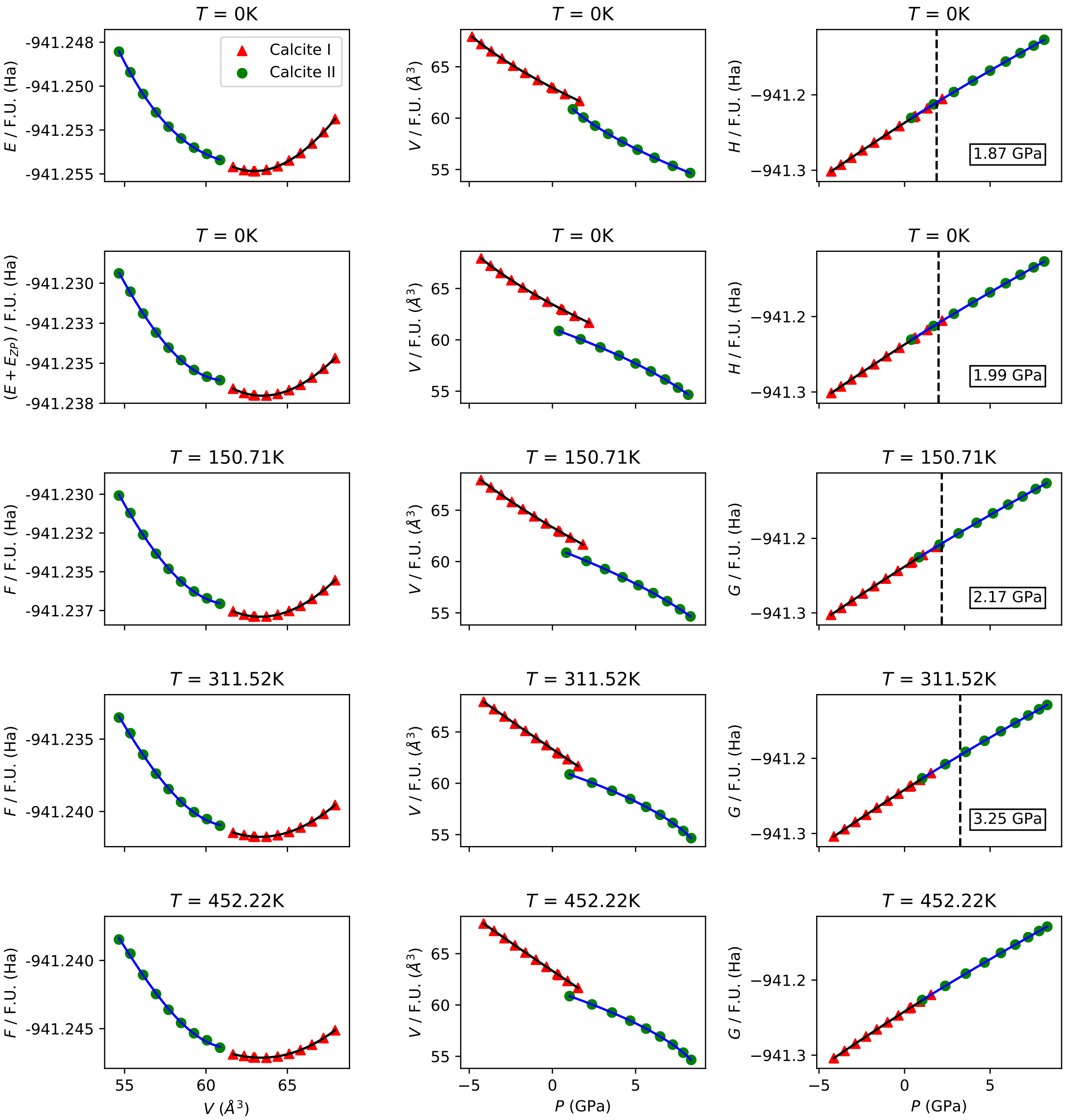

Figure 7.16: Energetics for the PBE-D3 level of theory

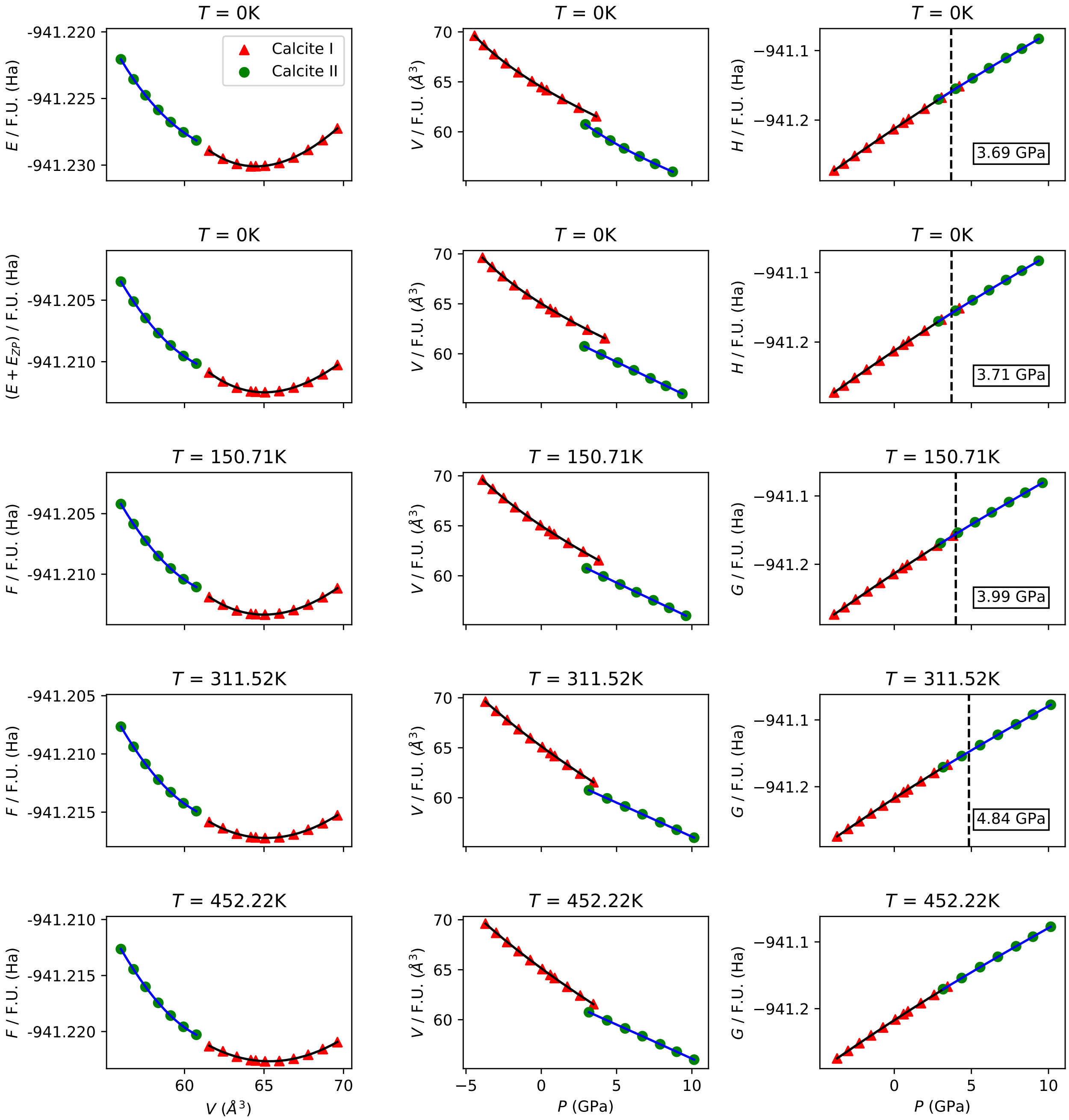

Figure 7.17: Energetics for the PBE level of theory

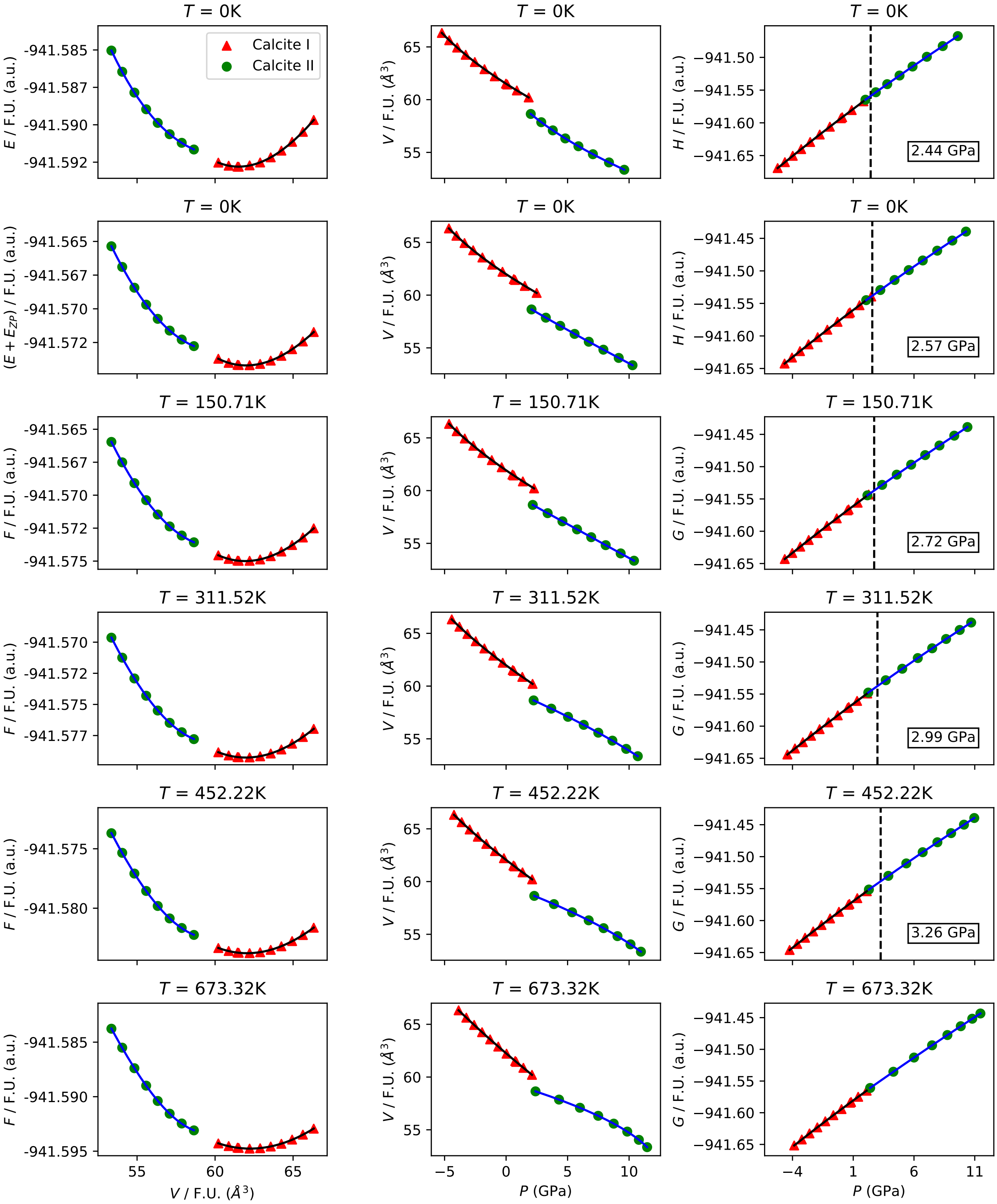

Figure 7.18: Energetics for the B3LYP-D3 level of theory

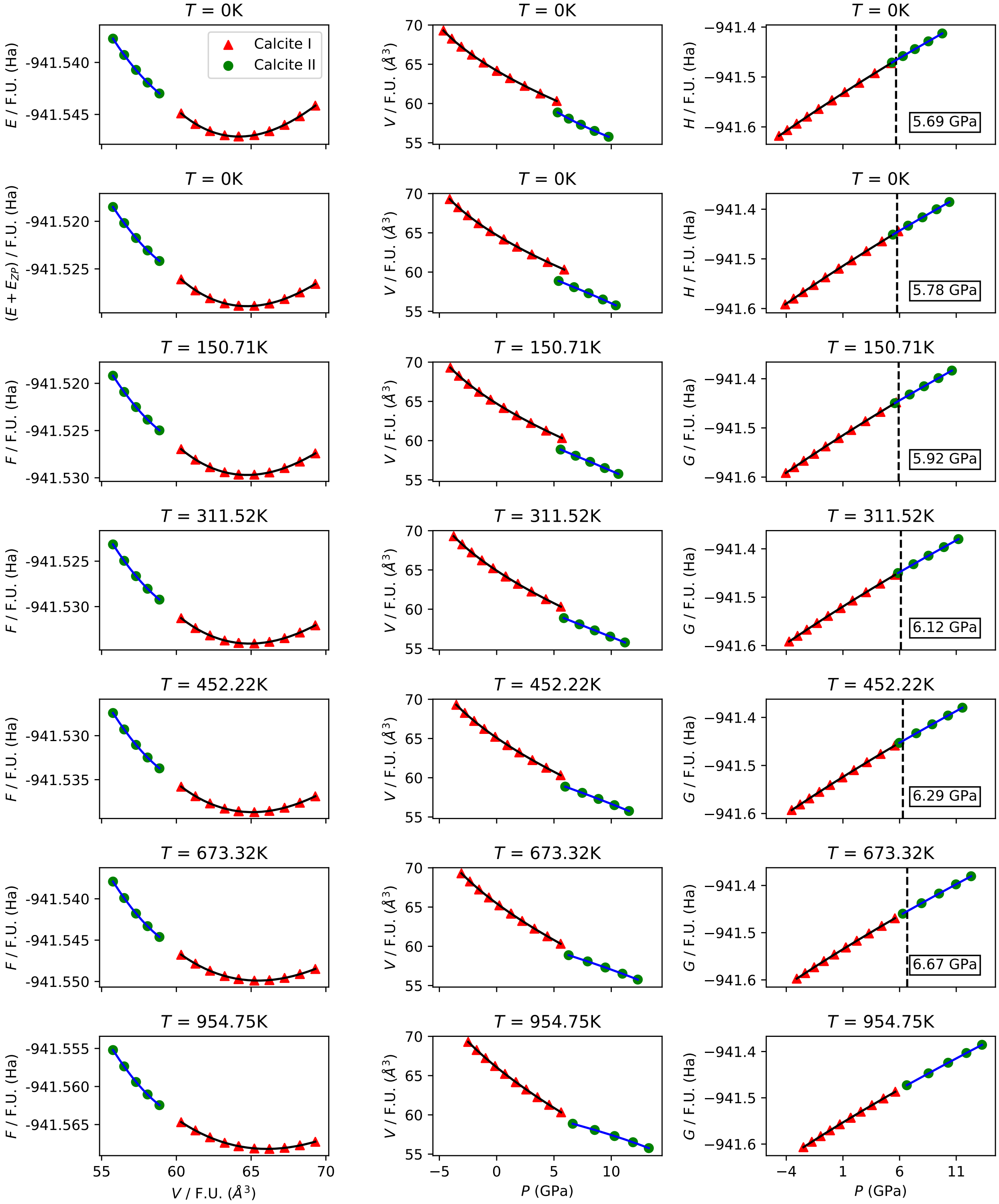

Figure 7.19: Energetics for the B3LYP level of theory

Figs. 7.16, 7.17, 7.18, 7.19: PBE-D3, PBE, B3LYP-D3, and B3LYP levels of theory respectively. First row: energy, pressure and enthalpy at 0 K, neglecting zero point motion. Second row: accounting for zero point energy. Rest of the rows: Helmholtz free energy, pressure and Gibbs free energy at different temperatures. For all the cases, the pressure has been obtained as the derivative of the energy (athermal limit) or Helmholtz free energy (finite temperature). The Enthalpy and Gibbs free energy fits correspond to cubic fits. The pressure of intersection between calcite I and II is also shown. In each case, the temperature at which the intersection between Gibbs free energy curves is located at very high values of pressure is also shown.

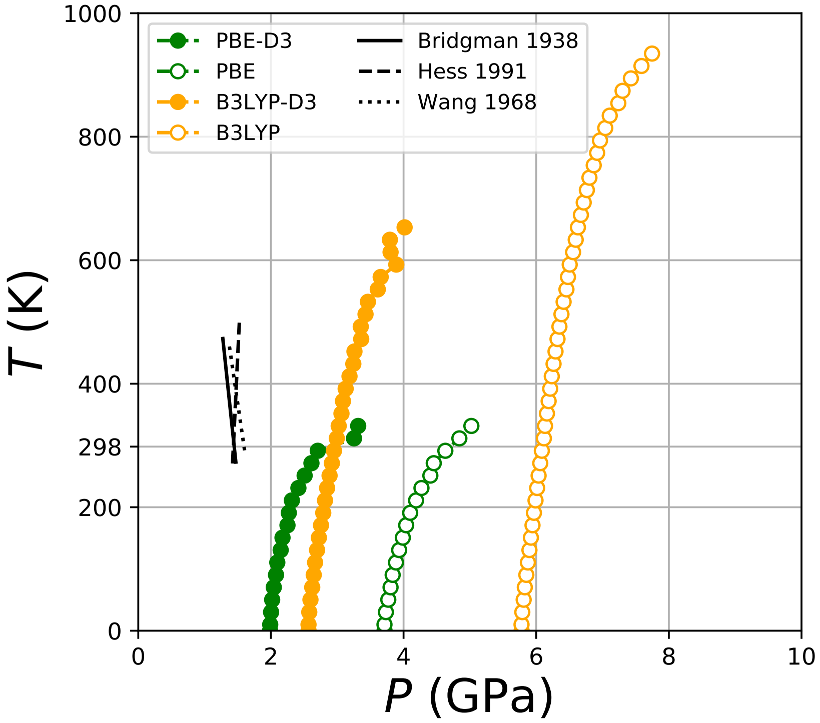

Figure 7.20: Theoretical result for the calcite I - calcite II phase boundary, using B3LYP, B3LYP-D3, PBE and PBE-D3. The experimental phase boundaries are also reported: Bridgman [113], Wang *et al.* [158] Hess *et al.* [119],

7.7 Justification of the theoretical results based on the Clapeyron equation

The slope of the temperature-pressure phase boundary of two phases in equilibrium is related with the change of the entropy and volume upon transition according to the Clapeyron equation:

$$\frac{dP}{dT} = \frac{\Delta \overline{S}_{\mathrm{trs}}}{\Delta \overline{V}_{\mathrm{trs}}} = \frac{\Delta \overline{H}_{\mathrm{trs}}}{T \Delta \overline{V}_{\mathrm{trs}}}, \tag{7.3}$$

where $\overline{X}$ represents a molar quantity, i.e. $N_A X/\mathrm{n}$ F.U., and $\Delta \overline{X}_{\mathrm{trs}} = \overline{X}^{\mathrm{II}}_{\mathrm{trs}} - \overline{X}^{\mathrm{I}}_{\mathrm{trs}}$, for a temperature and pressure along the phase boundary. Superindex I and II refer to calcite I and II respectively. The enthalpy along the pressure-temperature phase boundary must be an enthalpy at a finite temperature and pressure, so that it has been considered as:

$$H(P;T) = E + E_{ZP} + \mathcal{E}(T) + PV. \tag{7.4}$$

We have computed $\Delta\overline{H}_{\text{trs}}$, $\Delta\overline{S}_{\text{trs}}$ and $\Delta\overline{V}_{\text{trs}}$ as a function of temperature and pressure along the phase boundary (Fig. 7.21). Along the pressure-temperature phase boundary, $\Delta\overline{H}_{\text{trs}}$, $\Delta\overline{S}_{\text{trs}}$ and $\Delta\overline{V}_{\text{trs}}$ are negative, which implies a positive slope, in agreement with our theoretical calculations.

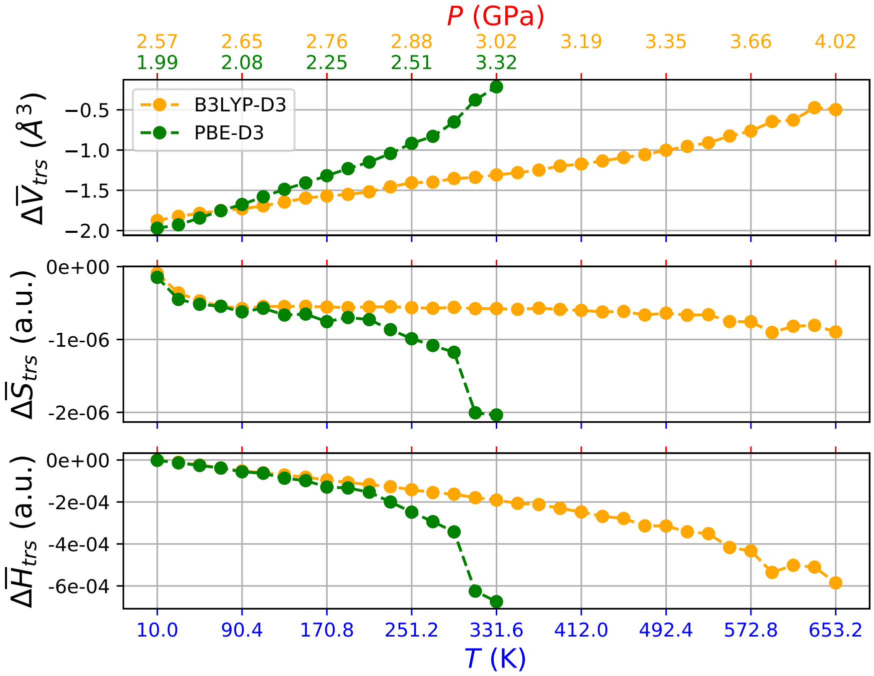

Figure 7.21: Evolution of $\Delta\overline{V}_{\text{trs}}$, $\Delta\overline{S}_{\text{trs}}$, and $\Delta\overline{H}_{\text{trs}}$ with temperature and pressure across the temperature-pressure phase boundary shown in Fig. 7.20, for the B3LYP-D3 and PBE-D3 levels of theory.

7.8 Phase transition on expanded supercells

As has been explained in the previous section, by computing the phonons in terms of the Landau supercell for calcite I, i.e.

$$\begin{bmatrix} 1 & 0 & 0 \\ 0 & -1 & 1 \\ 1 & -1 & -1 \end{bmatrix} \tag{7.5}$$

the thermodynamic quantities are calculated by summing frequencies over two dispersion k-points: Γ and F. The calcite II structure arises naturally via a distortion of the atomic co-ordinates along the imaginary phonon eigenvector at the F k-point. Once this structure was isolated, a further constant-volume-optimisation is required. The thermodynamic quantities for calcite II are then calculated at the Γ point. The temperature-pressure phase boundary presented so far has been obtained by computing the phonons in terms of the Landau supercell for calcite I and the primitive cell of calcite II. Table 7.7 summarizes the lattice parameters for these two cells, for a volume constraint of 56.9 $\AA^3$/formula unit. As can be seen, calcite I in the Landau supercell and calcite II contain a, b and c lattice parameters that only differ on the second decimal figure. Since the Landau supercell interconverts calcite I to calcite II, the lattice parameters for calcite I within the Landau supercell match the ones of calcite II for the same level of compression. The small difference is only due to the constant-volume-optimisations performed throughout the process.

If we would like to have a higher sampling of phonon dispersion k-points, we would need to increase the size of these supercells so that similar sized supercells are obtained in each case. For Calcite I, a convenient workflow would be to work in terms of integer multiples of the Landau supercell, e.g. $n = 1, 2, 3$ and 4 were the cases of study. In this way, we can end up with double, triple or quadruple times the Landau supercell candidates, as presented on Table 7.7. Because of the monoclinic lattice of calcite II, integer multiples of the diagonal supercell:

$$\begin{bmatrix} n & 0 & 0 \\ 0 & n & 0 \\ 0 & 0 & n \end{bmatrix} \tag{7.6}$$

are perfect candidate supercells to be considered; for instance, the $n = 2$ diagonal calcite II supercell yields lattice parameters almost equal to 2 times the landau supercell for calcite I (See table 7.7). Similarly, the equivalent is observed for $n = 3$ and $n = 4$.

	a	b	c	α	β	γ	N. of Atoms	Monkhorst-Pack mesh	N. of k-points in the IBZ	N. of dispersion k-points	A.O.
CI	6.01702	6.01702	6.01702	48.99139	48.99139	48.99139	10	8x8x8	65	1	190
CI + Landau sc	6.01702	4.98961	7.81670	90	103.91205	90	20	8x8x8	260	2	380
CII	6.11378	5.04374	7.65481	90	105.26647	90	20	8x8x8	170	1	380
CI + 2x Landau sc	12.03404	9.97923	15.63340	90	103.91205	90	160	4x4x4	36	16	3040
CII + 200 020 002 sc	12.22757	10.08748	15.30961	90	105.26647	90	160	4x4x4	36	8	3040
CI + 3x Landau sc	18.05106	14.96884	23.45010	90	103.91205	90	540	2x2x2	8	54	10260
CII + 300 030 003 sc	18.34135	15.13123	22.96442	90	105.26647	90	540	2x2x2	8	27	10260
CI + 4x Landau sc	24.06809	19.95845	31.26680	90	103.91205	90	1280	1x1x1	1	128	24320
CII + 400 040 004 sc	24.45514	20.17497	30.61922	90	105.26647	90	1280	1x1x1	1	64	24320

Table 7.7: Lattice parameters for the calcite I (CI) and calcite II (CII) structures, both volume-constrained at the same volume, 56.9 $\AA^3$/formula unit. The Landau supercell (sc) is the supercell expansion matrix (Eq. 7.5) studied for calcite I. Regarding calcite II, the primitive cell and an integer multiple of the diagonal supercell expansion matrix (Eq 7.6) have been studied. The number of dispersion k-points for the phonon calculation, the number of atomic orbitals (A.O.), number of atoms and the number of k-points in the Irreducible part of the Brillouin Zone (IBZ) according to the Monkhorst-Pack scheme are also reported.

The frequency calculation in the Landau supercell of calcite I and the primitive cell of calcite II were both performed with a k-point Monkhorst-Pack mesh of 8x8x8. When increasing the size of the supercell, i.e., two times the Landau supercell for calcite I and $n = 2$ for calcite II, this sampling has been reduced to 4x4x4. Similarly, for three times the Landau supercell (calcite I) and $n = 3$ (calcite II), both a Monkhorst-Pack mesh of 3x3x3 and 2x2x2 was tested. A difference smaller than 10^{-10} Ha in the energy was observed between these two meshes. Thus, a mesh of 2x2x2 was finally used due to its lower computationally cost. Finally, for the case of four times the Landau supercell (calcite I) and $n = 4$ (calcite II), a Monkhorst-Pack mesh of 1x1x1, i.e. 1 real k-point is enough sampling, since both cells already are very big (lattice parameters over 20 $\mathring{A}$).

7.9 Convergence study on calcite I

For each dispersion k-point, there are $3N$ frequencies, where N is the number of atoms in the cell. At the Γ point, three of these frequencies are zero and correspond to the three translational degrees of freedom.

Recalling the expression of the entropy:

$$S(V,T) = -k_B \sum_{i,\mathbf{k}} \ln \left[1 - \exp\left(\frac{-h\nu_{i,\mathbf{k}}(V)}{k_B T} \right) \right] + \frac{1}{T}\mathcal{E}(V,T), \qquad (\text{ 3.78 Previous Chapter})$$

since all thermodynamic quantities are computed as a sum over the frequencies, if this sum is performed over a greater number of dispersion k-points, the phonon-dependent thermodynamic quantities are expected to reach convergence.

We shall explain first the concept of cumulated entropy. CRYSTAL prints $3N$ frequencies at each dispersion k-point. Say we now set an upper bound of 300 cm^{-1}, so that we could calculate the total value of entropy we have reached, by summing all the frequencies below this upper bound (across all k-points). Computationally, an easy way of doing this is by extracting all the frequencies at all k-points, sort them on ascending order, set the upper bound, and sum the entropy at each step, until we reach that upper bound. This is what we have named cumulated entropy. The series of bash and python scripts that perform this operation are available in my GitHub repository named `ENTROPY_PDOS` [182].

The Phonon density of states (continuous line) and the cumulated entropy (dahsed line) are plotted in Fig. 7.22, as a function of the energy for integer multiples of the Landau supercell expansion matrix, for the equilibrium volume of calcite I. Lighter colors refer to smaller supercell (1 times Landau supercell), and the darkest represents the biggest supercell (4 times Landau supercell). The cumulated entropy increases quite rapidly for frequencies lower tan 400 cm^{-1}, while this increase is slower for frequencies above 400 cm^{-1}. This is showing that phonon modes below 400 cm^{-1} are the ones that contribute the most to the entropy. This statement is supported by the fact that the integrated area below the PDOS is greater in the frequency interval corresponding to 0-400 cm^{-1}. It can also be seen that when the number of dispersion k-points increase, the height of the PDOS peaks decrease, they become less sharp, while their width is increased. This is a quite known behaviour of the PDOS: whenever the phonon dispersion sampling is increased, peaks become less sharp and wider. The highest value reached by the cumulated entropy function corresponds to the summation over the highest and last frequency available, so that this value corresponds to the final entropy for the material. This value is reported in Fig. 7.22, for the supercells studied. The difference in entropy between supercells is shown in the third column: the difference in entropy between the Landau supercell and the primitive is $6 \cdot 10^{-3}$ mHartree/cell · K. An order of magnitude lower ($6 \cdot 10^{-4}$) occurs between 2 times and 3 times the Landau supercell. This effect can be considered as a very fast convergence. On the other hand, when passing from 3 times to 4 times the Landau supercell, the difference is just $3 \cdot 10^{-4}$ mHartree/cell · K. From this we conclude that by the time we reach 3 times the Landau supercell, convergence has been reached.

Calcite I + $\begin{bmatrix} n & 0 & 0 \\ 0 & -n & n \\ n & -n & -n \end{bmatrix}$ (Landau supercell)	Entropy (mHartree/cell · K) at 298.15K	Δ Entropy (mHartree/cell · K)
$n = 1$	0.061791907577	-
$n = 2$	0.068127898779	$\lvert(n = 1) - (n = 2)\rvert = 6 \cdot 10^{-3}$
$n = 3$	0.068783244632	$\lvert(n = 2) - (n = 3)\rvert = 6 \cdot 10^{-4}$
$n = 4$	0.0690823344822	$\lvert(n = 3) - (n = 4)\rvert = 3 \cdot 10^{-4}$

Table 7.8: Entropy and entropy difference between the Landau supercells studied for the equilibrium volume of calcite I

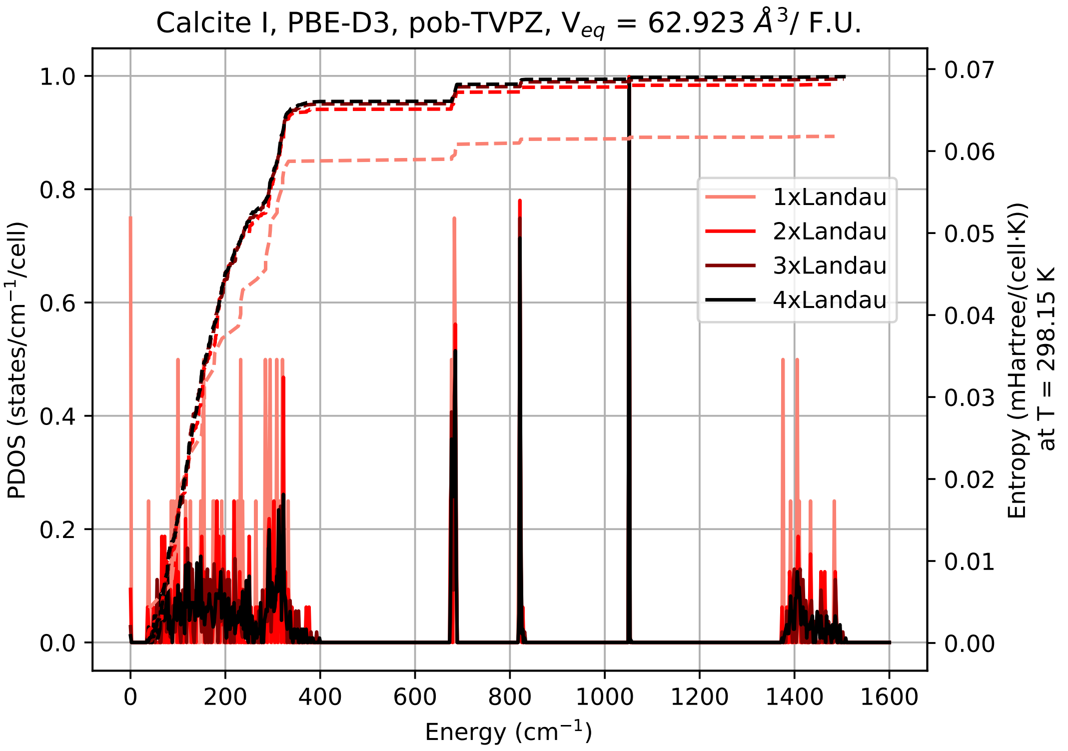

Figure 7.22: PDOS and cumulated entropy for the equilibrium volume of calcite I. The supercells studied are integer multiples of the Landau supercell.

7.10 Convergence study on calcite II

A similar convergence study can be conducted for calcite II. We will work in terms of the volume at 56.948 Å^3 / F.U. The PDOS and cumulated entropy are shown in Fig. 7.23. Interestingly, while all frequencies are positive for the primitive cell, a total number of one, four and six imaginary frequencies were found, respectively, for the diagonal supercells $n = 2, 3$ and 4, as reported in the legend of that figure. Because of the exponential dependence of the entropy on the phonon frequencies, a mathematical indetermination is found when plugging in negative frequencies in Eq. 3.78. Thus, the cumulated entropy shown is already neglecting negative frecuencies in the summation. As occured in calcite I, phonons below 400 cm^{-1} are the ones that contribute most to the entropy. The difference in entropy between the supercells of study is shown in the last column of Table 7.9. While a difference of $1.4 \cdot 10^{-2}$ mHartree/cell· K is observed between the primitive cell of calcite II and the $n = 2$ supercell, a difference of $1.7 \cdot 10^{-3}$ mHartree/cell· K, i.e., an order of magnitude higher separates $n = 3$ from $n = 2$. There is hardly gain in entropy when passing from $n = 3$ to $n = 4$, i.e., $1.0 \cdot 10^{-3}$ mHartree/cell· K. As in calcite I, convergence is reached with the $n = 3$ cell as well.

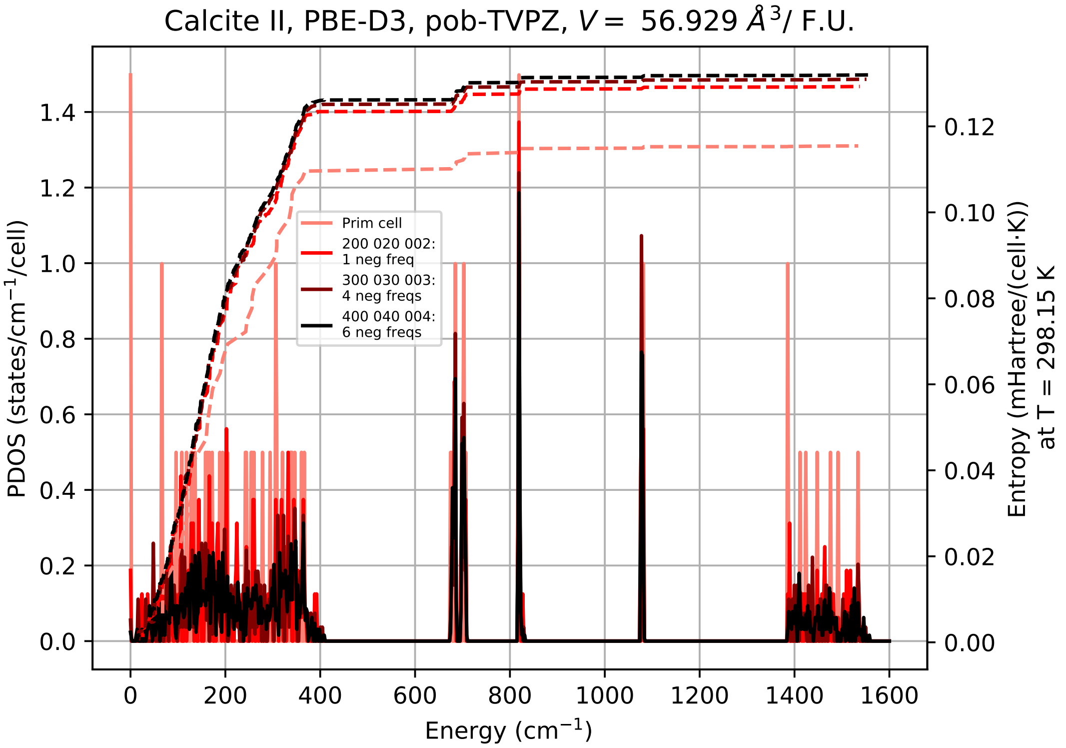

Figure 7.23: PDOS and cumulated entropy for the equilibrium volume of calcite II, at the volume of 56.948 $\AA^3$/F.U. The supercells studied are integer multiples of the diagonal supercell (Eq. 7.6).

	Calcite II	Entropy (mHartree/cell · K) at 298.15K	Δ Entropy
	Primitive cell	0.115451771327	-
Calcite II + $\begin{bmatrix} n & 0 & 0 \\ 0 & n & 0 \\ 0 & 0 & n \end{bmatrix}$	$n = 2$	0.129273062632	$\lvert\text{Prim cell} - (n = 2)\rvert = 1.4 \cdot 10^{-2}$
	$n = 3$	0.130951392433	$\lvert(n = 2) - (n = 3)\rvert = 1.7 \cdot 10^{-3}$
	$n = 4$	0.131966933294	$\lvert(n = 3) - (n = 4)\rvert = 1.0 \cdot 10^{-3}$

Table 7.9: Entropy and entropy difference between the diagonal supercells studied for the calcite II at the constrained volume of 56.948 $\AA^3$/F.U.

7.11 Stability of calcite II in expanded supercells

Even though all calcite II volumes contained positive frequencies at Γ, to our surprise, imaginary frequencies were found for the first expanded supercell studied, i.e. the $n = 2$ diagonal supercell. This is something that has already been observed for calcite II at 56.929 $\AA^3$/F.U (Fig. 7.23). As shown in Figs. 7.24, 7.25, 7.26, and 7.27, this issue is happening, respectively, across PBE-D3, PBE, B3LYP-D3 and B3LYP functionals.

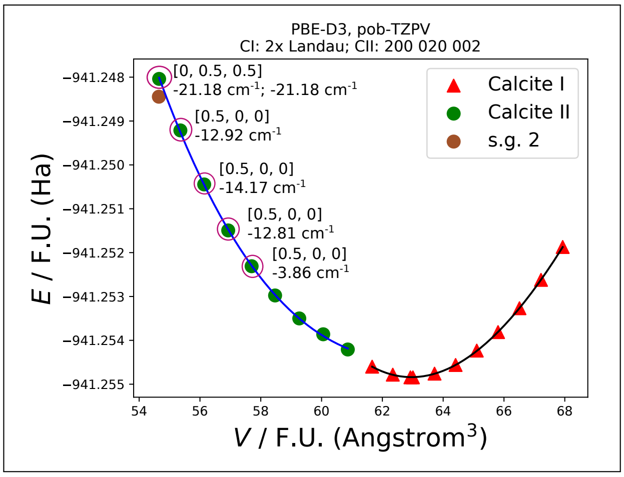

Figure 7.24

Volume / F.U. ($\AA^3$)	k-point	Imaginary Frequency (cm^{-1})
54.6569	[0, 0.5, 0.5]	-21.1818
		-21.1818
55.3555	[0.5, 0, 0]	-12.9294
		-12.9294
56.1392	[0.5, 0, 0]	-14.1722
56.9292	[0.5, 0, 0]	-12.8153
57.6992	[0.5, 0, 0]	-3.8663

Table 7.10

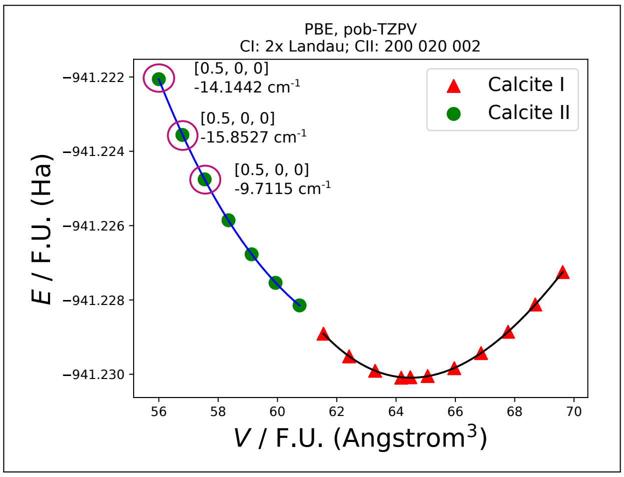

Figure 7.25

Volume / F.U. ($\AA^3$)	k-point	Imaginary Frequency (cm^{-1})
55.9991	[0.5, 0, 0]	-14.1442
56.7941	[0.5, 0, 0]	-15.8527
57.5445	[0.5, 0, 0]	-9.7115

Table 7.11

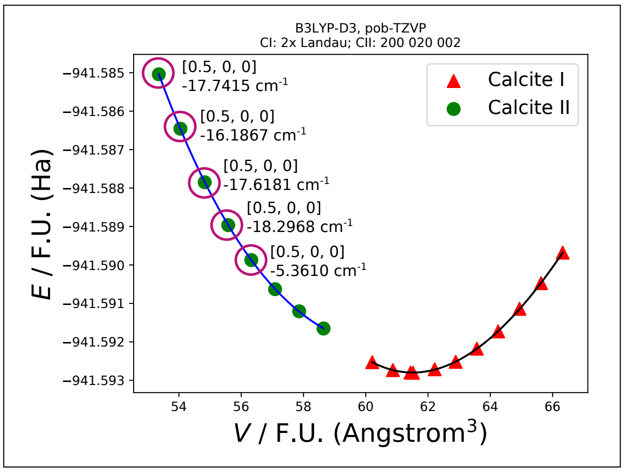

Figure 7.26

Volume / F.U. $(\AA^3)$	k-point	Imaginary Frequency (cm^{-1})
53.3543	[0.5, 0, 0]	-17.7415
54.0477	[0.5, 0, 0]	-16.1867
54.8281	[0.5, 0, 0]	-17.6181
55.5832	[0.5, 0, 0]	-18.2968
56.3249	[0.5, 0, 0]	-5.3610

Table 7.12

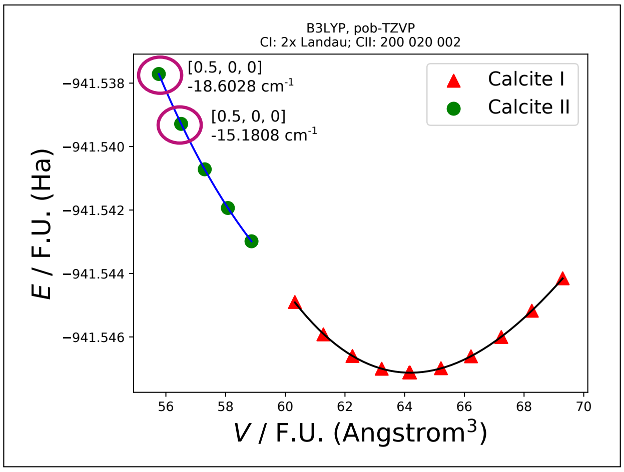

Figure 7.27

Volume / F.U. $(\AA^3)$	k-point	Imaginary Frequency(cm^{-1})
55.7627	[0.5, 0, 0]	-18.6028
56.5103	[0.5, 0, 0]	-15.1808

Table 7.13

Figs. 7.24, 7.25, 7.26, and 7.27, show the electronic energy as a function of volume for calcite I, calcite II and the space group 2 found, for the PBE-D3, PBE, B3LYP-D3 and B3LYP levels of theory respectively. Those calcite I volumes that present imaginary frequencies are rounded with circles. Calcite I, Calcite II, and s.g. 2 are represented, respectively, with filled red triangles, green filled circles and filled brown circles Tables 7.10, 7.11, 7.12 and 7.13 summarize the imaginary frequencies found in all the explored constrained volumes of calcite I. All data is fitted to a cubic polynomial.

The -21.18 cm^{-1} imaginary frequency found at the most compressed volume for the PBE-D3 level of theory was scanned. The eigenvectors along this phonon mode are shown in Fig. 7.28c. The animation for this eigenvector is displayed in Ref. [183]. Since this phonon mode is at a finite k-point, and the SCANMODE routine in crystal only works at the Γ point, it is necessary to perform the frequency calculation over the $n = 2$ diagonal supercell for calcite II, which means that there are no longer 5 irreducible atoms, but 80. Consequently, a frequency calculation for this case would require $80 \cdot 3 = 240$ displacements, which is quite expensive. After this calculation has been performed, then the scan of this imaginary phonon mode can be conducted (Fig. 7.28b). As can be seen, the depth of the double well potential is not as prominent as those shown in Fig. 7.3b for the soft phonon mode responsible for the transformation from calcite I to calcite II. After performing the steps 1-8 described in Section 7.4, the space group of the structure is found to be P-1 (space group 2) (Fig. 7.29). A constant volume optimization of this structure, gives the brown circle shown in Fig. 7.28a.

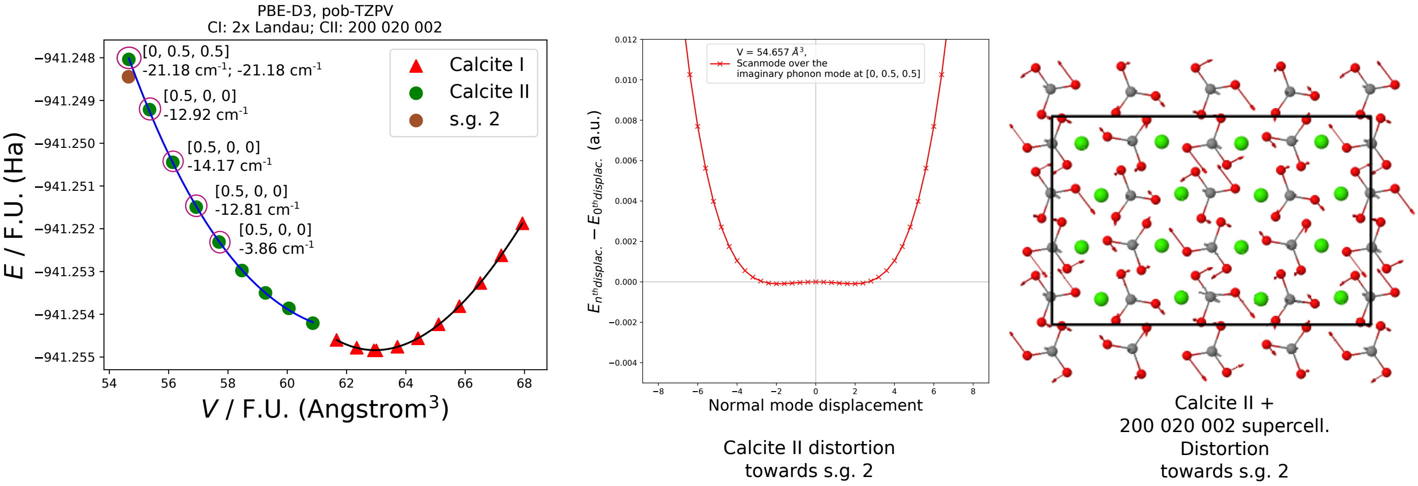

(a) **(b)** **(c)**

Figure 7.28: (a) Electronic energy vs volume curves for calcite I and II. In addition, the space group 2 is also shown, as a consecuence of distorting the atomic coordinates of the most compressed volume of calcite II. (b) Scanmode over the -21.18 cm^{-1} imaginary phonon mode encountered over the calcite II structure at 54.66 $\mathring{A}^3$. The depth of this minimum is very low. (c) Eigenvectors for this phonon mode. An animation for this eigenvector is shown in Ref. [183].

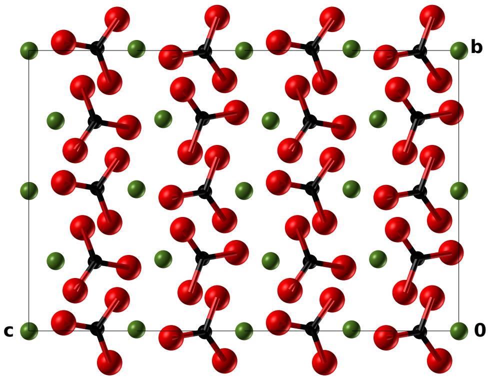

Calcite II
+ 200 020 002 supercell

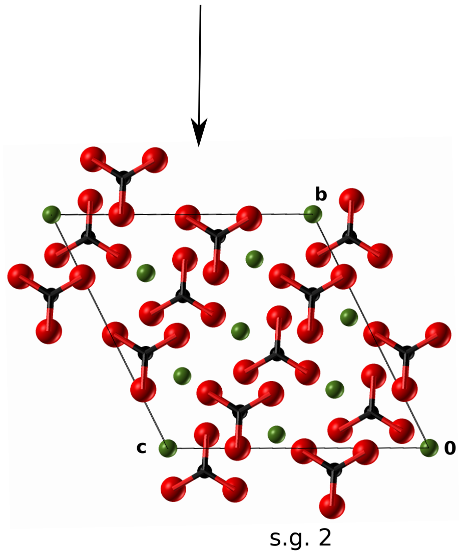

s.g. 2

Figure 7.29: Transformation from the $n = 2$ diagonal supercell of calcite II at the most compressed volume (56.66 Å^3) to the space group 2.

As shown in Figs. 7.24 and 7.25, only 4 volumes for calcite II do not contain imaginary frequencies, for both PBE-D3 and PBE respectively. Therefore, these are considered as the stable calcite II volumes, which we will take into account for the temperature - pressure phase boundary. On the other hand, there are only 3 calcite II stable volumes (Figs. 7.26 and 7.27). This is not enough data for a cubic fit for both the $E(V)$ and $F(V)$ curves. The temperature analysis of $F(V)$ and $G(P)$ has been performed considering these four calcite II stable volumes, for the PBE-D3 and PBE levels of theory. These results are shown in Figs. 7.30 and 7.31.

We must notice that a cubic fit for only four data points is not ideal; thus, the $F(V)$ curves, and consequently the first derivative which gives us the pressure, are results not to be considered as significant. For instance, a strange shape of the $V(P)$ curve at 0 K for PBE-D3 has been obtained for calcite II (Fig. 7.30). This can only be explained because we only start with four data points in the $E(V)$ or $F(V)$ curves respectively. The pressure of transition happens not to vary as the temperature increases, which leads to a temperature - pressure phase boundary that is almost a straight line (light green circles in Fig. 7.32).

An anomalous behaviour in the $V(P)$ curves at $T \geqslant 311.52$ K has been observed for the PBE level of theory as well (Fig. 7.31). Similarly, the explanation behind this is only because the starting point, 4 volumes for calcite II, is not ideal; hence, the temperature - pressure phase boundary obtained with this scheme in Fig. 7.33a with light green circles cannot be trusted completely.

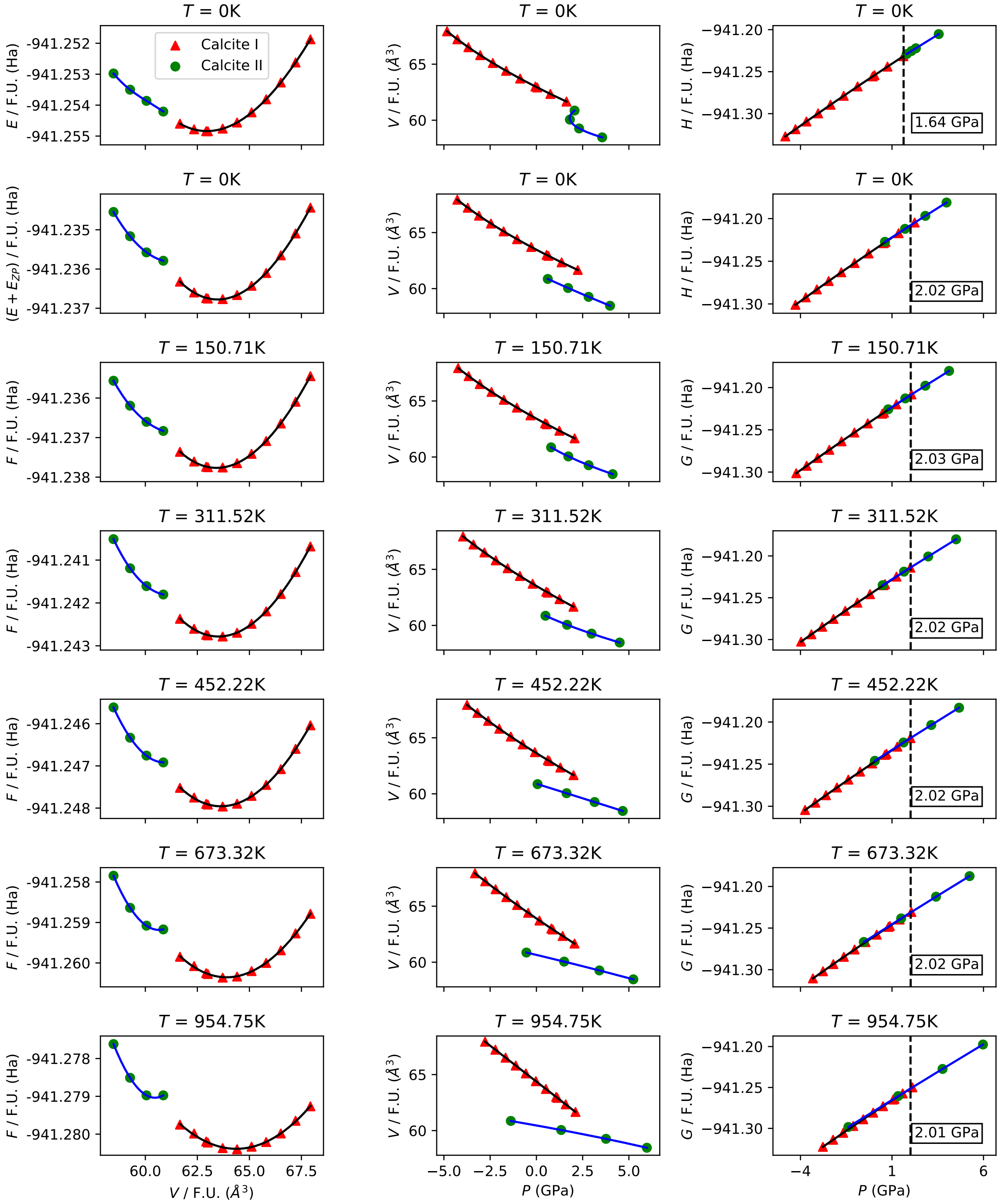

Figure 7.30: Energetics for the expanded supercells in the PBE-D3 level of theory.

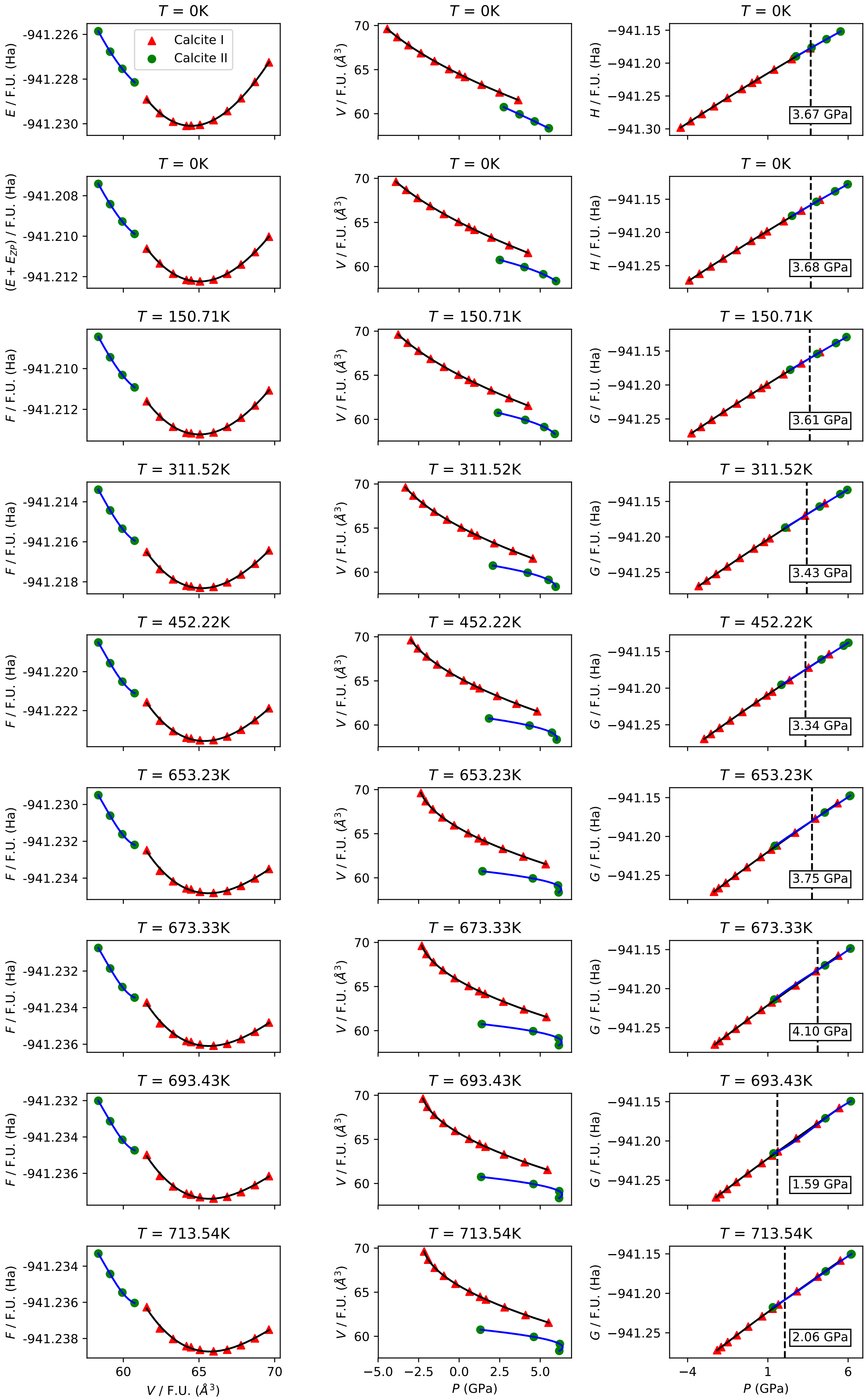

Figure 7.31: Energetics for the expanded supercells in the PBE level of theory.

Figs. 7.30, and 7.31: Results for the $n = 2$ supercell, for the PBE-D3 and PBE levels of theory respectively. First row: energy, pressure and enthalpy at 0 K, neglecting zero point motion. Second row: accounting for zero point energy. Rest of the rows: Helmholtz free energy, pressure and Gibbs free energy at different temperatures. For all the cases, the pressure has been obtained as the derivative of the energy (athermal limit) or Helmholtz free energy (finite temperature). The Enthalpy and Gibbs free energy fits correspond to cubic fits. The pressure of intersection between calcite I and II is also shown. In each case, the temperature at which the intersection between Gibbs free energy curves is located at very high values of pressure is also shown.

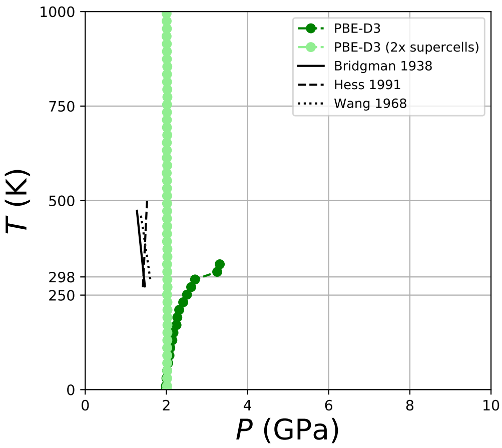

Figure 7.32: Temperature-pressure calcite I- calcite II phase diagram for the PBE-D3 level of theory, by considering the Landau supercell for calcite I and the primitive cell for calcite II (dark green), and two times the Landau supercell and the $n = 2$ diagonal supercell for calcite II (light green).

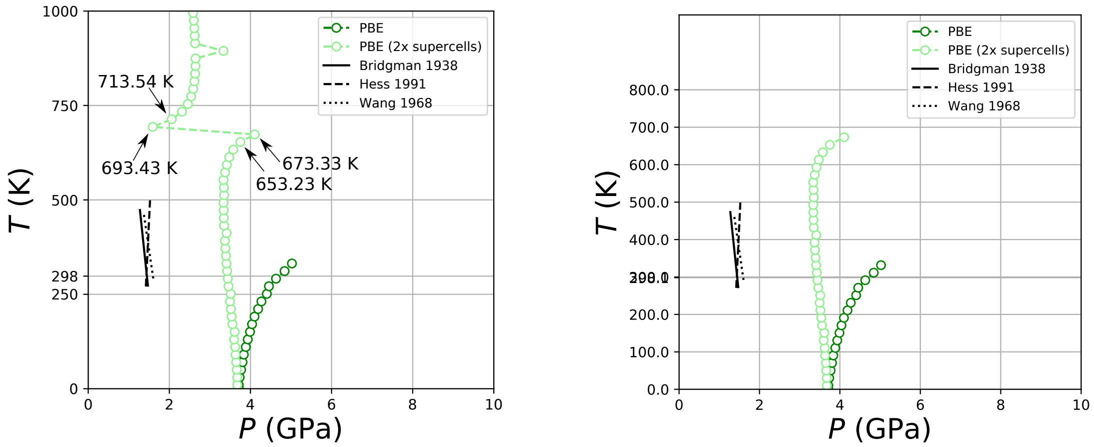

(a) **(b)**

Figure 7.33: All PBE level of theory, with calcite II using the $n = 2$ supercell (light green circles) or the primitive cell (dark green circles). Fig. 7.33a shows the temperatures; For the same reason as explained before, there is a critical temperature for which the Gibbs free energy curves coincide in a broad pressure range. This critical temperature is 673.33 K in this case. Fig. 7.33b is showing the same plot, but without temperatures.

Imaginary frequencies were also detected in almost all volumes for calcite II in the $n = 3$ diagonal cell for calcite II, as can be seen in Fig. 7.34.

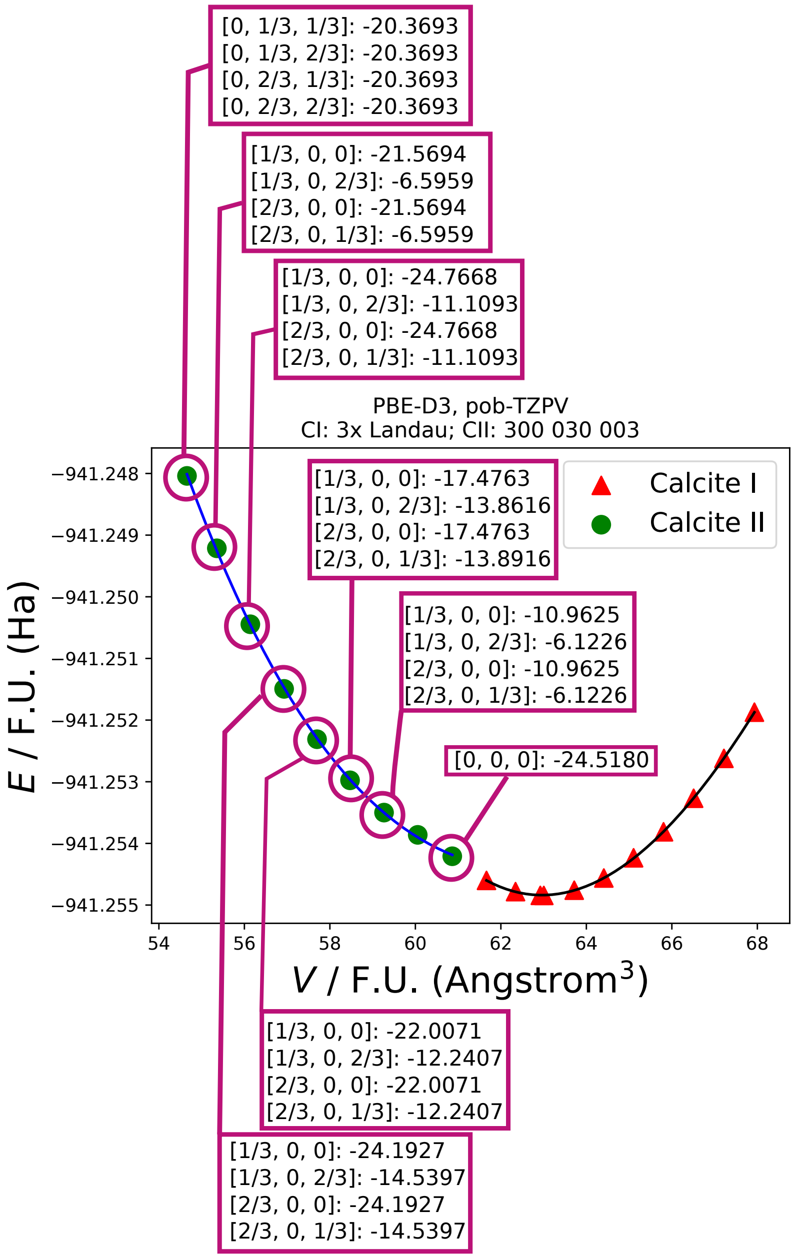

Figure 7.34: Electronic energy - volume curves for the three times the Landau supercell for calcite I and the $n = 3$ diagonal supercell for calcite II. Only one calcite II volume does not present imaginary frequencies.

7.12 A possible explanation for imaginary frequencies found at expanded supercells

Imaginary phonon frequencies have been found in the high-pressure simple cubic phase of calcium [184]. In that study, by fully including anharmonic effects, imaginary phonons become positive even at zero temperature so that the simple cubic phase becomes mechanically stable, in agreement with experiments.

Given the simplicity and high symmetry of the simple cubic calcium, all necessary anharmonic coefficients were calculated *ab initio* up to the fourth order in displacement. Techniques such as self-consistent harmonic approximation (SCHA) can be then applied to compute the temperature-dependent renormalized phonon frequencies.

One possible explanation for imaginary frequencies found at finite **k**-points in the $n = 2$ and $n = 3$ diagonal supercells for calcite II might be because of there is a need to account for anharmonicity. This is subject to a further study in the future.

7.13 Linear fit and other approaches for modeling $G(P)$

So far, the $G(P)$ curves have been fitted to a cubic polynomial. The pressure of intersection that arises from $G^{I}(P) - G^{II}(P) = 0$ is very sensitive to the order of the polynomial to which the curves have been fitted. This is because both $G(P)$ curves merge smoothly at pressures close to the pressure of transition. This effect is shown in Fig. 9.1 for three temperatures: 0 K (including zero point energy), 10.00 K, 90.40K and 311.52K.

For both the athermal limit and 10.00 K, a pressure of intersection of 1.99 and 1.57 GPa is predicted for cubic and linear fits respectively (Fig. 7.35a - 7.35d). This intersection corresponds to an interpolation within the range of data set available.

For 90.40 K, a cubic fit predicts a pressure of intersection of 2.08 GPa, and an extrapolation in the calcite I branch is necessary to yield the intersection (Fig. 7.35e). On the contrary, there is no need for an extrapolation within a linear fit, where the pressure of intersection is interpolated to 1.58 GPa (Fig 7.35f).

This effect is remarkable at 311.52 K: a cubic fit predicts a pressure of intersection of 3.25 GPa (again, extrapolation of the calcite I branch is necessary, Fig. 7.35g). For this temperature, the linear fit extrapolates as well, predicting a pressure of intersection of 1.58 GPa (Fig. 7.35h). In that figure, it can be easily seen that the highest pressure available for calcite I is not very well described by the linear fit. Consequently, a fit linear fit based on the last three volumes for each branch was proposed. This is shown in Fig. 7.35i, where an extrapolated pressure of intersection sits at 1.93 GPa.

Since both $G(P)$ curves are coincident in a wide range of pressure, the pressure of transition can also be estimated as the mean value of pressure located between the highest pressure of calcite I and the lowest pressure for calcite II. This range of pressures is shown with a pink window frame in Fig 7.36 for several temperatures: athermal limit (Fig. 7.36a), 10.00 K (Fig. 7.36b), 90.40 K (Fig. 7.36c) and 311.52 K (Fig. 7.36d). The error bar in these cases is given by the range of pressures inside this region.

The pressure - temperature phase boundary obtained by fitting to cubic, linear and linear restricted to last three volumes is shown in Fig. 7.37:

- The approach based on a cubic fit produces the green phase boundary, already shown in Fig. 7.20.
- The approach based on a linear fit restricted to last three points is shown in pink.
- The linear approach produces a phase boundary very close to the experiment (blue curve).
- The phase boundary originated as a consequence of the mean value of pressure located between the highest pressure of calcite I and the lowest pressure of calcite II is shown in orange.

From these results, we deduce that the linear approach is the closest to the experiment. The error bar for the phase boundary obtained through this approach has been determined in the following way. Given two linear fits, e.g. $G_1 = a_1 + b_1 P$ and $G_2 = a_2 + b_2 P$, the intersection is given by:

$$P = \frac{a_2 - a_1}{b_1 - b_2} \tag{7.7}$$

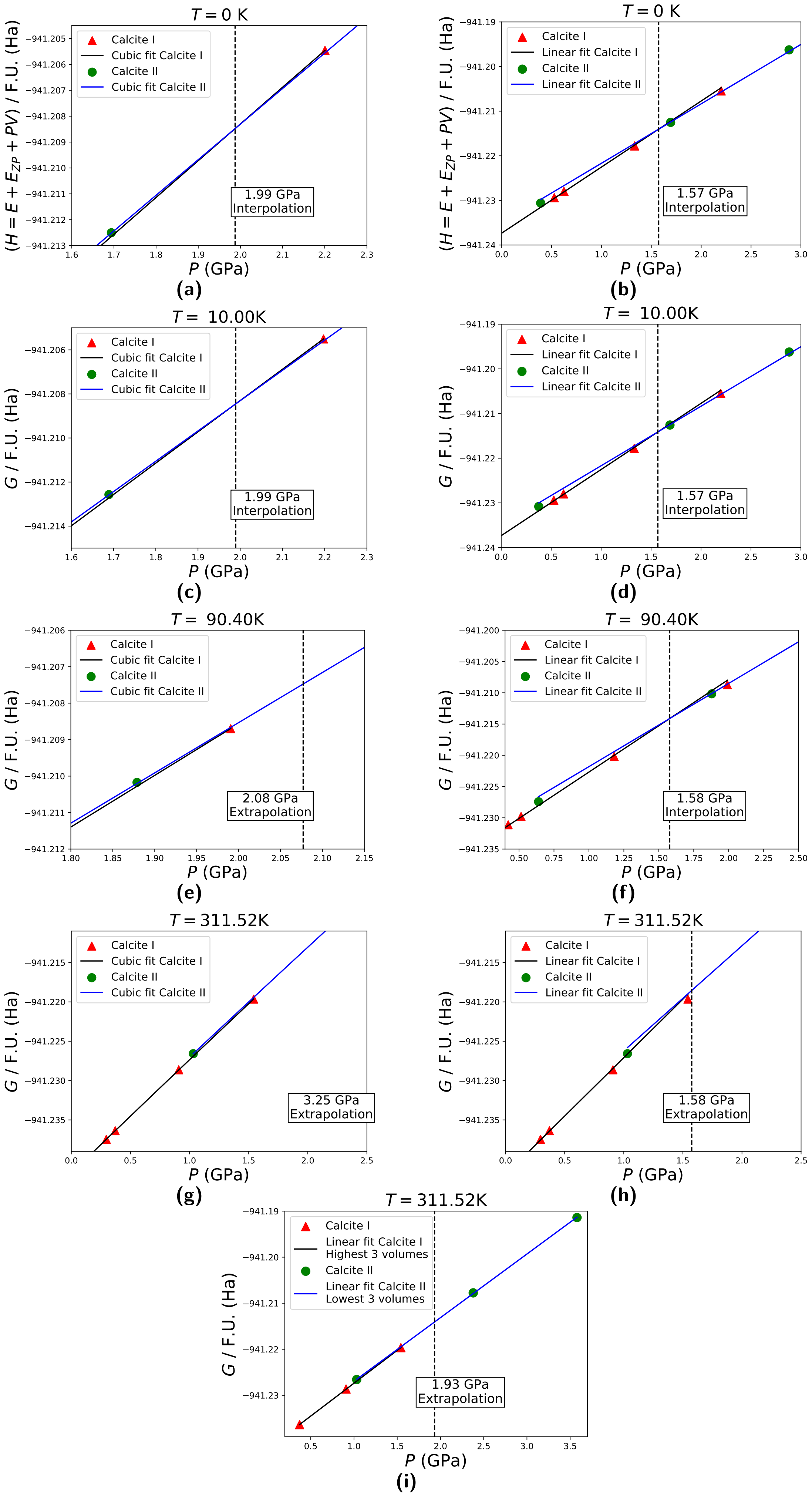

Figure 7.35: (Caption next page.)

Figure 7.35: (Previous page). $G(P)$ curves at four different temperatures for calcite I and calcite II, where a cubic (left panel) and linear fit (right panel) has been adopted. For 311.52 K, a linear fit to the last volumes of calcite I and II has been studied as well.

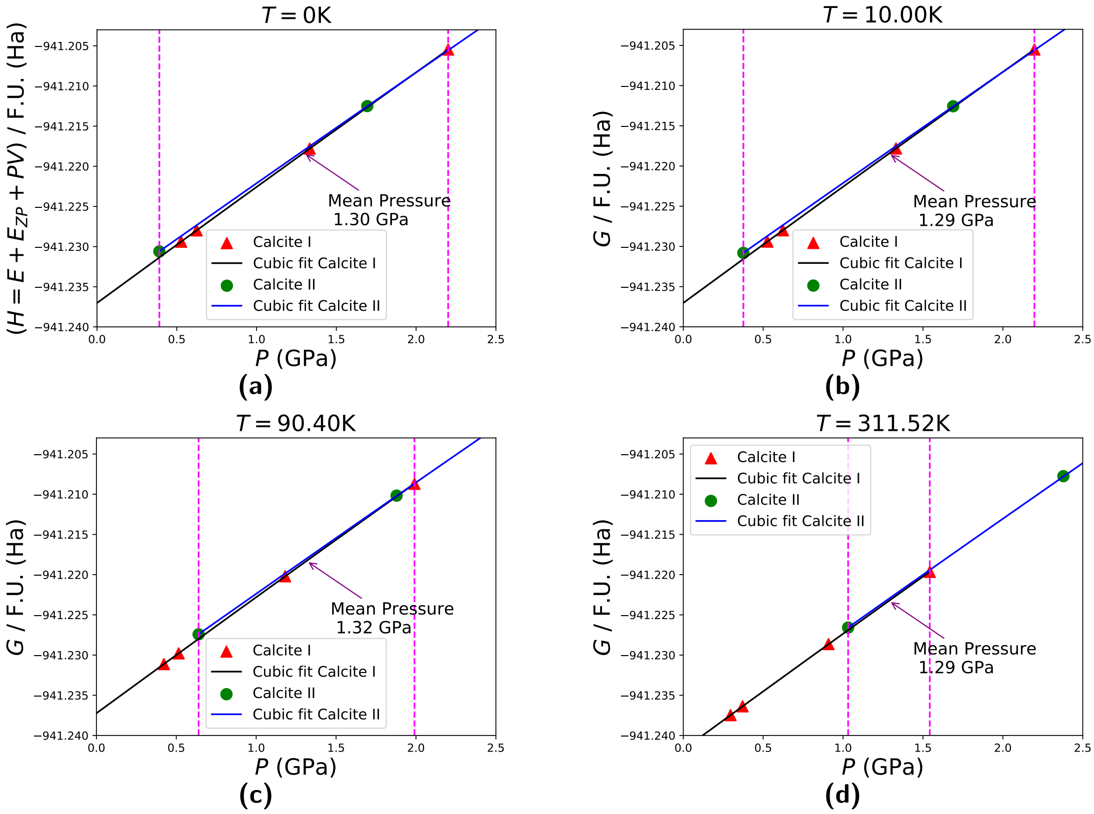

(a) **(b)** **(c)** **(d)**

Figure 7.36: $G(P)$ curves at four different temperatures for calcite I and calcite II. The range of pressures within a pink frame are those for which both curves are almost coincident. The mean value of pressure is also shown in this region.

so that P is a function of 4 variables: $P = P(a_1, a_2, b_1, b_2)$. Thus, the error on P is given by:

$$\delta P = \sqrt{\left(\frac{\partial P}{\partial a_1}\delta a_1\right)^2 + \left(\frac{\partial P}{\partial a_2}\delta a_2\right)^2 + \left(\frac{\partial P}{\partial b_1}\delta b_1\right)^2 + \left(\frac{\partial P}{\partial b_2}\delta b_2\right)^2} \tag{7.8}$$

where δb_i is the error in the slope, and δa_i is the error in the intercept. On the other hand these derivatives are:

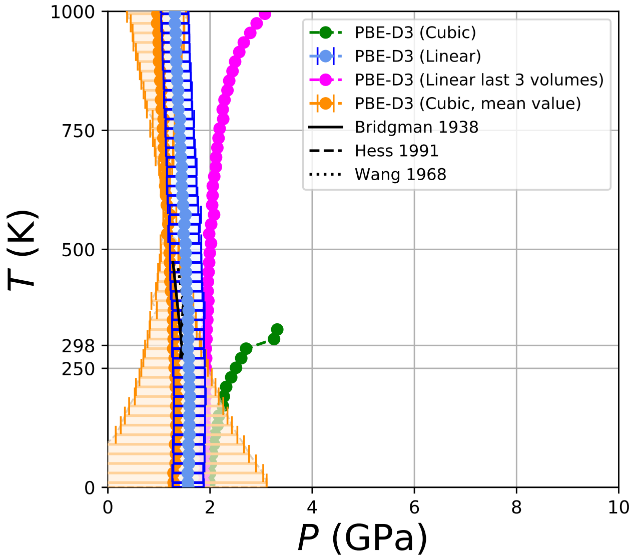

Figure 7.37: Temperature-pressure phase boundary obtained with the following approaches: cubic, linear, linear restricted to last 3 volumes and the approach based on the mean value of pressure located beteween the highest pressure of calcite I and the lowest pressure for calcite II.

$$\frac{\partial P}{\partial a_1} = \frac{1}{b_2 - b_1} \tag{7.9}$$

$$\frac{\partial P}{\partial a_2} = \frac{1}{b_1 - b_2} \tag{7.10}$$

$$\frac{\partial P}{\partial b_1} = \frac{a_1 - a_2}{(b_1 - b_2)^2} \tag{7.11}$$

$$\frac{\partial P}{\partial b_2} = \frac{a_2 - a_1}{(b_1 - b_2)^2} \tag{7.12}$$

The temperature - pressure phase diagram for each level of theory is shown in Fig. 7.38. PBE-D3 is the closest answer to the experiment, followed by B3LYP-D3, PBE and B3LYP. Clearly, dispersion effects lower down the pressure of transition at any temperature, as was observed with the cubic fit approach (Fig. 7.20). Unlike the cubic fit approach, the linear fit approach is capable of describing a calcite I - calcite II phase boundary up to 1000 K and beyond.

7.13.1 Second order phase transition at higher temperatures

There are some studies in the literature that focus on the nature of the calcite I - calcite II phase boundary at higher temperatures. The motivation behind these studies is driven by the fact

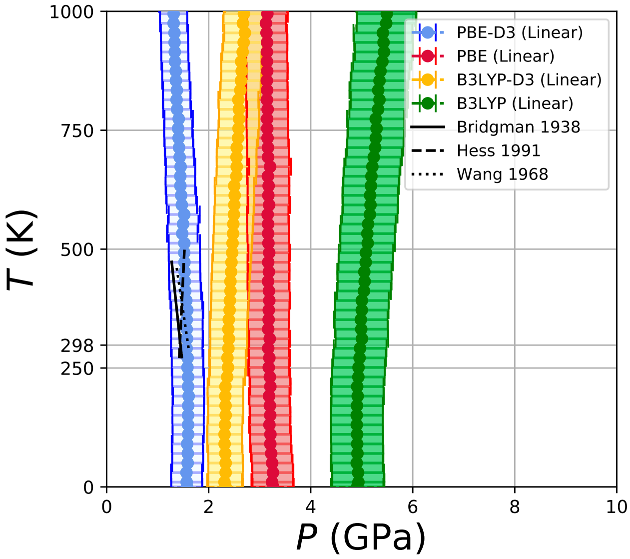

Figure 7.38: Temperature-pressure phase boundary using a linear approach, for the PBE-D3, PBE, B3LYP-D3 and B3LYP levels of theory. The error bar has been calculated according to Eq. 7.8.

that it has been observed that soft phonon mode phase transitions are commonly accompanied with a multicritical point phenomena and a change in the order of the transition (i.e. $BaTiO_3$, at 32 kbar and room temperature [185], or a bicritical point in $SrTiO_3$ [186]). In 1972, Kondo *et al.* [157] measured the change of longitudinal ultrasonic velocity up to 973 K and 2.5 GPa. In that study, a change of slope from negative to positive is found to occur at 573 K. Hatch and Merril [136] have used group-theoretical techniques based on the Landau criteria of second order phase transitions and have shown that the symmetry of the two structures is compatible for such a calcite I - calcite II second order phase transition to occur. On the contrary, Felix and Hatch [163] studied the transformation with renormalization-group techniques and concluded that the transition is not second order unless additional restrictions are imposed. Barnett *et al.* [159] performed Electron Paramagnetic Resonance experiments at 473 K and 1.5 GPa, and suggest the possibility of a critical point at 473 K.

In this section, we will discuss a potential change in the order of the transition at higher temperatures. As was explained in Section 2.6, a first order phase transition is discontinuous in the first derivative of $G(P)$, i.e. $V(P)$. In other words, a first order phase transition can be identified by a drop in the volume as a function of pressure. On the contrary, a second order phase transition does not present this discontinuity on $V(P)$.

The evolution of $V(P)$ for calcite I and II at 0 K, 10 K, 90.4 K, 311.52 K, 532.63 K, 693.43 K and 753.74 K are summarised in Fig. 7.39 for the PBE-D3 level of theory. For each temperature there is a pressure of transition (P_{trs}), with an error bar associated (δP), as was reported in Fig. 7.38. The pressure of transition P_{trs} at each temperature as well as the error bar δP is shown in Fig. 7.39, respectively, with an orange dashed line and a light blue area.

Given a P_{trs} for each temperature, an interpolation $V(P = P_{trs})$ generates the volumes $V_{\text{calcite I}}$ and $V_{\text{calcite II}}$, illustrated in Fig. 7.39 with dashed orange lines. A clear drop in the volume is observed for temperatures below 600 K. It is useful to quantify this drop in the volume with the quantity ΔV, defined as:

$$\Delta V = V_{\text{calcite I}} - V_{\text{calcite II}} \tag{7.13}$$

with an error bar associated:

$$\delta(\Delta V) = \sqrt{(\delta V_{\text{calcite I}})^2 + (\delta V_{\text{calcite II}})^2} \tag{7.14}$$

The evolution of $\Delta V \pm \delta(\Delta V)$ with temperature is shown in Fig. 7.40 for each level of theory. It can be noticed that this quantity ΔV decreases with temperature. The temperature at which $\Delta V = 0$ is a critical temperature at which the phase transition changes from first to second order. For instance, this critical temperature is $T_c = 684.9$ K for the PBE-D3 level of theory (Fig. 7.40a). The lower bound of the error associated with this critical temperature has been estimated as the temperature at which the error bar on ΔV crosses the $\Delta V = 0$ line. For instance, $\Delta V = 0$ is within the lower bound of the error on ΔV at $T = 532.6$ K (blue arrow in Fig. 7.40a). Thus, 532.6 K has been considered as the lower bound of the error on T_c.

Consequently, $T_c = 684.9 \pm 152$ K, 1430.2 ± 214 K and 732.6 ± 159 K for, respectively, PBE-D3, B3LYP-D3 and PBE levels of theory (see Fig. 7.40). B3LYP does not predict a $\Delta V = 0$ for the range of temperatures considered, but we can estimate the lower bound of critical temperature to be 1376.9 K (Fig. 7.40c).

The second order phase transition for each level of theory is represented along with the phase diagram in Fig 7.41.

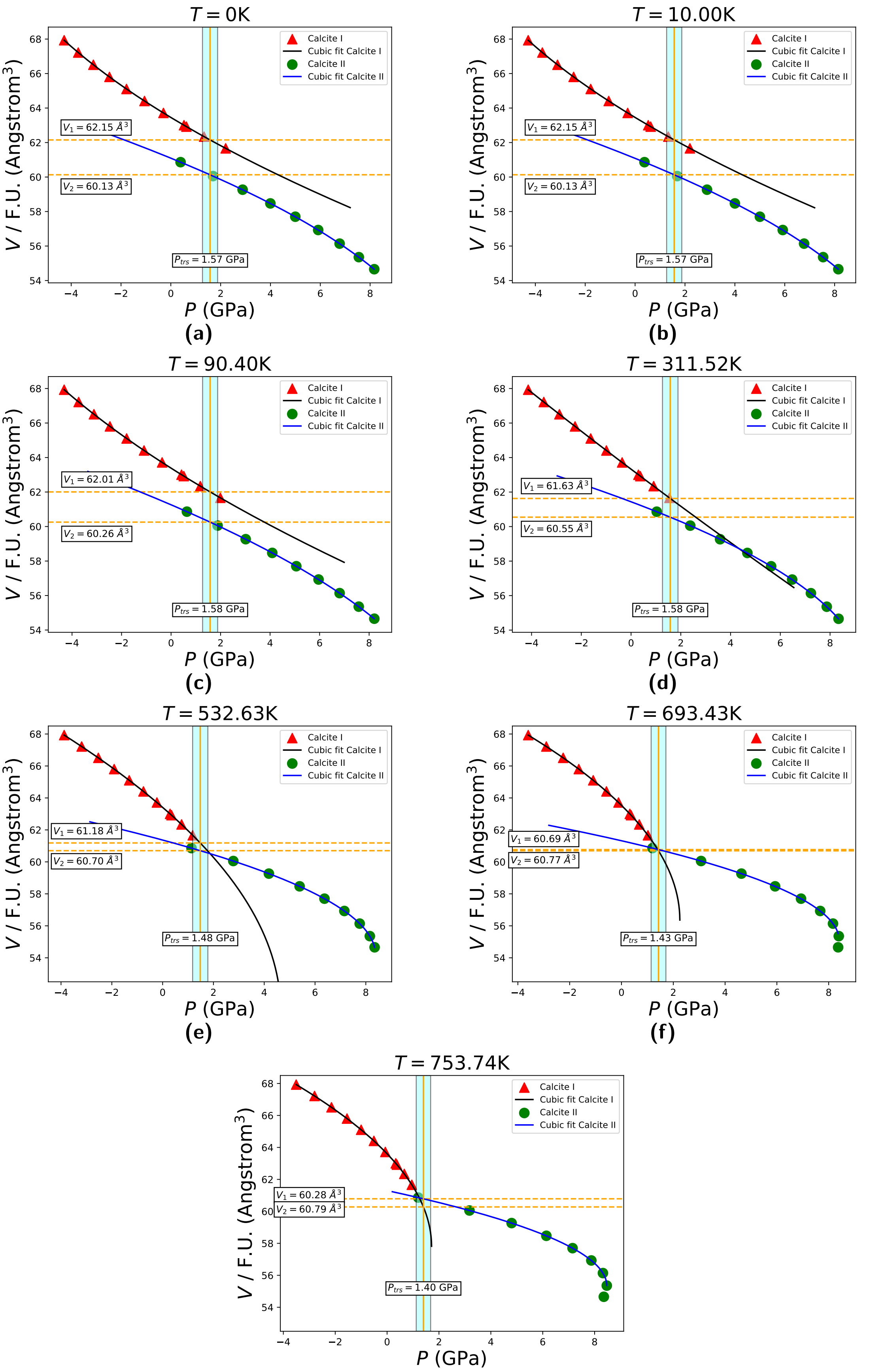

(a) **(b)** **(c)** **(d)** **(e)** **(f)** **(g)**

Figure 7.39: Evolution of $V(P)$ at 10.0, 90.40, 311.52, 532.63, 693.43 and 753.74 K for the PBE-D3 level of theory. At each temperature, the pressure of transition for a linear fit apporach and the error bar associated is shown, respectively, with orange line and a light blue shadow.

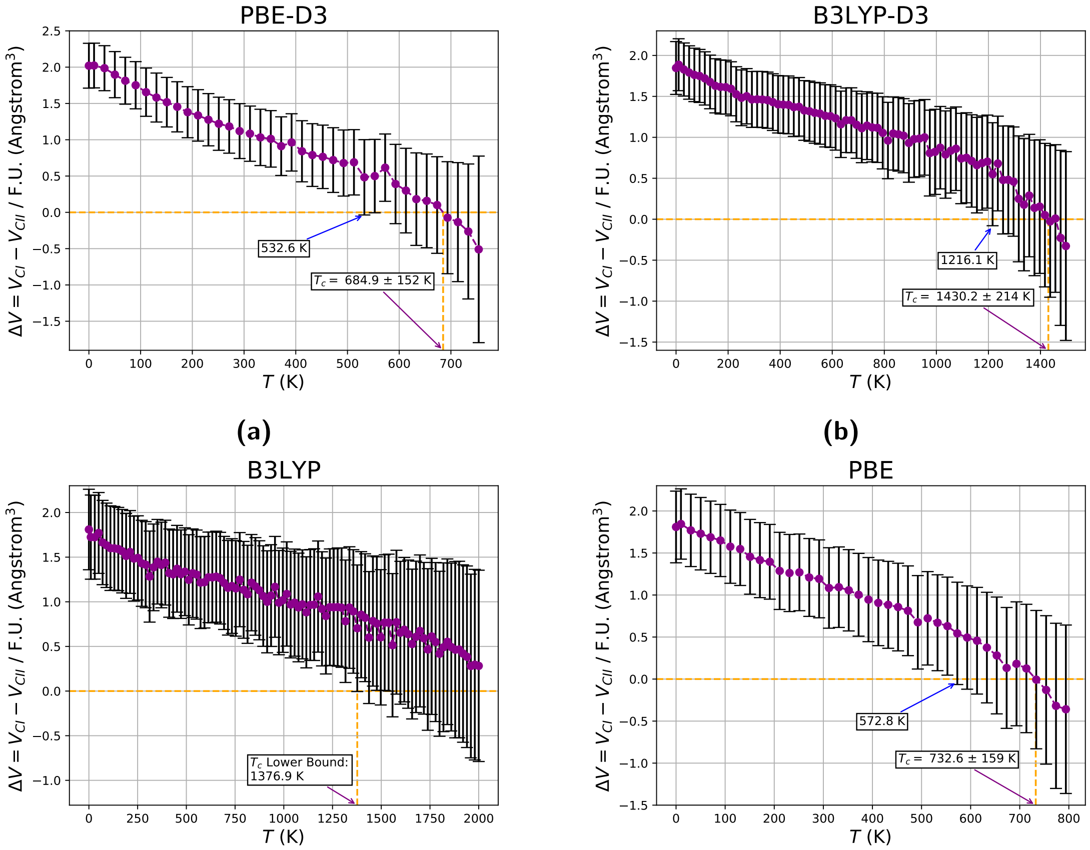

(a) **(b)**

(c) **(d)**

Figure 7.40: Evolution of ΔV with temperature for PBE-D3, B3LYP-D3, B3LYP and PBE levels of theory. The error on ΔV at each temperature has been calculated according to Eq. 7.14. The temperature at which $\Delta V = 0$ is the critical temperature, T_c, and corresponds to the temperature at which there is a change in the order of the transition. The lower bound error for this T_c is given by the temperature at which the error bar on ΔV crosses the $\Delta V = 0$ line.

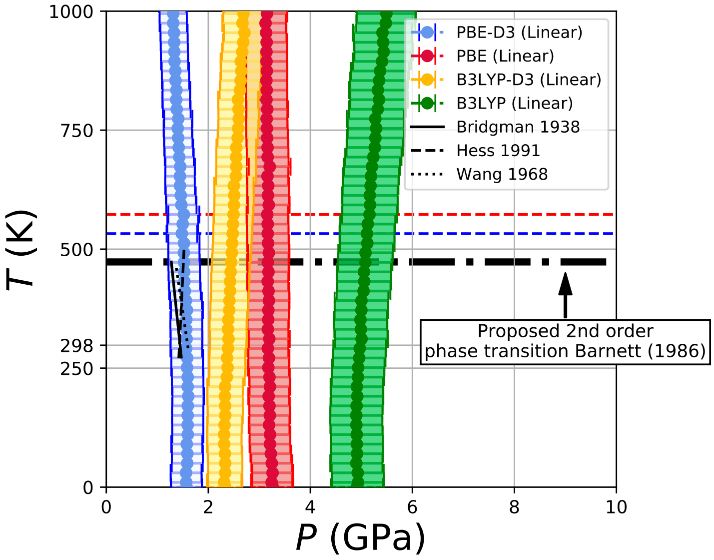

Figure 7.41: Temperature-pressure phase boundary using a linear approach, for the PBE-D3, PBE, B3LYP-D3 and B3LYP levels of theory. The error bar has been calculated according to Eq. 7.8. The experimental phase boundaries are also reported: Bridgman [113], Wang *et al.* [158] Hess *et al.* [119], as well as the critical point proposed by Barnett *et al.* [159] in thick dashed lines. The lower bound critical temperature obtained for PBE-D3 and B3LYP-D3 are shown with, respectively, dashed horizontal red and blue lines.

7.14 Common tangent approach

The last approach we tried in order to determine the pressure of transition for a given temperature is based on the analysis of the slope of the common tangent between both calcite I and II $F(V)$ curves.

Given two $F(V)$ curves for two phases, the slope of the common tangent gives the pressure of transition at finite temperature. Since the Hemholtz free energy is:

$$F = E - TS, \qquad \text{(Eq. 2.265 from Section 2.5.4)}$$

in the athermal limit ($T = 0$), the curves to be analyzed are $E(V)$, or $(E + E_{ZP})(V)$ if we include the zero point motion.

Given two energy-volume curves like the ones shown in Fig. 7.42a ($E_1(V)$ and $E_2(V)$, respectively for calcite I and II), the common tangent passes through both curves in points $[V_1, E_1(V_1)]$ and $[V_2, E_2(V_2)]$.The evaluation of E_1 and E_2 on V_1 and V_2 reads like:

$$E_1(V_1) = a_0 + a_1V_1 + a_2V_1^2 + a_3V_1^3 \tag{7.15}$$

$$E_2(V_2) = a_4 + a_5V_2 + a_6V_2^2 + a_7V_2^3, \tag{7.16}$$

where the first derivative is:

$$E_1'(V_1) = a_1 + 2a_2V_1 + 3a_3V_1^2 \tag{7.17}$$

$$E_2'(V_2) = a_5 + 2a_6V_2 + 3a_7V_2^2, \tag{7.18}$$

It is satisfied that m, the slope of the common tangent reads like:

$$m = \frac{E_1(V_1) - E_2(V_2)}{V_1 - V_2} = E_1'(V_1) = E_2'(V_2). \tag{7.19}$$

We can write down a system of two equations:

$$\begin{cases} \dfrac{E_1(V_1) - E_2(V_2)}{V_1 - V_2} - E_1'(V_1) = 0 & (7.20) \\ E_1'(V_1) - E_2'(V_2) = 0 & (7.21) \end{cases}$$

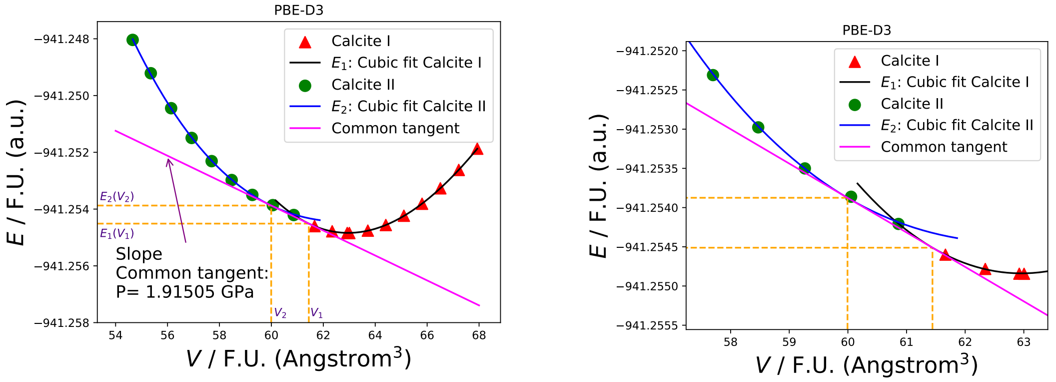

(a) **(b)**

Figure 7.42: $E(V)$ curves for calcite I and II in the athermal limit (neglecting zero-point motion). The slope of the common tangent is shown, which is an equation that passes through points $[V_1, E_1(V_1)]$ and $[V_2, E_2(V_2)]$ Fig 7.42b is just the zoomed version of 7.42a.

The system of equations 7.20 and 7.21 contain two unknowns, V_1 and V_2. Once solved this system of equations, and V_1 and V_2 are obtained, then m can be calculated with Eq. 7.19. Once obtained m, the common tangent equation just reads like:

$$E - E_1(V_1) = m(V - V_1)$$

$$\boxed{E = E_1(V_1) + m(V - V_1)} \tag{7.22}$$

The same formulation is valid at finite temperature, by replacing E with F in equations 7.15 - 7.22. An analysis of the slope of the common tangent across temperatures is shown in Fig. 7.43 for the PBE-D3 level of theory.

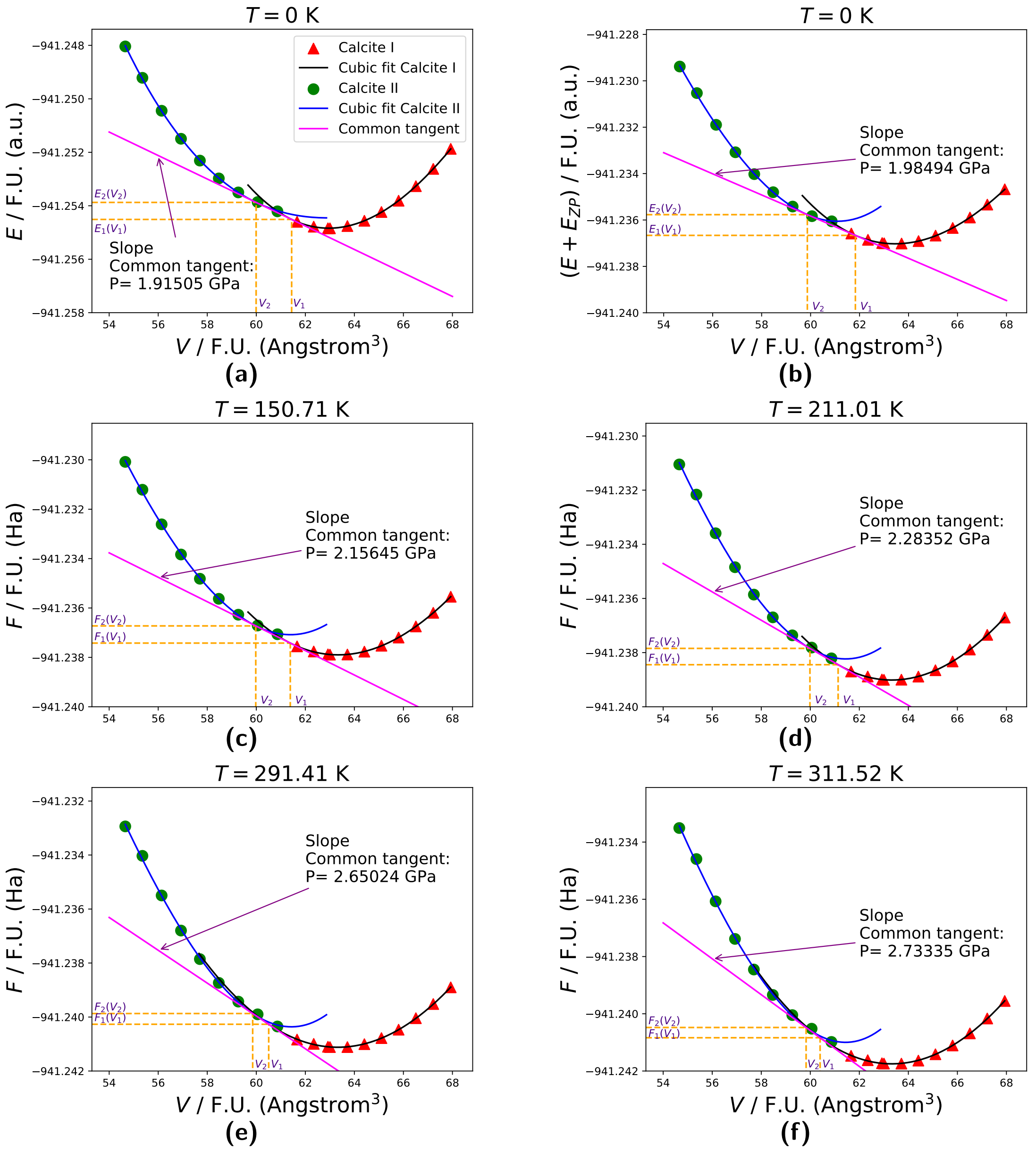

Figure 7.43: Common tangent for calcite I and II $E(V)$, $(E + E_{ZP})(V)$ and $F(V)$ curves, across temperatures.

The slope of the common tangent at each temperature gives the pressure of transition at a finite T, so that the temperature - pressure phase boundary can be generated. The search of the common tangent between two phases for an array of temperatures, and the consequent generation of the temperature-pressure phase boundary has been automated in a series of python and bash scripts available in my GitHub repository named `Common_Tangent` [187].

7.15 Comparison between the common tangent approach and the cubic fit approach

It is very interesting to compare both methods: the previous method based on the intersection of cubic or linear Gibbs free energies and the common tangent approach. As can be seen in Fig. 7.44, the overall temperature-pressure phase boundary obtained with the common tangent procedure yields a phase boundary almost coincident with the one obtained via the intersection of Gibbs free energies fitted to a cubic polynomial.

For temperatures below 300 K, the common tangent approach gives the same phase boundary as the cubic fit. It is only at higher temperatures that both approaches start to differ. As we already know, there is a temperature at which both $G(P)$ curves are coincident in a broad pressure range, and the non-complex root for $G^{I}(P) = G^{II}(P)$ is located at very high values of pressure. This effect is also transferred to the common tangent approach in the following way. By analyzing the shape of the $F(V)$ curves across temperatures, it can be noticed that for T=0 K, and up to 150.71 K (Figs. 7.43a - 7.43c), the volume V_1 (volume needed for sorting out the common tangent equation (Eq. 7.22)) is interpolated from the data set of calcite I volumes available. On the contrary, from 211.01 K onwards, the common tangent starts not being representative of the situation, since the volume V_1 is clearly extrapolated (this effect is remarkable at 311.52 K). This is the explanation for the phase boundary behaving abnormally from 331.52 K onwards. This coincides with the temperature at which the cubic fit approach starts to fail as well.

7.16 Determination of the TP phase boundary above the critical temperature

Both cubic and common tangent approaches are mathematically equivalent and indeed give the same phase boundary (Fig. 7.44). On the other hand, the linear approach fortuitously gives a phase boundary closer to the experiment (Fig. 7.41), but indeed this approach shall not be considered as reliable, since it does not agree with the phase boundary obtained through the common tangent approach.

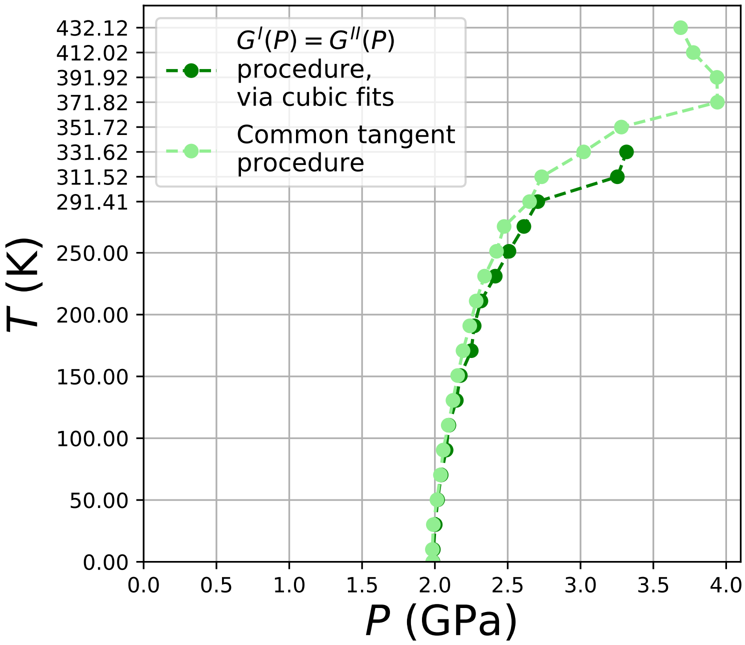

Figure 7.44: Temperature-pressure phase boundary obtained via intersection of Gibbs free energy curves (cubic fits) and by the common tangent procedure. All PBE-D3 level of theory.

For a fixed temperature T, the intersection of the cubic fits $G^I(P)$ and $G^{II}(P)$ (i.e. the solution for $G^I(P) - G^{II}(P) = 0$) gives us the pressure of transition. For temperatures and pressures lying on the equilibrium curve (i.e. phase boundary), both calcite I and II exist simultaneously and in contact. For every level of theory there is a temperature for which both $G(P)$ curves start to coincide in a broad pressure range, which makes the solution ($G^I(P) - G^{II}(P) = 0$) to occur at very high values of pressure. We will label this temperature as the critical temperature, T_c. Above this critical temperature, the order of the transition changes from first to second order. The difference between first and second order phase transitions was clearly presented in Fig. 2.35. A simplified version of this figure is presented in Fig. 7.45, where only the shapes of $G(P)$ and $V(P)$ are presented for a first and second order phase transition.

For $T \leqslant T_c$, the shape of $G(P)$ curves is such that this allows to identify an intersection between Gibbs free energy curves (Fig. 7.45a). On the contrary, for $T > T_c$, the shape of $G(P)$ curves do not allow for a clear intersection (Fig. 7.45c), and this is the reason why we cannot identify a clear crossing between $G^I(P)$ and $G^{II}(P)$ above this critical temperature.

A method to determine the second order phase boundary above this critical temperature is needed. As can be seen in Fig. 7.45d, this pressure of transition can be determined as the pressure where both $V(P)$ curves meet.

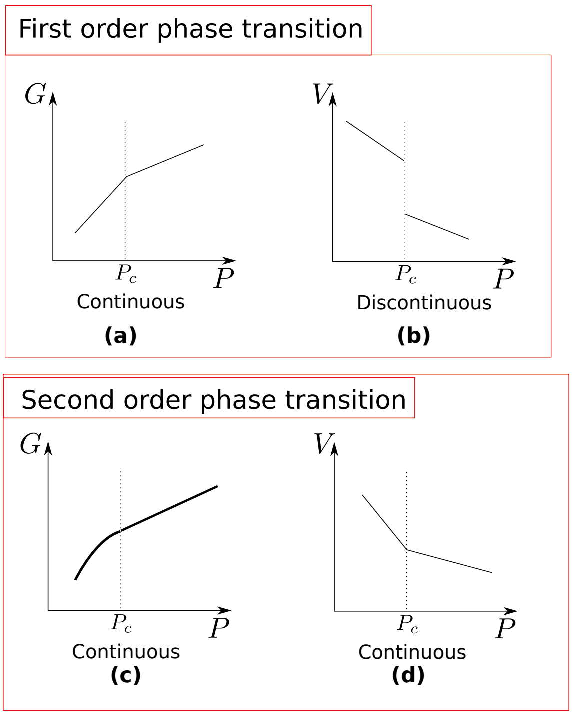

$$\boxed{V = \left(\frac{\partial G}{\partial P}\right)_T}$$

Figure 7.45: Summarized version of Fig. 2.35. In this figure, only the evolution of $G(P)$ and $V(P)$ are shown for a first and second order phase transition.

For $T \leqslant T_c$, the $V(P)$ curves are shown in Fig. 7.46. The pressure indicated as P_{trs} at each temperature is the pressure obtained from the cubic fit approach. Volumes V_1 and V_2 for calcite I and II respectively can be interpolated as shown in these figures.

Above the critical temperature, the equation $V^I(P) - V^{II}(P) = 0$ is solved so that we can sort out a pressure of transition for a fixed temperature (Fig. 7.47). In this way, a TP second order phase boundary can be obtained, which is presented in Fig 7.48 with crosses for the PBE-D3, PBE, B3LYP-D3 and B3LYP levels of theory. The position of the critical temperature T_c varies with the level of theory, and is summarized in Table 7.14.

Level of theory	T_c (K)
PBE-D3	331.62
PBE	331.62
B3LYP-D3	653.23
B3LYP	934.65

Table 7.14: Critical temperature T_c found for PBE-D3, PBE, B3LYP-D3 and B3LYP levels of theory

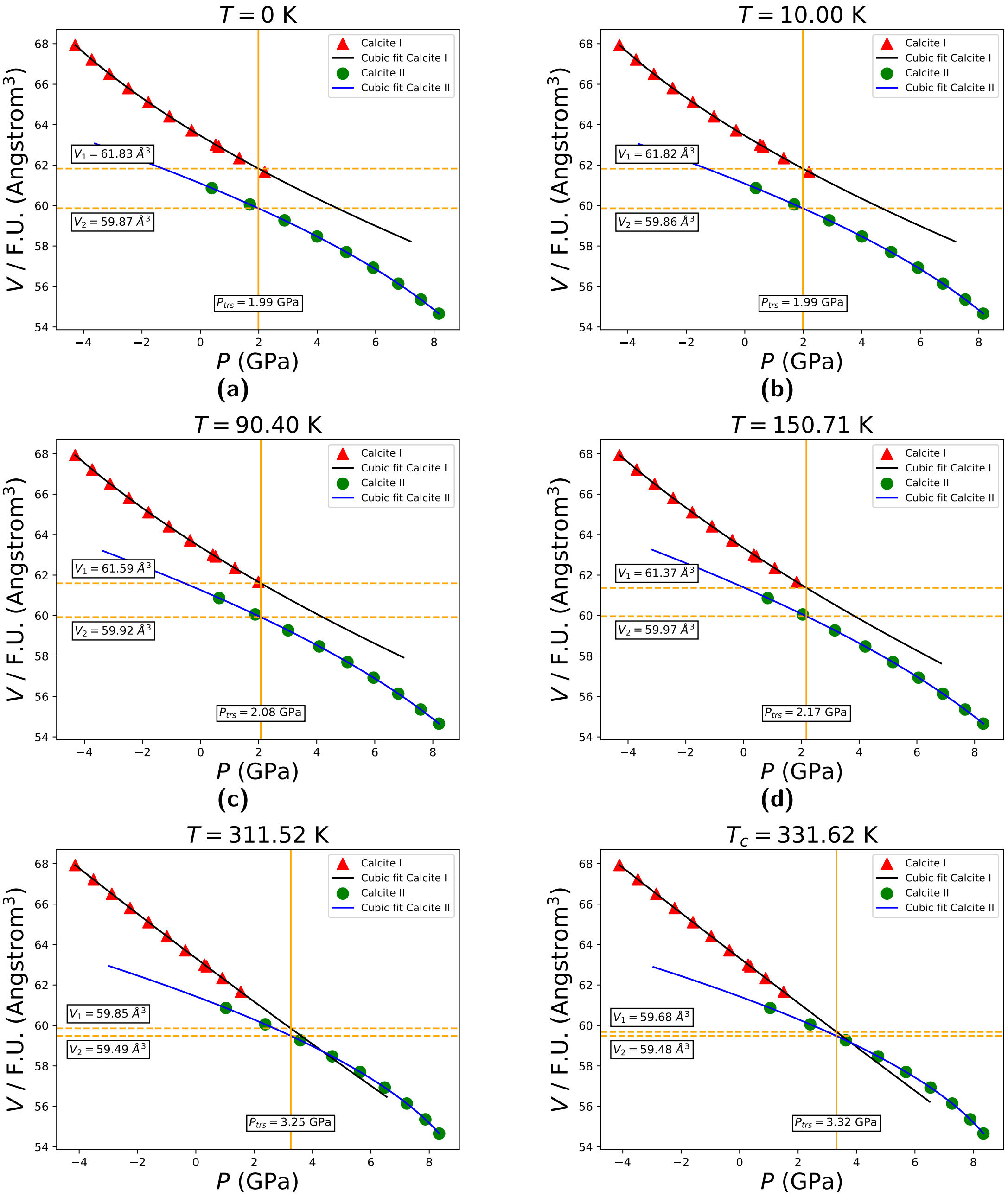

Figure 7.46: Evolution of $V(P)$ for several temperatures below and at the critical temperature ($T_c = 331.62$ K), according to the cubic approach, for the PBE-D3 level of theory. The pressure of transition P_{trs} indicated in each case is just the pressure of intersection at each temperature according to the cubic fit. For 0, 10.00 and 90.40 K, the volumes for calcite I and II are interpolated on the $V(P)$ curves. An extrapolation is needed in the calcite I branch at 150.71, 311.52 and 331.52 K.

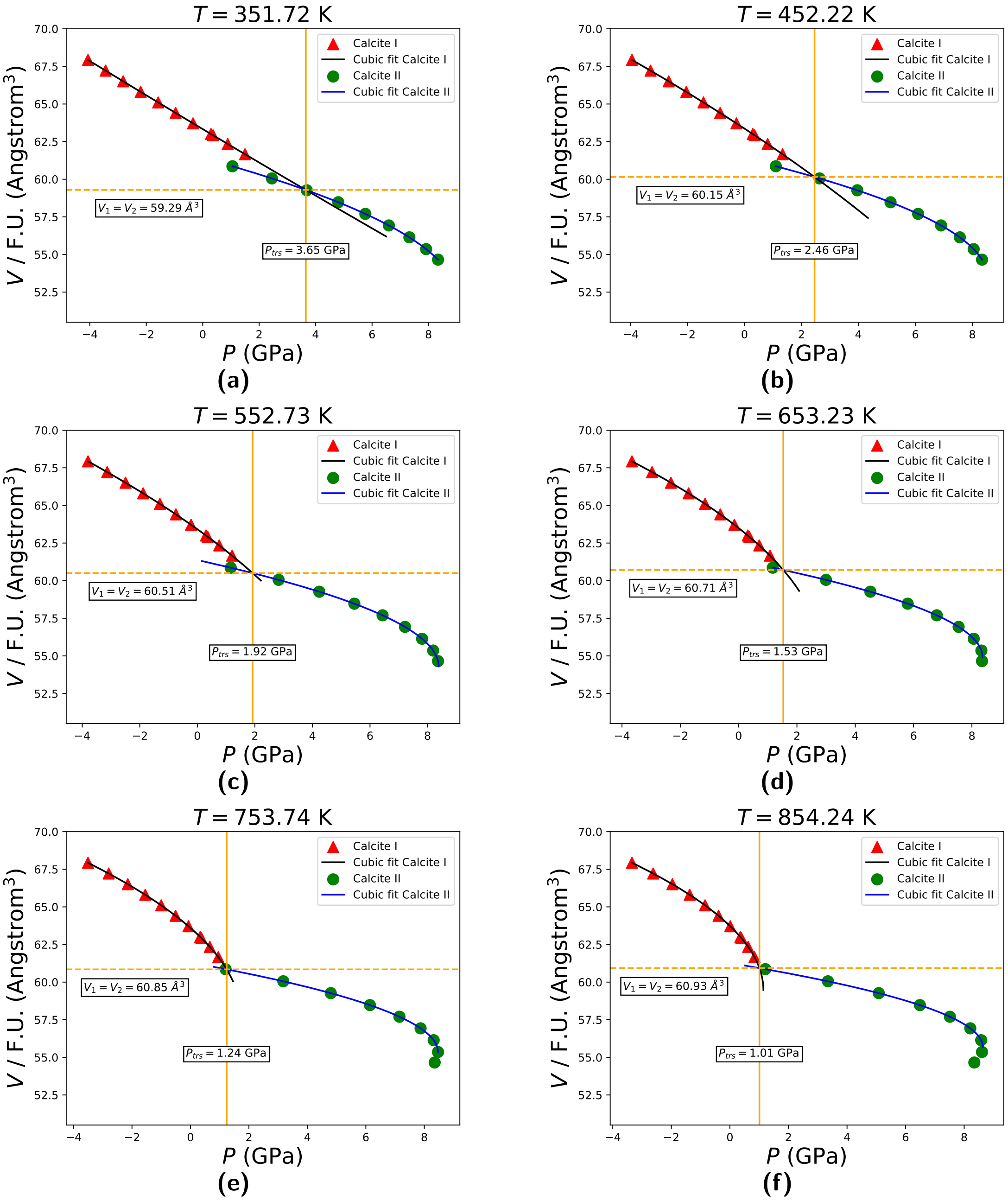

(a) (b)

(c) (d)

(e) (f)

Figure 7.47: Evolution of $V(P)$ for several temperatures above the critical temperature ($T_c = 331.62$ K), according to the cubic approach, for the PBE-D3 level of theory. The pressure of transition P_{trs} indicated in each case is the pressure at which both $V(P)$ curves for calcite I and II meet. For temperatures close to T_c, e.g. 351.72, 452.22 or 552.72 K this meeting point arises from an extrapolation on the calcite I curve.

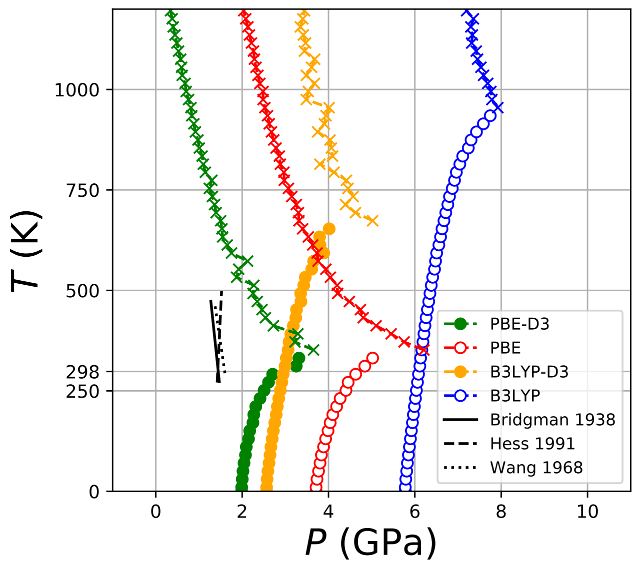

Figure 7.48: With circles: first order phase boundary corresponding to a first order phase transition. The cubic fit approach has been conducted. With crosses: a second order pressure-temperature phase boundary that corresponds to a second order phase transition. The pressure of transition at each temperature has been determined following the approach presented in Section 7.16.

Plots in Figs. 7.39e-7.39g and 7.47d-7.47f show that the tail of calcite II $V(P)$ curve tends to turn over with the increase of temperature. This indicates that there is a temperature, (e.g. 854.24K is a clear example) above which for a given value of pressure there are two possible volumes available. This means that there is in fact a phase transition occurring in calcite II at 854.24K and ≈ 8 GPa. The $F(V)$ curve at this temperature (Fig. 7.49a) presents some discontinuities in the lower volume range, that might support this hypothesis. Further analysis is needed in this respect.

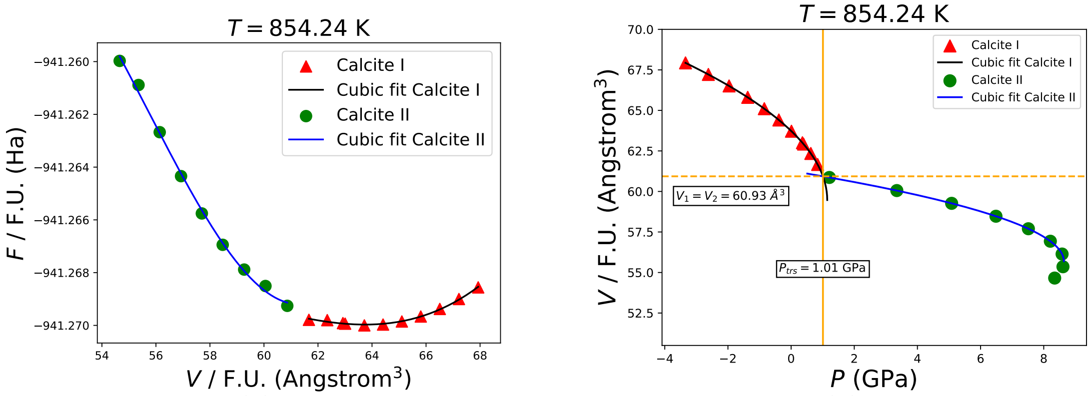

(a) **(b)**

Figure 7.49: Fig. 7.49a: $F(V)$ curve, and Fig. 7.49b: $V(P)$ curve at 854.24 K.

Chapter 8

Phase transitions in the thermodynamic stability field of Aragonite

Several studies have been encountered regarding the calcite I - Aragonite phase transition, e.g. Crawford and Hoersch [188] Johannes and Puhan [189]; both studies were conducted below 20 kb, and in a temperature range from 200°C to 700°C. These investigations are based on applying piston-cylinder pressures, and are gathered in a further revision by Carlson [190]. Differential thermal analysis (DTA) experiments were conducted by Mirwald [128], between 10 to 45 kbar, and up until 1000°C.

In this work, the stability of aragonite with respect to calcite I has been studied for PBE and B3LYP functionals, with and without the inclusion of the D3 Grimme dispersion correction. As can be seen in Fig. 8.1 and Table 8.1, aragonite becomes more stable than calcite I upon the inclusion of dispersion interactions, for both Hamiltonians. This effect is remarkable with the PBE-D3 level of theory, where aragonite is more stable with a Gibbs free energy difference of 2.102 KJ/mol. On the contrary, the hybrid B3LYP-D3 describes aragonite to be more stable than calcite I only by 0.094 KJ/mol.

At room temperature and pressure, calcite I is found to be experimentally more stable than aragonite (Table 8.1). The inclusion of dispersion thus leads to a wrong relative stability. Since aragonite is more dense than calcite I, the addition of dispersion interactions might lead to an

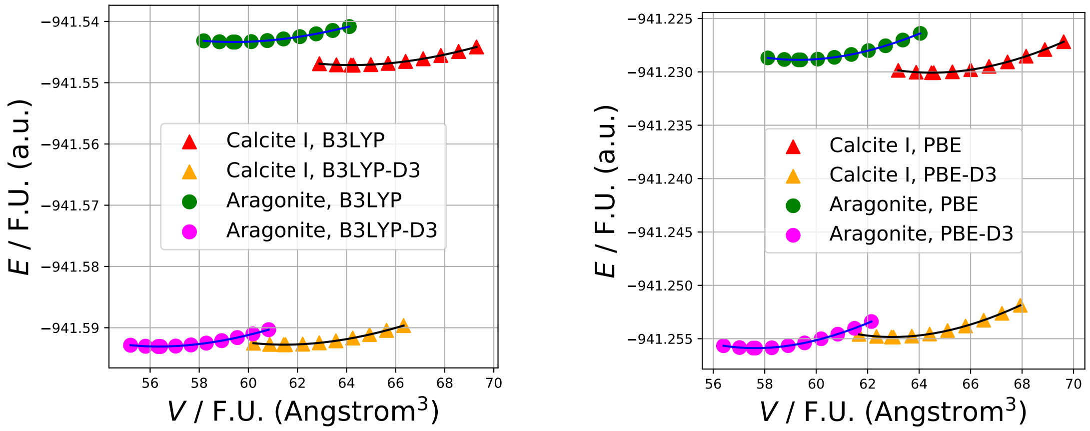

(a) **(b)**

Figure 8.1: Energy-volume curves for aragonite and calcite I for B3LYP and B3LYP-D3 (8.1a) and PBE and PBE-D3 (8.1b). The inclusion of dispersion yields a stabilization of Aragonite respect to calcite I.

Functional	ΔE (KJ/mol)	ΔG (1 atm, 298K) (KJ/mol)	Meaning
PBE	+3.13	+2.555	Calcite I more stable
PBE-D3	−2.74	−2.102	Aragonite more stable
B3LYP	+9.86	+8.437	Calcite I more stable
B3LYP-D3	−0.73	−0.094	Aragonite more stable
Experiment	$+0.8 \pm 0.2$ [191] +0.92 [192]		Calcite I more stable

Table 8.1: Experimentally, calcite I is found to be more stable than aragonite at 1 atm and 298K. This result is in agreement with PBE and B3LYP levels of theory. B3LYP-D3 stabilizes aragonite only by -0.094 KJ/mol, as opposed to PBE-D3 (-2.102 KJ/mol). ΔG has been calculated at 298 K and 1 atm, considering the transformation Calcite I → Aragonite, i.e. $\Delta G = G_{\mathrm{Arag}} - G_{\mathrm{C1}}$. ΔE has been calculated at 0 K and zero pressure.

extra stabilization, which might be the reason for aragonite being more stable than calcite I.

Several imaginary phonon modes are observed at expanded volumes in aragonite at Γ (Table 8.2). A distortion of the atomic positions along the eigenvector of the negative phonon mode produces similar energy scans as the ones presented for the calcite I - calcite II phase transition. The symmetry of the minimum energy structure is analyzed with the FINDSYM program [174], which yields a lower symmetry space group with respect to aragonite ($Pnma$, space group 62). A constant volume geometry optimization of the broken symmetry structure produces the pattern of structures shown in Table 8.2. Two structures with symmetry corresponding to space group 19 have been found: a lower energy (type I) and a higher energy (type II), as shown Fig. 8.2, panel A. Four structures belonging to space group 14 have been observed: type I, II, III and IV: type I has lower energy than type II for all the volumes explored, as shown in

Fig. 8.2, panel B. Regarding type III and IV, these are structures that exist at higher volumes. Only one structure belonging to space group 33 has been observed, labelled as 33 type I, whose energy is presented in Fig. 8.2, panel C. Since the energy of 19 type II is lower than the energy of 19 type I, the latter shall not be considered in the analysis. Similarly, the structure 14 type II will be discarded because its energy is higher than 14 type I. For the sake of simplicity, structures 14 type III and 14 type IV have also not been selected as potential candidates for the thermodynamic analysis.

Volume/F.U. ($\AA^3$)	Frequency (cm^{-1})	S.G. of the broken symmetry structure found	Frequency (cm^{-1})	S.G. of the broken symmetry structure found
63.1498	-10.8658	Note^a		
65.0238	-60.3124	19 type I		
	-49.4693	33 type II	-40.2000	4 type I
66.9315	-78.2389	19 type I		
	-67.2146	33 type II	-39.7351	4 type I
	-26.6283	14 type II	-71.6292	4 type II
			-49.7864	2
	-17.2844	14 type I		
68.8814	-92.9496	19 type I		
	-82.1308	33 type I		
	-56.5697	14 type II		
	-47.6817	14 type I		
70.8754	-103.5969	19 type I		
	-93.4809	33 type I		
	-75.3797	14 type II		
	-62.0736	14 type I		
	-31.5572	19 type II		
72.9069	-107.5144	19 type I		
	-96.8684	33 type I		
	-78.1545	14 type II		
	-72.2541	19 type II		
	-59.1385	14 type I		
74.9459	-97.6581	19 type I		
	-85.5900	19 type II		
	-85.3516	33 type I		
	-68.8401	14 type II	-52.6626	4 type III
	-34.6936	14 type IV		
77.0766	-81.2175	19 type II		
	-64.6552	19 type II		
	-48.0058	33 type I		
	-34.6231	14 type III		
	-7.9279	14 type IV		

Table 8.2: Imaginary phonon modes observed at Γ on the expanded volumes of aragonite. Once the broken symmetry structure has been isolated, a frequency calculation at Γ is conducted. There are some cases where an imaginary frequency is observed as well over this broken symmetry structure. All PBE level of theory. Note a: the constant volume optimization of this structure is a long process that requires more than 100 steps.

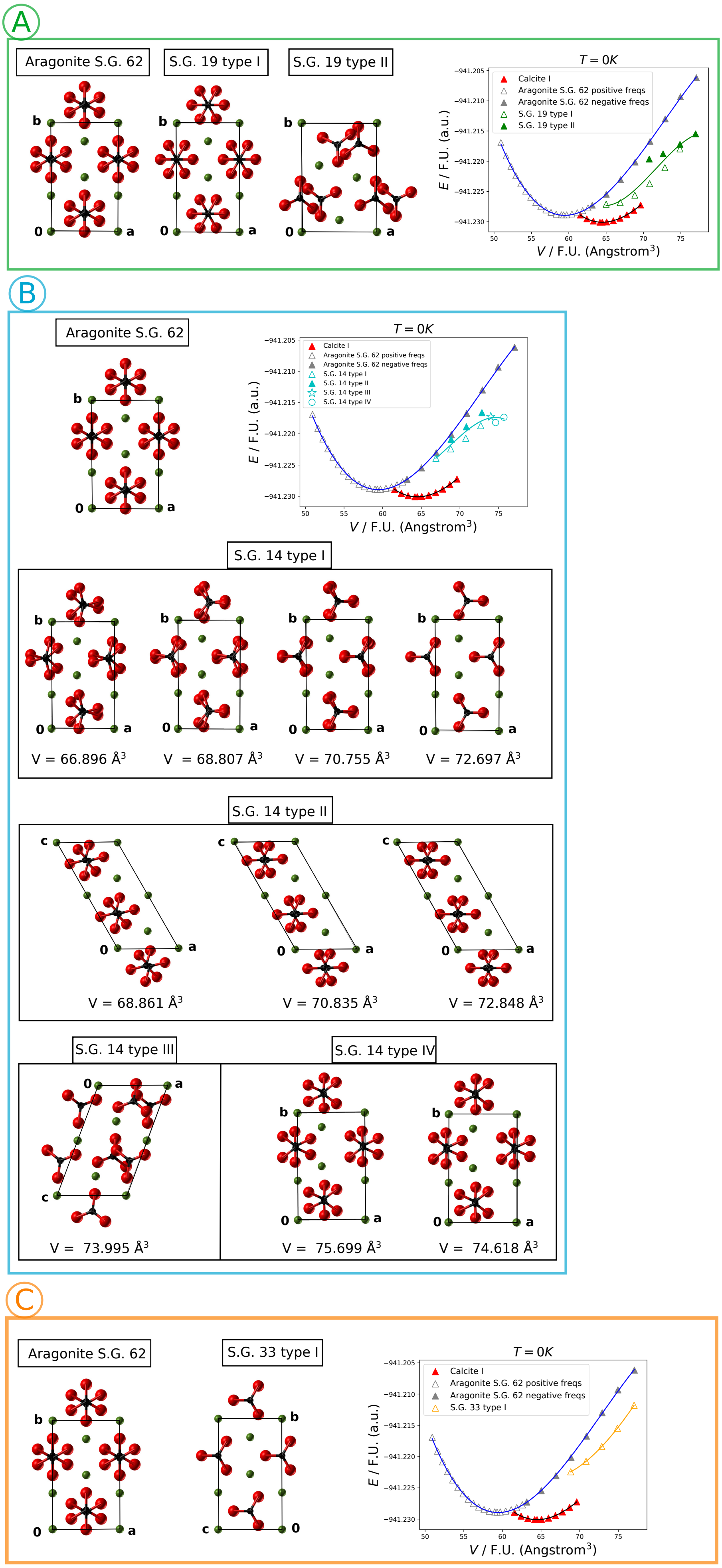

Figure 8.2: Broken symmetry structures found in the first set of imaginary phonon modes. All PBE level of theory

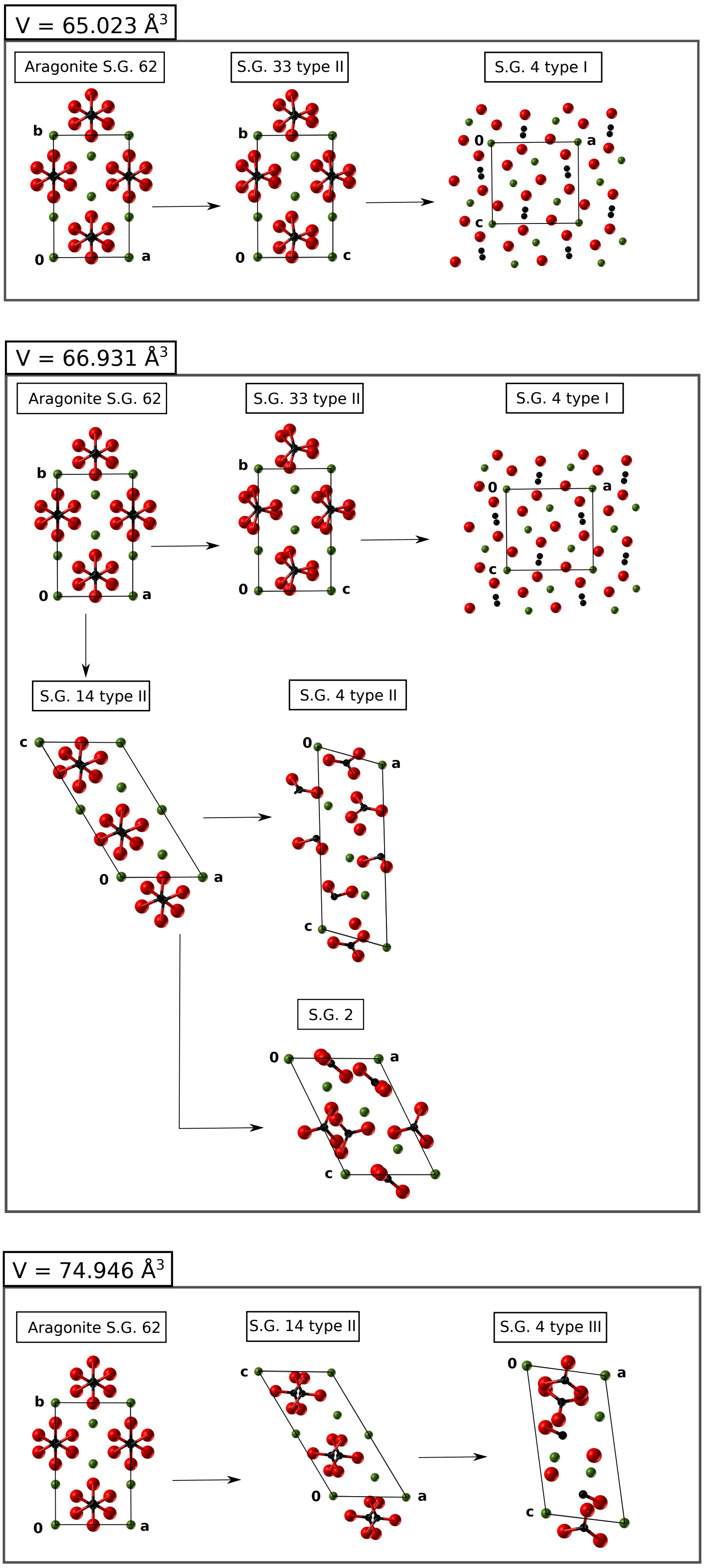

Figure 8.3: Broken symmetry structures found in the second set of imaginary phonon modes. All PBE level of theory.

All these broken symmetry structures do not present imaginary phonon modes at the Γ point. However, for some expanded volumes of aragonite (65.023, 66.931, 74.946 Å^3), the broken symmetry structures found in the first scan do contain imaginary phonon modes (Table 8.2). These structures have been labeled as space group 33 type II and space group 14 type II (shown in Fig. 8.3). In these cases, a second scan is necessary, which yields to the structures space group 2 and space group 4 type I, II and III shown in Fig. 8.3. From now on, the structures space group 2 and space group 4 type I, II and III will not be considered because its energy is noticeably higher.

The electronic energy and the Helmholtz free energy of the selected candidates (19 type I, 14 type I and 33 type I) is shown in Fig. 8.4 at different temperatures. At 0 K, the structures 14 type I and 33 type I have the same energy, and are less stable than the structure 19 type I. A soon as temperature increases (532.63 K), the structure 33 type I becomes slightly more stable than 14 type I. At 1075.35 K, 19 type I has the same energy as 33 type I. For all these temperatures, calcite I is more stable than the broken symmetry structures. However, when reaching 1537.68 K, space group 33 type I has the same energy as calcite I, and for a higher temperature of 2000 K, it becomes more stable than calcite I. As explained in Section 4.5, it has been observed experimentally that calcite I experiences a phase transition to calcite IV (s.g. 167) at 1151 K and to calcite V (s.g. 166) at 1275 K. This theoretical observation of space group 33 being more stable than calcite I at high temperatures might be the path for a phase transition to calcite IV or V.

It is very interesting the energetic evolution of aragonite and calcite I as a function of temperature: in the athermal limit, calcite I is more stable than aragonite (Fig. 8.4). A progressive stabilization of aragonite is observed with the increase of temperature. However, when reaching 532.63 K, no minimum in the Helmholtz free energy curve is observed, and an extrapolated minimum would be located at very low energy. In this respect, if the phase boundary calcite I - aragonite is deduced using the same framework, a negatively curved phase boundary is found at temperatures higher than 298 K (Fig. 8.5a). This negatively curved phase boundary means that the stability field of aragonite increases, which makes sense with the fact that the extrapolated minimum is located at very low energy. Calcite I is more stable than aragonite for pressures below the transition pressure (Fig. 8.5c), so that the stability field for calcite I and aragonite corresponds to lower and higher pressure respectively.

Similarly, the aragonite - space group 19 phase boundary is also curved (Fig. 8.5a) because of the thermal stability of aragonite already explained. Space group 19 is more stable than aragonite for pressures below the transition pressure (Fig. 8.5b). In addition, no intersection between Gibbs free energy curves of calcite I and space group 19 were observed, so that an hypothetical calcite I - space group 19 phase transition will not occur.

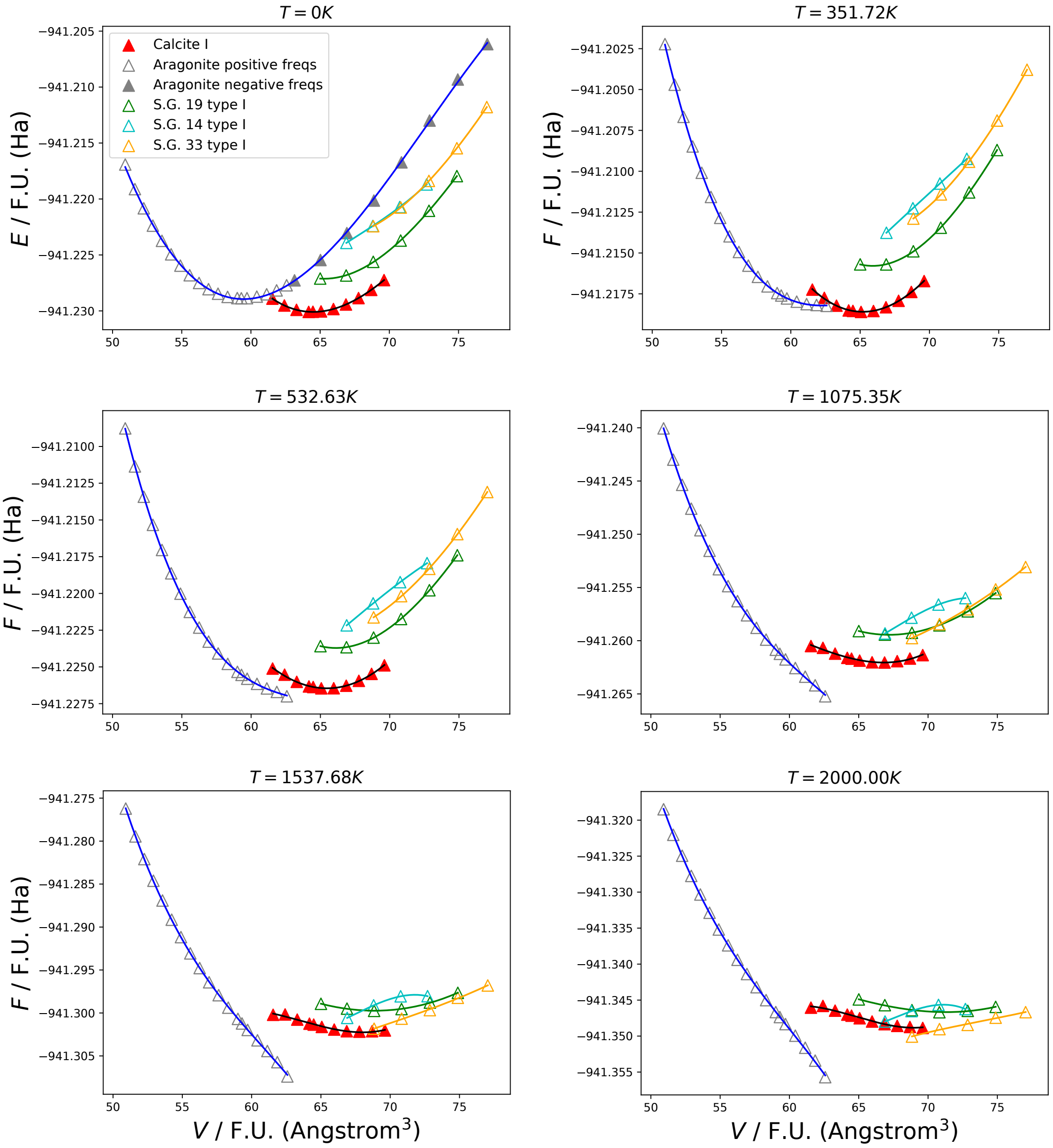

Figure 8.4: Electronic energy-volume curves for aragonite, calcite I and the broken symmetry structures found, at 0 K and at different temperatures for the PBE level of theory. See text for complete description on the evolution of the stability with temperature. All PBE level of theory.

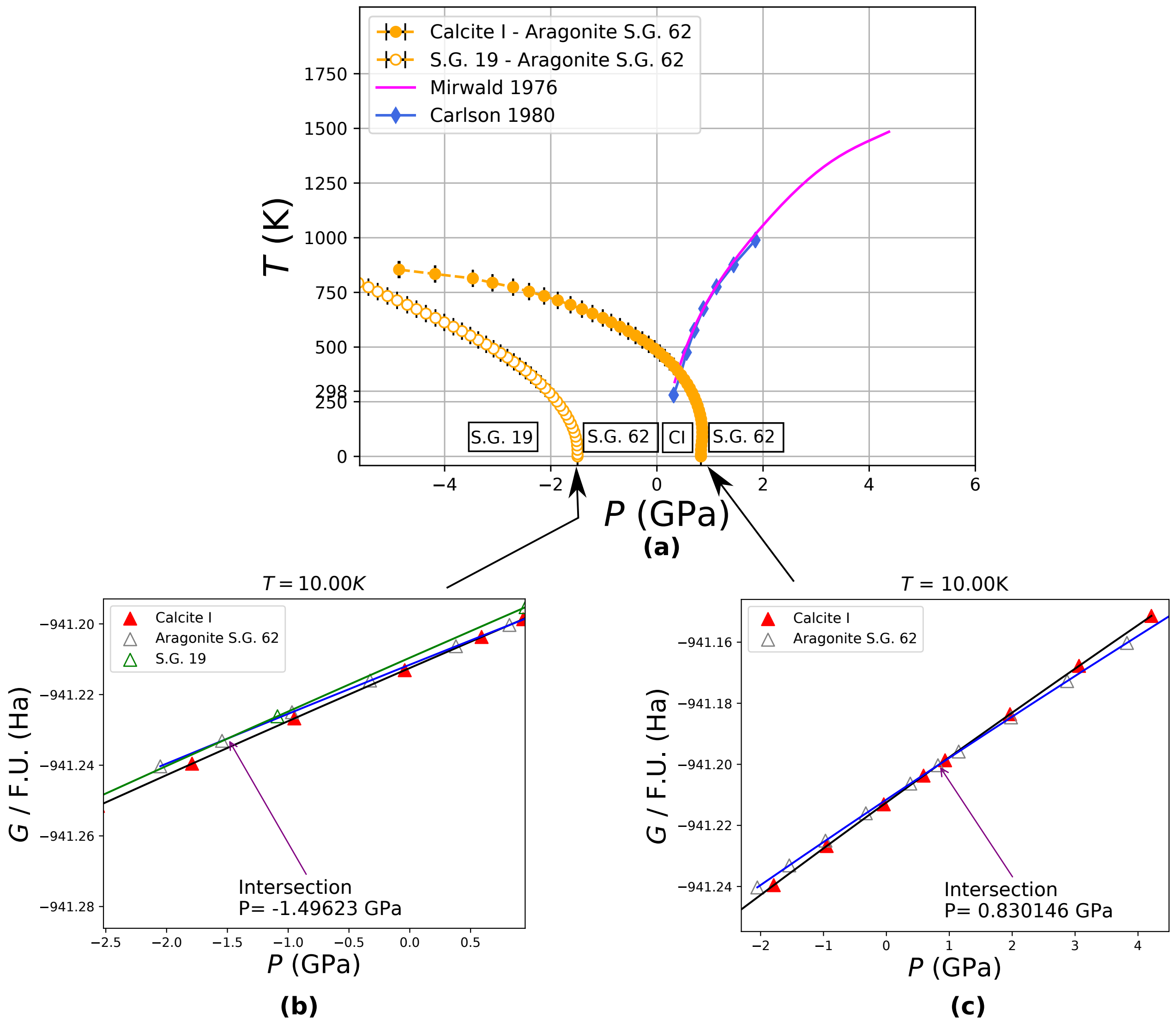

Figure 8.5: Calcite I - aragonite and aragonite - space group 19 phase boundaries.

Chapter 9

Conclusions

The thermodynamic stability field of solid $CaCO_3$ with temperature and pressure is a matter of ongoing debate due to its rich polymorphism. The purpose of this thesis has been to investigate the thermodynamic stability of the $CaCO_3$ solid system across some of its polymorphic variations, principally calcite I, calcite II and aragonite. Chapter 4 describes the atomic structure of the polymorphs of $CaCO_3$. The computational setup and thresholds used have been benchmarked in Chapter 5, followed by description of the electronic band structure of calcite I in Chapter 6.

In Chapter 7, the temperature-pressure phase boundary between calcite I and II has been theoretically determined for the first time. The mechanism that transforms calcite I into calcite II is due to a softening of a phonon mode when calcite I is compressed to higher pressures. On the other hand, several unknown broken symmetry structures on the stability field of aragonite have been documented for the first time, as well as its mechanisms of transformation, which are also due to softening of phonon modes. Finally, the relative stability of aragonite with respect to calcite I has also been examined.

The determination of the phase boundary requires the calculation of thermodynamic quantities, e.g. the pressure at finite temperature, the entropy, and the Helmholtz and Gibbs free energies. According to the harmonic approximation, thermodynamic quantities can be expressed as a sum over frequencies. On the other hand, within the quasi-harmonic approximation framework, there is a dependence of the phonon frequencies on volume. This dependence $\nu_{i,\mathbf{k}}(V)$ is correctly described with a polynomial fit. The pressure at finite temperature can be obtained by a direct sum over frequencies across volumes, or simply by differentiation of the Helmholtz free energy. The first approach requires monitoring the same phonon eigenvector across volumes. The latter approach is straightforward, and was the one pursued due to its simplicity.

In order to cover a wide range of pressures, both expanded and compressed volumes are explored, where imaginary phonons can appear at these extreme conditions. In these cases, a distortion of the atomic coordinates along the phonon eigenvector needs to be explored and a broken symmetry structure yields from this analysis. Two broken symmetry structures have been described when compressing calcite I: space group 14 (calcite II) and space group 161. In the case of aragonite, several broken symmetry strucures were found: space group 19 , space group 14 and space group 33.

When considering the computation of the phase boundary, volumes with imaginary phonon frequencies have not been considered in the thermodynamic analysis, as this aggravates the quality of the $F(V)$ fits.

The temperature-pressure coexistence line can be obtained by analyzing the intersection between two Gibbs free energy surfaces, i.e. $G^{I}(P,T) = G^{II}(P,T)$. A simplification is based on fixing a temperature, and analyzing the pressure at which two Gibbs free energy curves intersect, i.e. $G^{I}(P) = G^{II}(P)$, at $T =$ constant.

One characteristic of this phase transition is the fact that the Gibbs free energy curves of calcite I and II do not intersect with a clear angle; instead, they merge together. This effect is remarkable as soon as temperature increases from 10 K to room temperature and beyond. This effect is in agreement with the experiment, where calcite II cannot be quenched to ambient conditions, i.e. calcite I transforms to calcite II as soon as the pressure of transition is reached, and the transformation is reversible, obtaining calcite II when pressure is released.

Both $G(P)$ curves fit well to a cubic polynomial. However, there is a temperature at which the intersection between both cubic fits occurs at very high values of pressure, simply because both curves intersect with very low angle so that they are coincident in a wide pressure range. This temperature has been referred to as a critical temperature T_c. Within this formalism, the temperature-pressure phase boundaries obtained with different levels of theory are reported in Fig. 7.20. The value of pressure at which this phase boundary is located is found to be very sensitive to the inclusion of dispersion: the phase boundary is substantially shifted to lower pressures when accounting for van der Waals interactions.

A second approach is to fit linerarly both $G(P)$; in this case the curves intersect with greater angle, so that the pressure of intersection is lowered. Through this methodology there is no such temperature for which the intersection of $G(P)$ curves is located at very high values of pressure. Instead, the temperature - pressure phase boundary obtained runs to higher temperatures. A straightforward error bar on the pressure of intersection can be calculated. The phase boundaries obtained through this procedure are shown in Fig. 7.41.

A mathematically equivalent methodology is to calculate the pressure of intersection as the common tangent of two $F(V)$ curves. The pressure at each temperature yields a phase boundary very similar to the one obtained through the cubic fit intersection (Fig. 7.44). Since there is agreement between the cubic fit and the common tangent approaches, the cubic fit approach was considered as the path to follow for the determination of the phase boundary.

A completely different scenario is presented between the $G(P)$ curves for calcite I and aragonite: they do intersect with greater angle, which yields a clear pressure of intersection. Unlike calcite II, aragonite is thermodynamically stable at ambient conditions (Fig. 9.1a). The difference in Gibbs free energy between calcite I and aragonite is 1.46 KJ/mol (at 311 K and 1 bar). This scenario is very similar to the diamond - graphite equilibria, where both polymorphs exist at ambient conditions, and where ΔG is considerably higher, i.e. 2.9 KJ/mol (at room temperature and 1 bar, as reported in Ref. [193]). On the contrary, the difference in Gibbs free energy between calcite I and II can only be given at the short range of pressures where both coexist, i.e. 0.71 KJ/mol (at 311 K and 1.28 GPa, as shown in Fig. 9.1b).

Dispersion effects lower the pressure of the calcite I - calcite II transformation. On the contrary, because aragonite is a denser phase, dispersion effects yield a stabilization of aragonite with respect to calcite I. A clear calcite I - aragonite TP phase boundary is described up to room temperature (Fig. 8.5a). From 298K onwards, a negatively curved phase boundary is obtained as a consequence of aragonite not presenting an interpolated minimum in the $F(V)$ curves.

The possibility of a calcite I - calcite II second order phase transition above the critical temperature T_c has been investigated. The position of this temperature varies with the level of theory: 331 K for PBE and PBE-D3, and 653 K and 934 for, respectively, B3LYP-D3 and B3LYP (Table 7.14 and Fig. 7.20). For temperatures $T \leqslant T_c$, the phase transition is first order. Above

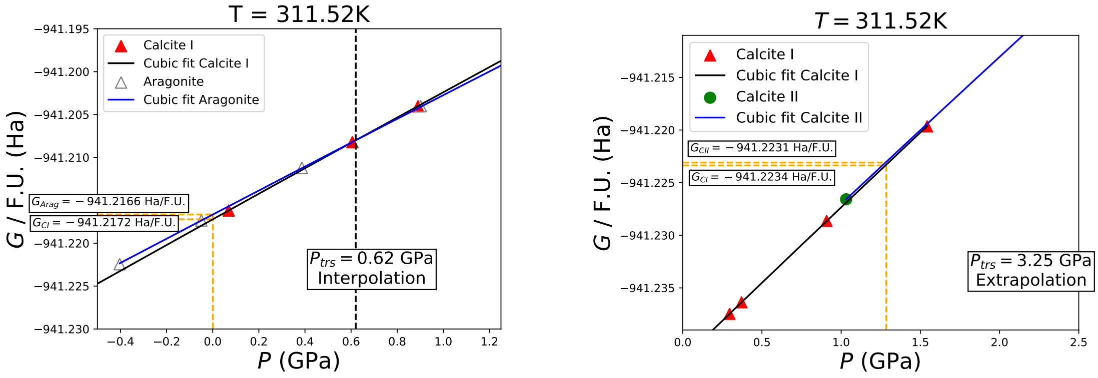

(a) **(b)**

Figure 9.1: 9.1a: $G(P)$ for calcite I and aragonite at 311.52 K, for the PBE level of theory. The value of Gibbs free energy for both phases at 1 bar is shown. 9.1b: $G(P)$ for calcite I and II at 311.52 K, for the PBE-D3 level of theory. The value of Gibbs free energy for both phases at 1.28 GPa is shown.

$G_{\mathrm{C1}}(T = 311.52\mathrm{K}, P = 1\mathrm{bar} \equiv 10^{-3}\mathrm{GPa})$	-941.21720 Ha/F.U.
$G_{\mathrm{C2}}(T = 311.52\mathrm{K}, P = 1.28\mathrm{GPa})$	-941.22309 Ha/F.U.
$G_{\mathrm{Arag}}(T = 311.52\mathrm{K}, P = 1\mathrm{bar} \equiv 10^{-3}\mathrm{GPa})$	-941.21665 Ha/F.U.
$\Delta G_{\mathrm{C1}\rightarrow\mathrm{Arag}}(T = 311.52\mathrm{K}, P = 1\mathrm{bar} \equiv 10^{-3}) = G_{\mathrm{Arag}} - G_{\mathrm{C1}}$	1.4599 KJ/mol
$\Delta G_{\mathrm{C1}\rightarrow\mathrm{C2}}(T = 311.52\mathrm{K}, P = 1.28\ \mathrm{GPa}) = G_{\mathrm{C2}} - G_{\mathrm{C1}}$	0.7134 KJ/mol

Table 9.1: Summary of the Gibbs free energy thermodynamic stability of calcite I, II and aragonite.

the T_c, both $V(P)$ intersect at a value of pressure that corresponds to the pressure of a second order phase transition. This leads to the second order TP phase boundary reported in Fig. 7.48.

Chapter 10

Appendix

10.1 Codes generated for this thesis

Several codes have been generated in this thesis, which can be found in each of my GitHub repositories described herein. Each repository is a series of bash and python scripts and there is a detailed explanation in `html` format on how to use them. These codes can be easily adapted to similar projects.

1. The repository `search_neg_freqs` [175] scans the frequencies of a given set of constrained-volume frequency outputs. This program will output the volumes for which an imaginary frequency has been encountered, and the dispersion k-point at which that negative eigenvalue belongs to.

2. The repository `EOS_2_phonons` [177] is a collection of bash and python scripts. These allow to automate the process based on the search for broken symmetry structures that arise from soft phonon mode mechanisms. The internal coordinates and lattice parameters at each volume are extracted, followed by a frequency calculation. Negative phonon modes are scanned and the symmetry is analysed. A constant volume optimization is then performed, over the broken symmetry structure found. A more detailed explanation of the process can be found in Section 7.4.

3. The repository named `QHA_3D` [179] allows the construction of Gibbs free energy surfaces $G(P, T)$.

4. The repository `QHA_2D` [180] automatically sets a temperature and produces the temperature-pressure phase boundary via $G^{I}(P) - G^{II}(P) = 0$, for an array of given temperatures. More information in Section 7.6.2.

5. The repository `Common_Tangent` [187] generates the temperature-pressure phase boundary by calculating the common tangent between two $F(V)$ curves (more information in Section 7.14).

6. The repository `ENTROPY_PDOS` [182] plots the cumulated entropy and phonon density of states. More information in Section 7.9.

7. Given a direct matrix lattice vectors, the repository `supercell_generator` [194] generates a set of supercell expansion matrix candidates for which the new lattice parameters are greater than a chosen value, and the three of them of the same size, within a tolerance. This allows to construct supercells for different polymorphs with lattice parameters of equal length, so that we ensure phonons are calculated within a ”sphere” of equal radius.

10.2 Bulk Modulus

The purpose of this section is to show how the bulk modulus at finite temperature is obtained. In addition, we will show how functions that depend on the second derivative of $F(V)$ (e.g. the bulk modulus) are extremely sensitive to the quality of the $F(V)$ fit. For a fixed temperature T, given the $F(V)$ curves fitted to a cubic polynomial:

$$F(V) = a_0 + a_1 V + a_2 V^2 + a_3 V^3 \tag{10.1}$$

The pressure is straightforward to obtain:

$$P(V) = -\frac{\partial F(V)}{\partial V} = -a_1 - 2a_2 V - 3a_3 V^2 \tag{10.2}$$

The bulk modulus is the inverse of the compressibility:

$$B_T = \frac{1}{K_T} = -V\frac{\partial P(V)}{\partial V} \tag{10.3}$$

Since $\frac{\partial P(V)}{\partial V} = -2a_2 - 6a_3V$, the bulk modulus then reads like:

$$B_T = 2a_2V + 6a_3V^2 \tag{10.4}$$

In the case of the athermal limit, $F(V)$ is just replaced by $E(V)$. The $E(V)$, $P(V)$, $B(V)$ and $B(P)$ plots for calcite I and II are shown in Figs. 10.1a - 10.1d. For calcite II, two different branches are reported: branch 1 (green circles) and branch 2 (purple circles). For the $E(V)$ and $P(V)$ plots, both branches 1 and 2 are almost coincident. For the $B(V)$ and $B(P)$ plots, both branch 1 and 2 are not exactly coincident. This is because the bulk modulus is related to the second derivative of $E(V)$, and is very sensitive to the curvature. Nevertheless, both branches describe the correct trend for calcite II: the bulk modulus increases with the decrease of volume, or increase of pressure. If zero point motion is considered (Figs. 10.1e - 10.1f), both branches 1 and 2 still coincide on the $E(V)$ and $P(V)$ curves. Now, a completely different trend on the bulk modulus is predicted for both branches (Figs. 10.1g - 10.1h): branch 1 preducts an increase on the bulk modulus with the increase of volume, and branch 2 the opposite behaviour. This clearly shows that second derivative thermodynamic quantities are very sensitive to the curvature of the $E(V)$ or $F(V)$ curves. A similar effect is observed at the finite temperature of 291.41 K (Figs. 10.1i - 10.1l).

Using the $B(P)$ curve for calcite I at finite temperature, it is possible to estimate the bulk modulus at finite temperature and pressure, which is found to be 60.87 GPa (Table 10.1).

Calcite I	Bulk Modulus (GPa)
DFT (PBE-D3) T = 0 K, P = 0 GPa	75.07
DFT (PBE-D3) T = 291.41 K, P = 1 bar	60.87
Experiment, at 298 K [161]	71.07

Table 10.1: Experimental and calculated bulk modulus for calcite I in the athermal limit (including zero point motion effects), and at 291.41 K with PBE-D3 level of theory and using molecular dynamics.

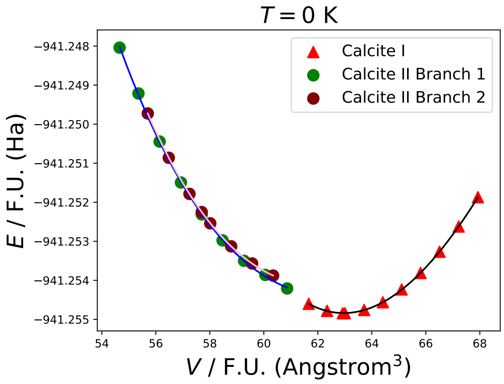
$T = 0$ K
E / F.U. (Ha)
−941.248
−941.249
−941.250
−941.251
−941.252
−941.253
−941.254
−941.255
54
56
58
60
62
64
66
68
V / F.U. (Angstrom^3)
▲ Calcite I
● Calcite II Branch 1
● Calcite II Branch 2

(a)

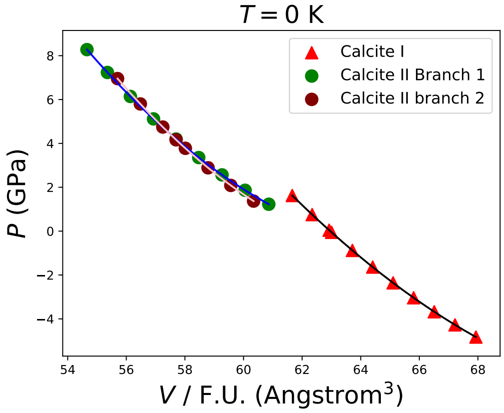
$T = 0$ K
P (GPa)
8
6
4
2
0
−2
−4
54
56
58
60
62
64
66
68
V / F.U. (Angstrom^3)
▲ Calcite I
● Calcite II Branch 1
● Calcite II branch 2

(b)

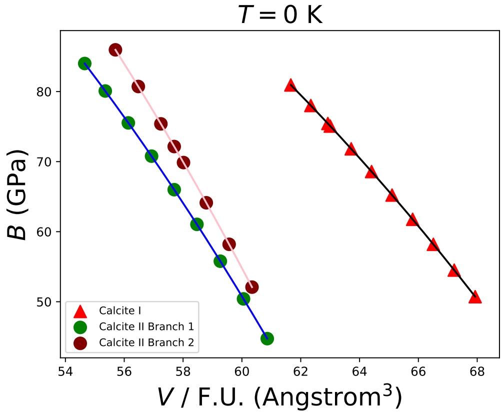
$T = 0$ K
B (GPa)
80
70
60
50
54
56
58
60
62
64
66
68
V / F.U. (Angstrom^3)
▲ Calcite I
● Calcite II Branch 1
● Calcite II Branch 2

(c)

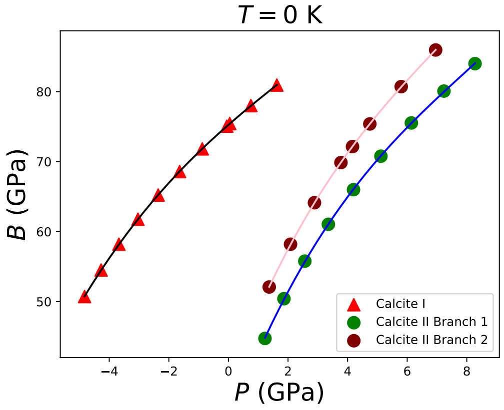
$T = 0$ K
B (GPa)
80
70
60
50
−4
−2
0
2
4
6
8
P (GPa)
▲ Calcite I
● Calcite II Branch 1
● Calcite II Branch 2

(d)

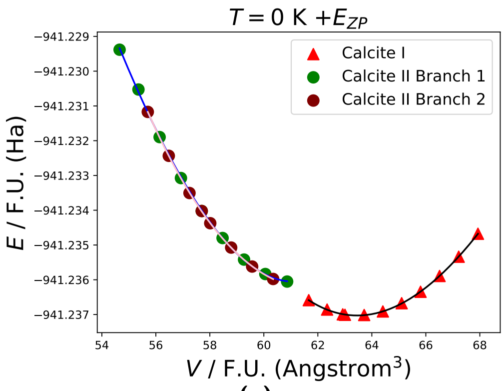
$T = 0$ K $+E_{ZP}$
E / F.U. (Ha)
−941.229
−941.230
−941.231
−941.232
−941.233
−941.234
−941.235
−941.236
−941.237
54
56
58
60
62
64
66
68
V / F.U. (Angstrom^3)
▲ Calcite I
● Calcite II Branch 1
● Calcite II Branch 2

(e)

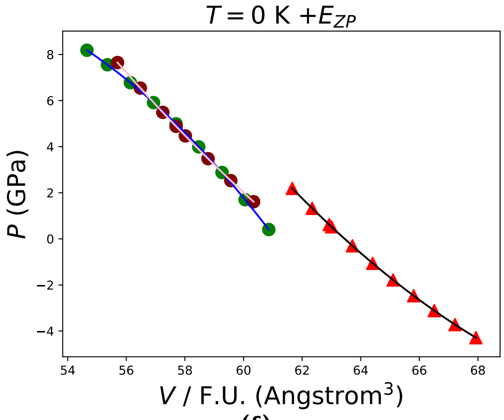
$T = 0$ K $+E_{ZP}$
P (GPa)
8
6
4
2
0
−2
−4
54
56
58
60
62
64
66
68
V / F.U. (Angstrom^3)

(f)

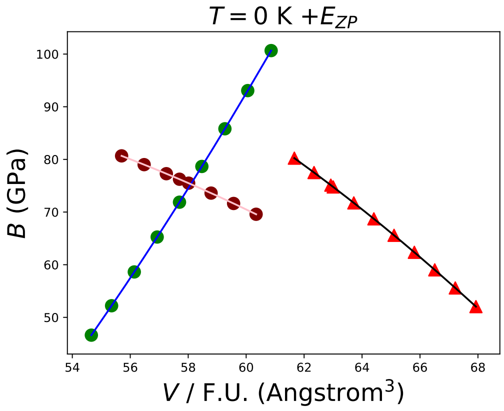
$T = 0$ K $+E_{ZP}$
B (GPa)
100
90
80
70
60
50
54
56
58
60
62
64
66
68
V / F.U. (Angstrom^3)

(g)

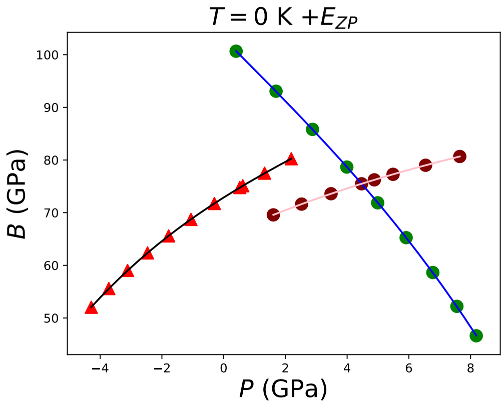
$T = 0$ K $+E_{ZP}$
B (GPa)
100
90
80
70
60
50
−4
−2
0
2
4
6
8
P (GPa)

(h)

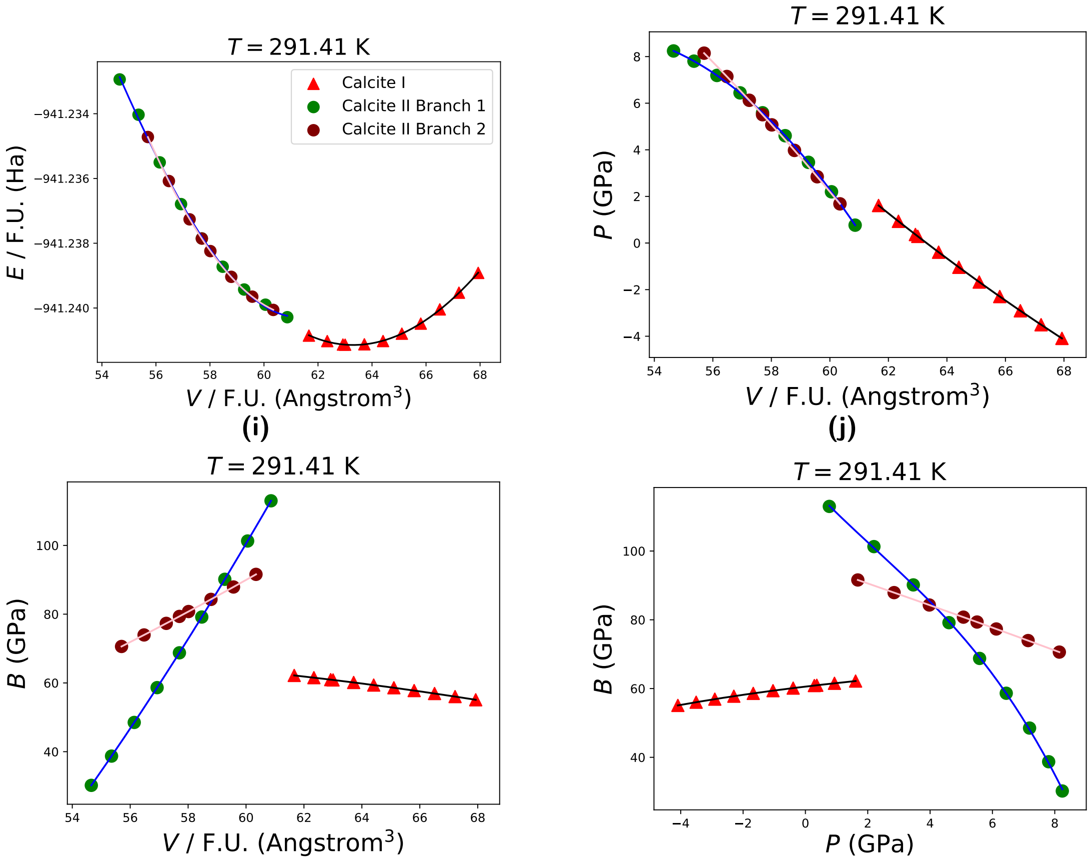

(i) (j)

(k) (l)

Figure 10.1: $E(V)$, $P(V)$, $B(V)$ and $B(P)$ plots for the athermal limit, without zero point motion (10.1a - 10.1d), with zero point motion (10.1e - 10.1h), and at a finite temperature of 291.41 K (10.1i - 10.1l).

Bibliography

[1] W. A. Deer, *An introduction to the rock-forming minerals*, third edition. ed., 2013. 35

[2] T. Scoffin, “An introduction to carbonate sediments and rocks.” 35

[3] E. Gartner, “Industrially interesting approaches to “low-CO_2” cements,” *Cement and Concrete Research*, vol. 34, no. 9, pp. 1489 – 1498, 2004, h. F. W. Taylor Commemorative Issue. [Online]. Available: http://www.sciencedirect.com/science/article/pii/S0008884604000468 35

[4] G. W. Scherer, “Stress from crystallization of salt,” *Cement and Concrete Research*, vol. 34, no. 9, pp. 1613 – 1624, 2004, h. F. W. Taylor Commemorative Issue. [Online]. Available: http://www.sciencedirect.com/science/article/pii/S0008884604000122 35

[5] B. Lubelli and R. P. van Hees, “Effectiveness of crystallization inhibitors in preventing salt damage in building materials,” *Journal of Cultural Heritage*, vol. 8, no. 3, pp. 223 – 234, 2007. [Online]. Available: http://www.sciencedirect.com/science/article/pii/S1296207407000672 35

[6] G. M. Friedman and D. J. Schultz, “Precipitation of vaterite ($CaCO_3$) during oil field drilling,” *Mineral. Mag.*, vol. 58, p. 401, 1994. 35, 149

[7] J. L. Provis, “Alkali-activated materials,” *Cement and Concrete Research*, 2017. 35

[8] J. Aizenberg, A. Tkachenko, S. Weiner, L. Addadi, and G. Hendler, “Calcitic microlenses as part of the photoreceptor system in brittlestars,” *Nature*, vol. 412, no. 6849, August 2001. 35

[9] Z. Liu, K. Kwok, R. Li, and C. Choy, “Effects of coupling agent and morphology on the impact strength of high density polyethylene/$CaCO_3$ composites,” *Polymer*, vol. 43, no. 8, pp. 2501 – 2506, 2002. 35

[10] W. Zuiderduin, C. Westzaan, J. Huétink, and R. Gaymans, “Toughening of polypropylene with calcium carbonate particles,” *Polymer*, vol. 44, no. 1, pp. 261 – 275, 2003. 35

[11] M. Akaishi, H. Kanda, and S. Yamaoka, “Synthesis of diamond from graphite-carbonate system under very high temperature and pressure,” *Journal of Crystal Growth*, vol. 104, no. 2, pp. 578 – 581, 1990. 35

[12] K. Suito, J. Namba, T. Horikawa, Y. Taniguchi, N. Sakurai, M. Kobayashi, A. Onodera, O. Shimomura, and T. Kikegawa, “Phase relations of $CaCO_3$ at high pressure and high temperature,” *American Mineralogist*, vol. 86, pp. 997 – 1002, 2001. 35, 151, 152, 153, 186, 187

[13] T. Chen, A. Neville, and M. Yuan, “Calcium carbonate scale formation—assessing the initial stages of precipitation and deposition,” *Journal of Petroleum Science and Engineering*, vol. 46, no. 3, pp. 185 – 194, 2005. 35

[14] J. M. Matter and P. B. Kelemen, “Permanent storage of carbon dioxide in geological reservoirs by mineral carbonation,” *Nature Geoscience*, vol. 2, no. 12, November 2009. 36

[15] M. Schaebitz, R. Wirth, C. Janssen, and G. Dresen, “First evidence of $CaCO_3$-III and $CaCO_3$-IIIb high-pressure polymorphs of calcite : Authigenically formed in near surface sediments,” *American Mineralogist*, pp. 1230–1235. 36, 37, 152

[16] P. Westbroek, C. W. Brown, J. van Bleijswijk, C. Brownlee, G. J. Brummer, M. Conte, J. Egge, E. Fernández, R. Jordan, M. Knappertsbusch, J. Stefels, M. Veldhuis, P. van der Wal, and J. Young, “A model system approach to biological climate forcing. the example of emiliania huxleyi,” *Global and Planetary Change*, vol. 8, no. 1, pp. 27 – 46, 1993. 36

[17] H. M. Merlini, M. and W. Crichton, “$CaCO_3$-III and $CaCO_3$-VI, high-pressure polymorphs of calcite: Possible host structures for carbon in the earth’s mantle,” *Earth and Planetary Science Letters*, vol. 333 - 334, pp. 265 – 271, 2012. 36, 37, 151, 152, 168, 169, 170, 186

[18] K. D. Litasov and E. Ohtani, “Solidus and phase relations of carbonated peridotite in the system CaO–Al_2O_3–MgO–SiO_2–Na_2O–CO_2 to the lower mantle depths,” *Physics of the Earth and Planetary Interiors*, vol. 177, no. 1, pp. 46 – 58, 2009. 36

[19] R. Dasgupta, “Ingassing, storage, and outgassing of terrestrial carbon through geologic time,” *Reviews in Mineralogy and Geochemistry*, vol. 75, no. 1, pp. 183–229, 2013. 36

[20] B. Chen, Z. Li, D. Zhang, J. Liu, M. Y. Hu, J. Zhao, W. Bi, E. E. Alp, Y. Xiao, P. Chow, and J. Li, “Hidden carbon in earth’s inner core revealed by shear softening in dense Fe_7C_3,” *Proceedings of the National Academy of Sciences*, vol. 111, no. 50, pp. 17 755–17 758, 2014. 36

[21] H. Keppler, M. Wiedenbeck, and S. S. Shcheka, “Carbon solubility in olivine and the mode of carbon storage in the earth’s mantle,” *Nature*, vol. 424, no. 6947, July 2003. 36

[22] B. Marty and A. Jambon, “C^3He in volatile fluxes from the solid Earth: implications for carbon geodynamics,” *Earth and Planetary Science Letters*, vol. 83, no. 1, pp. 16–26, 1987. 36

[23] W. Hans-Rudolf and A. G. Bulakh, *Minerals : their constitution and origin.* Cambridge University Press, 2004. 25, 36

[24] B. Metz, O. Davidson, H. de Coninck, M. Loos, and L. M. C. U. Press, *IPCC Special Report on Carbon Dioxide Captue and Storage (Intergovernmental Panel on Climate Change, 2005).* 36

[25] A. M. Belcher, X. H. Wu, R. J. Christensen, P. K. Hansma, G. D. Stucky, and D. E. Morse, “Control of crystal phase switching and orientation by soluble mollusc-shell proteins,” *Nature*, vol. 381, no. 6577, May 1996. 36

[26] A. Marshall and P. Clode, “Calcification rate and the effect of temperature in a zooxanthellate and an azooxanthellate scleractinian reef coral,” *Coral Reefs*, vol. 23, no. 2, pp. 218–224, Jul 2004. [Online]. Available: https://doi.org/10.1007/s00338-004-0369-y 36

[27] Z. Dubinsky and N. Stambler, *Coral calcification, cells to reefs*, 2011. 37

[28] A. Sellinger, P. M. Weiss, A. Nguyen, Y. Lu, R. A. Assink, W. Gong, and C. J. Brinker, "Continuous self-assembly of organic–inorganic nanocomposite coatings that mimic nacre," *Nature*, vol. 394, pp. 256–260, 1998. 37

[29] J. D. Hartgerink, E. Beniash, and S. I. Stupp, "Self-assembly and mineralization of peptide-amphiphile nanofibers," *Science*, vol. 294, no. 5547, pp. 1684–1688, 2001. [Online]. Available: http://science.sciencemag.org/content/294/5547/1684 37

[30] D. Gebauer, A. Völkel, and H. Cölfen, "Stable prenucleation calcium carbonate clusters," *Science*, vol. 322, no. 5909, pp. 1819–1822, 2008. 37, 150

[31] F. C. Meldrum and R. P. Sear, "Now you see them," *Science*, vol. 322, no. 5909, pp. 1802–1803, 2008. 37, 150

[32] W. D. Carlson, "The polymorphs of $CaCO_3$ and the aragonite-calcite transformation," *Reviews in Mineralogy and Geochemistry*, vol. 11, no. 1, pp. 191–225, jan 1983. [Online]. Available: http://rimg.geoscienceworld.org/cgi/content/long/11/1/191 37

[33] R. Car and M. Parrinello, "Unified approach for molecular dynamics and density-functional theory," *Phys. Rev. Lett.*, vol. 55, pp. 2471–2474, Nov 1985. [Online]. Available: https://link.aps.org/doi/10.1103/PhysRevLett.55.2471 38, 141

[34] F. Buda, R. Car, and M. Parrinello, "Thermal expansion of c-si via ab initio molecular dynamics," *Phys. Rev. B*, vol. 41, pp. 1680–1683, Jan 1990. [Online]. Available: https://link.aps.org/doi/10.1103/PhysRevB.41.1680 38, 141

[35] F. D. Vila, V. E. Lindahl, and J. J. Rehr, "X-ray absorption debye-waller factors from ab initio molecular dynamics," *Phys. Rev. B*, vol. 85, p. 024303, Jan 2012. [Online]. Available: https://link.aps.org/doi/10.1103/PhysRevB.85.024303 38, 141

[36] C. Kittel, *Introduction to Solid State Physics*, 6th ed. New York: John Wiley & Sons, Inc., 1986. 25, 41, 42

[37] https://andreaslm.wordpress.com/tag/crystal-structure/. 25, 44

[38] http://www.xtal.iqfr.csic.es/Cristalografia/parte_03_4-en.html. 25, 45

[39] C. Møller and M. S. Plesset, “Note on an approximation treatment for many-electron systems,” *Phys. Rev.*, vol. 46, pp. 618–622, Oct 1934. [Online]. Available: https://link.aps.org/doi/10.1103/PhysRev.46.618 59

[40] J. A. Pople, R. Seeger, and R. Krishnan, “Variational configuration interaction methods and comparison with perturbation theory,” *International Journal of Quantum Chemistry*, vol. 12, no. S11, pp. 149–163. [Online]. Available: https://onlinelibrary.wiley.com/doi/abs/10.1002/qua.560120820 59

[41] R. J. Bartlett and G. D. Purvis, “Many-body perturbation theory, coupled-pair many-electron theory, and the importance of quadruple excitations for the correlation problem,” *International Journal of Quantum Chemistry*, vol. 14, no. 5, pp. 561–581. [Online]. Available: https://onlinelibrary.wiley.com/doi/abs/10.1002/qua.560140504 59

[42] W. Kohn, “Nobel lecture: Electronic structure of matter¯wave functions and density functionals,” *Rev. Mod. Phys.*, vol. 71, pp. 1253–1266, Oct 1999. [Online]. Available: http://link.aps.org/doi/10.1103/RevModPhys.71.1253 59

[43] S. H. Vosko, L. Wilk, and M. Nusair, “Accurate spin-dependent electron liquid correlation energies for local spin density calculations: a critical analysis,” *Canadian Journal of Physics*, vol. 58, no. 8, pp. 1200–1211, 1980. [Online]. Available: http://dx.doi.org/10.1139/p80-159 68

[44] J. P. Perdew and Y. Wang, “Accurate and simple analytic representation of the electron-gas correlation energy,” *Phys. Rev. B*, vol. 45, pp. 13 244–13 249, Jun 1992. [Online]. Available: http://link.aps.org/doi/10.1103/PhysRevB.45.13244 68

[45] Perdew, John P. and Wang, Yue, “Accurate and simple analytic representation of the electron-gas correlation energy,” *Phys. Rev. B*, vol. 45, pp. 13 244–13 249, Jun 1992. [Online]. Available: https://link.aps.org/doi/10.1103/PhysRevB.45.13244 69

[46] A. D. Becke, “Density-functional exchange-energy approximation with correct asymptotic behavior,” *Phys. Rev. A*, vol. 38, pp. 3098–3100, Sep 1988. [Online]. Available: https://link.aps.org/doi/10.1103/PhysRevA.38.3098 69

[47] J. P. Perdew, K. Burke, and M. Ernzerhof, “Generalized gradient approximation made simple,” *Phys. Rev. Lett.*, vol. 77, pp. 3865–3868, Oct 1996. [Online]. Available: https://link.aps.org/doi/10.1103/PhysRevLett.77.3865 69

[48] R. Neumann and N. C. Handy, “Higher-order gradient corrections for exchange-correlation functionals,” *Chemical Physics Letters*, vol. 266, no. 1, pp. 16 – 22, 1997. [Online]. Available: http://www.sciencedirect.com/science/article/pii/S0009261496014960 69

[49] J. P. Perdew, S. Kurth, A. Zupan, and P. Blaha, “Accurate density functional with correct formal properties: A step beyond the generalized gradient approximation,” *Phys. Rev. Lett.*, vol. 82, pp. 2544–2547, Mar 1999. [Online]. Available: http://link.aps.org/doi/10.1103/PhysRevLett.82.2544 69

[50] T. V. Voorhis and G. E. Scuseria, “A novel form for the exchange-correlation energy functional,” *The Journal of Chemical Physics*, vol. 109, no. 2, pp. 400–410, 1998. [Online]. Available: http://dx.doi.org/10.1063/1.476577 69

[51] C. Lee, W. Yang, and R. G. Parr, “Development of the colle-salvetti correlation-energy formula into a functional of the electron density,” *Phys. Rev. B*, vol. 37, pp. 785–789, Jan 1988. [Online]. Available: http://link.aps.org/doi/10.1103/PhysRevB.37.785 69

[52] A. D. Becke, “Density-functional thermochemistry. III. The role of exact exchange,” *The Journal of Chemical Physics*, vol. 98, no. 7, pp. 5648–5652, 1993. [Online]. Available: http://dx.doi.org/10.1063/1.464913 69, 70

[53] J. Muscat, A. Wander, and N. Harrison, “On the prediction of band gaps from hybrid functional theory,” *Chemical Physics Letters*, vol. 342, no. 3–4, pp. 397 – 401, 2001. [Online]. Available: //www.sciencedirect.com/science/article/pii/S0009261401006169 70

[54] K. Burke, “Perspective on density functional theory,” *J. Chem. Phys.*, vol. 136, p. 150901, 2012. [Online]. Available: http://link.aip.org/link/doi/10.1063/1.4704546 70

[55] J. P. Perdew, M. Ernzerhof, A. Zupan, and K. Burke, “Nonlocality of the density functional for exchange and correlation: Physical origins and chemical consequences,” *The Journal of Chemical Physics*, vol. 108, no. 4, pp. 1522–1531, 1998. [Online]. Available: http://dx.doi.org/10.1063/1.475524 70

[56] C. Adamo and V. Barone, "Physically motivated density functionals with improved performances: The modified perdew–burke–ernzerhof model," *The Journal of Chemical Physics*, vol. 116, no. 14, pp. 5933–5940, 2002. [Online]. Available: http://dx.doi.org/10.1063/1.1458927 70

[57] J. Heyd, G. E. Scuseria, and M. Ernzerhof, "Hybrid functionals based on a screened coulomb potential," *The Journal of Chemical Physics*, vol. 118, no. 18, pp. 8207–8215, 2003. [Online]. Available: http://dx.doi.org/10.1063/1.1564060 70

[58] J. Israelachvili, *Intermolecular & Surface Forces*, 3rd ed. Elsevier Ltd. Academic Press, 2011. 70

[59] S. Grimme, "Semiempirical gga-type density functional constructed with a long-range dispersion correction," *Journal of Computational Chemistry*, vol. 27, no. 15, pp. 1787–1799. [Online]. Available: https://onlinelibrary.wiley.com/doi/abs/10.1002/jcc.20495 71

[60] S. Grimme, J. Antony, S. Ehrlich, and H. Krieg, "A consistent and accurate ab initio parametrization of density functional dispersion correction (DFT-D) for the 94 elements H-Pu," *The Journal of Chemical Physics*, vol. 132, no. 15, p. 154104, 2010. 71, 126

[61] S. Grimme, S. Ehrlich, and L. Goerigk, "Effect of the damping function in dispersion corrected density functional theory," *Journal of Computational Chemistry*, vol. 32, no. 7, pp. 1456–1465, 2011. [Online]. Available: http://dx.doi.org/10.1002/jcc.21759 71

[62] S. Grimme, A. Hansen, J. G. Brandenburg, and C. Bannwarth, "Dispersion-corrected mean-field electronic structure methods," *Chemical Reviews*, vol. 116, no. 9, pp. 5105–5154, 2016, pMID: 27077966. [Online]. Available: https://doi.org/10.1021/acs.chemrev.5b00533 71

[63] Dovesi, V. R. Saunders, C. Roetti, R. Orlando, C. M. Zicovich-Wilson, F. Pascale, B. Civalleri, K. Doll, N. M. Harrison, I. J. Bush, P. D'Arco, M. Llunell, M. Causà, Y. Noël, L. Maschio, A. Erba, M. Rerat and S. Casassa, "CRYSTAL17 User's Manual," 2017. 71, 90, 173

[64] R. Hoffmann, “How chemistry and physics meet in the solid state,” *Angewandte Chemie International Edition in English*, vol. 26, no. 9, pp. 846–878, 1987. [Online]. Available: http://dx.doi.org/10.1002/anie.198708461 26, 79, 80, 83

[65] http://lampx.tugraz.at/~hadley/ss1/bzones. 26, 84, 86, 87

[66] R. Dovesi, B. Civalleri, C. Roetti, V. R. Saunders, and R. Orlando, *Ab Initio Quantum Simulation in Solid State Chemistry.* John Wiley and Sons, Inc., 2005, pp. 1–125. 90, 126

[67] C. Pisani, R. Dovesi, and C. Roetti, *Hartree-Fock Ab Initio Treatment of Crystalline Solids, Lecture Notes in Chemistry, Vol. 48.* Springer, Berlin Heidelberg New York, 1988. 90

[68] C. Pisani, *Quantum-Mehanial Ab-Initio Calulation of the Properties of Crystalline Materials, Lecture Notes in Chemistry, Vol. 67.* Springer Verlag, Berlin, 1996. 90, 126

[69] R. Dronskowski, *Computational Chemistry of Solid State Materials.* Wiley, Weinheim, 2005. 126

[70] F. D. Murnaghan, “The compressibility of media under extreme pressures,” *Proceedings of the National Academy of Sciences*, vol. 30, no. 9, pp. 244–247, 1944. [Online]. Available: http://www.pnas.org/content/30/9/244 126

[71] F. Birch, “Finite elastic strain of cubic crystals,” *Phys. Rev.*, vol. 71, pp. 809–824, Jun 1947. [Online]. Available: https://link.aps.org/doi/10.1103/PhysRev.71.809 126, 142

[72] J.-P. Poirier and A. Tarantola, “A logarithmic equation of state,” *Physics of the Earth and Planetary Interiors*, vol. 109, no. 1, pp. 1 – 8, 1998. [Online]. Available: http://www.sciencedirect.com/science/article/pii/S0031920198001125 126

[73] P. Vinet, J. Ferrante, J. R. Smith, and J. H. Rose, “A universal equation of state for solids,” *Journal of Physics C: Solid State Physics*, vol. 19, no. 20, p. L467, 1986. [Online]. Available: http://stacks.iop.org/0022-3719/19/i=20/a=001 126

[74] M. Marshall and H. Leung, *Solutions manual to accompany Quantum chemistry.* University Science Books, U.S., 2007. 27, 129

[75] N. W. Ashcroft and M. N. D, *Solid State Physics.* Holt, Rinehart and Winston, 1976. 141

[76] S. Baroni, P. Giannozzi, and E. Isaev, “Density-functional perturbation theory for quasi-harmonic calculations,” *Reviews in Mineralogy and Geochemistry*, vol. 71, no. 1, p. 39, 2010. [Online]. Available: +http://dx.doi.org/10.2138/rmg.2010.71.3 141

[77] A. A. Maradudin, E. W. Montroll, and G. H. Weiss, *Theory of Lattice Dynamics in the Harmonic Approximation, Vol. 3.* Academic, New York, 1963. 142

[78] R. E. Allen and F. W. de Wette, “Calculation of dynamical surface properties of noble-gas crystals. I. the quasiharmonic approximation,” *Phys. Rev.*, vol. 179, pp. 873–886, Mar 1969. 142

[79] L. L. Boyer, “Calculation of thermal expansion, compressiblity, an melting in alkali halides: NaCl and KCl,” *Phys. Rev. Lett.*, vol. 42, pp. 584–587, Feb 1979. 142

[80] A. Erba, “On combining temperature and pressure effects on structural properties of crystals with standard ab initio techniques,” *The Journal of Chemical Physics*, vol. 141, no. 12, p. 124115, 2014. [Online]. Available: https://doi.org/10.1063/1.4896228 145, 190

[81] M. Neff and G. Rauhut, “Toward large scale vibrational configuration interaction calculations,” *The Journal of Chemical Physics*, vol. 131, no. 12, p. 124129, 2009. [Online]. Available: https://doi.org/10.1063/1.3243862 145

[82] J. O. Jung and R. B. Gerber, “Vibrational wave functions and energy levels of large anharmonic clusters: A vibrational scf study of (ar)13,” *The Journal of Chemical Physics*, vol. 105, no. 24, pp. 10 682–10 690, 1996. [Online]. Available: https://doi.org/10.1063/1.472876 145

[83] C. Y. Lin, A. T. B. Gilbert, and P. M. W. Gill, “Calculating molecular vibrational spectra beyond the harmonic approximation,” *Theoretical Chemistry Accounts*, vol. 120, no. 1, pp. 23–35, May 2008. [Online]. Available: https://doi.org/10.1007/s00214-007-0292-8 145

[84] D. A. Broido, M. Malorny, G. Birner, N. Mingo, and D. A. Stewart, “Intrinsic lattice thermal conductivity of semiconductors from first principles,” *Applied Physics Letters*,

vol. 91, no. 23, p. 231922, 2007. [Online]. Available: https://doi.org/10.1063/1.2822891 145

[85] D. Vanderbilt, S. H. Taole, and S. Narasimhan, "Anharmonic elastic and phonon properties of si," *Phys. Rev. B*, vol. 40, pp. 5657–5668, Sep 1989. [Online]. Available: https://link.aps.org/doi/10.1103/PhysRevB.40.5657 145

[86] P.-C. Chen, C. Y. Tai, and K. Lee, "Morphology and growth rate of calcium carbonate crystals in a gas-liquid-solid reactive crystallizer," *Chemical Engineering Science*, vol. 52, no. 21–22, pp. 4171 – 4177, 1997. [Online]. Available: http://www.sciencedirect.com/science/article/pii/S0009250997002595 149

[87] D. Kralj, L. Brečević, and A. E. Nielsen, "Vaterite growth and dissolution in aqueous solution i. kinetics of crystal growth," *Journal of Crystal Growth*, vol. 104, no. 4, pp. 793 – 800, 1990. [Online]. Available: http://www.sciencedirect.com/science/article/pii/002202489090104S 149

[88] Y. Sheng Han, G. Hadiko, M. Fuji, and M. Takahashi, "Crystallization and transformation of vaterite at controlled pH," *Journal of Crystal Growth*, vol. 289, no. 1, pp. 269–274, 2006. 149

[89] Y. Han, G. Hadiko, M. Fuji, and M. Takahashi, "Crystallization and transformation of vaterite at controlled ph," *Journal of Crystal Growth*, vol. 289, pp. 269 – 274, 2006. 149

[90] J. Wang and U. Becker, "Structure and carbonate orientation of vaterite (caco$_3$)," *American Mineralogist*, vol. 94, pp. 380 – 386, 2009. 149, 151, 163

[91] A. Turnbull, "A thermochemical study of vaterite," *Geochimica et Cosmochimica Acta*, vol. 37, pp. 1593 – 1601, 1973. 149

[92] D. J. Sutor and S. E. Wooley, "X-ray diffraction studies of the composition of gallstones from english and australian patients," *Science*, vol. 159, p. 1113, 1968. 149

[93] R. R. Lakshminarayanan, E. O. Chi-Jin, X. J. Loh, R. M. Kini, and S. Valiyaveettil, "Purification and characterization of a vaterite-inducing peptide, pelovaterin, from the eggshells of pelodiscus sinensis (chinese soft-shelled turtle)," *Biomacromolecules*, vol. 6, p. 1429, 2005. 149

[94] U. Wehrmeister, D. E. Jacob, A. L. Soldati, N. Loges, T. Häger, and W. Hofmeister, "Amorphous, nanocrystalline and crystalline calcium carbonates in biological materials," *J. Raman Spectrosc.*, vol. 42, p. 926, 2010. 149, 151, 162

[95] L. Qiao, F. Qing-Ling, and L. Zhuo, "Special vaterite found in freshwater lackluster pearls," *Cryst. Growth Des.*, vol. 7, pp. 275 – 279, 2007. 149

[96] M.-P. Isaure, G. Sarret, E. Harada, Y.-E. Choi, M. A. Marcus, S. C. Fakra, N. Geoffroy, S. Pairis, J. Susini, S. Clemens, and A. Manceau, "Calcium promotes cadmium elimination as vaterite grains by tobacco trichomes," *Geochimica et Cosmochimica Acta*, vol. 74, no. 20, pp. 5817 – 5834, 2010. [Online]. Available: http://www.sciencedirect.com/science/article/pii/S001670371000400X 150

[97] L. Kabalah-Amitai, B. Mayzel, Y. Kauffmann, A. N. Fitch, L. Bloch, P. U. P. A. Gilbert, and B. Pokroy, "Vaterite crystals contain two interspersed crystal structures," vol. 340, no. 6131, pp. 454–457, 2013. 150, 151, 163

[98] G. Falini, S. Fermani, M. Gazzano, and A. Ripamonti, "Oriented crystalization of vaterite in collagenous matrices," *Chemistry: A European Journal*, vol. 4, pp. 1048 – 1052, 1998. 150

[99] S. Champ, J. A. Dickinson, P. S. Fallon, B. R. Heywood, and M. Mascal, "Hydrogen-bonded molecular ribbons as templates for the synthesis of modified mineral phases," *Angewandte Chemie International Edition*, vol. 39, pp. 2716 – 2719, 2000. 150

[100] S. K. Medeiros, E. L. Albuquerque, F. F. Maia, E. W. S. Caetano, and V. N. Freire, "First-principles calculations of structural, electronic, and optical absorption properties of $CaCO_3$ vaterite," *Chemical Physics Letters*, vol. 435, pp. 59 – 64, 2007. 150, 151, 163

[101] H. J. Meyer, *Angew. Chem.*, vol. 71, p. 678, 1959. 151, 161

[102] Meyer, H. J., *Fortsch. Mineral.*, vol. 38, p. 186, 1960. 151, 161, 163

[103] S. K. Medeiros, E. L. Albuquerque, F. F. Maia, E. W. S. Caetano, and V. N. Freire, "On the structure of vaterite $CaCO_3$," *Acta Crystallographica*, vol. 16, pp. 770 – 772, 1963. 151, 161

[104] H. J. Meyer, "Struktur und fehlordnung des vaterits," *Zeitschrift fur Kristallographie*, vol. 128, pp. 183 – 212, 1969. 151, 162

[105] F. Lippmann, "Sedimentary carbonate materials," *Zeitschrif*, vol. 128, pp. 183 – 212, 1969. 151, 162

[106] C. Gabrielli, R. Jaouhari, S. Joiret, and G. Maurin, *J. Raman Spectrosc.*, vol. 31, p. 497, 2000. 151, 162

[107] A. Le Bail, S. Ouhenia, and D. Chateigner, *Powder Diffraction*, vol. 26, p. 16, 2011. 151, 162

[108] E. Mugnaioli, A. Iryna, T. Schüler, N. Loges, and E. R. Dinnebier, *Angew. Chem.*, vol. 51, pp. 7041 – 7045, 2012. 151, 162

[109] R. Demichelis, P. Raiteri, J. D. Gale, and R. Dovesi, "The multiple structures of vaterite," *Crystal Growth and Design*, vol. 13, no. 6, pp. 2247–2251, 2013. 151, 163, 164

[110] R. Demichelis, P. Raiteri, J. Gale, and R. Dovesi, "A new structural model for disorder in vaterite from first-principles calculations," *Cryst. Eng. Comm.*, vol. 14, no. 21, p. 44, 2012. 151, 163

[111] K. M. N. Burgess and D. L. Bryce, "On the crystal structure of the vaterite polymorph of $CaCO_3$: A calcium-43 solid-state nmr and computational assessment," *Solid State Nuclear Magnetic Resonance*, vol. 65, pp. 75 – 83, 2015. 28, 151, 162, 164

[112] Y. Li, Y. T. Zou, T. Chen, X. Wang, X. T. Qi, H. Y. Chen, J. G. Du, and B. S. Li, "P-v-t equation of state and high-pressure behavior of caco3 aragonite," *American Mineralogist*, vol. 100, pp. 2323 – 2329, 2015. 151

[113] P. Bridgman, "The high pressure behaviour of miscellaneous minerals," *Amer. Jour. Sci.*, vol. 237, pp. 7 – 18, 1939. 31, 33, 151, 186, 187, 217, 242

[114] L. Merrill and W. Bassett, "The crystal structure of $CaCO_3$ (II), a high-pressure metastable phase of calcium carbonate," *Acta Cryst.*, vol. B31, pp. 343 – 349, 1975. 151, 165, 186, 189, 194

[115] B. Davis, "X-ray diffraction data on two high- pressure phases of calcium carbonate," *Science*, vol. 145, pp. 489–491, 1964. 151

[116] M. Fong and M. Nicol, "Raman spectrum of calcium carbonate at high pressures," *J. Chem. Phys.*, vol. 16, pp. 579 – 585, 1971. 151

[117] D. Vo-Thanh and A. Lacam, "Experimental study of the elasticity of single crystalline calcite under high pressure (the calcite-i/calcite-ii transition at 14.6 kbar)," *Phys. Earth Planet. Int.*, vol. 34, pp. 195 – 203, 1984. 151

[118] M. Y. Fong and M. Nicol, "Raman spectrum of calcium carbonate at high pressures," *The Journal of Chemical Physics*, vol. 54, no. 2, pp. 579–585, 1971. [Online]. Available: http://scitation.aip.org/content/aip/journal/jcp/54/2/10.1063/1.1674881 151

[119] N. Hess, G. Exarhos, and S. Ghose, *Raman spectroscopy at simultaneous pressure and temperature: Phase relations and lattice dynamics of* $CaCO_3$. In: Singh AK (ed) Recent trends in high pressure research: proceed- ings XIIIth AIRAPT international conference on high pressure science and technology, Oxford, New Delhi, pp 236–241, Oct 1991. 31, 33, 151, 186, 187, 217, 242

[120] L. G. Liu and T. P. Mernagh, "Phase transitions and raman spectra of calcite at high pressures and room temperature," *Am. Mineral.*, vol. 75, pp. 801 – 806, 1990. 151

[121] G. Fiquet, F. Guyot, and J. P. Itie, "High-pressure x-ray diffraction study of carbonates: $Mgco_3$, $camg(co_3)_2$, and $caco_3$," *Am. Mineral.*, vol. 79, pp. 15 –23, 1994. 151

[122] J. R. Smyth and T. J. Ahrens, "The crystal structure of calcite iii," *Geophys. Res. Lett.*, vol. 24, pp. 1595 – 1598, 1997. 151

[123] K. Hagiya, M. Matsui, Y. Kimura, and Y. Akahama, "The crystal data and stability of calcite iii at high pressures based on single-crystal x-ray experiments," *J. Min. Pet. Sci.*, vol. 100, pp. 31 – 36, 2005. 151

[124] J. A. Tyburczy and T. J. Ahrens, "Dynamic compression and volatile release of carbonates," *Journal of Geophysical Research: Solid Earth*, vol. 91, no. B5, pp. 4730–4744, 1986. [Online]. Available: http://dx.doi.org/10.1029/JB091iB05p04730 152

[125] K. Catalli and Q. Williams, "A high-pressure phase transition of calcite-iii," *Am. Mineral.*, vol. 90, pp. 1679 – 1682, 2005. 152

[126] H. Boeke, “Die Schmelzerscheinungen und die umkehrbare Umwandlung des Calciumcarbonats.” *N. Jb. Mineral.*, vol. 1, pp. 91 – 121, 1912. 152

[127] L. Cohen and W. Klement, “Determination of high temperature transition in calcite to 5 kbar by differential thermal analysis in hydrostatic apparatus,” *J. Geol.*, vol. 81, pp. 724 – 726, 1973. 152

[128] P. Mirwald, “A differential thermal analysis study of the high-temperature polymorphism of calcite at high pressure.” *Contrib. Mineral. Petrol.*, vol. 59, pp. 33 – 44, 1976. 152, 252

[129] Mirwald, P.W., “The electrical conductivity of calcite between 300 and 1200$\circ$C at a CO_2 pressure of 40 bars.” *Phys. Chem. Minerals*, vol. 4, pp. 291 – 297, 1979. 152

[130] M. Dove and B. Powell, “Neutron diffraction study of the tricritical orientational order/disorder phase transition in calcite at 1260 K,” *Phys. Chem. Minerals*, vol. 16, pp. 503 – 507, 1989. 152

[131] N. Ishizawa, H. Setoguchi, and K. Yanagisawa, “Structural evolution of calcite at high temperatures: Phase v unveiled,” *Sci Rep.*, vol. 3, p. 2832, 2013. 29, 152, 170, 172

[132] A. J. Irving and P. J. Wyllie, “Subsolidus and melting relationships for calcite, magnesite and the join caco3-mgco3 36 kb,” *Geochimica et Cosmochimica Acta*, vol. 39, no. 1, pp. 35 – 53, 1975. [Online]. Available: http://www.sciencedirect.com/science/article/pii/0016703775901830 153

[133] E. N. Maslen, S. V. A., and N. R. Streltsova, “X-ray study of the electron density in calcite, $caco_3$,” *Acta Cryst.*, vol. B49, pp. 636 – 641, 1993. 158

[134] A. Dal Negro and L. Ungarett, “Refinement of crystal structure of aragonite,” *American Mineralogist*, vol. 56, p. 768, 1971. 160

[135] J. P. R. Villiers, “Crystal structures of aragonite, strontianite, and witherite,” *American Mineralogist*, vol. 56, pp. 758 – 767, 1971. 160

[136] D. M. Hatch and L. Merrill, “Landau description of the calcite-$CaCO_3$(II) phase transition,” *Phys. Rev. B*, vol. 23, pp. 368–374, Jan 1981. [Online]. Available: https://link.aps.org/doi/10.1103/PhysRevB.23.368 165, 186, 187, 189, 238

[137] C. Biellmann and G. P. Guyot, F. and, "High-pressure stability of carbonates: quenching of calcite-II, high-pressure polymorph of $CaC0_3$," *Eur. J. Mineral.*, vol. 5, pp. 503 – 510, 1993. 165

[138] M. T. Dove, I. P. Swainson, B. M. Powell, and D. C. Tennant, "Neutron powder diffraction study of the orientational order–disorder phase transition in calcite, $caco_3$," *Phys. Chem. Minerals*, vol. 32, pp. 493 – 503, 2005. 170

[139] L. Valenzano, F. T. Torres, K. Doll, F. Pascale, C. M. Zicovich-Wilson, and R. Dovesi, "Ab initio study of the vibrational spectrum and related properties of crystalline compounds; the case of $CaCO_3$ calcite," *Z. Phys. Chem.*, vol. 220, pp. 893 – 912, 2006. 173

[140] J. D. Pack and H. J. Monkhorst, "Special points for brillouin-zone integrations," *Phys. Rev. B*, vol. 16, pp. 1748–1749, Aug 1977. 173

[141] A. Erba, A. Mahmoud, D. Belmonte, and R. Dovesi, "High pressure elastic properties of minerals from ab initio simulations: The case of pyrope, grossular and andradite silicate garnets," *The Journal of Chemical Physics*, vol. 140, no. 12, p. 124703, 2014. [Online]. Available: https://doi.org/10.1063/1.4869144 175, 188, 190

[142] M. F. Peintinger, D. V. Oliveira, and T. Bredow, "Consistent gaussian basis sets of triple-zeta valence with polarization quality for solid-state calculations," *Journal of Computational Chemistry*, vol. 34, no. 6, pp. 451–459, 2013. [Online]. Available: http://dx.doi.org/10.1002/jcc.23153 175

[143] Mulliken, R. S., "Electronic population analysis on LCAO-MO molecular wave functions. I," *The Journal of Chemical Physics*, vol. 23, no. 10, pp. 1833–1840, 1955. [Online]. Available: https://doi.org/10.1063/1.1740588 180

[144] R. S. Mulliken, "Electronic population analysis on LCAO-MO molecular wave functions. II. overlap populations, bond orders, and covalent bond energies," *The Journal of Chemical Physics*, vol. 23, no. 10, pp. 1841–1846, 1955. [Online]. Available: https://doi.org/10.1063/1.1740589 180

[145] Mulliken, R. S., "Electronic population analysis on LCAO-MO molecular wave functions. III. effects of hybridization on overlap and gross AO populations," *The*

Journal of Chemical Physics, vol. 23, no. 12, pp. 2338–2342, 1955. [Online]. Available: https://doi.org/10.1063/1.1741876 180

[146] R. S. Mulliken, "Electronic population analysis on LCAO-MO molecular wave functions. IV. Bonding and antibonding in LCAO and valence-bond theories," *The Journal of Chemical Physics*, vol. 23, no. 12, pp. 2343–2346, 1955. [Online]. Available: https://doi.org/10.1063/1.1741877 180

[147] P.-O. Löwdin, "On the nonorthogonality problem," ser. Advances in Quantum Chemistry, P.-O. Löwdin, Ed. Academic Press, 1970, vol. 5, pp. 185 – 199. [Online]. Available: http://www.sciencedirect.com/science/article/pii/S0065327608603391 180

[148] A. E. Reed, R. B. Weinstock, and F. Weinhold, "Natural population analysis," *The Journal of Chemical Physics*, vol. 83, no. 2, pp. 735–746, 1985. [Online]. Available: https://doi.org/10.1063/1.449486 180

[149] J. P. Foster and F. Weinhold, "Natural hybrid orbitals," *Journal of the American Chemical Society*, vol. 102, no. 24, pp. 7211–7218, 1980. [Online]. Available: https://doi.org/10.1021/ja00544a007 180

[150] A. E. Reed, L. A. Curtiss, and F. Weinhold, "Intermolecular interactions from a natural bond orbital, donor-acceptor viewpoint," *Chemical Reviews*, vol. 88, no. 6, pp. 899–926, 1988. [Online]. Available: https://doi.org/10.1021/cr00088a005 180

[151] R. Bader and T. Nguyen-Dang, "Quantum theory of atoms in molecules–dalton revisited," ser. Advances in Quantum Chemistry, P.-O. Löwdin, Ed. Academic Press, 1981, vol. 14, pp. 63 – 124. [Online]. Available: http://www.sciencedirect.com/science/article/pii/S0065327608603263 180

[152] R. F. W. Bader, *Atoms in molecules: a quantum theory.* International Series of Monographs on Chemistry, 1994. 180

[153] Bader, R. F. W., "A quantum theory of molecular structure and its applications," *Chemical Reviews*, vol. 91, no. 5, pp. 893–928, 1991. [Online]. Available: https://doi.org/10.1021/cr00005a013 180

[154] D. Baer and D. L. Blanchard, "Studies of the calcite cleavage surface for comparison with calculation," *Applied Surface Science*, vol. 72, no. 4, pp. 295 – 300, 1993. [Online]. Available: http://www.sciencedirect.com/science/article/pii/016943329390365I 182, 183

[155] J. Muscat, A. Wander, and N. M. Harrison, "On the prediction of band gaps from hybrid functional theory," *Chem. Phys. Lett*, vol. 342, pp. 397 – 401, 2001. 182

[156] J. D. Barnett, H. M. Nelson, and S. D. Tyagi, "High-pressure EPR study of the calcite-$CaCO_3$(II) displacive phase transformation near 1.6 GPa," *Phys. Rev. B*, vol. 31, pp. 1248–1257, Feb 1985. 186

[157] S. Kondo, K. Suito, and S. Matsushima, "Ultrasonic observation of calcite I-II inversion to 700°C," *Journal of Physics of the Earth*, vol. 20, no. 3, pp. 245–250, 1972. 186, 187, 238

[158] C.-Y. Wang, "Ultrasonic study of phase transition in calcite to 20 kilobars and 180°C," *Journal of Geophysical Research*, vol. 73, no. 12, pp. 3937–3944, 1968. 31, 33, 186, 187, 217, 242

[159] J. D. Barnett and H. M. Nelson, "Preliminary EPR study of a solid-solid critical point in $CaCO_3$ near 200°C and 1.5 GPa," *Phys. Rev. B*, vol. 33, pp. 4464–4470, Apr 1986. 33, 186, 187, 238, 242

[160] S. N. Vaidya, S. Bailey, T. Pasternack, and G. C. Kennedy, "Compressibility of fifteen minerals to 45 kilobars," *Journal of Geophysical Research*, vol. 78, no. 29, pp. 6893–6898, 1973. 186

[161] A. K. Singh and G. C. Kennedy, "Compression of calcite to 40 Kb," *Journal of Geophysical Research*, vol. 79, no. 17, pp. 2615–2622, 1974. 186, 267

[162] M. Y. Fong and M. Nicol, "Raman spectrum of calcium carbonate at high pressures," *The Journal of Chemical Physics*, vol. 54, no. 2, pp. 579–585, 1971. [Online]. Available: https://doi.org/10.1063/1.1674881 187

[163] J. W. Felix and D. M. Hatch, "New fluctuation-induced first-order antiferrodistortive phase transitions," *Phys. Rev. Lett.*, vol. 53, pp. 2425–2428, Dec 1984. [Online]. Available: https://link.aps.org/doi/10.1103/PhysRevLett.53.2425 187, 238

[164] T. D. Archer, S. E. A. Birse, M. T. Dove, S. A. T. Redfern, J. D. Gale, and R. T. Cygan, "An interatomic potential model for carbonates allowing for polarization effects," *Physics and Chemistry of Minerals*, vol. 30, no. 7, pp. 416–424, Aug 2003. [Online]. Available: https://doi.org/10.1007/s00269-002-0269-z 187

[165] J. Kawano, A. Miyake, N. Shimobayashi, and M. Kitamura, "Molecular dynamics simulation of the phase transition between calcite and $CaCO_3$-II." *Journal of physics. Condensed matter : an Institute of Physics journal*, vol. 21, no. 27, p. 275403, 2009. [Online]. Available: http://www.ncbi.nlm.nih.gov/pubmed/21828487 187

[166] M. Ukita, K. Toyoura, A. Nakamura, and K. Matsunaga, "Pressure-induced phase transition of calcite and aragonite: A first principles study," *Journal of Applied Physics*, vol. 120, no. 14, p. 142118, 2016. [Online]. Available: http://dx.doi.org/10.1063/1.4961723 187, 191

[167] M.-S. Miao, "Caesium in high oxidation states and as a p-block element," *Nature Chemistry*, vol. 5, no. 10, September 2013. 189

[168] F. Pascale, C. M. Zicovich-Wilson, F. López Gejo, B. Civalleri, R. Orlando, and R. Dovesi, "The calculation of the vibrational frequencies of crystalline compounds and its implementation in the crystal code," *Journal of Computational Chemistry*, vol. 25, no. 6, pp. 888–897, 2004. [Online]. Available: http://dx.doi.org/10.1002/jcc.20019 190

[169] C. M. Zicovich-Wilson, F. Pascale, C. Roetti, V. R. Saunders, R. Orlando, and R. Dovesi, "Calculation of the vibration frequencies of α-quartz: The effect of hamiltonian and basis set," *Journal of Computational Chemistry*, vol. 25, no. 15, pp. 1873–1881, 2004. [Online]. Available: http://dx.doi.org/10.1002/jcc.20120 190

[170] A. Erba, M. Ferrabone, R. Orlando, and R. Dovesi, "Accurate dynamical structure factors from ab initio lattice dynamics: The case of crystalline silicon," *Journal of Computational Chemistry*, vol. 34, no. 5, pp. 346–354, 2013. [Online]. Available: http://dx.doi.org/10.1002/jcc.23138 190

[171] K. Parlinski, Z. Q. Li, and Y. Kawazoe, "First-principles determination of the soft mode in cubic ZrO_2," *Phys. Rev. Lett.*, vol. 78, pp. 4063–4066, May 1997. [Online]. Available: https://link.aps.org/doi/10.1103/PhysRevLett.78.4063 190

[172] A. Togo, F. Oba, and I. Tanaka, "First-principles calculations of the ferroelastic transition between rutile-type and cacl$_2$-type sio$_2$ at high pressures," *Phys. Rev. B*, vol. 78, p. 134106, Oct 2008. [Online]. Available: https://link.aps.org/doi/10.1103/PhysRevB.78.134106 190

[173] [Online]. Available: http://davidcdeb.com/calcite_vibs/Jmolvib/index.html?name=calcite_II.xyz&spt=calcite_II.spt 30, 191

[174] H. T. Stokes and D. M. Hatch, "*FINDSYM*: program for identifying the space-group symmetry of a crystal," *Journal of Applied Crystallography*, vol. 38, no. 1, pp. 237–238, Feb 2005. [Online]. Available: https://doi.org/10.1107/S0021889804031528 192, 253

[175] [Online]. Available: https://github.com/DavidCdeB/search_neg_freqs 198, 265

[176] T. Björkman, "Cif2cell: Generating geometries for electronic structure programs," *Computer Physics Communications*, vol. 182, no. 5, pp. 1183 – 1186, 2011. [Online]. Available: http://www.sciencedirect.com/science/article/pii/S0010465511000336 199

[177] [Online]. Available: https://github.com/DavidCdeB/EOS_2_phonons 199, 265

[178] "Bradley Hacker's lecture notes," http://www.geol.ucsb.edu/faculty/hacker/geo124T/lecture.html. 31, 206

[179] [Online]. Available: https://github.com/DavidCdeB/QHA_3D 209, 265

[180] [Online]. Available: https://github.com/DavidCdeB/QHA_2D 211, 266

[181] A. Erba, M. Shahrokhi, R. Moradian, and R. Dovesi, "On how differently the quasi-harmonic approximation works for two isostructural crystals: Thermal properties of periclase and lime," *The Journal of Chemical Physics*, vol. 142, no. 4, p. 044114, 2015. [Online]. Available: https://doi.org/10.1063/1.4906422 212

[182] [Online]. Available: https://github.com/DavidCdeB/ENTROPY_PDOS 220, 266

[183] [Online]. Available: http://davidcdeb.com/calcite_vibs/Jmolvib/CII_SCELPHONO_200_020_002_V_218/index.html?name=calcite_2x2x2_version_2.xyz&spt=calcite_2x2x2_version_2.spt 32, 225, 226

[184] I. Errea, B. Rousseau, and A. Bergara, “Anharmonic stabilization of the high-pressure simple cubic phase of calcium,” *Phys. Rev. Lett.*, vol. 106, p. 165501, Apr 2011. [Online]. Available: https://link.aps.org/doi/10.1103/PhysRevLett.106.165501 233

[185] R. Clarke and L. Benguigui, “The tricritical point in $BaTiO_3$,” *Journal of Physics C: Solid State Physics*, vol. 10, no. 11, p. 1963, 1977. [Online]. Available: http://stacks.iop.org/0022-3719/10/i=11/a=030 238

[186] A. Aharony and A. D. Bruce, “Polycritical points and floplike displacive transitions in perovskites,” *Phys. Rev. Lett.*, vol. 33, pp. 427–430, Aug 1974. [Online]. Available: https://link.aps.org/doi/10.1103/PhysRevLett.33.427 238

[187] [Online]. Available: https://github.com/DavidCdeB/Common_Tangent 245, 266

[188] W. A. Crawford and W. S. Fyfe, “Calcite-aragonite equilibrium at 100°c,” *Science*, vol. 144, no. 3626, pp. 1569–1570, 1964. [Online]. Available: http://science.sciencemag.org/content/144/3626/1569 252

[189] W. Johannes and D. Puhan, “The caleite-aragonite transition, reinvestigated,” *Contr. Mineral. and Petrol.*, vol. 31, p. 28, 1971. 252

[190] W. D. Carlson, “The calcite-araqonite equilibrium: effects of sr substitution and anion orientational disorder,” *American Mineralogist*, vol. 65, pp. 1252–1262, 1980. 252

[191] G. Wolf, J. Lerchner, H. Schmidt, H. Gamsjäger, E. Königsberger, and P. Schmidt, “Thermodynamics of $CaCO_3$ phase transitions,” *Journal of Thermal Analysis*, vol. 46, no. 2, pp. 353–359, 1996. 253

[192] E. Königsberger, L.-C. Königsberger, and H. Gamsjäger, “Low-temperature thermodynamic model for the system Na_2CO_3-$MgCO_3$-$CaCO_3$-H_2O,” *Geochimica et Cosmochimica Acta*, vol. 63, no. 19, pp. 3105 – 3119, 1999. [Online]. Available: http://www.sciencedirect.com/science/article/pii/S0016703799002380 253

[193] T. A. Paoletti, A., *The Physics of Diamond*, 1997. 263

[194] [Online]. Available: https://github.com/DavidCdeB/supercell_generator 266